THESIS FOR THE DEGREE OF DOCTOR OF PHILOSOPHY

Electromagnetic Modeling based Life Cycle Assessment of Rare-Earth-Free Propulsion Electric Machines for Vehicles

Meng-Ju Hsieh

Department of Electrical Engineering
Chalmers University of Technology
Gothenburg, Sweden, 2025

Electromagnetic Modeling based Life Cycle Assessment of Rare-Earth-Free Propulsion Electric Machines for Vehicles

Meng-Ju Hsieh
ISBN 978-91-8103-331-1

Acknowledgements, dedications, and similar personal statements in this thesis, reflect the author's own views.

Doktorsavhandlingar vid Chalmers tekniska högskola
Ny serie nr 5788
ISSN 0346-718X

Department of Electrical Engineering
Chalmers University of Technology
SE-412 96 Gothenburg, Sweden
Phone: +46 (0)31 772 1000

Cover:
The scope of this work.

Printed by Chalmers Digital Printing
Gothenburg, Sweden, December 2025

Electromagnetic Modeling based Life Cycle Assessment of Rare-Earth-Free Propulsion Electric Machines for Vehicles

Meng-Ju Hsieh
Department of Electrical Engineering
Chalmers University of Technology

Abstract

This work evaluates representative automotive electric traction machines (e-machines) that do not rely on rare-earth elements (REEs) using finite element method (FEM) simulations and life cycle assessment (LCA) to compare their technical and environmental performance against PMSMs with REE-based magnets. The alternative machine types considered are the induction machine (IM), synchronous reluctance machine (SynRM), and electrically excited synchronous machine (EESM). Specifically, three IM configurations, two SynRM configurations, and two EESM configurations were analyzed, incorporating different combinations of conductor materials, aluminum (Al) and copper (Cu).

The analysis reveals that Cu-based configurations generally exhibit lower greenhouse gas (GHG) emissions due to superior efficiency and power density, while Al-based machines demonstrate reduced environmental impacts in categories such as toxicity and acidification. Notably, EESM and IM, both utilizing full copper conductors, emerge as promising alternatives to the Ref. PMSM in terms of global warming potential for high- or low-GHG electricity scenarios.

Beyond baseline comparisons, the study explores strategies for further GHG reduction, including the use of green virgin aluminum and improved material utilization during the punching process of electrical steel sheets, collectively referred to as "green manufacturing." A sensitivity analysis on magnet production further suggests that, under favorable conditions, REE-free machines with Al conductors may achieve a lower carbon footprint than for the Ref. PMSM.

This work underscores the environmental trade-offs inherent in e-machine selection for EVs and highlights the critical importance of sustainable materials and manufacturing practices in future e-machine design, in addition to

high efficiency and power density.

Keywords: Life cycle assessment (LCA), Electric vehicle, Electric traction machine, rare-earth-element-free, Induction machine (IM), Synchronous reluctance machine (SynRM), Electrically excited synchronous machine (EESM)

List of Publications

[A] **Meng-Ju Hsieh**, Emma Grunditz, and Torbjörn Thiringer, "Improved Parametric Representation of IM from FEM for More Accurate Torque Predictions". In *2022 International Conference on Electrical Machines (ICEM)*, pages 599–605, 2022.

[B] **Meng-Ju Hsieh**, and Torbjörn Thiringer, "An alternative to determine IM parameters trends affected by magnetic saturation using two-stage flux-decay test by FEM". In *In 2023 IEEE International Electric Machines & Drives Conference (IEMDC)*, pages 1–5, 2023.

[C] **Meng-Ju Hsieh**, and Torbjörn Thiringer, "Maximum Torque Control Operating Points Estimation for Variable-Speed IM Applications by Parameter-Based Model". In *IECON 2023- 49th Annual Conference of the IEEE Industrial Electronics Society*, pages 1–6, 2023.

[D] **Meng-Ju Hsieh**, Emma Grunditz, Torbjörn Thiringer, "Improved parametric representation of IM from FEM for more accurate torque predictions: Simulations and experimental validations". Published in *IEEE Transactions on Industry Applications*, 2024.

[E] **Meng-Ju Hsieh**, Anders Nordelöf, Emma Grunditz, Torbjörn Thiringer, "Life cycle assessment of electric traction induction machines". *The International Journal of Life Cycle Assessment*, 2025 **(Accepted)**.

Contents

Acknowledgments

I sincerely appreciate the financial support from the Swedish Electromobility Center and the Swedish Energy Agency.

I want to express my deepest gratitude to my supervisor, Torbjörn Thiringer, for his invaluable guidance, encouragement, and insightful comments throughout my Ph.D. journey. His support has been instrumental in my professional and personal growth. I would also like to thank my co-supervisors, Emma Grunditz and Anders Nordelöf, for their guidance on writing and for the valuable discussions that contributed to the completion of this work. I am also grateful to my examiner, Ola Carlson, for his advice on study planning. Special thanks to my former office mates, Zeyang Geng and Elizabeth Jansson, as well as other amazing colleagues, Chengjun Tang, Babak Alikhanzadehalamdari, Sima Soltanipour, Sepideh Amirpour, Daniel Poposki, Peiyuan Chen, Evelina Wikner, Sindhu Kanya, and Qixuan Wang, for their kindness and for creating a warm and welcoming working environment.

I am also thankful to the members of the reference group for this project: Joachim Lindström, Zhe Huang, Rasmus Andersson, Alexandra Tokat, Sandra Eriksson, and Marcelo Silva, for the insightful discussions and enjoyable afterwork gatherings.

Finally, I am deeply thankful to my partner, Shao-Lien Hung, and our two cats for their love and unwavering support, and to my friends and family for shaping the person I am today.

Meng-Ju Hsieh
Gothenburg, Sweden
November, 2025

Acronyms

GHG	Green House Gas
EV	Electric Vehicle
e-machine	Electrical Traction Machine
PMSM	Permanent Magnet Synchronous Machine
REE	Rare-earth Element
REE-free	Rare-earth-element-free
IM	Induction Machine
SynRM	Synchronous Reluctance Machine
EESM	Electrical Excited Synchronous Machine
FEM	Finite Element Method
PI	Proportional-Integral
V/f	Volts-per-Hertz
MPC	Model Predictive Control
DTC	Direct Torque Control
FOC	Field-Oriented Control
PWM	Pulse Width Modulation
MTC	Maximum Torque Control
MTPA	Maximum Torque per ampere
FW	Field-Weakening
MTPV	Maximum Torque per Voltage
IGFM	inverse Γ-form model

EMF	Electromotive Force
LCA	Life Cycle Assessment
LCI	Life Cycle Inventory
LCIA	Life Cycle Impact Assessment
EoL	End-of-Life
WLTC	Worldwide Harmonised Light Vehicles Test Cycle
CSI	Crustal Scarcity Indicator
REO	Rare Earth Oxide
IACS	International Annealed Copper Standard
VOC	volatile organic compound
GWP100	Global Warming Potential over 100 years

Part I

Overview

CHAPTER 1

Introduction

1.1 Background

To mitigate emissions, including greenhouse gas (GHG) from the transportation sector, a transition to electric vehicles (EVs) is being strongly advocated by actors such as IPCC and IEA [1], [2]. In response, EV manufacturers are prioritizing improvements in charging time and driving range, two critical factors that influence consumer adoption [3]. This has led to a focus on enhancing the energy efficiency and cost-effectiveness of powertrain components, including electric traction machines (e-machines) with high power density (measured in W/kg and W/L) and energy efficiency. Among these, permanent magnet synchronous machines (PMSMs) using rare-earth elements (REEs) like neodymium (Nd) and dysprosium (Dy) have become the dominant choice [4].

The uncertain global supply of REEs is driven by geopolitical factors, primarily since China is responsible for producing more than 95% of the world's REEs, as well as the surge in EV demand [5], which underscores the importance of evaluating REE-free alternatives. Popular alternatives are either REE-free magnets or magnet-free topologies. Magnet-free alternatives

comprise the induction machine (IM), the synchronous reluctance machine (SynRM), and the electrically excited synchronous machine (EESM).

While these alternatives eliminate dependence on REEs, they often suffer from reduced technical performance, such as lower power density or efficiency. Advanced electromagnetic finite element method (FEM) simulations have become essential tools for estimating the performance of e-machines during the design phase across a wide range of speed and torque conditions. Although these simulations provide accurate technical estimates, the trade-offs between performance, material selection, and environmental impact remain insufficiently understood.

The performance prediction of the e-machines during the use phase is of high importance. Among all investigated e-machine types in this study, IMs present greater complexity, as multiple slip rate configurations can yield the same torque and speed output. Additionally, due to the presence of windings in both the stator and rotor, the computational effort for simulating a single operating point in IMs is significantly higher than that for other synchronous machines. Thus, it would be beneficial to have an improved modeling efficiency for this type of machine.

When environmental sustainability is considered in e-machine design, the trade-offs between performance, cost, and environmental impact become increasingly complex. For example, high-performance materials such as copper (Cu) hairpin windings and cobalt-alloyed electrical steels can improve efficiency but also increase production costs and environmental burdens. Similarly, optimizing for energy efficiency may reduce emissions during operation but require advanced cooling systems or specialized materials, which can offset the environmental benefits.

To identify the key factors of these challenges, Life Cycle Assessment (LCA) is introduced as a comprehensive tool for quantifying environmental impacts. LCA evaluates each stage of a product's life cycle, including raw material extraction, manufacturing, operation, maintenance, and end-of-life disposal. This systematic approach helps identify environmental hotspots and assess the cumulative effects of design decisions, supporting the development of e-machines that are both technically and environmentally viable.

1.2 Previous work

To reduce the computational cost of FEM-based performance prediction for IMs, equivalent circuit models are widely used. Conventional parameter identification via no-load and locked-rotor tests [6] provides values at rated conditions but has limitations. The locked-rotor test requires a reduced stator frequency to mitigate skin effects, yet must remain high enough for induction. A recommended 25% of rated frequency still exceeds typical rotor operating levels. Moreover, stator and rotor leakage inductances cannot be separated, relying on assumed ratios [7].

To improve control-oriented design, several FEM-based studies have predicted IM parameters while accounting for saturation effects [8]–[11]. Magnetostatic solvers offer faster simulations [8], but are less accurate for deep-bar rotors [12]. Time-harmonic models incorporating saturation and deep-bar effects show good agreement with transient FEA [11], though experimental validation is pending. Transient solvers are used for torque prediction in nonlinear models [13], and in parameter extraction via inverter-fed tests [9]. Mölsä *et al.* [10] proposed a dynamic model validated through standstill commissioning, though tests were limited to low rotor frequencies and lacked torque validation.

This work introduces a FEM-based procedure to extract dynamic equivalent circuit parameters as functions of magnetizing current, for the IM. Using transient simulations under load and no-load conditions, the method captures saturation and deep-bar effects for the IM. Parameters are derived from current and flux linkage phasors, and torque prediction accuracy is verified. The approach enables precise control and operating point optimization with minimal simulation effort.

Although LCA studies on e-machines are highly relevant, the literature remains limited in scope and detail, especially for automotive applications and performance-integrated assessments.

Several studies compare machine topologies. For example, Schillingmann *et al.* [14] analyzed four 100kW machines: PMSM, IM, SynRM, and EESM. SynRM was found to be the most sustainable due to minimal Cu and REE use. However, the study excluded the use phase and lacked detailed performance comparisons. Similarly, Cassoret *et al.* [15] compared IMs with aluminum (Al) and Cu rotors. While Al variants had lower manufacturing impacts, reduced efficiency during operation led to a higher overall environmental burden.

Performance-driven comparisons include Rassõlkin *et al.* [16], who evaluated IMs, SynRMs, and PMa-SynRMs. PMa-SynRM was the most energy-efficient and environmentally favorable despite its higher cost. de Souza *et al.* [17] assessed IM (IE3), SynRM, and PMSM (IE5) for 11kW industrial motors, showing that PMSMs and SynRMs offer higher efficiency and lower lifetime energy use, though PMSMs have greater manufacturing impacts due to REE. In consumer products, Wrobel *et al.* [18] examined three PMSMs in cordless drills. Motor1 used ferrite magnets (budget), Motor2 REE magnets (mid-range), and Motor3 REE magnets (premium). Motor2 was most favorable, balancing material use and life-cycle efficiency.

Component-level studies include Antonacci *et al.* [19], who performed a cradle-to-gate LCA of an IM for a standby hydraulic pump. Raw material extraction and manufacturing were major impact sources, but the narrow industrial context limits relevance to automotive applications.

Zhang *et al.* [20] assessed carbon emissions of four 30kW, 1500rpm machines: WFSM, IM, and two REE-based PMSMs. High-carbon materials like REE magnets, Al, and Cu were key contributors. WFSMs were most material-efficient but may have higher operational emissions. IMs were lighter but emitted more due to Al use. PMSMs had the highest embedded emissions but performed best over the lifetime due to superior efficiency.

Recent studies focus more directly on automotive applications. Mafrici *et al.* [21] compared an SRM and baseline PMSM for similar vehicles. Use-phase impacts depended on motor efficiency and vehicle matching. The Cu-wound SRM had comparable resource use but slightly higher climate impact due to oversizing. Replacing Cu with Al in the SRM stator reduced energy demand and material intensity. The study highlighted SRM's benefits: lower cost, durability, and REE-free design. It also noted that as renewable energy adoption increases, production impacts become more significant.

Complementing this, Mafrici *et al.* [22] conducted a comparative LCA of the Nissan Leaf's PMSM across EV platforms and manufacturing locations. While the use phase dominates climate and fossil resource impacts, manufacturing becomes increasingly important with greener electricity mixes.

These findings align with Nordelöf *et al.* [23], who assessed three traction machines with different magnet configurations. The Nd(Dy)FeB PMSM had the lowest weight and highest power density, but also the highest toxicity and climate impacts due to drive-cycle losses. The PMa-SynRM traded power

density for efficiency, resulting in better overall environmental performance. Major impact contributors included Cu windings, Al housings, and electrical steel sheets, with virgin Cu extraction and high steel loss rates as key hotspots.

Schreiber *et al.* [24] reviewed LCA studies on REO extraction and production, noting GHG emissions per kg of REO vary by a factor of five depending on ore type. Nordelöf and Bongards [25] applied economic allocations to two REO supply routes in a cradle-to-gate LCA of PMSM in EVs. The supply route choice accounted for 11%-–13% of total production emissions, underscoring the importance of magnet supply chain data.

Overall, despite significant variation in REO data, cradle-to-gate assessments consistently show that REE magnets, electrical steel, and housings are the primary contributors to environmental impact [14], [19], [20]. When the use phase is included without low-GHG electricity scenarios, efficiency becomes the dominant factor [15]–[18], [20], [22]. Two studies [18], [21] demonstrate that overrating machines increases environmental burden in both production and operation, emphasizing the importance of appropriate sizing. Mafrici *et al.* [22] and Nordelöf *et al.* [23] present comprehensive LCAs with detailed designs and strong rating rationale, concluding that while the use phase remains dominant, production impacts gain relevance as electricity sources become cleaner. However, no existing study includes EESM, IM, and SynRM topologies with detailed designs and rating considerations tailored to EV applications.

This work conducts an attributional LCA, which builds on the research from Nordelöf *et al.* [23] by expanding the scope to include magnet-free e-machine alternatives (EESM, IM, and SynRM) designed particularly for EV application within the same boundary conditions. Furthermore, this work also integrates manufacturing-induced iron loss by a factor of 1.7 to better represent the loss of e-machines, and performs a sensitivity analysis on magnet supply chain data to identify how sensitive the result is to the magnet data.

1.3 Aim

The primary aim of this study is to assess whether REE-free alternatives can effectively replace PMSMs that use REE magnets, in terms of both technical and environmental performance for EV propulsion systems. When it comes to the IM, the aim was to improve the modelling to ensure the correct mag-

netization level when determining the efficiency over the operating points.

A key objective is to support stakeholders involved in the development and manufacturing of electric traction technologies, as well as companies seeking to procure such systems. The insights gained from this research can help balance component-level requirements and guide the selection of suitable e-machine types at the powertrain level. Additionally, the findings are relevant to governmental agencies and academic institutions focused on evaluating the environmental impact of emerging automotive technologies.

1.4 Contributions

The specific contribution of this work are listed below.

- Proposed and validated methods to extract IM circuit parameters from FEM evaluations for circuit model implementations.
- Defined the design and electromagnetic performance of three e-machine types with harmonized specifications.
- Expanded previous life cycle inventory (LCI) models to also include IMs, EESM, and SynRMs.
- Conducted an LCA comparison of a reference PMSM with three REE-free machine types: IMs, SynRMs, and EESMs, each with varying Cu and Al conductor combinations, based on electromagnetic finite element modeling.
- Quantified the effect of selected GHG reduction strategies, including the use of green virgin Al and improved material utilization during electrical steel sheet punching (“green manufacturing”).
- Performed a sensitivity analysis on magnet production, indicating that REE-free machines with Al conductors may achieve lower carbon footprints under favorable conditions.

CHAPTER 2

Theory

The primary function of e-machines is to facilitate the conversion between electrical and mechanical power through the interaction of magnetic fields. The stator of the e-machine includes electrically insulated windings that carry alternating currents, providing a rotating magnetic field. A laminated iron core leads this field and crosses an airgap to interact with a magnetic flux from the rotor. The origin of the rotor flux differs in representative machine types, which will be elaborated on further in the following sections.

Propulsion in EVs places high demands on e-machines, which must operate efficiently and precisely across a broad range of torques and speeds. To meet acceleration requirements, high maximum torque is needed, even at elevated speeds. At the same time, maximizing efficiency is essential to extend driving range and overall vehicle performance.

2.1 Operating principles and control of traction e-machines

Modern EV drives rely on high-performance torque control, such as field-oriented control (FOC), which is the most widely adopted strategy [26]. FOC decouples torque and flux in a rotating reference frame, enabling precise control, smooth torque, and high efficiency.

In Figure 2.1, the EV drive system implementing FOC is illustrated. The driver perceives car speed (v_{car}) through the console and demands positive or negative acceleration through the pedal or brake. This demand is perceived as the torque reference ($T_{em,ref}$) for the FOC reference current generator. Together with the e-machine rotor speed (ω_r), they are subsequently translated into current references in the synchronous d-q plane ($i^d_{s,ref}$ and $i^q_{s,ref}$) depending on the e-machine types.

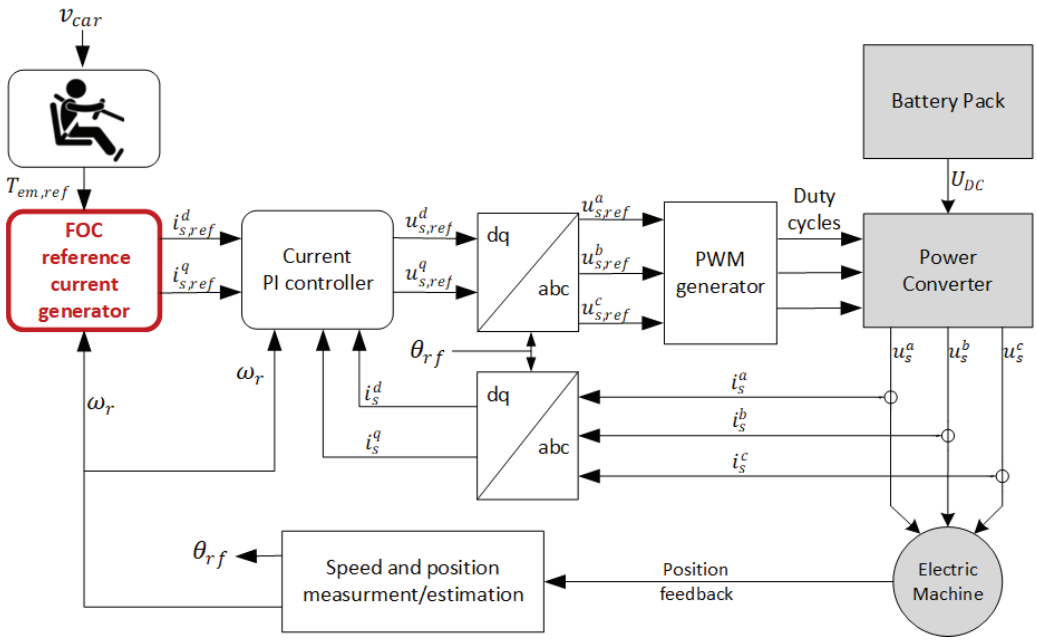

Figure 2.1: Block diagram of a variable speed control architecture for e-machine drive [27].

The inner loop employs PI controllers again for the d- and q-axis currents. These controllers generate voltage references ($u^d_{s,ref}$ and $u^q_{s,ref}$) in the

synchronous frame, which are then transformed into three-phase quantities ($u^a_{s,ref}$, $u^b_{s,ref}$, and $u^c_{s,ref}$) via an inverse Park transformation. The resulting voltages are modulated through a Pulse Width Modulation (PWM) generator to produce duty cycles for the power converter.

Additionally, successfully implementing the control strategy requires precise feedback on currents, voltages, and rotor position, which can be obtained through sensors in the case of synchronous machines or a combination of sensors and estimators in the case of IMs. Sensorless control is also possible for PMSM, but it is not commonly used for EVs.

In FOC method, the rotor flux $\underline{\psi}_{\text{rotor}}$ is aligned with the d-axis, while the stator current phasor $\underline{i}_s$ is regulated at an angle $\theta_{i,dq}$ in the d–q plane by adjusting the stator voltage phasor $\underline{u}_s$, as illustrated in Figure 2.2.

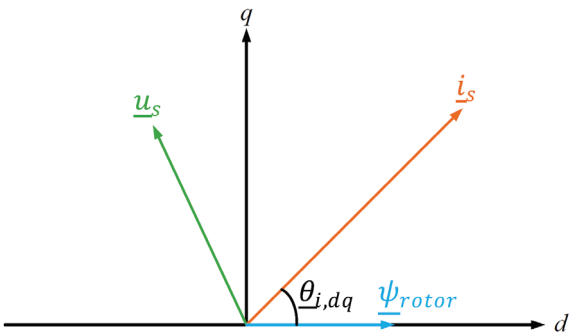

Figure 2.2: Conceptual diagram of stator current phasor, stator voltage phasor, and rotor flux phasor on d-q plane.

Moreover, to fully exploit machine capabilities, FOC is often combined with maximum torque per ampere control (MTPA) [28]. A specific torque-speed operating point can be achieved through multiple stator current phasors, each associated with different stator current magnitudes I_s and angles $\theta_{i,dq}$, as illustrated in Figure 2.3. For example, the stator current phasor $\underline{i}_{s1}$ can generate the same torque as $\underline{i}_{s2}$ but with a lower ohmic loss in the stator windings, since it has a lower magnitude.

To address this, the MTPA strategy is implemented. Its objective is to achieve the highest possible electromagnetic torque for a given stator current by selecting the optimal current vector that minimizes I_s, thereby reducing stator ohmic losses. However, due to inverter current and battery pack voltage constraints as well as the inherent characteristics of the e-machine, different operating limitations apply across a range of speeds.

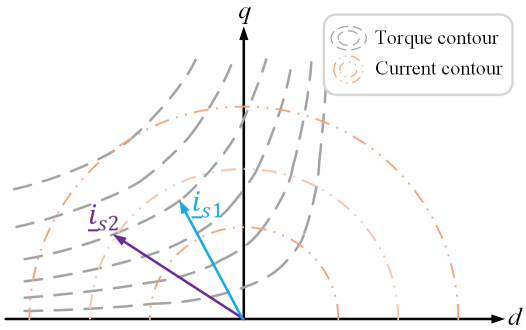

Figure 2.3: Conceptual diagram for stator current phasors of the PMSM on *d*-*q* plane.

In the low-speed region, the only active constraint is the stator current limit. The optimal operating points correspond to the maximum torque achievable for a given current magnitude, which defines the MTPA region.

At a certain level of torque and speed, the DC bus voltage and current limits are reached, and the field-weakening (FW) strategy is applied to enable the highest torque possible at a higher speed. This requires reducing the rotor flux Ψ_r as frequency increases to keep the stator phase voltage within its permissible range. The adjustment is achieved by increasing the stator current angle $\theta_{i,dq}$ in the *d*-*q* plane.

As the rotor speed and injected frequency continue to rise, $\theta_{i,dq}$ reaches the breakdown torque point, marking the onset of the maximum torque per voltage (MTPV) region. In this region, each boundary speed curve has a maximum torque point where the stator current is below its maximum limit due to the need to weaken the field further, making the DC bus voltage the sole factor restricting torque production.

2.1.1 Permanent magnet synchronous machine (PMSM)

In the case of PMSMs, the rotor's magnetic flux is generated by permanent magnets embedded within the rotor structure. This design means that the strength and stability of the rotor's magnetic field are inherently dependent on the properties and configuration of the magnets. These magnets provide a constant magnetic field, eliminating the need for rotor excitation currents, which contributes to higher efficiency and power density compared to other motor types.

Furthermore, synchronous machines, such as PMSMs, exhibit a more straightforward decoupling of the d-axis and q-axis components in the rotor reference frame. This decoupling simplifies control strategies, allowing for more precise torque and flux regulation. The absence of rotor current dynamics in PMSMs also simplifies modeling and control. The equivalent circuit model for the control template used in this study is illustrated in Figure 2.4 [29].

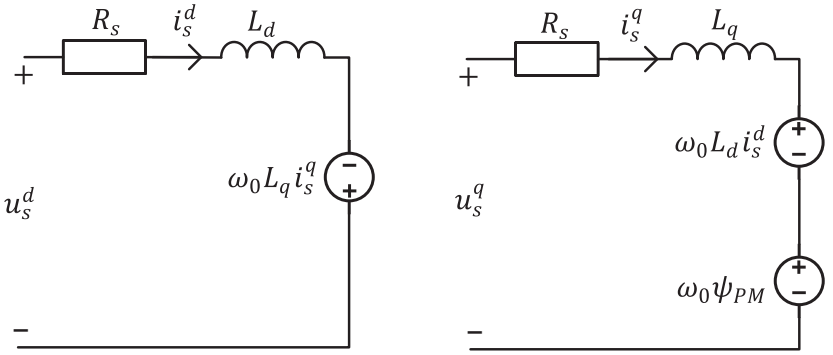

Figure 2.4: Dynamic model of PMSMs.

L_d and L_q are d-axis and q-axis equivalent stator winding inductances, R_s is the equivalent stator winding resistance, respectively, ψ_{PM} is the flux linkage due to the permanent magnets, and $\omega_0 = 2\pi f_0$ is the electrical synchronous speed in rad/s and f_0 is the supplied frequency in Hz.

The equivalent d-axis and q-axis flux linkages can be expressed by

$$\begin{cases} \psi_s^q = L_q \, i_s^q \\ \psi_s^d = \psi_{PM} + L_d \, i_s^d \end{cases} \tag{2.1}$$

Then the electromagnetic torque can be stated as [29], [30]

$$T_{em} = \frac{3}{2} N_p \left[\psi_{PM} \, i_s^q + (L_d - L_q) i_s^q \, i_s^d \right] \tag{2.2}$$

where N_p represents the number of pole pairs.

Since the L_d is typically smaller than L_q for PMSM, the current trajectory of MTPA for PMSM is located in the second quadrant as Figure 2.5.

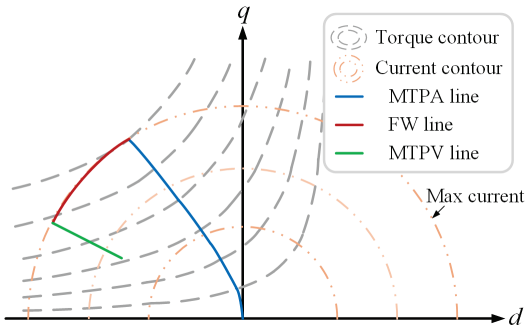

Figure 2.5: Conceptual diagram of current trajection on d-q plane for MTPA of the PMSM.

Moreover, the stator phase voltage quantities at the d-q plane of PMSM can be stated as

$$\begin{cases} u_s^d = R_s i_s^d + L_d \dfrac{di_s^d}{dt} - \omega_0 L_q i_s^q \\ \\ u_s^q = R_s i_s^q + L_q \dfrac{di_s^q}{dt} + \omega_0 (\psi_{PM} + L_d i_s^d) \end{cases} \tag{2.3}$$

2.1.2 Induction machine (IM)

In an IM, the rotor voltage, current, and magnetic field are induced by the magnetic field generated in the stator. Consequently, the energy sustaining the rotor magnetic field ultimately originates from the electrical supply of the stator windings, making the decoupling of the d-axis and q-axis components more complicated than for synchronous machines. When the IM is subjected to a mechanical load, the rotor speed decreases slightly below the synchronous speed, creating the necessary slip that enables torque production to drive the load.

The FOC scheme based on the inverse Γ-form model (IGFM) is employed as the control framework for IMs in this work. The dynamic representation of the IGFM is shown in Figure 2.6 [31].

In this model, $\underline{u}_s$ and $\underline{i}_s$ denote the stator voltage and current phasors, R_s and R_R represent the stator and transformed rotor resistances, $\underline{i}_M$ and $\underline{i}_R$ are the transformed magnetizing and rotor current phasors, and $\underline{\psi}_R$ and $\underline{u}_R$ correspond to the transformed rotor flux and induced voltage phasors. The parameters L_σ and L_M are the transformed leakage and magnetizing

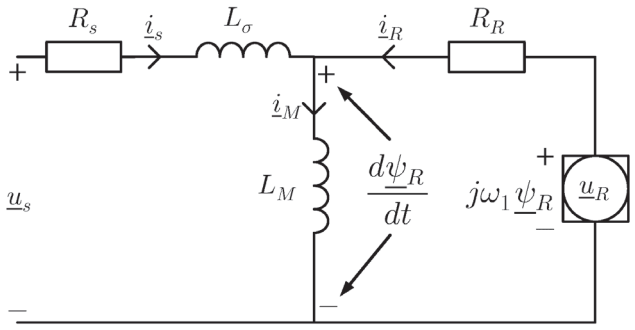

Figure 2.6: Dynamic inverse Γ-form model of IMs.

inductances, and ω_1 is the rotor electrical speed, which can be expressed as

$$\omega_1 = \omega_0 - \omega_2 \tag{2.4}$$

where ω_0 is the synchronous electrical speed provided by stator windings, and ω_2 is the slip electrical speed ($Slip = \omega_2/\omega_0$).

The rotor flux linkage $\underline{\psi}_R$ is aligned with the d-axis and the d-quantity ψ_R^d equals the amplitude of $\underline{\psi}_R$ as shown in Figure 2.2. The amplitude of the magnetizing and the rotor current is equal to i_s^d and i_s^q, respectively.

$$\begin{cases} |\underline{\psi}_R| = \psi_R^d \\ |\underline{i}_M| = i_s^d = I_s cos(\theta_{i,dq}) \\ |\underline{i}_R| = i_s^q = I_s sin(\theta_{i,dq}) \end{cases} \tag{2.5}$$

Accordingly, the d-axis rotor flux linkage, electromagnetic torque T_{em}, and electrical slip speed ω_2 can be expressed as [30]

$$\psi_R^d = L_M \; i_s^d \tag{2.6}$$

$$T_{em} = \frac{3}{2} N_p \; \psi_R^d \; i_s^q = \frac{3}{2} N_p \; L_M \; i_s^d \; i_s^q \tag{2.7}$$

$$\omega_2 = \frac{R_R \; i_s^q}{\psi_R^d} = \frac{R_R}{L_M} tan(\theta_{i,dq}) \tag{2.8}$$

The parameters R_R, L_M, and ψ_R^d are therefore essential for predicting operating points.

Equation (2.7) can also be rewritten as

$$T_{em} = \frac{3}{4} N_p \; L_M \; I_s^2 \; sin(2\theta_{i,dq}) \tag{2.9}$$

where the maximum torque occurs at $\theta_{i,dq} = 45°$ if L_M remains constant. However, due to iron core saturation, typical the value of L_M decreases with increasing d-axis current. Figure 2.7 illustrates the optimal stator current trajectory for MTPA for IMs. The blue, red, and green curves represent the trajectories in the MTPA, FW, and MTPV regions, respectively.

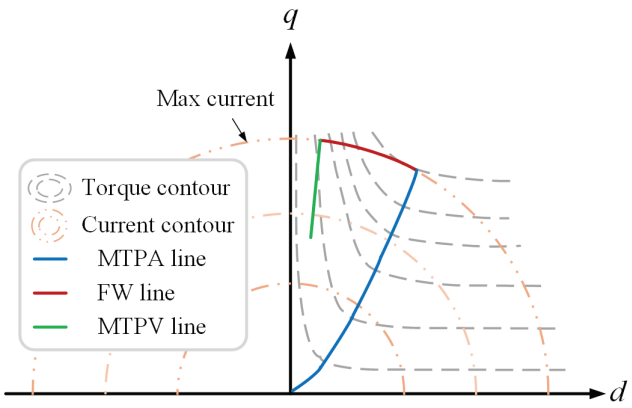

Figure 2.7: Conceptual diagram of current trajection on d-q plane for MTPA of the IM.

Finally, the stator phase voltage components in the d-q plane are given by

$$\begin{cases} u_s^d = (R_s + R_R) i_s^d + L_\sigma \dfrac{di_s^d}{dt} - \omega_0 L_\sigma i_s^q - \dfrac{R_R}{L_M} \psi_R^d \\ \\ u_s^q = (R_s + R_R) i_s^q + L_\sigma \dfrac{di_s^q}{dt} + \omega_0 L_\sigma i_s^d + \omega_1 \psi_R^d \end{cases} \tag{2.10}$$

Insert (2.6) into (2.10), the stator phase voltage components in the d-q plane can also be expressed as

$$\begin{cases} u_s^d = R_s i_s^d + L_\sigma \dfrac{di_s^d}{dt} - \omega_0 L_\sigma i_s^q \\ \\ u_s^q = R_s i_s^q + L_\sigma \dfrac{di_s^q}{dt} + \omega_0 (L_\sigma + L_M) i_s^d \end{cases} \tag{2.11}$$

2.1.3 Synchronous reluctance machine (SynRM)

The rotor of a SynRM consists of laminated iron sheets with flux barriers that create anisotropic magnetic properties. This design results in different

inductances along the d-axis and q-axis, enabling torque generation through magnetic reluctance. Flux barriers are aligned along the q-axis to form high-reluctance paths, while the d-axis contains flux-conducting regions that create low-reluctance paths. When the stator produces a rotating magnetic field, the rotor aligns its low-reluctance axis with the stator field, allowing synchronous operation without permanent magnets or rotor windings.

The absence of magnets and rotor windings reduces material costs and eliminates the associated losses [32]. Compared to PMSMs, SynRMs do not generate back electromotive force (EMF) under no-load conditions, eliminating no-load iron losses caused by permanent magnet flux. Moreover, unlike IMs and EESMs, the SynRM rotor carries no currents, meaning no rotor ohmic losses, which makes SynRM competitive in terms of efficiency. However, without the contribution of permanent magnets or rotor windings, SynRMs require a larger iron core to achieve a similar torque level, resulting in lower torque and power density. Additionally, torque production relies solely on rotor saliency, making it more sensitive to magnetic saturation and slot harmonics, which leads to higher torque ripple compared to PMSMs.

The control equivalent circuit for SynRM is shown in Figure 2.8 [29].

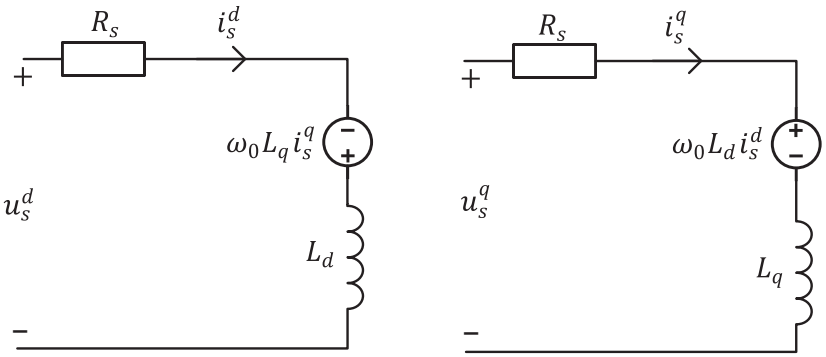

Figure 2.8: Dynamic model of SynRMs.

The flux linkages in the d-q frame are expressed as

$$\begin{cases} \psi_s^q = L_q \, i_s^q \\ \psi_s^d = L_d \, i_s^d \end{cases} \tag{2.12}$$

The electromagnetic torque of SynRM is given by

$$T_{em} = \frac{3}{2} N_p (L_d - L_q) \, i_s^q \, i_s^d = \frac{3}{4} N_p (L_d - L_q) \, I_s^2 \, sin(2\theta_{i,dq}) \tag{2.13}$$

From (2.13), torque depends on the saliency difference $(L_d - L_q)$ and the product of i_s^d and i_s^q. Therefore, torque can be increased by optimizing rotor geometry and adding multiple flux barriers to increase the saliency ratio L_d/L_q [32]. It can also be observed that MTPA will operate in the first quadrant for SynRM starts with $\theta_{i,dq} = 45°$. Additionally, since L_d and L_q decrease with increasing current due to core saturation, the stator current trajectory on the *d-q* plane resembles that shown in Figure 2.7.

The stator voltage equations in the *d-q* frame are the same as for the PMSM but with $\psi_{PM} = 0$ giving

$$\begin{cases} u_s^d = R_s i_s^d + L_d \dfrac{di_s^d}{dt} - \omega_0 L_q i_s^q \\ \\ u_s^q = R_s i_s^q + L_q \dfrac{di_s^q}{dt} + \omega_0 L_d i_s^d \end{cases} \tag{2.14}$$

2.1.4 Electric excited synchronous machine (EESM)

EESMs operate on the principle of synchronism between the rotor and stator magnetic fields. Unlike PMSMs, EESMs employ an electromagnetically excited rotor, where a controllable direct current is supplied to the field windings. This excitation generates a magnetic field that interacts with the stator's rotating magnetic field to produce torque.

A key advantage of EESMs is the ability to dynamically adjust the excitation current I_f, enabling optimization of machine performance under varying load conditions [33]. For example, reducing I_f at low torque or no-load decreases the back electromotive force, thereby lowering iron losses compared to PMSMs. In this way, a thermal balance between rotor and stator can also be achieved, if needed. However, this benefit comes at the cost of rotor ohmic losses due to the presence of field windings, which makes EESMs less efficient than PMSMs at medium to heavy load when both stator and field currents become high. Additionally, exciting and controlling the rotor field requires extra power electronics and a slip ring or rotating transformer, which makes EESMs more costly and less robust when compared to IMs.

The dynamic control equivalent circuit for EESM is shown in Figure 2.9 [34], where u_f, I_f, R_f, and L_f denote the field voltage, current, resistance, and inductance, respectively.

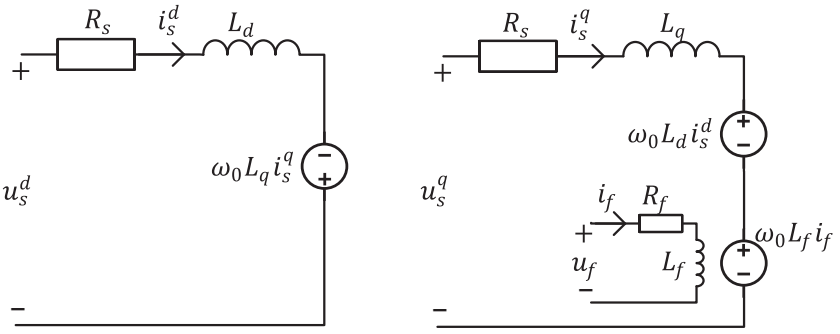

Figure 2.9: Dynamic model of EESM.

The flux linkages in the *d-q* frame and the field flux ψ_f are expressed as

$$\begin{cases} \psi_s^q = L_q \; i_s^q \\ \psi_s^d = \psi_f + L_d \; i_s^d \\ \psi_f = L_f \; I_f \end{cases} \tag{2.15}$$

The electromagnetic torque is given by

$$T_{em} = \frac{3}{2} N_p \left[\psi_f \; i_s^q + (L_d - L_q) i_s^q \; i_s^d\right] = \frac{3}{2} N_p \left[L_f \; I_f \; i_s^q + (L_d - L_q) i_s^q \; i_s^d\right] \tag{2.16}$$

Apart from *d-q* current components, the field current I_f provides an additional degree of freedom for torque control. A desired operating point can be achieved through various combinations of *d-q-f* currents. To determine the optimal combination, MTPA is also applied to the field circuit by minimizing the ohmic loss P_{ohmic} in both stator $P_{ohmic,s}$ and rotor $P_{ohmic,r}$

$$P_{ohmic} = P_{ohmic,s} + P_{ohmic,r} = \frac{3}{2} R_s I_s^2 + R_f I_f^2 \tag{2.17}$$

The MTPA lines of the EESM for different field current levels from 0 to $1.2\,p.u.$ are shown in Figure 2.10a, and the corresponding maximum torque envelopes versus rotor speed are presented in Figure 2.10b. As seen in Figure 2.10a, the MTPA line without field current resembles that of a SynRM, while increasing I_f shifts the trajectory toward that of a PMSM, located in the second quadrant. It is also observed that the trajectories for $I_f = 1.0\,p.u.$ and $1.2\,p.u.$ overlap due to saturation of ψ_f with respect to I_f, which also

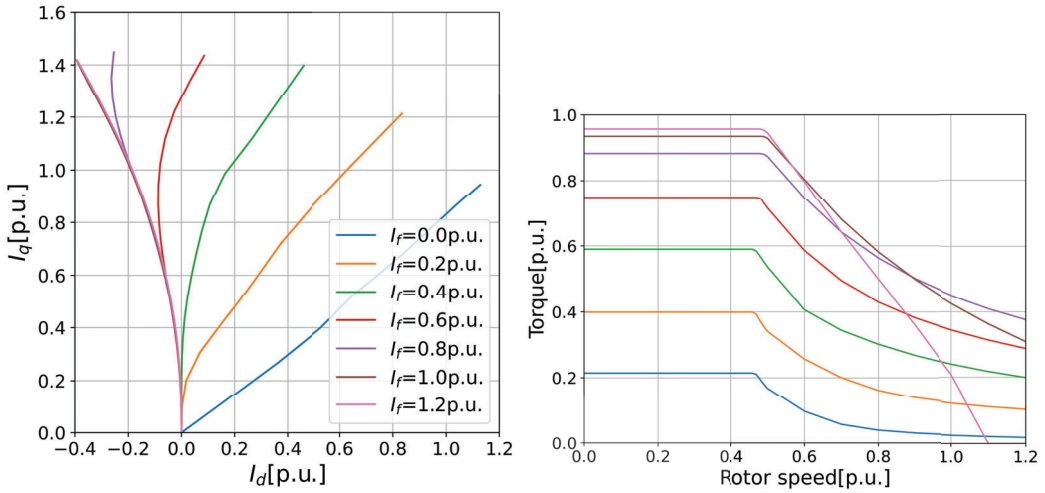

(a) MTPA lines.

(b) Maximum torque envelopes varying with rotor speed.

Figure 2.10: Different field current levels of EESMs.

explains the diminishing torque increment at higher excitation levels. Additionally, in Figure 2.10b, when the $I_f = 1.0$ $p.u.$ and 1.2 $p.u.$ the maximum torque drop from rotor speed equal 0.8 $p.u.$ and 0.6 $p.u.$, respectively due to reaching their MTPV region, which can be observed in the equations of stator voltage in the d-q frame in

$$\begin{cases} u_s^d = R_s i_s^d + L_d \dfrac{di_s^d}{dt} - \omega_0 L_q i_s^q \\ \\ u_s^q = R_s i_s^q + L_q \dfrac{di_s^q}{dt} + \omega_0 (L_f I_f + L_d i_s^d) \end{cases} \tag{2.18}$$

2.2 Environmental assessment by LCA

Environmental challenges associated with industrial activities, product development, and infrastructure projects have led to the growing need for comprehensive tools to evaluate and mitigate environmental impacts. Traditional environmental assessments often focus on localized and immediate effects, such as emissions, land use, and ecological disruption during specific project phases. While valuable, these assessments may overlook broader, systemic

impacts that occur throughout the entire life span of a product or system or a service.

To address their limitations, Life cycle assessment (LCA) has emerged as a robust and standardized methodology for environmental assessment across all stages of a product's life cycle, from raw material extraction and manufacturing to use and end-of-life disposal. This cradle-to-grave perspective enables more informed decision-making in design, production, and policy, supporting the transition toward more sustainable systems.

In this context, environmental assessment by LCA represents a shift from reactive, site-specific evaluations to proactive, system-wide sustainability analysis.

2.2.1 Framework

The methodological framework of LCA is defined by the ISO 14040 and ISO 14044 standards. ISO 14040 outlines the principles and structure of LCA illustrated in Figure 2.11, while ISO 14044 specifies the requirements and guidelines for conducting LCA studies [35], [36]. According to these standards, an LCA study should consist of the four main phases shown in Figure 2.11. However, the work process is likely to be iterative rather than linear, as indicated by the dual directional arrows.

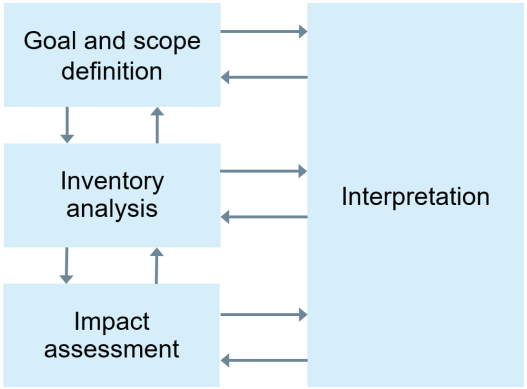

Figure 2.11: LCA framework outlined by ISO 14040 [35].

2.2.2 Goal and Scope Definition

The goal and scope definition is the foundational phase of an LCA. It establishes the purpose of the study, the intended audience, and the specific product or system under investigation. This phase is critical because it directly influences the methodological choices and the interpretation of results throughout the assessment.

The **goal** of an LCA must be clearly stated at the outset. It includes the reason for conducting the study, the intended application of the results, and the target audience. As an example in the LCA study [23], the goal was to compare the environmental impacts of PMSMs with different magnet types for EV applications to guide decisions by manufacturers and policymakers.

The **scope** defines the boundaries and level of detail of the study. Key elements include:

- **Functional Unit**: This is the reference unit used to quantify inputs and outputs and should be common for all objects under the LCA study. For an e-machine in EV applications, the primary function is to provide propulsion. Therefore, one option for the functional unit could be the *driven distance* of a specified EV driving a certain operating profile, typically expressed in kilometer (km). This allows for consistent comparison of environmental impacts per unit of mobility delivered.

- **System Boundaries**: These determine which life cycle stages are included in the analysis. Common boundary types include cradle-to-gate, gate-to-gate, and cradle-to-grave, as shown in Figure 2.12. For an e-machine in EV, a cradle-to-gate boundary would encompass raw material extraction and manufacturing, such as REE extraction and magnet production, e.g. in China, and transport to the European e-machine factory for assembly, e.g. in Europe. A cradle-to-grave boundary would additionally include the operation phase (i.e., driving the EV) and end-of-life treatment (i.e., recycling of the e-machine along with the EV).

- **Impact Categories**: These specify the types of environmental impact to be assessed. Common categories include global warming potential, energy use, resource depletion, and toxicity. The selection of impact categories should reflect the environmental concerns relevant to the product under study and its application.

- **Data Quality Requirements**: These define the resolution and reliability of the data used, including whether site-specific or average data are applied.

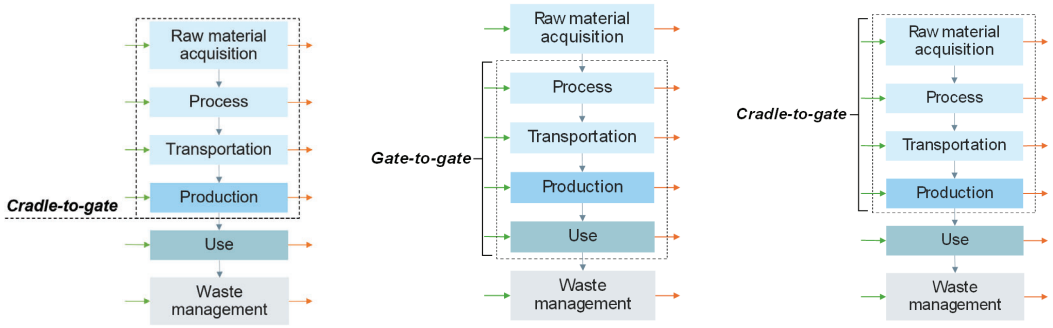

(a) Cradle-to-gate. **(b)** Gate-to-gate. **(c)** Cradle-to-grave.

Figure 2.12: System Boundaries.

A clearly defined goal and scope ensures that the LCA results are meaningful, transparent, and applicable to the intended decision-making context. In the case of e-machines for EVs, using driven distance as the functional unit aligns the environmental assessment with the product's core function, thereby enhancing the relevance and interpretability of the results.

2.2.3 Life Cycle Inventory (LCI)

The life cycle inventory (LCI) phase is the second major component of an LCA study and involves collecting and quantifying data on energy and material inputs, as well as environmental releases such as emissions and waste, across all processes within the defined system boundaries.

A flow model is constructed to represent the product or system life cycle, typically consisting of interconnected unit processes with defined inputs and outputs. Data requirements include raw materials, energy use, transportation, manufacturing, use-phase activities, and end-of-life treatments.

Data quality is critical for reliable results. Primary data can be obtained from direct measurements or company records, while secondary data often comes from databases or literature. Consistency in data collection and documentation of assumptions, allocation rules, and data gaps is essential.

The outcome of the LCI phase is a dataset of elementary flows, such as kilograms of CO_2 emitted or kWh of electricity consumed, as illustrated in Figure 2.13. These results serve as inputs for the LCIA phase.

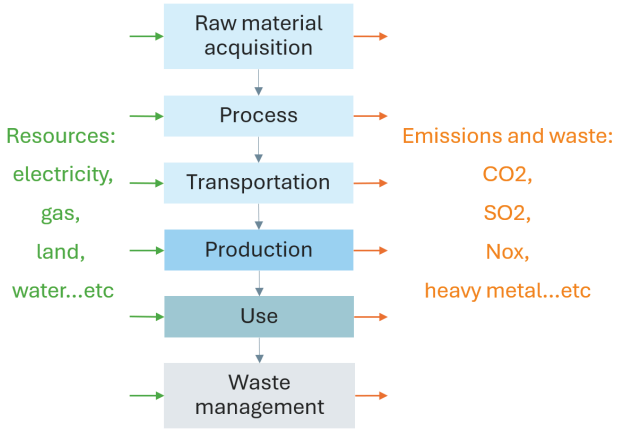

Figure 2.13: LCI flowchart illustrating resource inputs and emissions across all life cycle stages.

To facilitate LCI, software tools such as **OpenLCA** are widely used. In this study, OpenLCA is employed to construct process models by linking unit processes through input-output relationships. Each process specifies material, energy, emission, and waste flows, and integrates background data from databases such as **ecoinvent** (used in this study), Agribalyse, and ELCD. The software supports the system boundaries defining allocaton of flows, and scaling of results to the functional unit, ensuring consistency and transparency.

2.2.4 Life Cycle Impact Assessment (LCIA)

The life cycle impact assessment (LCIA) phase translates inventory data into potential environmental impact using LCA software. It evaluates how emissions and resource use contribute to various environmental consequences, for example global warming, acidification, or human toxicity.

The process includes:

- **Classification**: Group inventory flows into impact categories (e.g., climate change, acidification).
- **Characterization**: Convert flows into common units using equivalency

factors (e.g., methane's higher global warming potential 28-36 times than CO_2). Results are expressed as indicators like kg CO_2-Eq for global warming potential or kg SO_2-Eq for acidification.

- **Normalization (optional)**: Compare impacts to reference values to provide context. For endpoint indicators, results may be expressed in units like DALYs, representing years of healthy human life lost.
- **Weighting (optional)**: Assign relative importance to impact categories based on stakeholder values, enabling aggregation into a single score for easier interpretation.

Common LCIA methods include **CML**, **ReCiPe**, **TRACI**, and **IMPACT World+**. This study uses **ReCiPe**, illustrated in Figure 2.14.

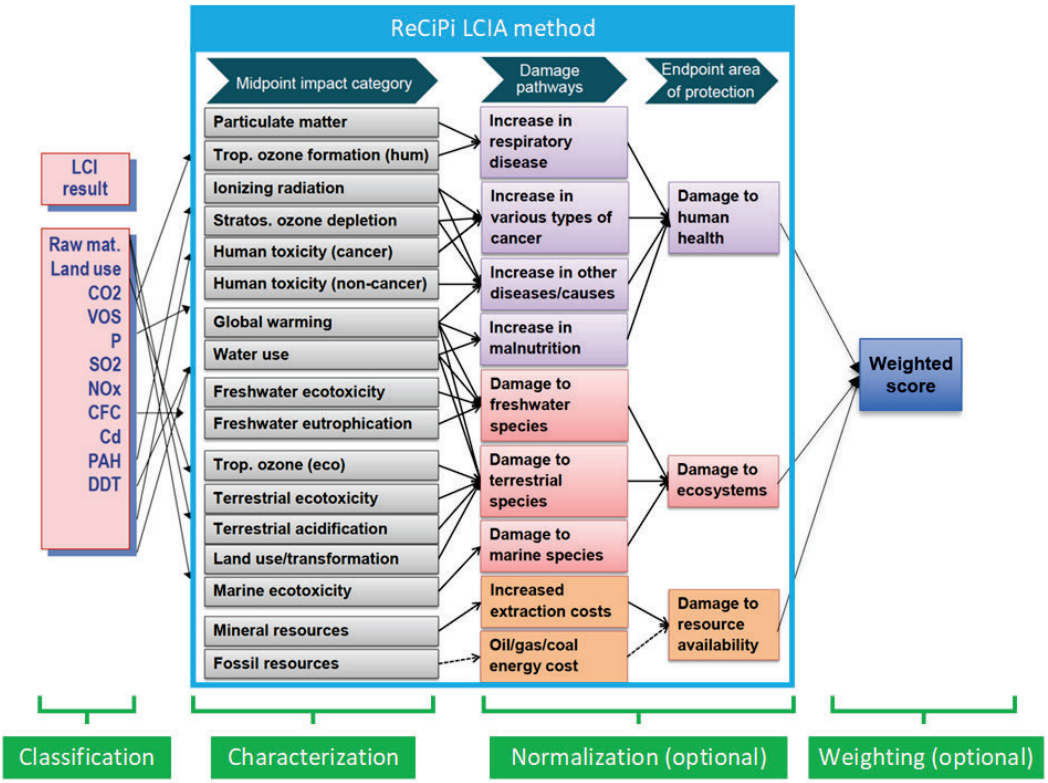

Figure 2.14: LCIA method using ReCiPe. Adapted from [37].

As shown in Figure 2.14, flows like CO_2, SO_2, and NO_x are classified into midpoint categories and characterized into indicators. These propagate to

endpoint areas: *human health*, *ecosystem quality*, and *resource availability*. Optional weighting aggregates results for decision-making. OpenLCA automates this process and supports multiple LCIA methods.

2.2.5 Midpoint vs. Endpoint Indicators in LCA

Midpoint indicators reflect impacts at an intermediate stage, such as CO_2 emissions. They are closely tied to inventory data, making them easier to calculate and compare across studies. However, they may not fully capture broader consequences and often require multiple indicators.

Endpoint indicators represent final outcomes, such as damage on ecosystem in species.yr, meaning natural species loss in one year. They offer a larger degree of integrated view and are useful for policy and communication, but involve more assumptions and uncertainty.

The choice between providing midpoint or endpoint related LCA results depends on the study's goals and audience. Midpoints support detailed analysis, while endpoints aid strategic decisions. In this study where different e-machines are compared, endpoint results guide which midpoint categories are most relevant for e-machine applications in EVs, while conclusions are drawn from midpoint results to evaluate technical options.

CHAPTER 3

Reference case

3.1 Objects of LCA study and functional unit

This LCA compares eight different e-machine configurations: (1) a PMSM with distributed (dist.) Cu stator windings and Nd(Dy)FeB magnets (Ref. PMSM), as described in [23]; (2) an IM with Cu stator dist. windings and Cu rotor bars (IM1); (3) an IM with Cu stator dist. windings and aluminum (Al) rotor bars (IM2); (4) an IM using Al for both stator dist. windings and rotor bars (IM1); (5) a SynRM with Cu stator dist. windings (SynRM1); (6) a SynRM with Al stator dist. windings (SynRM2); (7) an EESM using Cu for both stator dist. and rotor concentrated windings (EESM1); and (8) an EESM with Al in both stator dist. and rotor concentrated windings (EESM2).

All machines are assumed to include a cooling circuit integrated into the housing and liquid coolant for thermal management. The energy demand for stator cooling is excluded since it is considered identical across all machine types. In contrast, IMs and EESMs require additional rotor cooling, and the corresponding power consumption is estimated and added to the use-phase energy demand. The boundary conditions for e-machine design are listed in Table 3.1, which are applied to all technical options. All eight traction e-

Table 3.1: Boundary conditions for e-machine design

Parameters	Value
Total driven distance	200,000 km
Battery pack peak voltage	430 V
Maximum converter RMS current	260 A
Stator core outer diameter	200 mm
Minimum requirement for maximum torque at low speed	239 Nm
Maximum rotor speed	12,000 rpm

machines were designed to provide a minimum torque of 239 Nm at low speeds up to the base speed. Beyond the base speed, the maximum torque differs among the designs, which results in variations in high-speed acceleration performance. The energy consumption during the use phase was evaluated using the "Worldwide harmonized light-duty driving test cycle" (WLTC), as illustrated in Figure 3.1. Each e-machine configuration is required to meet the operating points defined by the WLTC. The **functional unit** is defined as **one driven kilometer**, consistent with common practice in LCA studies of EVs [38].

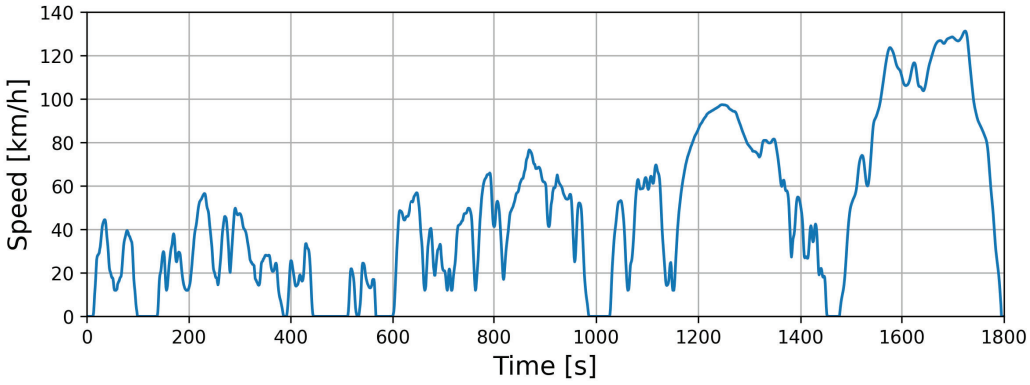

Figure 3.1: Worldwide harmonized light-duty driving test cycle.

3.2 Type of LCA and system boundaries

This study applies an attributional LCA approach, consistent with previous research [23]. The assessment follows a cradle-to-grave perspective, encompassing all life cycle stages from mineral extraction to the end-of-life (EoL) of the e-machine. For the EoL stage, the cut-off approach was adopted [39]. Under this approach, all waste separation and treatment processes are fully included, while recycling flows are only traced until they align with the upstream input of secondary raw materials.

During the use phase, each e-machine configuration was evaluated for a single vehicle type and a representative driving cycle (WLTC, as presented in Figure 3.1). The background system, representing the technical context of the studied options, was modeled using version 3.9.1 of the Ecoinvent database [40], [41]. This database was used to represent inputs to the e-machine factory, the magnet supply chain, the use phase, and EoL processes. Global averages were applied for materials, sub-components, and processing chemicals whenever available; otherwise, European averages were used. For the magnet supply chain, Chinese national data was applied for energy supply, as the production of rare-earth magnets predominantly occurs in China, which accounts for more than 95% of global rare-earth element production [42]. To assess the influence of magnet production on the overall carbon footprint, a sensitivity analysis was also conducted.

Two electricity supply scenarios were considered for the foreground system: the current Norwegian supply mix and the European average mix. These scenarios were applied to e-machine production, EV charging, and the initial post-use separation process in EoL. Since global electricity GHG intensity is decreasing [43], these two scenarios were chosen to represent a low and a high GHG-intensity mix, respectively. No additional temporal changes in electricity GHG intensity were modeled, as the two scenarios are assumed to capture this variability despite being based on geographical differences rather than time. Combined with the four technical e-machine configurations, these two electricity scenarios result in eight baseline study cases, prior to exploring green manufacturing strategies and sensitivity to magnet supply chain data.

The design and inventory data used in this study are expected to remain relevant for at least the next decade. This estimate extends beyond the 5–7 year validity suggested for the reference PMSM in Nordelöf *et al.* [23], as the continued dominance of this design indicates its long-term relevance.

For LCIA, the ReCiPe 2016 v1.03 method [37], widely recognized in LCA practice [44], was applied using both midpoint and endpoint indicators. Endpoint results were used to identify the most significant midpoint categories from an e-machine life cycle perspective. To incorporate the latest global warming characterization factors, the IPCC 2021 midpoint method [45] was also included. Additionally, the crustal scarcity indicator (CSI) 2020 method [46] was employed to assess resource use impacts, replacing the short-term mineral resource indicator in ReCiPe, as long-term resource availability is considered a critical sustainability aspect [47].

3.3 EV powertrain modeling

Figure 3.2, adapted from a previous study [48], presents a schematic representation of an EV powertrain architecture, which is meant to represent the most sold battery electric vehicle models at the time of the fist study (Nisan Leaf and Volkswagen e-Golf) [23], emphasizing the energy flow and associated conversion efficiencies throughout the system.

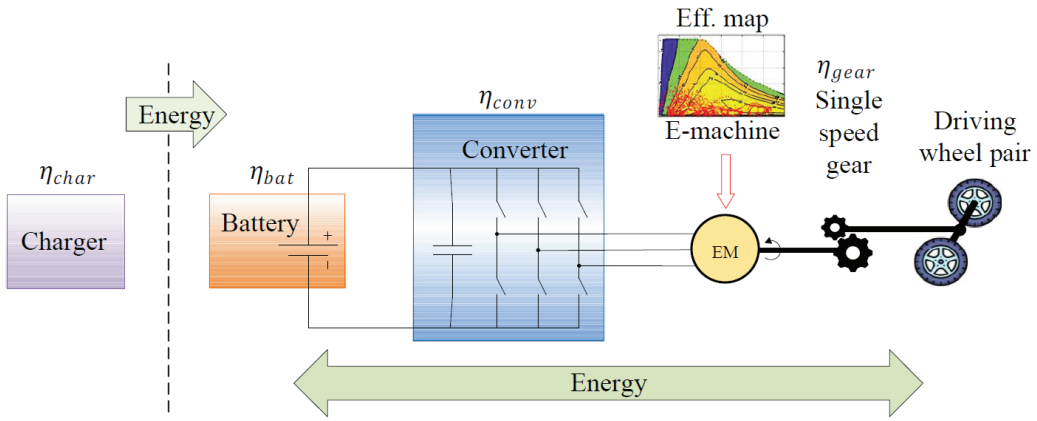

Figure 3.2: Schematic representation of the electric vehicle powertrain architecture [48].

The charging system, with efficiency η_{char}, supplies electrical energy to the onboard battery. The battery, operating at efficiency η_{bat}, serves as the EV's energy storage unit. It interfaces with the converter, which functions with efficiency η_{conv}, and either receives or delivers energy depending on the

operating mode of the e-machine. The e-machine then drives or brakes the wheels via a single-speed gear system, which operates at efficiency η_{gear}.

Energy flow within the EV powertrain is bidirectional. The e-machine operates in two distinct modes: *motor* and *generator*, with efficiency dependent on the torque-speed operating point, best represented by a loss map but typically illustrated by an efficiency map ("Eff. map") at the system level. In motor mode, electrical energy flows from the battery through the converter to the stator windings of the e-machine. This energy is converted into mechanical energy via magnetic fields and transmitted to the rotor, propelling the vehicle. In generator mode, commonly activated during regenerative braking, the e-machine converts mechanical energy back into electrical energy. This energy is routed through the converter and returned to the battery, i.e., a direction of reverse energy flow compared to motoring mode.

To evaluate the propulsion behavior and energy consumption of the vehicle under realistic driving conditions, a simplified vehicle dynamics model is employed, which is inherited from previous work presented in [23]. It represents a small passenger car equipped with a single electric machine functioning as the traction unit. For vehicle dynamics evaluation, the vehicle is approximated as a rigid body, a valid assumption when the primary objective is to analyze energy levels within the propulsion drivetrain, as discussed in [49]. The vehicle's motion is simplified to a single spatial dimension, specifically the longitudinal direction, assuming dynamic stability throughout operation. Under these conditions, the motion of the vehicle is described by Newton's second law,

$$m_{car}\frac{dv_{car}(t)}{dt} = F_{tractive}(t) - F_{resistive}(t) \tag{3.1}$$

where m_{car} is the total vehicle mass in kg, v_{car} is the vehicle speed in m/s, $F_{tractive}$ is the tractive force provided by the EV powertrain in N, and $F_{resistive}$ is the sum of resistive forces in N, which includes aerodynamic drag $F_{drag}(t)$, rolling resistance $F_{roll}(t)$, and grading force $F_{grade}(t)$:

$$F_{resistive}(t) = F_{drag}(t) + F_{roll}(t) + F_{grade}(t) \tag{3.2}$$

These resistive forces are defined as:

$$\begin{cases} F_{drag}(t) = \frac{1}{2}\rho_{air}C_dA_{front}\left[v_{car}(t) - v_{wind}(t)\right]^2 \\ F_{roll}(t) = C_r m_{car} g\cos\alpha(t) \\ F_{grade}(t) = m_{car} g\sin\alpha(t) \end{cases} \tag{3.3}$$

where C_d is the aerodynamic drag coefficient, ρ_{air} is the air density in kg/m^3, A_{front} is the EV's frontal area in m^2, $v_{wind}(t)$ is the wind speed in m/s, and $\alpha(t)$ is the road inclination angle. In this study, $v_{wind}(t)$ and $\alpha(t)$ are set to zero, as road grade and wind effects are not considered.

The tractive force thus becomes:

$$F_{tractive}(t) = m_{car}\frac{dv_{car}(t)}{dt} + F_{drag}(t) + F_{roll}(t) \tag{3.4}$$

Using the gear ratio k_{gear}, wheel radius r_{wheel}, and gear efficiency η_{gear}, the torque in motor and generator modes ($T_{em,mot}(t)$ and $T_{em,gen}(t)$ in Nm), and the rotor speed $n_r(t)$ in rpm of the traction e-machine are calculated as:

$$\begin{cases} T_{em,mot}(t) = \frac{r_{wheel}}{k_{gear}\eta_{gear}}\left(m_{car}\frac{dv_{car}(t)}{dt} + F_{drag}(t) + F_{roll}(t)\right) \\ T_{em,gen}(t) = \frac{r_{wheel}\eta_{gear}}{k_{gear}}\left(m_{car}\frac{dv_{car}(t)}{dt} + F_{drag}(t) + F_{roll}(t)\right) \\ n_r(t) = \frac{k_{gear}}{r_{wheel}}v_{car}(t)\frac{60}{2\pi} \end{cases} \tag{3.5}$$

The power provided by the e-machine in motor mode $P_{em,mot}(t)$ in W, and the required battery input power $P_{bat,mot}(t)$ in W, are given by:

$$\begin{cases} P_{em,mot}(t) = T_{em,mot}(t)n_r(t) \\ P_{bat,mot}(t) = \frac{P_{em,mot}(t)+P_{em,loss}(t)}{\eta_{conv}\eta_{bat}} \end{cases} \tag{3.6}$$

where $P_{em,loss}(t)$ is the total loss of the e-machine.

In generator mode, the mechanical input power $P_{em,gen}(t)$ in W and the regenerated battery power $P_{bat,gen}(t)$ in W are

$$\begin{cases} P_{em,gen}(t) = T_{em,gen}(t)n_r(t) \\ P_{bat,gen}(t) = [P_{em,gen}(t) - P_{em,loss}(t))]\eta_{conv}\eta_{bat} \end{cases} \tag{3.7}$$

Then, the total energy consumption from the battery $E_{bat,net}$ is estimated as

$$E_{bat,net} = \int P_{bat,mot}(t)dt - \int P_{bat,gen}(t)dt \tag{3.8}$$

Consistent with the previous study [23], to focus on the impact of the e-machine, only the energy consumption due to the e-machine $E_{bat,net,due-to-EM}$

is included, and it can be expressed as

$$E_{bat,net,due-to-EM} = E_{bat,net} - E_{bat,net,ideal-EM} \tag{3.9}$$

where $E_{bat,net,ideal-EM}$ is excluded $P_{em,loss}$ meaning no energy loss from e-machine, and the weight of e-machine is 0 ($m_{em} = 0$). Finally, the energy consumption from the grid due to e-machine can be expressed as

$$E_{grid,due-to-EM} = \frac{E_{bat,net,due-to-EM}}{\eta_{char}} \tag{3.10}$$

The corresponding parameters are listed in Table 3.2.

Table 3.2: EV powertrain model parameters [23]

Parameters	Value
Gravity constant, g	9.81 m/s^2
Curb and driver weight of the EV, m_{car}	1,575 kg
Aerodynamic drag coefficient, C_d	0.28
Mass density of air, ρ_{air}	1.225 kg/m^3
Front cross-sectional area of EV, A_{front}	2.2 m^2
Rolling resistance coefficient, C_r	0.009
Wheel radius, r_{wheel}	0.316 m
Gear ratio, k_{gear}	9.747
Gear efficiency, η_{gear}	97 %
Converter efficiency, η_{conv}	97 %
Battery efficiency, η_{bat}	99 %
Charging system efficiency, η_{char}	85 %

3.4 Reference PMSM with Nd(Dy)FeB magnet (Ref. PMSM) modeling

3.4.1 Energy loss model

The cross-section of Ref. PMSM is depicted in Figure 3.3, and its design parameters are in Table 3.3.

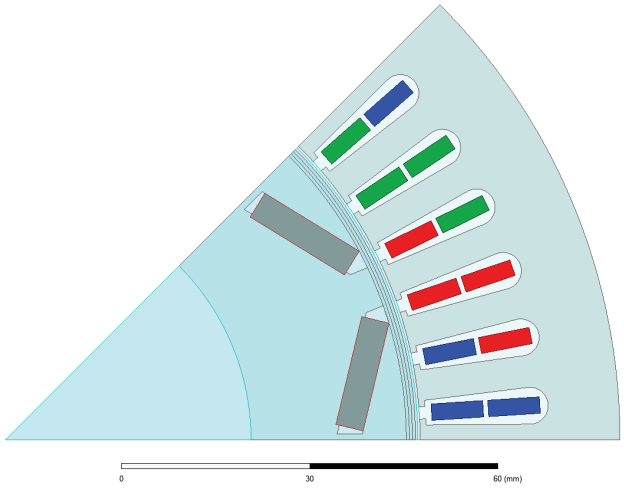

Figure 3.3: Cross-section of Ref. PMSM.

Table 3.3: Design summary of Ref. PMSM.

Machines	**Ref. PMSM**
Number of poles	8
Conductor and magnet materials in stator/rotor	Cu/Nd(Dy)FeB
Stack length [mm]	127
Number of stator slots	48
Number of turns of stator winding per slot	14
Winding layers per slot	2
Number of stator winding parallel branches	4
Stator outer diameter, *dso* [mm]	200
Stator inner diameter, *dsi* [mm]	135
Air gap length, l_g [mm]	0.75
Maximum RMS current density $[A/mm^2]$	20
Stator winding temperature $[°C]$	120
Magnet temperature $[°C]$	70
Material loss rate during punching used in LCI [%]	48

Apart from the ohmic loss, iron loss, and magnet loss, which were obtained from FEM simulation, the bearing friction loss is the same one in the previous study [50] and can be concluded in

$$P_{friction} = \frac{d_{Be}\mu_{Be}T_{em}}{d_{ro}}\frac{2\pi n_r}{60} \tag{3.11}$$

where $P_{friction}$ is bearing friction loss in W, d_{Be} is the bearing bore diameter which is 40 mm, μ_{Be} is the bearing friction coefficient which is set to be 0.0015, d_{ro} is the outer diameter of rotor can be calculated by

$$d_{ro} = d_{si} - 2l_g \tag{3.12}$$

A key addition in this study, compared to previous work, is the inclusion of an iron-loss factor of 1.7, which accounts for additional core loss effects not captured in earlier models. This refinement enhances the accuracy of the loss estimation and is reflected in the updated efficiency and loss maps.

The bearing friction loss map is shown in Figure 3.4.

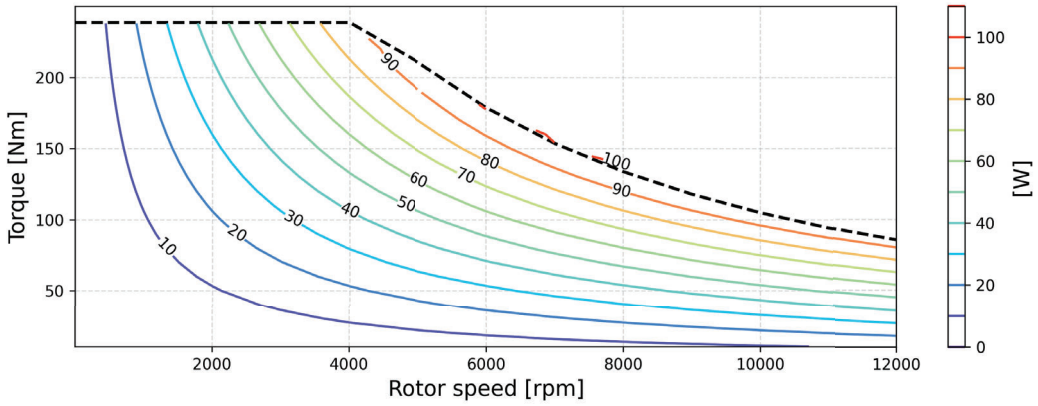

Figure 3.4: The bearing friction loss of Ref. PMSM.

Furthermore, the efficiency map with the operating points from WLTC and loss map of Ref. PMSM are shown in Figure 3.5 and 3.6.

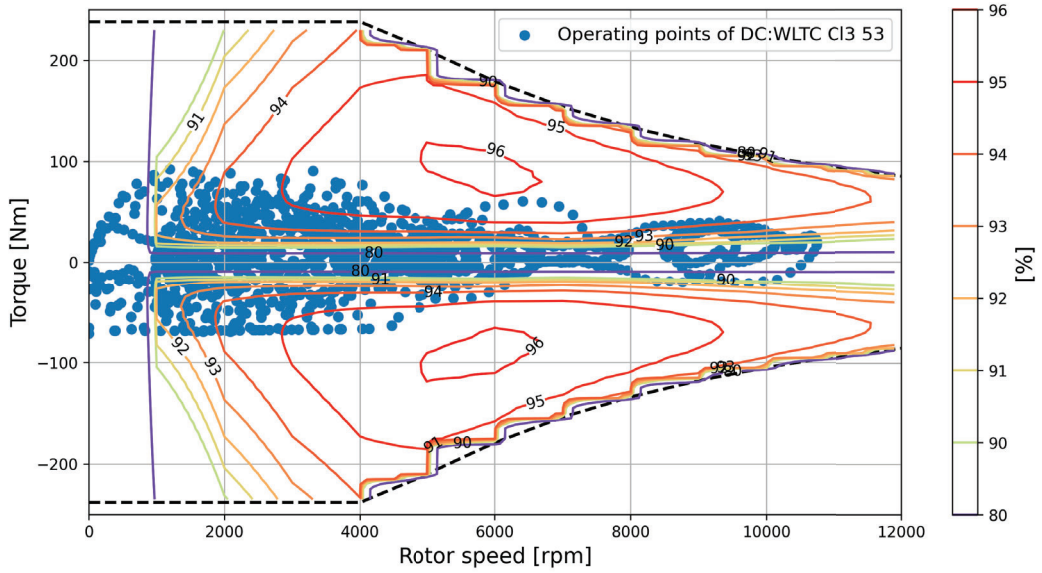

Figure 3.5: The efficiency map with the operating points from WLTC of Ref. PMSM.

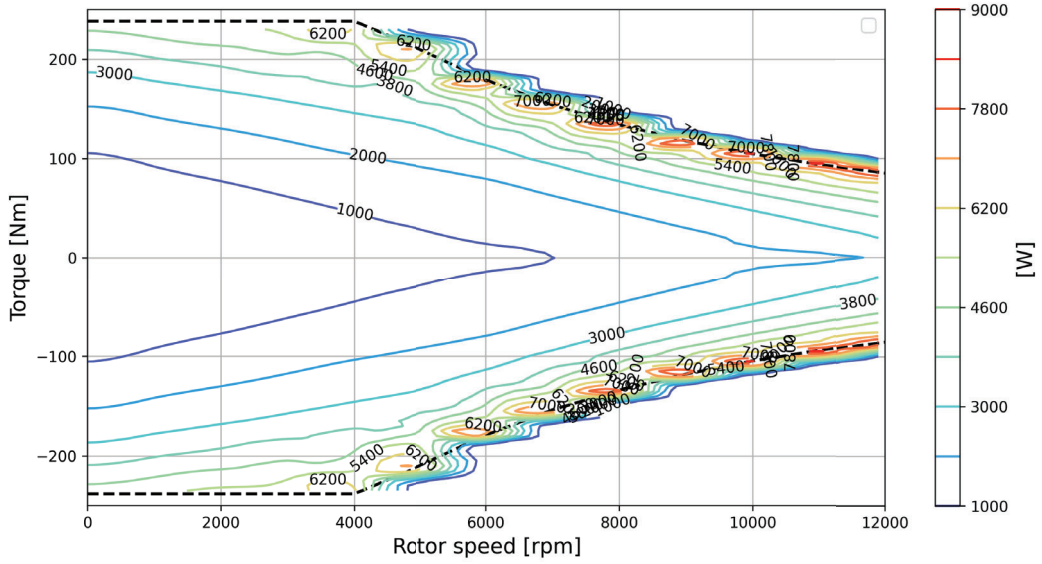

Figure 3.6: The loss map with the operating points of WLTC of Ref. PMSM.

3.4.2 Life cycle inventory (LCI) model

The general exploded-view of a PMSM is shown in Figure 3.7 [23], highlighting its principal components and their spatial arrangement, and also illustrates the parts included in the LCI.

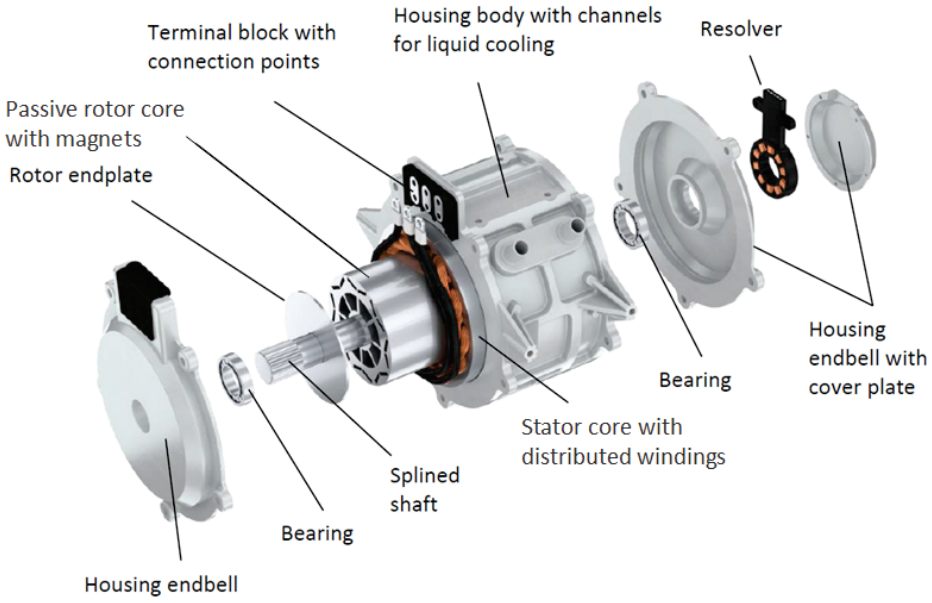

Figure 3.7: General exploded-view drawings of a PMSM.

The stator, equipped with distributed windings, forms the stationary part of the machine and is responsible for generating the rotating magnetic field. The rotor, which contains embedded permanent magnets, interacts with this field to produce torque in a synchronous manner. The splined shaft transmits mechanical power to the load, while the bearings provide radial and axial support, ensuring smooth and stable rotation. The housing body incorporates channels for liquid cooling, which is essential for maintaining thermal stability under high-load conditions. Additionally, the resolver is integrated to provide accurate rotor position feedback, enabling precise control strategies such as field-oriented control. The terminal block facilitates electrical connections for both power and signal transmission.

A system overview of the life cycle up to the production stage of the Ref. PMSM is presented in Figure 3.8. As shown, most of the data originates from the PMSM LCI model developed by Nordelöf et al. in a series of pub-

lications [51]–[53], while the remaining data is sourced from a previous study [23]. The diagram is organized into three hierarchical sections: (1) Ecoinvent representation of production efforts, (2) Magnet factory, and (3) E-machine factory.

The upper section represents upstream processes such as injection molding, extrusion, hot rolling, wire drawing, and zinc coating, which collectively produce intermediate components, including Cu parts, steel parts, and electrical steel sheets. To model these processes, version 3.9.1 of the Ecoinvent database [40], [41], one of the most widely recognized and comprehensive LCI databases, was employed to capture representative activities.

The central section focuses on the magnet production chain, where rare earth oxides (REOs) and iron-based materials undergo transformation processes, including die casting, to produce pre-magnetized Nd(Dy)FeB magnets. This stage is particularly significant due to the high environmental and economic implications associated with the processing of rare earth elements. The magnet production chain is modeled as located in China, which accounts for over 95% of global rare-earth element production [42]. As a result, the Chinese electricity mix is used in the life cycle assessment, which has notable implications for the overall environmental impact due to its relatively high carbon intensity compared to other regions.

The lower section illustrates the PMSM assembly phase, which integrates inputs from both upstream material preparation and magnet manufacturing to produce the final PMSM unit. Further details of this assembly process are provided in Figure 3.9, based on the PMSM LCI model in [51].

Figure 3.10 is the weight share for Ref. PMSM reworked from Nordelöf et al. [23].

3.5 Electricity production and supply

Building on a similar setup as in the previous study [23], the model of electricity supply was formed with Ecoinvent version 3.9 data [40], where electricity used for production is assumed to be medium voltage (1-24kV [40]) and charging batteries is considered low voltage (below 1kV [40]).

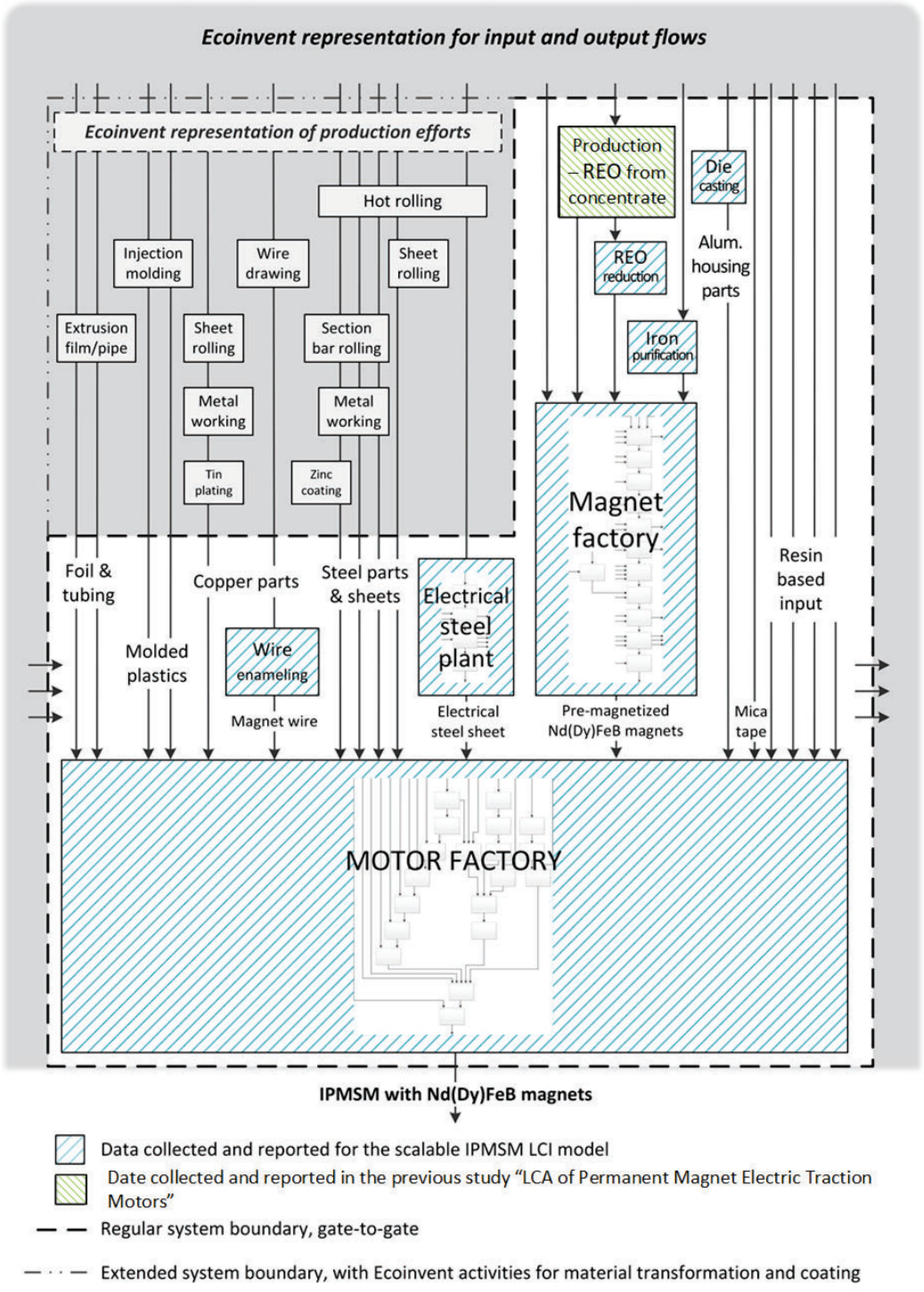

Figure 3.8: Overviewing system model for the production steps of Ref. PMSM [23], [51]–[53].

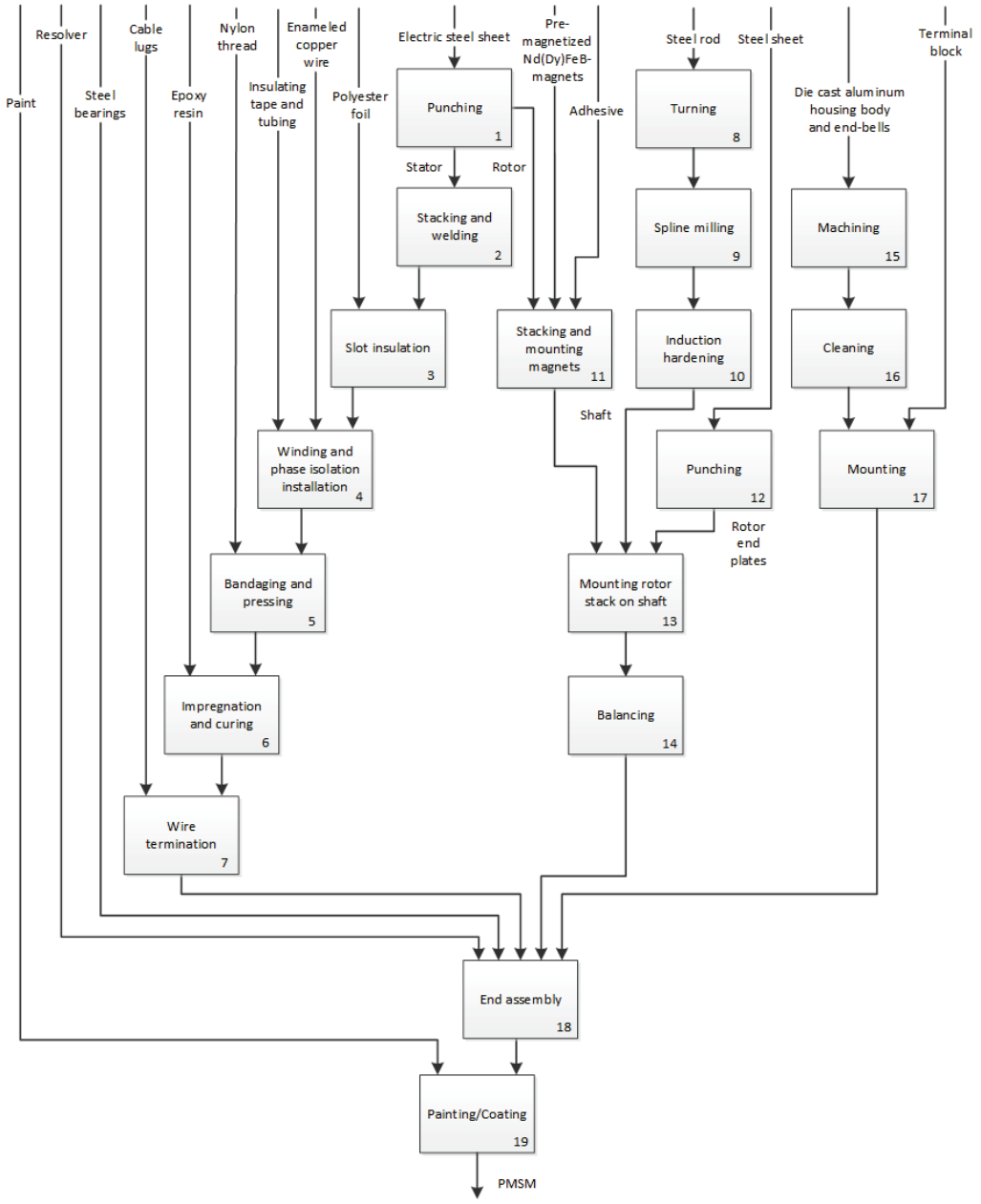

Figure 3.9: PMSM factory process flow chart for Ref. PMSM, divided into 19 processes [51].

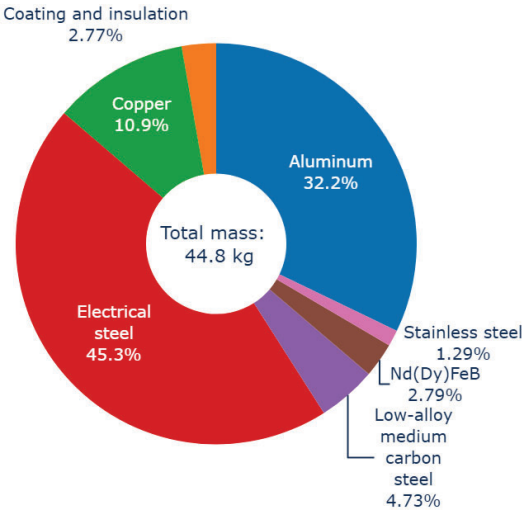

Figure 3.10: Weight share of Ref. PMSM. Reworked from Nordelöf et al. [23].

3.5.1 High greenhouse gas (GHG) intensity electricity (European country's average)

In this study, the average electricity mix of European countries (EU mix) is used to represent a high GHG intensity scenario, with an emission factor of 356 g CO_2-Eq/kWh. According to the Ecoinvent Knowledge Base for the energy sector [55], the electricity supply mix data in Ecoinvent version 3.9 is based on information provided by the IEA for the year 2021. Table 3.4 presents the electricity production mix for European countries as reported by the IEA [54], which is the foundational dataset for the electricity supply mix in Ecoinvent 3.9.

3.5.2 Low GHG intensity electricity (Norway)

The low GHG intensity electricity scenario in this study is set to be the electricity mix in Norway, of which data is also primarily from IEA [55]. Table 3.5 displays the electricity generation mix for Norway, as reported by the IEA [56] for 2021, which forms the basis for the electricity supply mix used in Ecoinvent 3.9. This resulted in an emission of 34 g CO_2-Eq/kWh from the electricity mix of Norway in 2021.

Table 3.4: The European countries' electricity production mix as reported by IEA [54] for 2021, the overarching data source for the electricity generation data in Ecoinvent used in this LCA study.

Production facility type	Amount	Share
Biomass-fired	196 TWh	5.0%
Coal-fired	663 TWh	16.7%
Natural gas	896 TWh	22.6%
Oil-fired	52 TWh	1.3%
Waste incineration	53 TWh	1.3%
Nuclear power	889 TWh	22.4%
Hydropower	679 TWh	17.1%
Wind power	500 TWh	12.6%
Solar	206 TWh	5.2%
Geothermal	23 TWh	0.6%
Other sources	8 TWh	0.2%

Table 3.5: The Norwegian electricity production mix as reported by IEA [56] for 2021, the overarching data source for the electricity generation data in Ecoinvent used in this LCA study.

Production facility type	Amount	Share
Coal-fired	192 GWh	0.1%
Natural gas	305 GWh	0.2%
Oil-fired	400 GWh	0.3%
Waste incineration	363 TWh	0.2%
Hydropower	144 TWh	91.6%
Wind power	12 TWh	7.5%
Solar	108 GWh	0.1%
Other sources	412 GWh	0.2%

3.5.3 Electricity to produce Nd(Dy)FeB magnet (China)

The electricity scenario to manufacture the Nd(Dy)FeB magnet is the electricity mix in China in 2020, the data of which is mainly derived from IEA as well [55]. It resulted in an emission of 845 g CO_2-Eq/kWh from the Chinese electricity mix.

Table 3.6: The Chinese electricity production mix as reported by IEA [57] for 2020, the overarching data source for the electricity generation data in Ecoinvent used in this LCA study.

Production facility type	Amount	Share
Biomass-fired	164 TWh	1.9%
Coal-fired	5431 TWh	64.1%
Natural gas	291 TWh	3.4%
Oil-fired	12 TWh	0.1%
Waste incineration	7 TWh	0.1%
Nuclear power	408 TWh	4.8%
Hydropower	1339 TWh	15.8%
Wind power	656 TWh	7.7%
Solar	329 TWh	3.9%
Other sources	210 GWh	0.0%

3.6 Transport and end-of-life (EoL)

In Figure 3.11, four transport models: T1-T4, are depicted between different stages of the life cycle, where T1 represents the transport of magnets from China to the e-machine factory in Europe, T2 represents the average transport of different subparts to the e-machine factory to and within Europe, T3 is the transport of scrap from the e-machine factory to the recycling center within Europe, and T4 is the transport for collection of EoL e-machine to recycling centers.

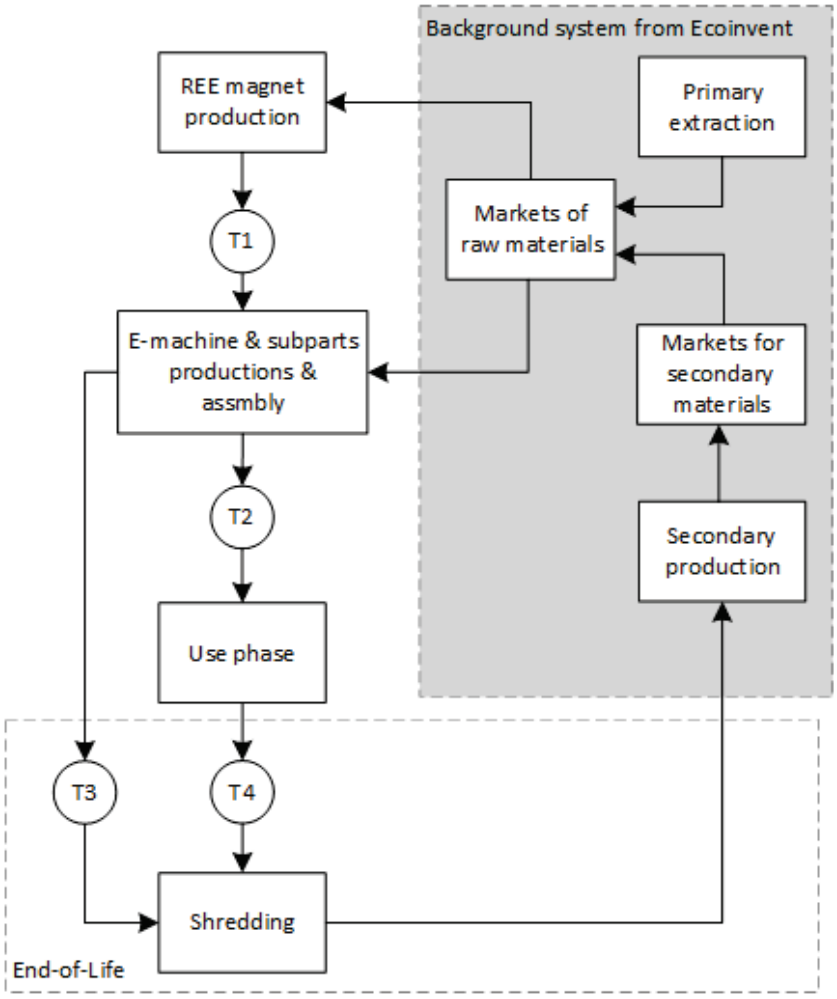

Figure 3.11: Transportation between different life-cycle stages and how they are modelled in the study.

3.6.1 Transports for productions

Inherited from the previous work [23], this study incorporated the transportation of materials and subparts for each technical option, employing a simple approach based on estimated geographical distances, both on land and along typical oceanic routes as stated in Table 3.7-3.10.

T1 is the transportation model of delivering REEs-magnets from China to Europe described in Table 3.7 and its transported weight is in Table 3.8. It was assumed that magnets and magnetic materials are transported by train through China, starting from the mine and raw material processing in Bayan Obo, Inner Mongolia, to further processing at a magnet factory in Baotou, and finally to the port. Subsequently, the materials are shipped by boat to Europe via the shortest available route. Any additional transport of magnets within Europe was disregarded.

Table 3.7: Estimations made for the distance and mode in the transportation of magnets produced in China, measured per 1 ton-km, to Europe. European mainland transportation was neglected (T1).

Route	Type	Distance	Linked flow	Location
In mainland China	Train	1000 km	Transport, freight train	China
China to Europe	Ship	21000 km	Transport, freight, sea, container ship	Global

Table 3.8: Estimations made of masses transported to and from the magnet production site in China, and to the e-machine assembly in Europe (T1).

Route	Type	Nd(Dy)FeB magnets
In mainland China	Train	2 kg
China to Europe	Ship	1.26 kg

For transportation of all other subparts modelled in T2 and its transported distances and masses are stated in Table 3.9-3.10., it was assumed that they would arrive at the e-machine factory with an average transportation load equivalent to 1000 km by truck within Europe.

Table 3.9: Estimations made for the average total distance and mode in the transportation of all other e-machine subparts, from material production via subpart manufacturing to the e-machine factory, measured per 1 ton-km, to and within Europe (T2).

Route	Type	Distance	Linked flow	Location
In Europe	Truck	1000 km	Transport, freight, lorry >32 metric ton, EURO6	Europe

Table 3.10: Estimations made of masses transported to the e-machine assembly to and within Europe (T2).

Route	Type	Transported mass [kg]							
		Ref. PMSM	IM1	IM2	IM3	Syn-RM1	Syn-RM2	EE-SM1	EE-SM2
To or within Europe	Truck	61.0	84.5	89.4	104	131.3	154.7	77.5	86

3.6.2 Transports for EoL

Table 3.11 declares the transportation data to deliver manufacturing scrap from the e-machine factory to the recycling center based on the average transport of steel scrap from Ecoinvent for the European market of steel scrap. These values are, in turn, approximated from global market processes, based on original data derived from expert judgment. It is assumed that manufacturing scrap is treated in the same region as the e-machine is produced, where regional market activities are, in this case, adequate; thus, the distance between the two facilities is rather close, within 20 km. The transported masses from manufacturing scrap are listed in Table 3.12, mainly from the process of punching electrical steel sheets, which could be observed in Table 3.15.

The transportation data in Table 3.13 is based on the Ecoinvent average transportation of iron scrap for the global market from sorting to secondary steel production. In this study, this data was used to represent the transport of the collections of EoL e-machines to the recycling centers globally. Their distances and the transport types are rather scattered, from 20 km to 211 km by train, ship, or lorry. It is assumed that the collection points of EoL EVs and

Table 3.11: Estimations made for the average total distance and mode in the transportation of manufacturing scrap from the e-machine factory to the recycling center, measured per 1 ton-km, within Europe (T3).

Route	Type	Distance	Linked flow	Location
In Europe	Train	11.2 km	Transport, freight train	Europe
In Europe	Truck	19.32 km	Transport, freight, lorry, unspecified	Europe

Table 3.12: Estimations made for masses of manufacturing scrap transported from the e-machine factory to the recycling center (T3)

Route	Type	Transported mass [kg]							
		Ref. PMSM	IM1	IM2	IM3	Syn-RM1	Syn-RM2	EE-SM1	EE-SM2
Within Europe	Train and Truck	20.6	25	27	32.9	48.1	57.9	24.4	31.1

recycling centers have distances that are less than 220 km. The transported masses of the four technical options are listed in Table 3.14, which are the masses of their full products' weights.

Table 3.13: Estimations made for the average total distance and mode in the transportation of EoL e-machines, from collection points to the recycling centers, measured per 1 ton-km, from and within Europe (T4).

Route	Type	Distance	Linked flow	Location
Global	Train	112 km	Transport, freight train	Europe
Global	Ship	19.9 km	Transport, freight, inland waterways, barge	Europe
Global	Truck	193.2 km	Transport, freight, lorry, unspecified	Europe
Global	Ship	211.5 km	Transport, freight, sea, container ship	Global

Table 3.14: Estimations made for the masses of EoL e-machines from collection points to the recycling centers from and within Europe (T4).

Route	Type	Transported mass [kg]							
		Ref. PMSM	IM1	IM2	IM3	Syn-RM1	Syn-RM2	EE-SM1	EE-SM2
From and within Europe	Train, ship, and truck	44.9	59.5	62.9	71.2	83.2	96.8	52.1	54.9

3.6.3 EoL

In this study, only part of EoL included in the model is the shredding process, which is the standard method used by most recycling centers for the e-machine recycling [58]. As illustrated in Figure 3.11, scrap from the e-machine factory, along with EoL e-machines, is assumed to be transported to recycling centers for processing. The masses of different scrap are listed in Table 3.15.

Table 3.15: Mass of main scraps from the e-machine factory.

E-machines	Scraps of steel sheet		Scraps of Al and Cu	
	[kg]	[%]	[kg]	[%]
Ref. PMSM	19.7	30%	0.9	1%
IM1	21.8	26%	3.2	4%
IM2	25.8	29%	1.2	1%
IM3	31.6	30%	1.2	1%
SynRM1	46.9	36%	1.3	1%
SynRM2	56.6	37%	1.3	1%
EESM1	23.3	29%	1.1	1%
EESM2	30.1	36%	1.1	1%

CHAPTER 4

Induction machine modeling

In this chapter, a method for identifying IM parameters is presented first. Next, built on the proposed method, three induction machines were designed and examined:

1. IM with dist. Cu stator windings and Cu rotor bars (IM1).
2. IM with dist. Cu stator windings and Al rotor bars (IM2).
3. IM with dist. Al stator windings and Al rotor bars (IM3).

Their electromagnetic FEM models are built to resemble their energy loss models. Thirdly, the LCI models of IMs are constructed and presented. Finally, in this chapter, their LCA results are benchmarked against those of the Ref PMSM in Chapter 3.

The design summary of three IMs is listed in Table 4.1.

4.1 IM Parameter Identification

Accurate parameter estimation is essential in early design stages to reduce prototyping and enable precise performance evaluation. Traditional methods,

Table 4.1: Design summary of investigated IMs.

Machines	**IM1**	**IM2**	**IM3**
Number of poles	4		
Conductor materials in stator/rotor	Cu / Cu	Cu / Al	Al / Al
Stack length l_a [mm]	158	178	218
Number of stator/rotor slots	S48 / R60		
Number of winding turns in stator N_s	13	6	5
Number of stator winding parallel branches N_{pb}	4	2	
Stator outer diameter [mm]	200		
Stator inner diameter [mm]	127.3	133.3	
Air gap length [mm]	0.5		
Maximum RMS current density $[A/mm^2]$	20		16.7
Stator winding temperature $[°C]$	120		
Rotor winding temperature $[°C]$	150		
Material loss rate during punching used in LCI [%]	47	46	

such as no-load and locked-rotor tests [6], are limited by fixed flux levels and inseparable leakage inductances.

Advanced techniques [59]–[61] utlize load tests, online estimation, and flux-decay analysis, but they rarely integrate with FEM for early-stage design. FEM-based approaches [8]–[11] address saturation and deep-bar effects using equivalent circuit models like the T-form (TFM) and inverse Γ-form (IGFM). However, many remain unvalidated or restricted to standstill conditions.

This work introduces a FEM-based method to extract dynamic equivalent circuit parameters as functions of magnetizing current, accounting for iron saturation and deep-bar effects. Parameters for both TFM and IGFM are derived from current and flux linkage phasors under no-load and load conditions using a transient solver. The approach enhances torque prediction accuracy compared to conventional tests and supports optimal operating point selection with minimal FEM effort. Experimental validation demonstrates its effectiveness against traditional and proposed methods.

4.1.1 Equivalent Model

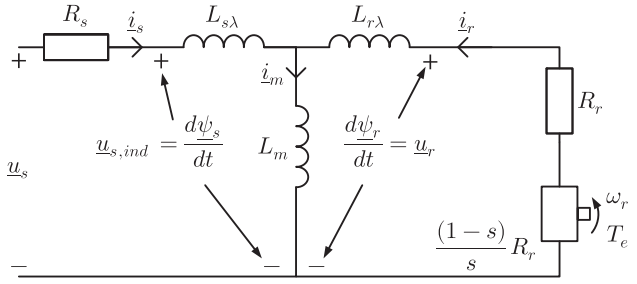

Figure 4.1: Steady-state T-form model of IMs.

The classical steady-state TFM in the α-β stationary frame with amplitude-invariant scaling is shown in Figure 4.1. The current relationship is

$$\underline{i}_m = \underline{i}_s + \underline{i}_r \tag{4.1}$$

Stator and rotor flux linkages are

$$\underline{\psi}_s = L_s \underline{i}_s + L_m \underline{i}_r, \quad \underline{\psi}_r = L_r \underline{i}_r + L_m \underline{i}_s \tag{4.2}$$

where $L_s = L_m + L_{s\lambda}$ and $L_r = L_m + L_{r\lambda}$, both varying with magnetizing current I_m due to saturation. FEM simulations provide currents and flux

linkages, enabling estimation of L_m, L_s, L_r, and $\underline{i}_m$ via (4.1–4.2). Rotor resistance R_r is computed from torque T_{em} and rotor current I_r

$$R_r = \frac{2T_{em}\omega_r}{3I_r^2} \cdot \frac{s}{1-s} \tag{4.3}$$

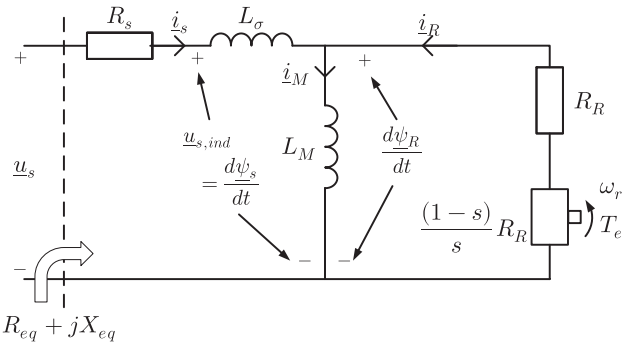

Figure 4.2: Steady-state inverse Γ-form model of IMs.

The IGFM, shown in Figure 4.2, is widely used in control due to reduced parameterization [30]. Its parameters are obtained from TFM as

$$R_R = \left(\frac{L_m}{L_r}\right)^2 R_r, \quad L_M = \frac{L_m^2}{L_r}, \quad L_\sigma = L_s - L_M \tag{4.4}$$

and rotor flux linkage

$$\underline{\psi}_R = \frac{L_m}{L_r}\underline{\psi}_r \tag{4.5}$$

Under Park transformation and PFOC, $\underline{\psi}_R$ aligns with the d-axis, yielding

$$\omega_2 = \frac{R_R i_s^q}{\psi_R^d} \tag{4.6}$$

$$T_{em} = \frac{3}{2} N_p \psi_R^d i_s^q \tag{4.7}$$

Accurate prediction of R_R, L_M, and ψ_R^d ensures precise torque estimation from i_s^d and i_s^q.

4.1.2 Rotor-Fixed u-v Coordinate System

Using a FEM tool such as Ansys/Maxwell, the induced voltage, current, and flux linkage in individual rotor bars can be computed. Following [13], a transient solver is preferred over a time-harmonic solver to capture saturation and deep-bar effects; thus, it is adopted in this work. To aggregate variables from multiple bars into one pole, a rotor-fixed u-v coordinate system is introduced, where u and v represent the real and imaginary axes, respectively.

Figure 4.3 illustrates the coordinate systems in the cross-section of a six-pole 15 kW IM FEM model. On the stator side, the α-axis aligns with the flux linkage of phase A, while the β-axis lags by $\pi/2$. On the rotor side, the u-axis and v-axis correspond to electrical angles π (Bar07) and $3\pi/2$, respectively. The rotor flux linkage $\underline{\psi}_r$ defines the d-axis orientation.

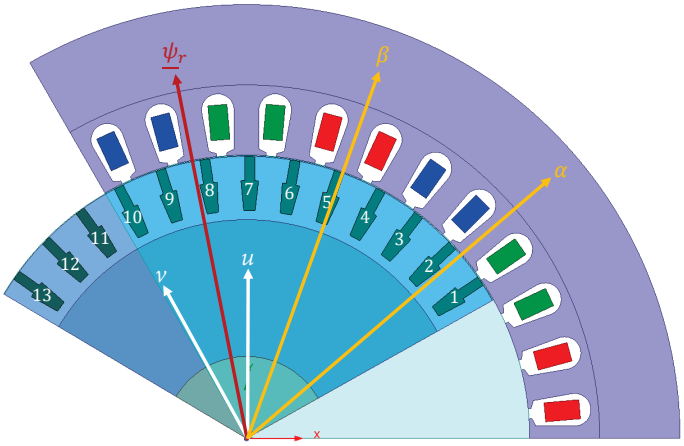

Figure 4.3: Coordinate systems in the 15 kW IM FEM model.

For a rotor segment, time-varying quantities in different bars share the same amplitude and frequency ω_2, with a phase shift of $(2\pi N_p)/Q_r$ between adjacent bars [62]. Thus, in the u-v plane

$$x^{uv}_{bar,k}(t) = X^{uv}_{bar} \cos\left(\omega_2 t - \frac{(k-1)2\pi N_p}{Q_r}\right), \quad k = 1, 2, \ldots, \frac{Q_r}{2N_p} \tag{4.8}$$

where $x \in \{u, i, \psi\}$ and $X \in \{U, I, \Psi\}$.

Projecting these variables onto the rotor-fixed axes gives

$$\begin{cases} x_r^u(t) = \sum_{k=1}^{Q_r/2N_p} x_{bar,k}^{uv}(t) \cos\left(\pi - (k-0.5)\frac{2\pi N_p}{Q_r}\right) \\ x_r^v(t) = \sum_{k=1}^{Q_r/2N_p} x_{bar,k}^{uv}(t) \sin\left(\pi - (k-0.5)\frac{2\pi N_p}{Q_r}\right) \end{cases} \tag{4.9}$$

From ψ_r^u and ψ_r^v at $t = 0$, the initial electrical angle between α-β and d-q frames is

$$\theta_{rf0} = \theta_{u,0} + \theta^{uv}_{\underline{\psi}_r 0} \tag{4.10}$$

where $\theta_{u,0}$ is the u-axis angle in α-β and $\theta^{uv}_{\underline{\psi}_r 0}$ is the rotor flux angle in u-v.

Rotor quantities can be referred to the stator side as

$$\Psi_r = \frac{2N_s q_s k_1 N_p}{c_s} \Psi_{bar}^{uv}, \qquad I_r = \frac{Q_r c_s}{6N_s q_s k_1 N_p} I_{bar}^{uv} \tag{4.11}$$

4.1.3 Conventional Method

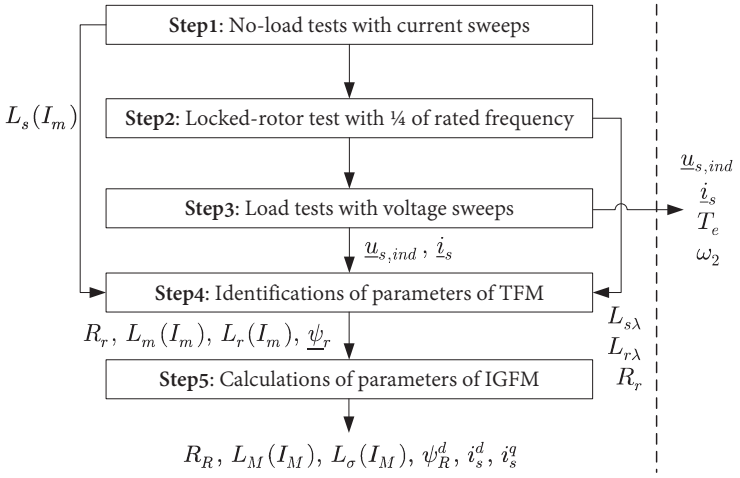

Figure 4.4: Flowchart of the conventional method.

The IEEE standard method [6] estimates IM parameters at rated conditions using no-load and locked-rotor tests. Since the locked-rotor test only provides total leakage inductance $L_{s\lambda} + L_{r\lambda}$, their ratio is assumed as $L_{s\lambda}/L_{r\lambda} = 1$ per [6]. The procedure (Figure 4.4) is implemented in Ansys/Maxwell

- **Step 1:** Perform no-load tests at various stator currents to determine $L_s(I_m)$.
- **Step 2:** Conduct a locked-rotor test at 25% rated frequency to obtain R_r and $L_{s\lambda} + L_{r\lambda}$.
- **Step 3:** From load test phasors $\underline{u}_{s,ind}$ and $\underline{i}_s$, compute

$$\underline{u}_m = \underline{u}_{s,ind} - j\omega_0 L_{s\lambda}, \qquad \underline{i}_m = \underline{i}_s + \frac{\underline{u}_m}{R_r + j\omega_0 L_{r\lambda}} \tag{4.12}$$

  Then derive $L_m(I_m)$, $L_r(I_m)$, and $\underline{\psi}_r$ using (4.2).
- **Step 4:** Apply (4.4)–(4.5) to compute R_R, $L_M(I_m)$, $L_\sigma(I_m)$, and ψ_R^d. Finally

$$i_s^d = \frac{\psi_R^d}{L_M}, \qquad i_s^q = \sqrt{I_s^2 - (i_s^d)^2} \tag{4.13}$$

4.1.4 Proposed Method

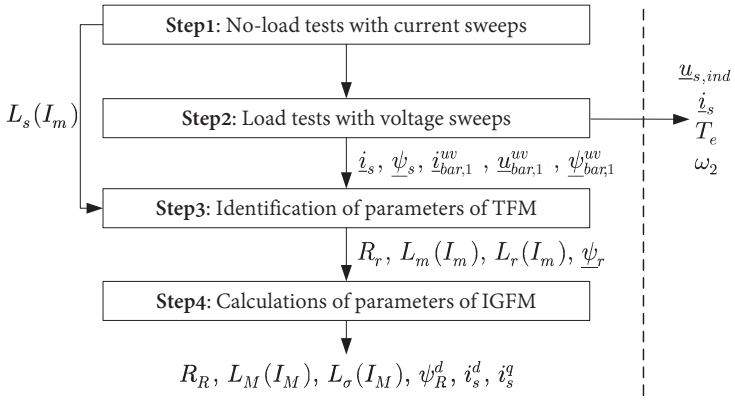

Figure 4.5: Flowchart of the proposed procedure.

The proposed method, illustrated in Figure 4.5, begins with a no-load test to establish the L_m–I_m relationship. In the second step, stator phasors are directly extracted from FEM results. To capture rotor branch information, the induced voltage and current phasors of a rotor bar, $\underline{u}^{uv}_{bar,1}$ and $\underline{i}^{uv}_{bar,1}$, are obtained from the end-connection in Ansys/Maxwell, which represents the

end-rings in 2D FEA. The rotor bar flux linkage is then computed as

$$\psi_{bar,1}^{uv}(t) = \int u_{bar,1}^{uv}(t)\, dt \tag{4.14}$$

and referred to the stator side using (4.11), avoiding the locked-rotor test approach.

With $L_s(I_m)$ from Step 1 and phasors from Step 2, Step 3 determines R_r, $L_m(I_m)$, $L_r(I_m)$, and $\underline{\psi}_r$. Step 4 follows the same procedure as in the conventional method to compute IGFM parameters.

4.1.5 Verification by FEM simulations for a 15 kW IM

Previous work [63] showed that the proposed method outperforms the IEEE standard [6] under varying input voltages at constant speed (980 rpm). Here, robustness is further tested for rotor speeds from 995 rpm to 950 rpm (slip 0.5%–5%) at constant voltage.

The investigated 15 kW IM design is summarized in Table 4.2, and its cross-section is shown in Figure 4.3.

Table 4.2: Design details of the 15 kW IM.

Parameter	Value	Unit
Rated output power	15	kW
Rated speed	980	rpm
Rated line-to-line voltage (RMS)	380/50	V/Hz
Pole pairs N_p	3	-
Core stack length	230	mm
Stator outer/inner diameter	291.2 / 190.2	mm
Rotor outer/inner diameter	189.3 / 55	mm
Rotor end-ring diameter	163.3	mm
Stator slots Q_s / Rotor slots Q_r	36 / 39	-
Turns per coil N_s	38	-
Stator conductor area	1.98	mm^2
Parallel strands per turn	2	-
Parallel branches N_{pb}	3	-
Connection	Y	-
Stator/Rotor temperature	70 / 102	°C
Materials (Stator/Rotor/Iron)	Cu / Al / M700-50A	-

To validate the proposed model, IGFM parameters are used to predict IM performance and compared with FEM results. The electromagnetic torque is given by (4.7). The equivalent impedance in Figure 4.2 is

$$\begin{cases} R_{eq} = R_s + \dfrac{\omega_0^2 L_M^2 \frac{R_R}{s}}{\left(\frac{R_R}{s}\right)^2 + \omega_0^2 L_M^2} \\ X_{eq} = \omega_0 \left[L_\sigma + \dfrac{L_M \left(\frac{R_R}{s}\right)^2}{\left(\frac{R_R}{s}\right)^2 + \omega_0^2 L_M^2} \right] \end{cases} \tag{4.15}$$

The input voltage, active/reactive power, and power factor are

$$\begin{cases} U_s = I_s \sqrt{R_{eq}^2 + X_{eq}^2} \\ P_{in} = \frac{3}{2} I_s^2 R_{eq} \\ Q_{in} = \frac{3}{2} I_s^2 X_{eq} \\ p.f. = \frac{P_{in}}{\frac{3}{2} U_s I_s} \end{cases} \tag{4.16}$$

Two IGFM parameter sets, obtained using the conventional and proposed methods (see Figure 4.4 and Figure 4.5), are compared. The transformed magnetizing inductance curves and key parameters are shown in Figure 4.6 and Table 4.3.

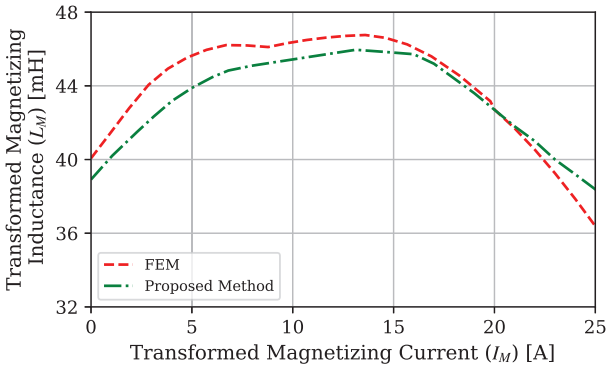

Figure 4.6: Transformed magnetizing inductance curve.

Using these parameters, the d- and q-components of stator current (i_s^d, i_s^q) are computed, and IM performance is predicted via (4.15–4.16). Comparative results between FEM simulations and IGFM-based predictions are shown in Figure 4.7a–4.8d. FEM results (blue solid lines with triangles) correspond

Table 4.3: Transformed rotor resistance and leakage inductance.

Parameter	Unit	Conventional	Proposed
L_σ	mH	4.38	3.89
R_R (102°C)	Ω	0.199	0.215

to rated voltage and slip values from 0.5% to 5%. Predictions from the proposed method are shown as red dashed lines with stars, while the conventional method results are green dash-dotted lines with squares.

Both methods exhibit small deviations from FEM results, with phase voltage amplitude (U_s) errors under 6% (Figure 4.7a). For electromagnetic torque (T_{em}), input active power (P_{in}), reactive power (Q_{in}), and power factor ($p.f.$), the proposed method generally provides closer agreement with FEM than the conventional approach (Figure 4.7b–4.8d).

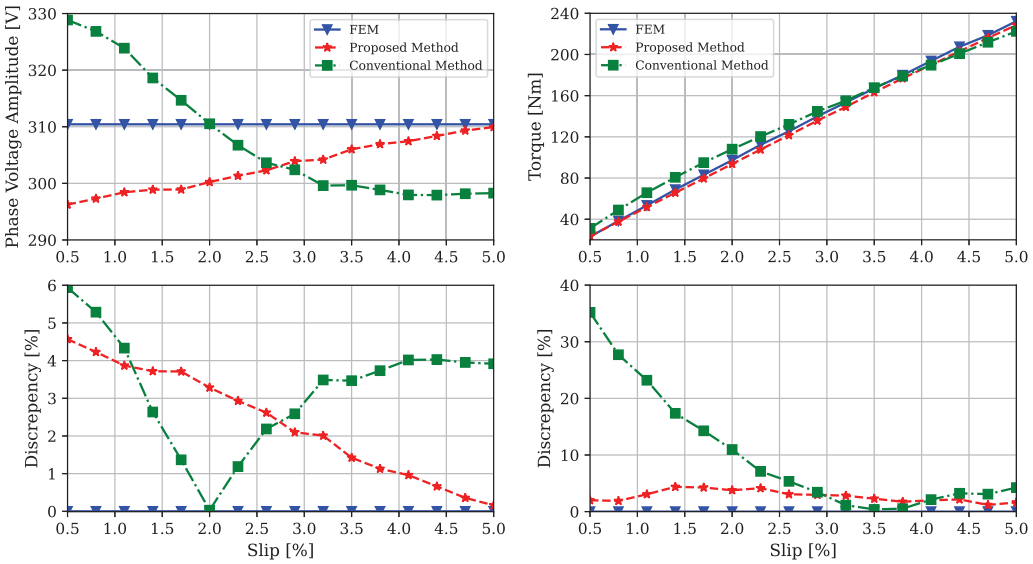

(a) Phase voltage amplitude (U_s). **(b)** Electromagnetic torque (T_{em}).

Figure 4.7: Comparisons of various variables from the FEM model, and two IGFMs.

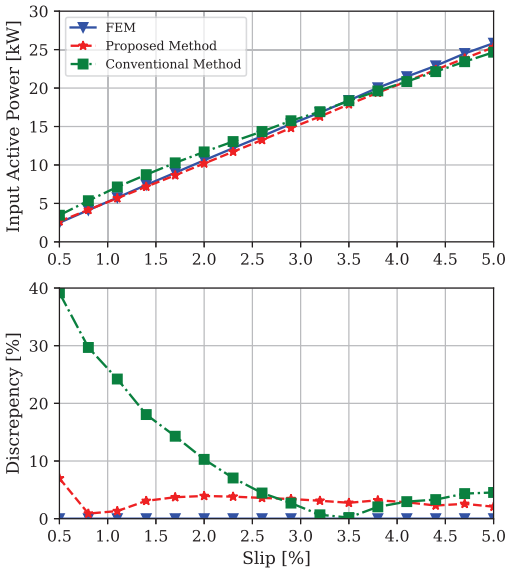

(a) Input active power (P_{in}).

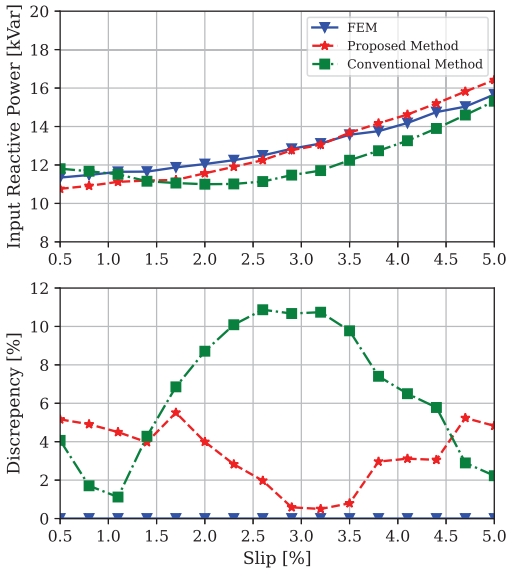

(b) Input reactive power (Q_{in}).

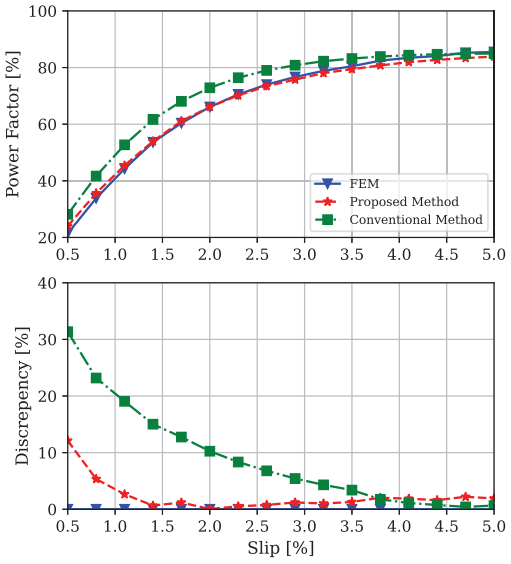

(c) Power factor ($p.f.$).

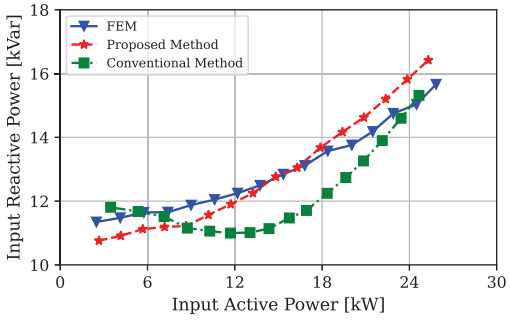

(d) Power curves.

Figure 4.8: Comparisons of various variables from the FEM model, and two IGFMs.

4.1.6 Verification by experimental results for a 15 kW IM

Experimental validation is performed on a 15 kW, 6-pole IM [64]. Five no-load and three load tests with sinusoidal supply were conducted for four hours to ensure thermal steady state. Figure 4.9 shows an example of ambient temperature variation during tests. Stator and rotor conductor temperatures were monitored using PT100 sensors.

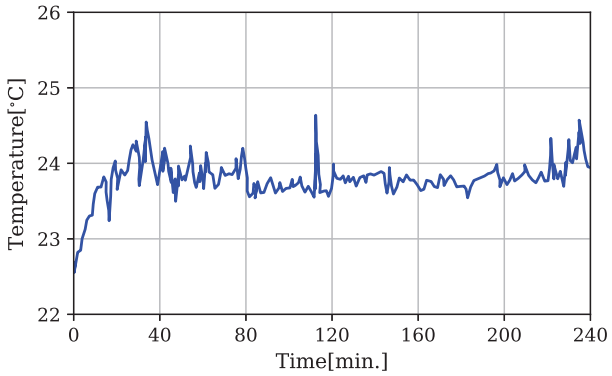

Figure 4.9: Example of ambient temperature fluctuations during tests.

The tested machine was an ABB MBT-180L (15 kW, 970 rpm, 380 V, 32 A), coupled to a DC drive (DMP 160-4S, 40.1 kW, 2470 rpm) powered by a TYRAK S 120 A converter. Power was measured using a Siemens B4301 meter, and torque with a 500 Nm HBM sensor.

Figure 4.10 shows the IGFM updated with iron loss resistance R_{fe}, extracted from no-load tests.

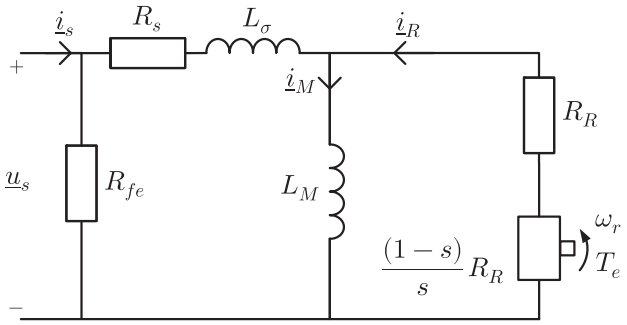

Figure 4.10: Inverse-Γ model including iron loss resistance R_{fe}.

No-Load Tests

Results of five no-load tests at 50 Hz are listed in Table 4.4.

Table 4.4: Experimental results of no-load tests.

Test	1	2	3	4	5
U_{LL} [V]	94.4	203.8	270.2	336	380.7
I_s [A]	4.2	8.1	10.8	14.1	16.9
P_{in} [kW]	0.296	0.494	0.701	0.953	1.178
Winding temp [°C]	28.4	34.3	39.5	46.3	52.5

Figure 4.11 compares stator inductance vs. current from FEM and experiments. The FEM model assumes an airgap of 0.45 mm. Discrepancies decrease at higher currents. Causes include: (i) high sensitivity of L_m to airgap length (0.05 mm variation changes L_s by ≈5 mH [59]), and (ii) omission of end-winding leakage in 2D FEM.

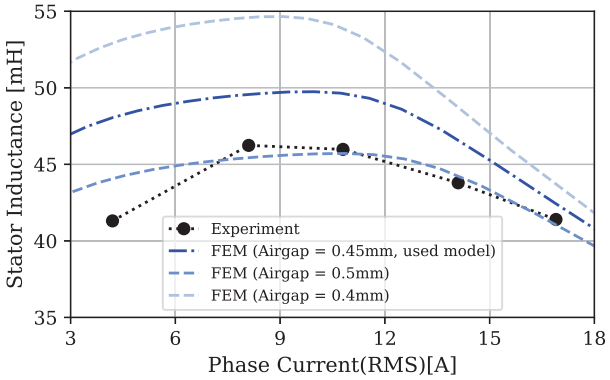

Figure 4.11: Stator inductance vs. stator current: FEM vs. experiment.

Since output power is zero in no-load tests, input power equals stator Cu loss (P_{strand}), core loss (P_{fe}), and friction loss ($P_{friction}$). Using Table 4.2 and winding temperature, R_s and P_{strand} are computed and subtracted. Figure 4.12 shows $(P_{fe}+P_{friction})$ vs. U_{ph}^2. The y-intercept gives $P_{friction}$, listed in Table 4.5.

To align FEM with reality, iron loss is scaled by a factor of 2 (per [65]) to account for manufacturing effects [66]. Figure 4.12 compares adjusted FEM and experimental results.

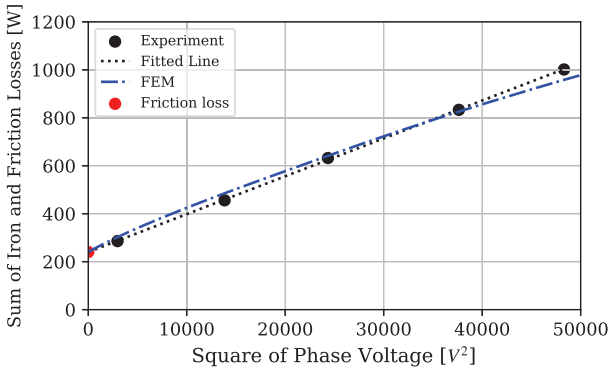

Figure 4.12: Iron and friction loss vs. voltage squared: FEM vs. experiment.

Table 4.5: Extracted no-load loss parameters.

Parameter	Unit	Value
R_{fe}	Ω	191.02
$P_{friction}$	W	240.29

Load Tests

Three load test results at 50 Hz are listed in Table 4.6. Output power and torque are computed by subtracting losses (P_{strand} from R_s, P_{fe} and $P_{friction}$ from no-load tests).

Table 4.6: Experimental results of load tests.

Test	1	2	3
U_{LL} [V]	385.1	380.2	378.7
I_s [A]	19.5	24.8	32
P_{in} [kW]	6.15	11.54	17.08
Speed [rpm]	990.9	980.2	964.9
Stator temp [°C]	57.3	69.8	102.8
Rotor temp [°C]	78.8	102.5	158.3

Comparison with FEM and IGFM Predictions

Figures. 4.13a–4.14b compare experimental results with FEM and IGFM predictions (proposed vs. conventional). FEM predictions are closest overall, but the proposed method provides the best torque estimates (Figure 4.13b). Discrepancies in P_{in} (10–15%) arise mainly from underestimation of U_s, which affects iron loss calculations in circuit-based models. Nevertheless, the proposed method improves predictions of U_s, T_{em}, and Q_{in} compared to the conventional approach.

4.1.7 Flux-Decay Tests

A flux-decay test was performed on the 15 kW IM to estimate rotor resistance, as this method is particularly suited for that purpose. Since no standard exists for this test, the procedure in [6] was used as a reference.

The test consists of two stages: (i) magnetizing the core under no-load conditions, and (ii) disconnecting the supply, causing stator current to drop to zero. After an initial voltage spike, the rotor flux decays to zero, reflected in the stator voltage.

Several tests were conducted at different flux levels. The case presented uses $U_s = 54$ $\mathrm{V_{rms}}$ and $f = 20$ Hz, producing $I_s \approx 10$ $\mathrm{A_{rms}}$. This setting ensures moderate saturation and a relatively constant L_M during the initial decay.

Figure 4.15 shows the three-phase stator voltages and their envelope. The step change at $t = 0$ s is attributed to stator leakage inductance [61]. The stator leakage inductance is estimated as

$$L_{s\lambda} = \frac{U_{s,NL} - U_{s,FD0}}{2\pi f_0 I_{s,NL}} \tag{4.17}$$

where $U_{s,NL}$ and $I_{s,NL}$ are the stator voltage and current amplitudes before disconnection, $U_{s,FD0}$ is the initial voltage amplitude after disconnection, and f_0 is the supply frequency.

The voltage envelope is fitted by:

$$U_{s,FD}(t) = U_{s,FD0} e^{-t/\tau_r} \tag{4.18}$$

where τ_r is the rotor time constant

$$\tau_r = \frac{L_r}{R_r} \tag{4.19}$$

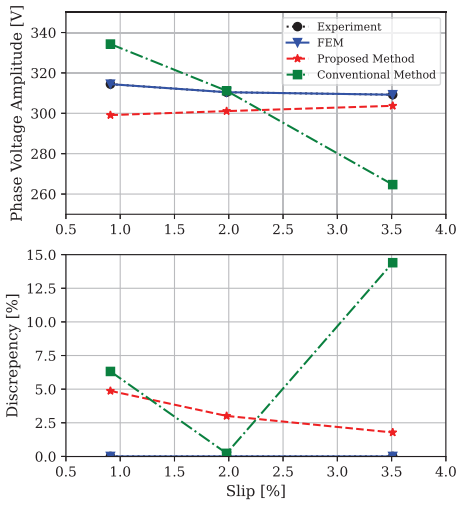

(a) Voltage (Amplitude U_s).

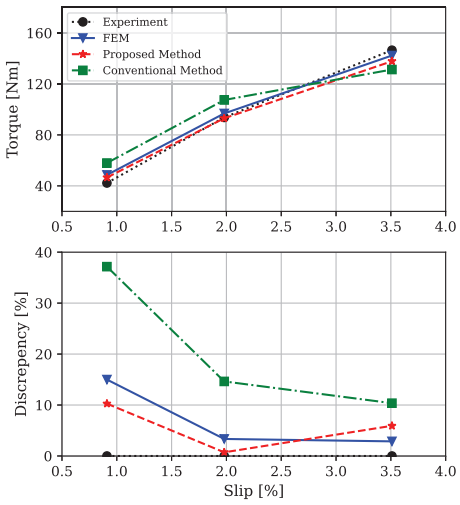

(b) Torque (T_{em}).

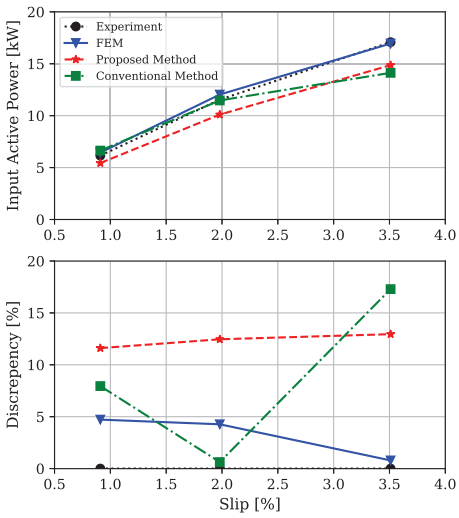

(c) Input active power (P_{in}).

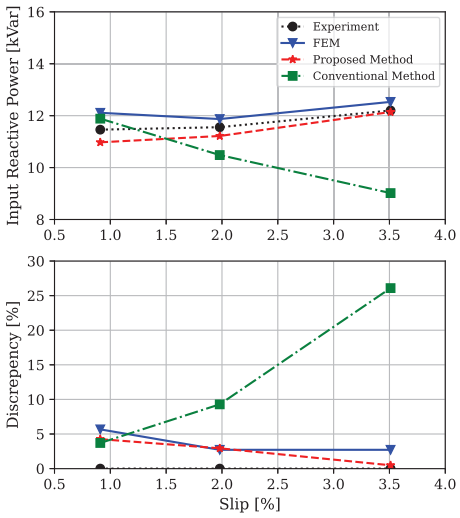

(d) Input reactive power (Q_{in}).

Figure 4.13: Comparisons of various variables from experiments, the FEM model, and two IGFMs.

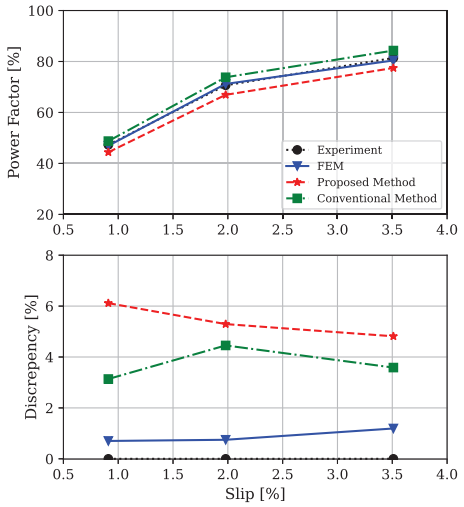

(a) Power factor (*p.f.*).

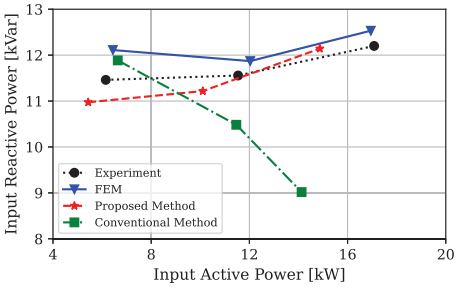

(b) Power curve.

Figure 4.14: Comparisons of various variables from experiments, the FEM model, and two IGFMs.

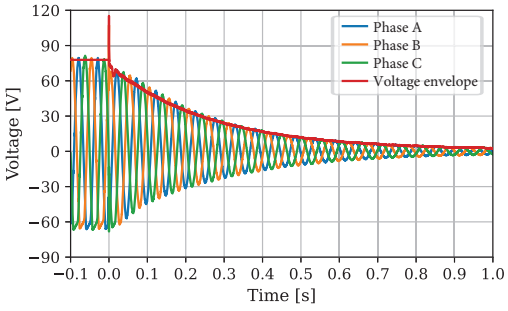

Figure 4.15: Stator phase voltages and envelope during flux-decay test.

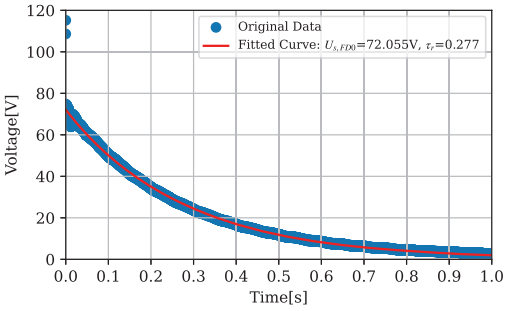

Figure 4.16: Original voltage envelope and fitted curve during flux-decay test.

Assuming $L_{r\lambda} = L_{s\lambda}$, then $L_r = L_s$ for this test.

Table 4.7 compares parameters from the flux-decay test and the conventional method [59].

Table 4.7: Parameters from flux-decay and conventional methods (resistances at 20°C).

Parameter	Flux-decay	Conventional	Unit
L_s	46.56	47.55	mH
R_r	0.168	0.190	Ω
$L_{s\lambda}$	2.38	2.55	mH
$L_{r\lambda}$	2.38	2.00	mH

Figure 4.17 compares R_r estimates from three approaches: (i) locked-rotor test at 10 Hz [59] (red dotted line), (ii) flux-decay test using 0.1 s intervals assuming constant L_M (blue dots), and (iii) full-period curve fitting (green dashed line). The trend aligns with [61], though that work suggested reducing R_r by 20% to account for iron losses, which would yield unrealistically low values compared to load test predictions.

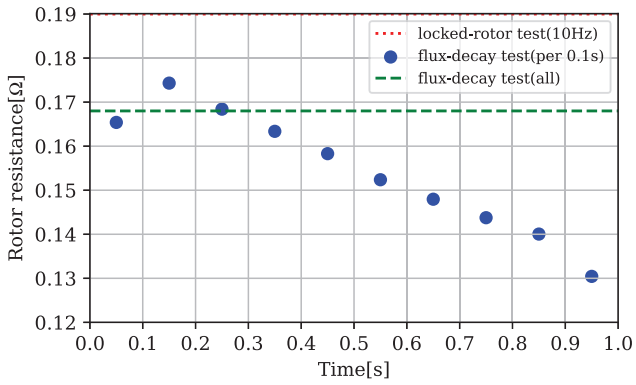

Figure 4.17: Comparison of rotor resistance estimates at 20°C from three methods.

4.2 Energy Loss Model

Figures. 4.18a and 4.18b show the cross-sections of IM1, IM2, and IM3 (IM2 and IM3 share the same geometry). A squirrel-cage rotor was selected as it

is the most common design for EV traction IMs [67], used in vehicles such as Tesla Model S/X (2015), Audi e-Tron (2019), and Mercedes-Benz EQC (2020) [12], [68].

The rotor consists of a laminated iron core with uniformly distributed slots, rotor bars, and a shaft integrated into the core. The bars are short-circuited by two end rings, forming a closed circuit. This configuration induces rotor currents from the stator flux, generating electromagnetic torque.

Industrial IMs up to several hundred kilowatts typically use die-cast Al rotors due to the cost-effectiveness and maturity of the pressure die-casting process [67], [69]. However, the automotive sector's demand for compact, efficient machines has driven interest in Cu rotors, manufactured via die-casting or mechanical methods such as laser welding or brazing [70]. Advances in casting technology have enabled mass production of die-cast Cu rotors [15], [71], [72].

The choice between Cu and Al involves trade-offs summarized in Table 4.8. Al has a conductivity of 61% IACS, which means its conductivity is 39% less than pure annealed Cu. Replacing the rotor bar material with Cu can therefore enhance IM efficiency [15], [73]. However, Cu rotors have higher inertia and cost due to material density and price [72]. Furthermore, Cu is classified as a strategic raw material under the EU Critical Raw Materials Act [42], while Al is abundant in the Earth's crust [74]. This is reflected in their crustal scarcity potential (CSP) [75], an indicator of long-term resource availability. For comparison, Nd(Dy)FeB magnets exhibit extremely high CSP values (Dy: 79 ton Si eq/kg, Nd: 14 ton Si eq/kg, B: 26 ton Si eq/kg), highlighting their criticality.

Table 4.8: Properties of Cu and Al [67], [75]–[78].

Property	**Cu**	**Al**
Density [kg/m^3]	8,890–8,940	2,700
Melting point [°C]	1083	660
Electrical conductivity [% IACS]	100	61
Avg. price (2023) [$USD/ton]	8,490	2,256
CSP [kg Si eq/kg]	10,000	3.4

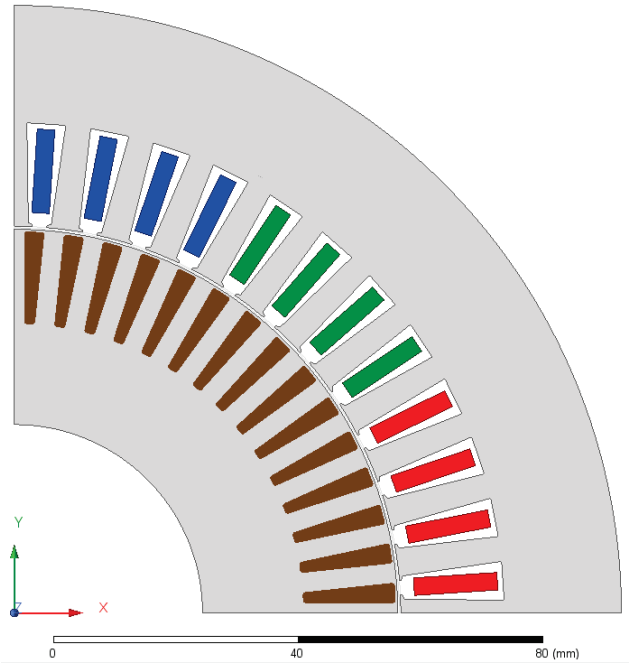

(a) IM1.

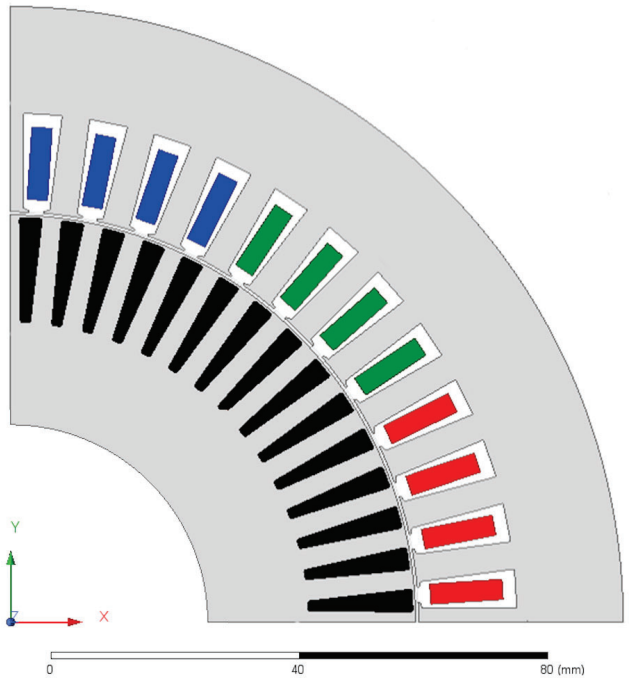

(b) IM2 and IM3.

Figure 4.18: Cross-section of IM for one pole pitch.

4.2.1 Thermal Management and Cooling Losses

Thermal management is critical for e-machine performance and reliability. Excessive heat can cause insulation degradation, failure, or magnet demagnetization (in PMSMs). Higher temperatures also increase conductor resistivity, raising losses, and reducing PMSM magnet strength, requiring higher stator currents for the same torque.

Due to high power density requirements, traction e-machines typically use closed-loop liquid cooling, categorized as [79], [80]:

1. Indirect cooling (water or oil):
   a) Cooling jacket
   b) Hollow shaft
2. Direct cooling (oil):
   a) Direct winding cooling
   b) Fluid bath
   c) Fluid spray

Indirect cooling uses a coolant in indirect contact with heat sources (stator and rotor conductors, laminated core). Direct cooling, where coolant contacts the heat source, enables higher power density. Oil is often used for direct cooling due to its high boiling point and insulation properties, though it increases pumping losses and rotor friction in fluid-bath systems. Water-based indirect cooling is common in EVs [79]. In this study, water-jacket and hollow-shaft cooling are adopted.

4.2.1.1 Stator thermal design considerations

The water jacket circulates a water-glycol mixture through channels in the stator frame, transferring heat to a heat exchanger. Water-glycol is preferred for its high heat capacity, thermal conductivity, and freeze resistance.

All IMs share the same stator outer diameter and use the same cooling jacket design as in [23], ensuring similar heat removal per mm (kW/mm). Thus, the same winding temperature is assumed for all designs.

Ohmic loss depends on the conductor current and resistance. To achieve equal stator Ohmic loss per mm:

- Cu-wound machines (Ref. PMSM, IM1, IM2): max current density = 20 A/mm^2.
- IM3 (Al winding): reduced current density to match Ohmic loss per mm.

IM1's smaller rotor (due to Cu's higher conductivity) allows more stator turns and a shorter active length than IM2 while maintaining peak torque. IM3 compensates for lower current density with a longer active length.

4.2.1.2 Extra loss due to rotor cooling

Rotor cooling is challenging due to the air gap limiting heat transfer. Hollow-shaft cooling, as used in Tesla Model S/X (2015) and Audi e-Tron (2019), addresses this by integrating a coolant path through the shaft [81]. The system includes a hollow shaft, seals, and an Al pipe guiding coolant jets inside the shaft.

However, integrated cooling systems increase energy consumption for pumping and introduce friction losses from seals [82], [83]. These factors are included in the life-cycle use-phase power loss estimation.

The additional friction loss due to shaft-bearing seals is estimated using the SKF model [84]:

$$P_{friction} = 1.05 \times 10^{-4} \times M \times n_r \tag{4.20}$$

where $P_{friction}$ is bearing friction loss (W), M is total frictional moment (Nmm)

$$M = M_{be} + M_{seal} \tag{4.21}$$

M_{be} accounts for rolling, sliding, and drag losses, while M_{seal} is due to seals (data from [85]). Thus, extra friction loss from seals is:

$$P_{friction,sealing} = 1.05 \times 10^{-4} \times M_{seal} \times n_r \tag{4.22}$$

Figure 4.19 shows the friction loss map for IM1.

The Darcy-Weisbach equation estimates pressure losses in cooling channels

$$\Delta p = f_{DW} \frac{l_{cooling}}{d_{cooling}} \times \frac{1}{2} \rho Q^2 \tag{4.23}$$

where f_{DW} is the Darcy friction factor, $l_{cooling}$ and $d_{cooling}$ are the length and diameter of the cooling path (m), ρ is fluid density (kg/m^3), and Q is coolant flow rate (m/s).

Based on [82], for $l_{cooling}/d_{cooling} = 10$ (stationary) and 30 (rotating) with $Q = 8$ L/min, the pressure drops are

$$\Delta p_s = (0.028 n_r + 434.5) \frac{l_a/d_s}{10} \left(\frac{Q}{8} \right)^2 \tag{4.24}$$

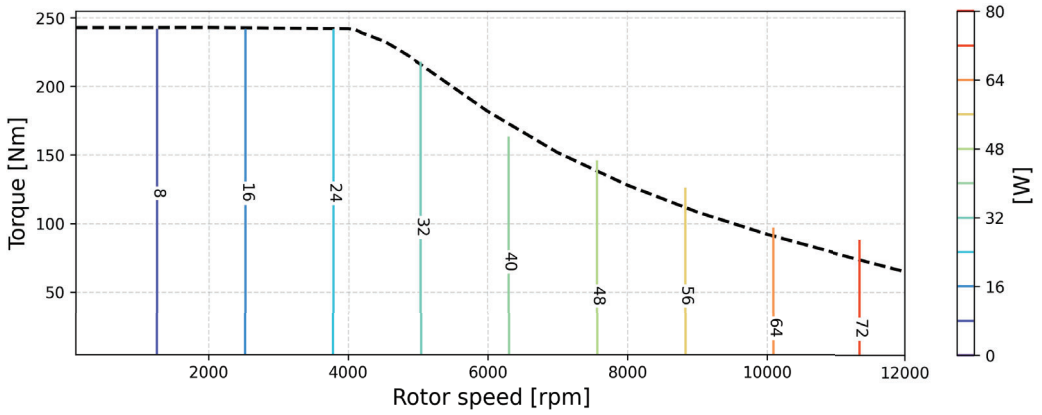

Figure 4.19: Extra friction loss due to hollow-shaft cooling seals (IM1).

$$\Delta p_r = (0.028 n_r + 660.6) \frac{l_a / d_r}{30} \left(\frac{Q}{8} \right)^2 \tag{4.25}$$

where Δp_s and Δp_r are pressure drops in stationary and rotating paths (Pa), n_r is rotor speed (rpm), l_a is active length (mm), and d_s, d_r are diameters of stationary and rotating paths (mm).

The total pressure drop due to the cooling path can be denoted as

$$\Delta p = \Delta p_s + \Delta p_r \tag{4.26}$$

In Figures. 4.20a–4.20c, the pressure drop maps for IM1, IM2, and IM3 due to the hollow-shaft cooling path are shown. The pressure drop increases with rotor speed and, for a given speed, with active length, as a longer cooling path adds resistance.

The additional power required by the cooling pump to circulate coolant through the hollow shaft is

$$P_{pump} = \frac{Q \Delta p}{\eta_{pump}} \tag{4.27}$$

where P_{pump} is the extra pump power (W), Δp is the pressure drop from Figure 4.20a–4.20c, Q is the coolant flow rate, and η_{pump} is pump efficiency (assumed 80%). Figures 4.21a–4.21c present the extra pump power maps for IM1, IM2, and IM3. Figures 4.22a–4.22c illustrate the efficiency maps with WLTC operating points, while Figures 4.23a–4.23c show the corresponding loss maps for IM1, IM2, and IM3, respectively.

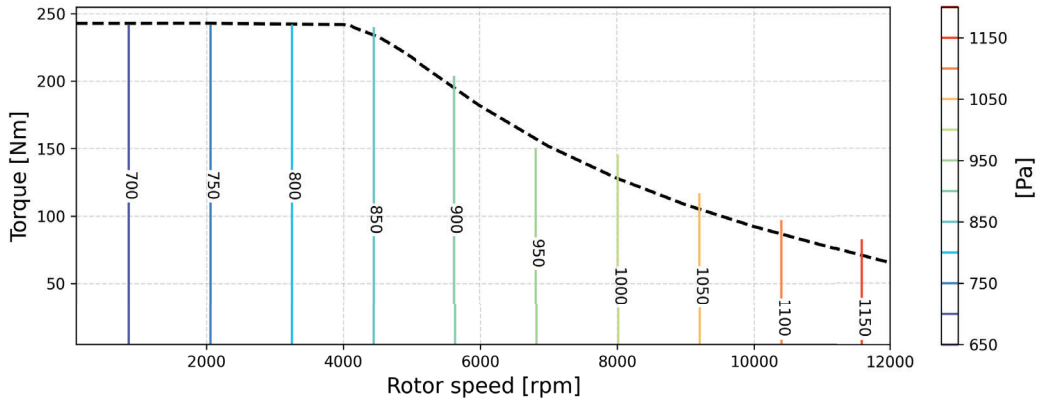

(a) IM1.

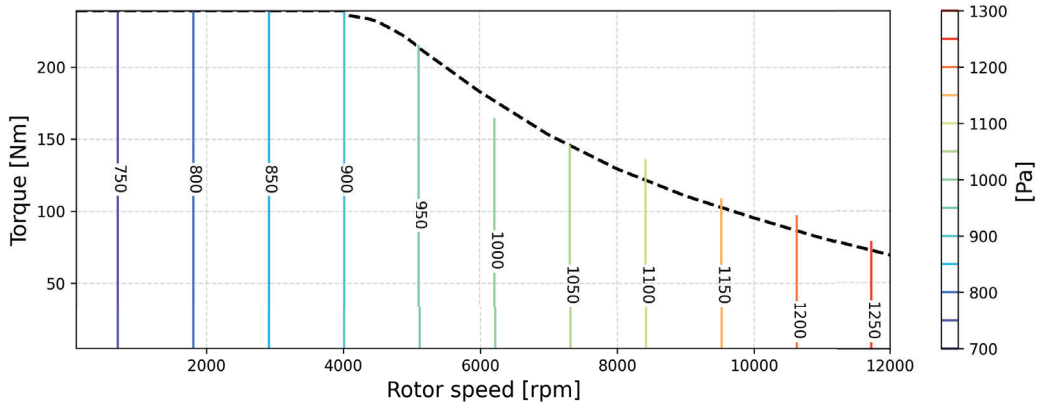

(b) IM2.

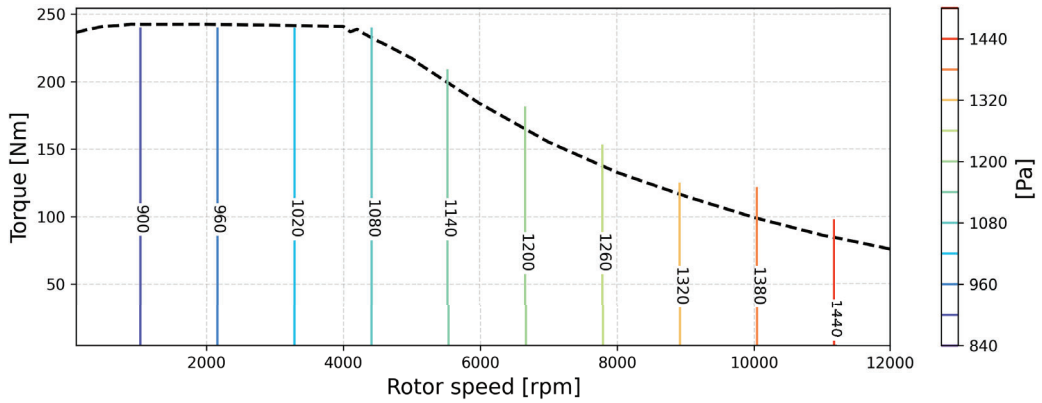

(c) IM3.

Figure 4.20: Pressure drop maps of rotor hollow-shaft cooling systems.

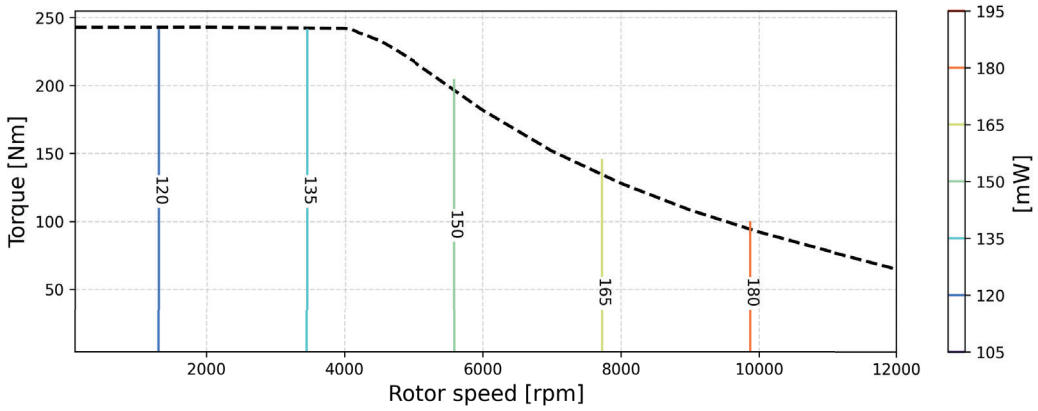

(a) IM1.

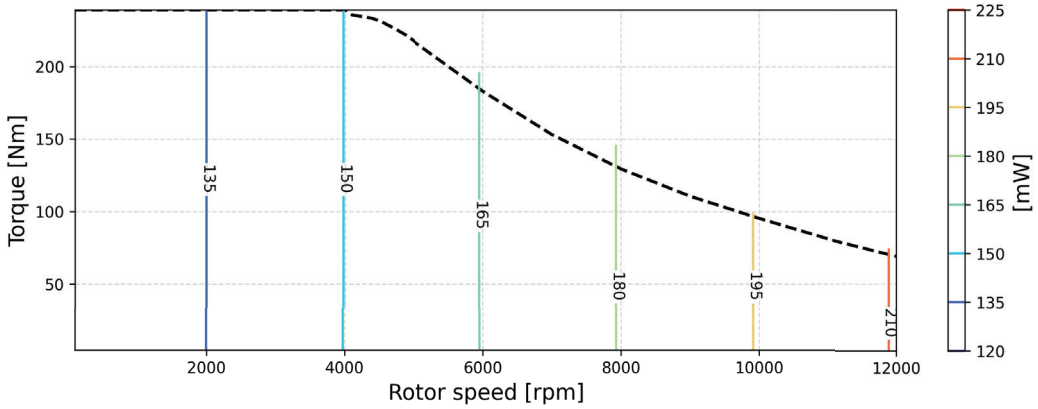

(b) IM2.

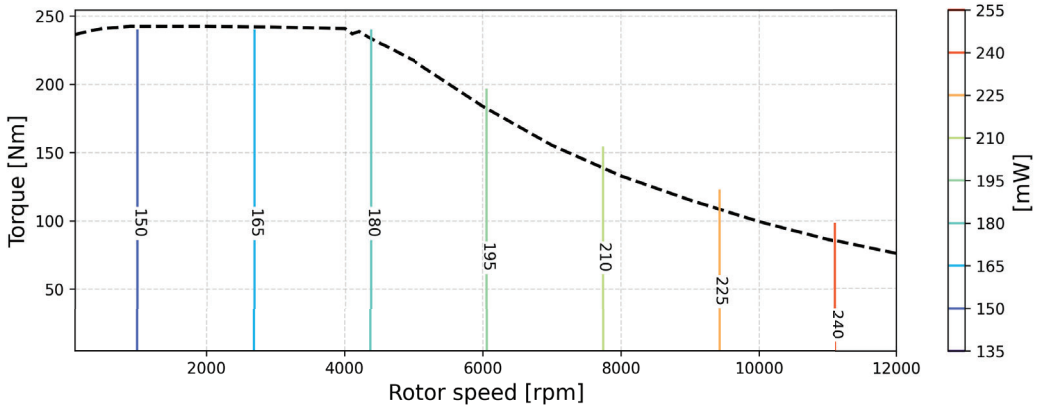

(c) IM3.

Figure 4.21: Extra pump power for rotor hollow-shaft cooling.

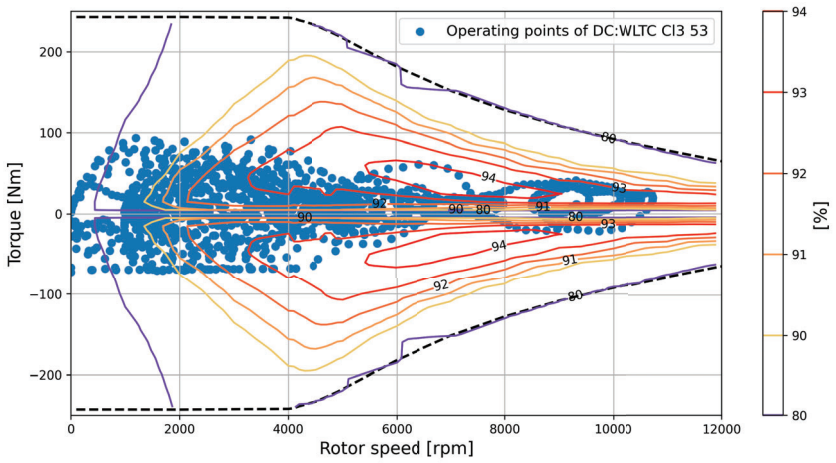

(a) IM1.

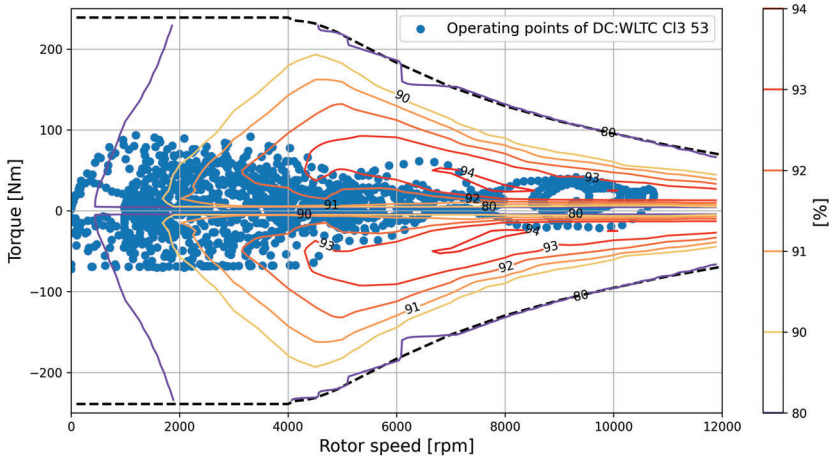

(b) IM2.

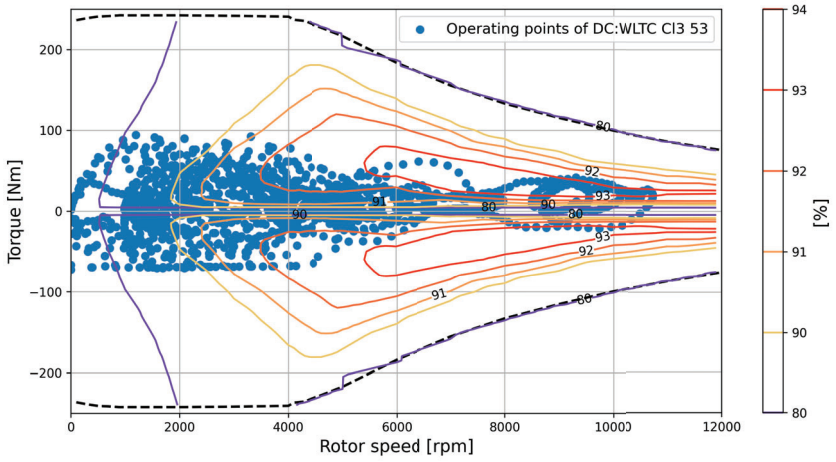

(c) IM3.

Figure 4.22: Efficiency maps with the operating points from WLTC of IMs.

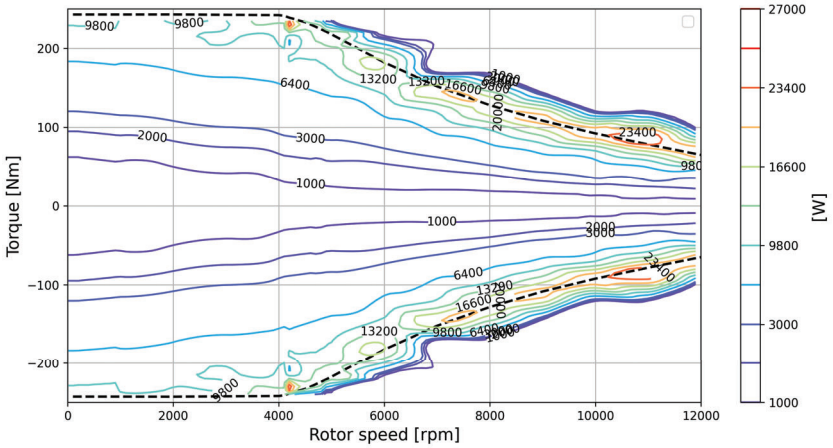

(a) IM1.

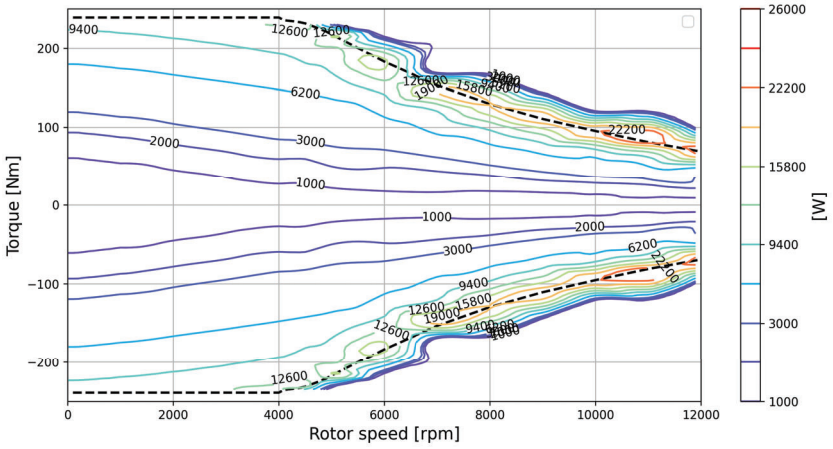

(b) IM2.

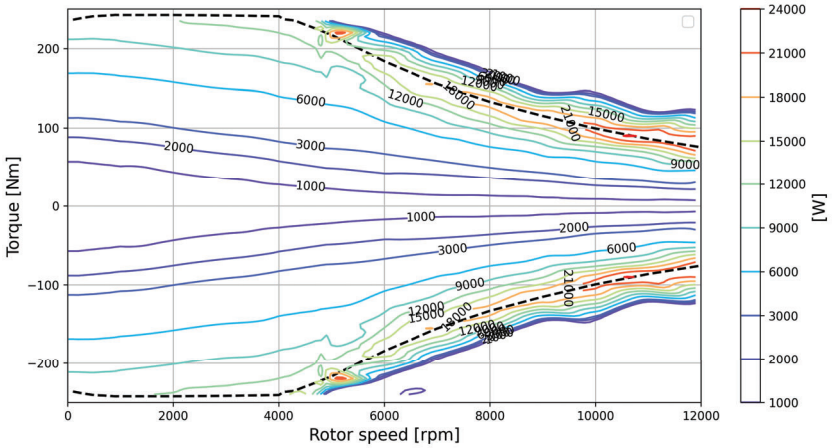

(c) IM3.

Figure 4.23: Loss maps of IMs.

4.3 LCI model

In Figure 4.24, the exploded-view drawings of a PMSM and an IM derived from Nordelöf et al. [23] are shown, where all updates from PMSM to IM are highlighted in blue and bold fonts. The critical difference between PMSMs and IMs is the rotor package and the rotor cooling system. Compared to a PMSM, in IMs, the components of permanent magnets, the passive rotor core to save mass of the rotor and venting air, and the endplates of the rotor to fix magnets and rotor steel sheets can be removed, and instead, rotor conductors are needed. Furthermore, a rotor hollow-shaft cooling system is often implemented in traction IMs due to the higher losses in the rotor.

A system overview of the life cycle till the production stage of the three IM options is provided in Figure 4.25. As the figure indicates, most of the data is based on the work from the IPMSM LCI model reported by Nordelöf et al. in a series of publications [51]–[53]. The updated models are highlighted in orange and explained in the section 4.3.1 and 4.3.2.

4.3.1 Die casting Al housing and rotor cooling parts

This study uses the same model to calculate the weight of the Al housing, as the one presented in Nordelöf et al. [51]. In addition to housing itself, the water inner lance and coolant collector are assumed to be manufactured with Al housing. The masses of die-casting parts are listed in Table 4.9, where the masses for cooling parts are estimated by the geometries in the report by Doerr et al. [81].

Table 4.9: Estimations made for the masses of Al housing and rotor cooling parts of e-machines from the die casting foundry.

Parts	**Mass [kg]**			
	Ref. PMSM	IM1	IM2	IM3
Housing body	9.4	12.5	14.5	18.6
One endbell	2.5			
Coolant collector	0	0.75		
Water inner lance	0	0.05	0.06	0.07

The process of Al die-casting is similar to that described in Nordelöf et al.

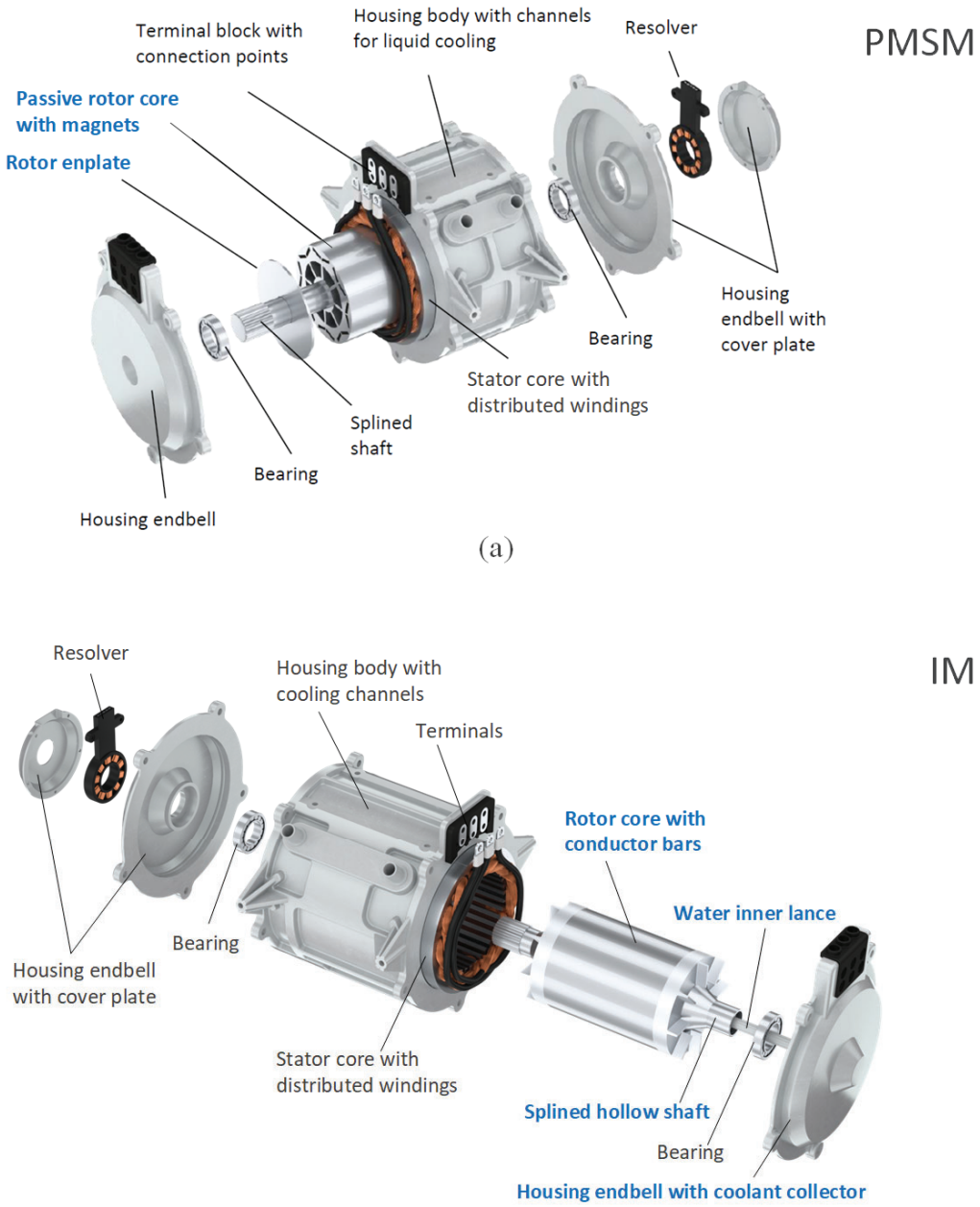

Figure 4.24: General exploded-view drawings of (a) a PMSM and (b) an IM [23], [81].

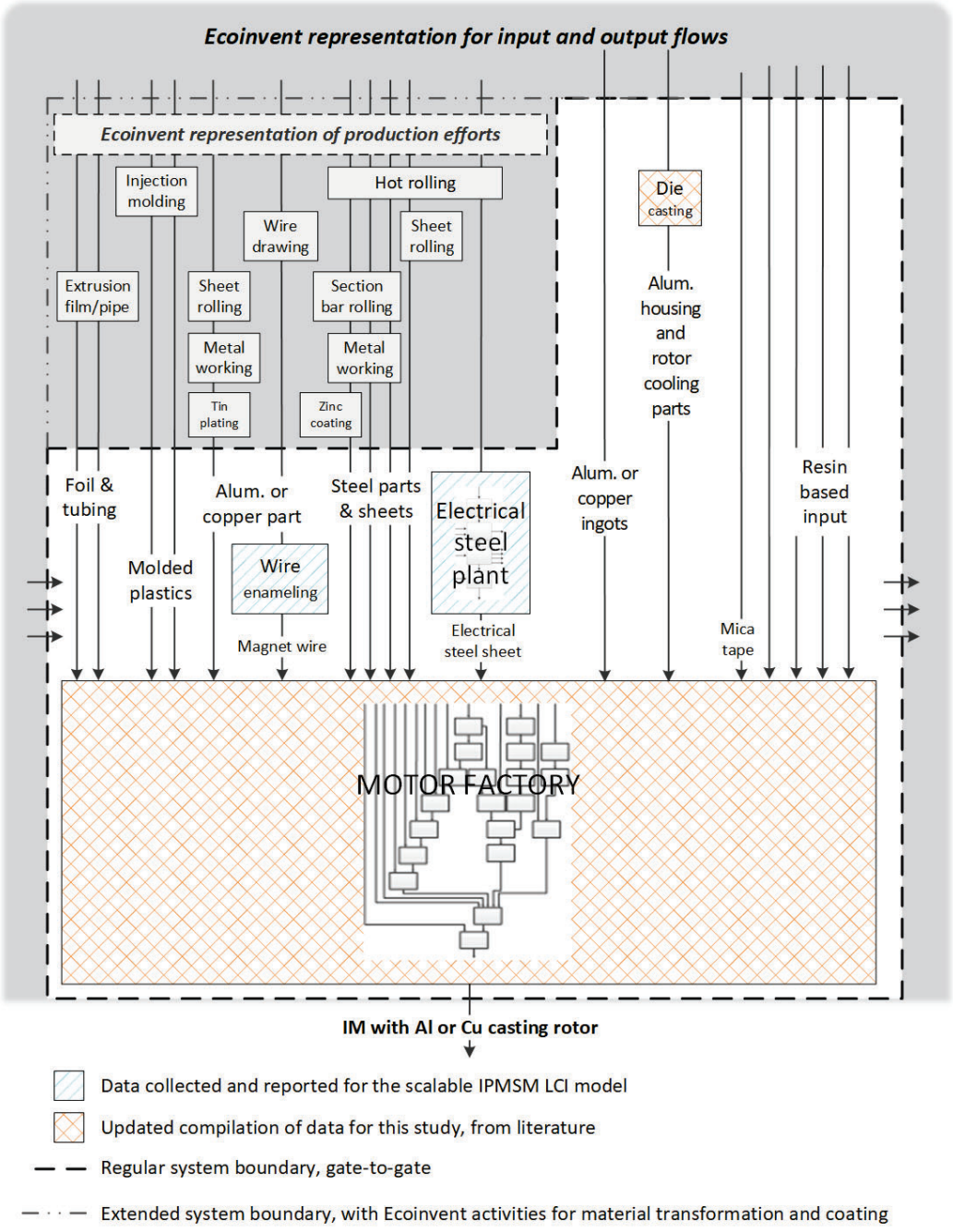

Figure 4.25: Overview of the system model for the production steps of three IMs. Reworked from Nordelöf et al. [51]–[53]

[51]. However, in Nordelöf et al. [51], the energy carriers are natural gas for melting Al and electricity for powering the die-casting machine. In this study, the energy carrier is updated to be fully electrified, in line with current developments in Europe. Additionally, the data found in the accessible literature utilized electric furnaces [71], [86], [87]. The data used in this study for the Al die casting process are listed in Table 4.10 and S 4.11, where the emission of volatile organic compounds (VOCs) came from the use of lubricating oil [88].

Table 4.10: Process input for the production of 1 kg die-cast Al housing and rotor cooling parts.

Process input	**Amount per kg**	**Source**	**Linked flow**	**Location**
Al	1.06 kg	[89]	Al, primary, ingot	In line with electricity scenario electricity scenario
Electricity for melting and holding Al	2.1 kWh	[87]	Electricity, medium voltage	
Electricity for the rest	2.6 kWh	[89]	Electricity, medium voltage	
Lubricating oil	20 g	[89]	Lubricating oil	

Table 4.11: Emissions from the production of 1 kg die-cast Al housing and rotor cooling parts.

Emissions	**Amount per kg**	**Source**	**Linked flow**	**Location**
Al	0.4 g	[89]	Al, unspecified	In line with electricity scenario
VOC	1 g	[88]	NMVOC	
Al scrap	0.06 kg	[89]	Al scrap for recycling	

4.3.2 IM factory

The manufacturing processes of the three IM technical options are depicted in Figure 4.26, updated from the PMSM LCI model in Nordelöf et al. [51]. The red-dotted lines in Figure 4.26 circle the updated processes. The needed data were found in available scientific literature.

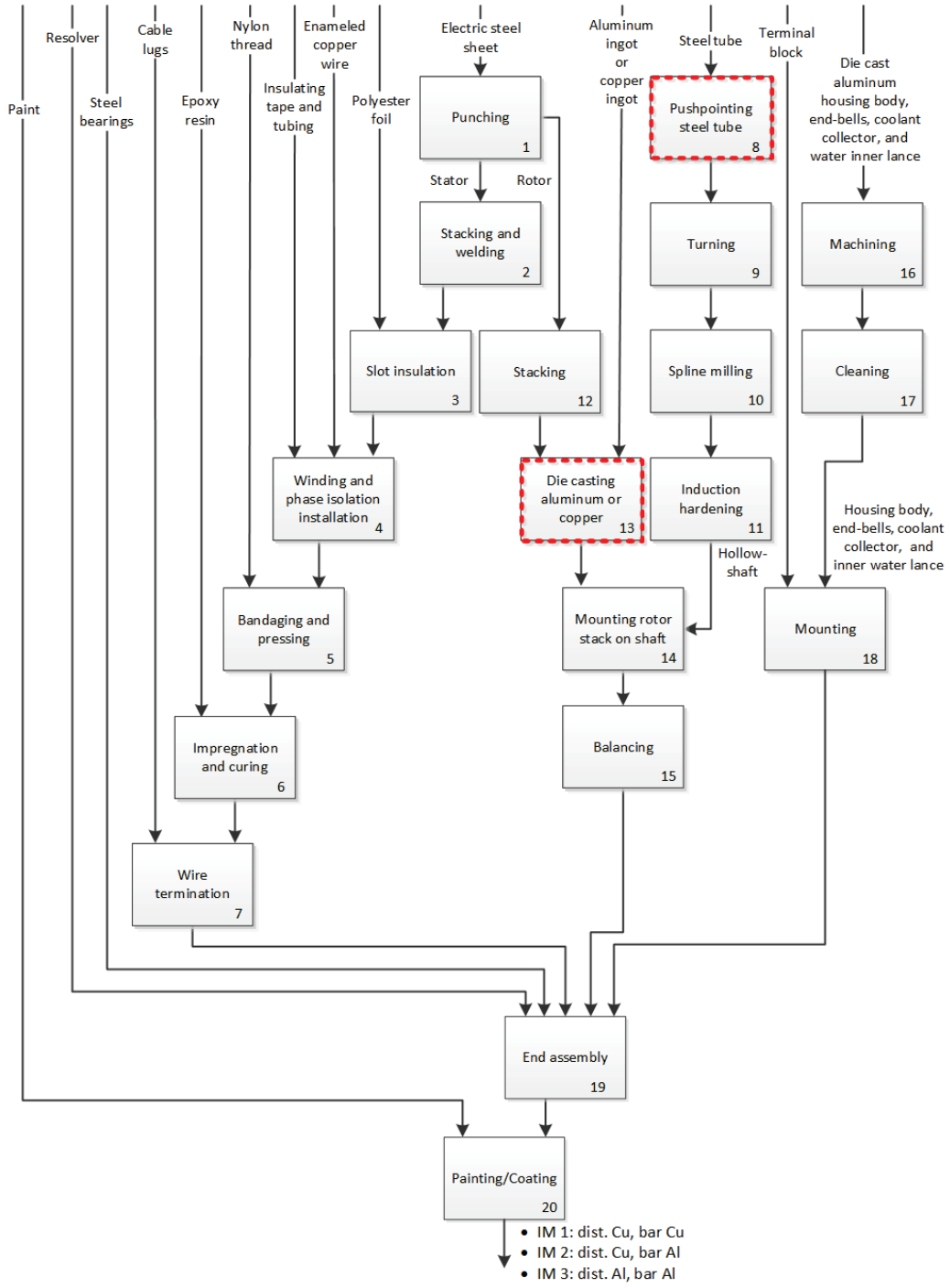

Figure 4.26: IM factory process flow chart for the three IMs (IM1, 2, 3), divided into 20 processes. Reworked from Nordelöf et al. [51].

4.3.2.1 Die casting rotor conductor bars

The process of die-casting Al rotor bars is almost the same as that of die-casting Al housing listed in Tables S 4.12 and S 4.13, but without the electricity required to maintain other necessary facilities, such as office heaters. Such electricity has been included in the technical building services within the e-machine factory, as described in Section 5.4.9 of the previous study [23]. The data for the required energy and Cu ingot as input and Cu scrap as output for die-casting Cu rotor bars are derived primarily from a comparative LCA study by Cassoret et al. [15] and an LCA report by Schiesser et al. [87]. The data on the needed lubricating oil is modified from the model of die-casting Al rotor bars according to the ratio between the density of Al and Cu.

Table 4.12: Process input for the production of 1 kg die-casted Al bars in the rotor core.

Process input	Amount per kg	Source	Linked flow	Location
Al	1.06 kg	[89]	Al, primary, ingot	In line with electricity scenario
Electricity for melting and holding Al	2.1 kWh	[87]	Electricity, medium voltage	
Lubricating oil	20 g	[89]	Lubricating oil	

Table 4.13: Emissions from the production of 1 kg die-casted Al bars in the rotor core.

Emissions	Amount per kg	Source	Linked flow	Location
Al	0.4 g	[89]	Al, unspecified	In line with electricity scenario
VOC	1 g	[88]	NMVOC	
Al scrap	0.06 kg	[89]	Al scrap for recycling	

Table 4.14: Process input for the production of 1 kg die-casted Cu bars in the rotor core.

Process input	Amount per kg	Source	Linked flow	Location
Cu	1.52 kg	[87]	Cu, primary, ingot	In line with electricity scenario
Electricity for melting and holding Cu	1.325 kWh	[87]	Electricity, medium voltage	
Lubricating oil	6 g	[87], [89]	Lubricating oil	

Table 4.15: Emissions from the production of 1 kg die-casted Cu bars in the rotor core.

Emissions	Amount per kg	Source	Linked flow	Location
VOC	0.3 g	[87], [88]	NMVOC	In line with electricity scenario
Cu scrap	0.52 kg	[87]	Cu scrap for recycling	

4.3.2.2 Hollow shaft

In Nordelöf et al. [51], a simple model to calculate the mass of the shaft is applied by

$$m_{shaft} = \pi \left[\frac{(20 + 0.07(T_{max} - 48))}{2} \right]^2 \times (120 + l_a) \times 10^{-9} \times 7870 \quad (4.28)$$

where m_{shaft} is the mass of the shaft in kg, T_{max} is the maximum torque in Nm, and l_a is the axial length of the iron core in mm. The model was derived from the statistics of T_{max} and l_a of eight e-machines and their shaft weights.

To examine if this model can be used to calculate the masses of hollow shafts, another approach to estimate the shaft mass of two IMs in Audi e-Tron (2019) by geometries in Doerr et al. [81] was also applied and compared with the ones derived from (4.28) in Table 4.16. The results indicate a maximum difference of 17% between the two estimation approaches, leading to the decision to use the same shaft mass model in this study.

The process of pushpointing (process 8 in Figure 4.26) is chosen to make a

Table 4.16: Estimated masses of hollow shafts for IMs of Audi e-Tron (2019) [81].

Max torque	**Shaft length**	**Shaft weight** m_{shaft}	
Stated in Doerr et al. [81]	Estimated from the geometries in Doerr et al. [81]	Estimated from the geometries in Doerr et al. [81]	Calculated by (4.28)
247 Nm	120 mm	2 kg	1.7 kg
314 Nm	210 mm	2.9 kg	3 kg

Table 4.17: Process input for the production of 1 hollow shaft.

Process input	**Amount per kg**	**Source**	**Linked flow**	**Location**
Electricity	43.42 Wh	[90]	Electricity, medium voltage	In line with electricity scenario

tapper shape on both ends of a steel tube [91]. The data for the energy consumption of the pushpointing process is found in Dohi et al.[90] and presented in Table 4.17.

Figure 4.27a - 4.27c are the weight share for IM1, IM2, and IM3 respectively.

4.4 Technical performance

Table 4.18 summarizes key technical performance and drive-cycle energy losses of the investigated induction machines (IM1–IM3) compared to the Ref. PMSM. All machines deliver similar maximum torque (239–242 Nm) and rated power (100 kW), ensuring a fair basis for comparison. However, significant differences appear in power density and weight distribution. The PMSM achieves the highest volumetric and gravimetric power densities (25.1 kW/L and 2.2 kW/kg), outperforming all IMs. Among the IMs, IM1 (full Cu conductors) is the lightest and most compact, while IM3 (full Al conductors) is the heaviest, reflecting the need for a longer active length to compensate for Al's lower conductivity.

While these differences in power density and weight highlight important design trade-offs, another critical aspect influencing overall efficiency and lifecycle performance is the accurate estimation of iron losses, which remains a

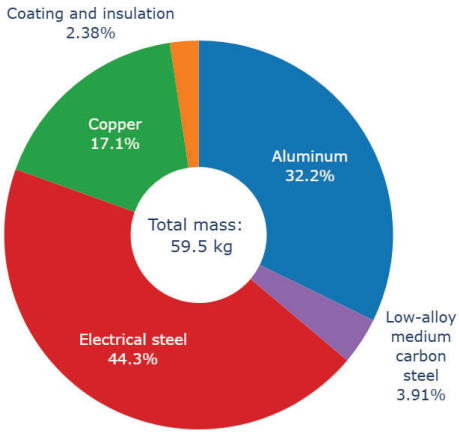

(a) IM1.

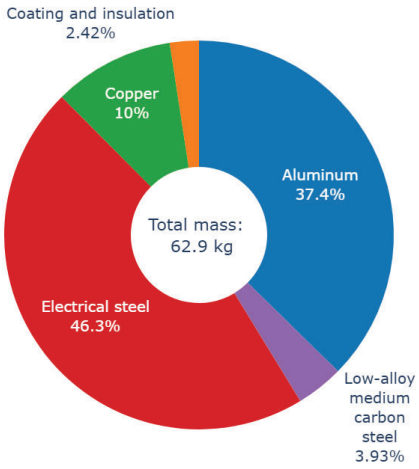

(b) IM2.

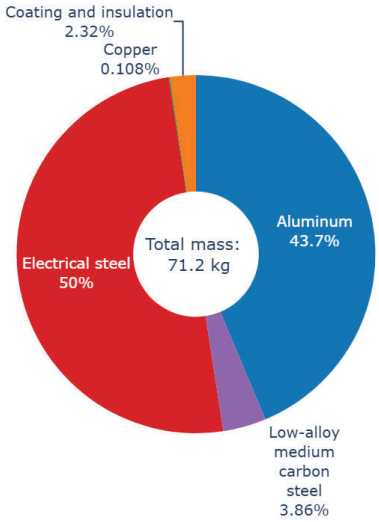

(c) IM3.

Figure 4.27: Weight share.

significant challenge during the design phase. This complexity arises because iron loss depends on several interdependent factors:

- Applied magnetic field strength,
- Cross-sectional geometry of the electric machine,
- Electrical steel sheet material properties,
- Pulse-width modulation (PWM) feeding,
- Manufacturing and processing parameters.

Although FEM simulations are widely used for iron loss prediction, they struggle to capture the effects of PWM excitation and manufacturing-induced variations. Incorporating PWM into FEM significantly increases computational effort, and uncertainties from processes such as stamping, annealing, and coating further complicate accurate modeling. To compensate for these unmodeled effects, a correction factor known as the iron loss factor (f_{fe}), typically ranging from 1.7 to 2, is commonly applied [65], [92]. However, applying the same factor across machine types could, in the worst case, distort efficiency comparisons. For example, when f_{fe} is applied uniformly, the Ref. PMSM appears less efficient than IM1 because iron losses cause more than 60% of total energy consumption due to e-mahcine in the PMSM, compared to about 24% in IM1. This disproportionate impact highlights the relative advantage of induction machines under realistic operating conditions.

4.5 Environmental Performance by LCIA

This section presents the results of the life cycle impact assessment (LCIA). Subsection 4.5.1 examines endpoint impact categories related to ecosystem quality and human health using the ReCiPe 2016 v1.03 method. The primary purpose of including endpoint analysis is to identify the categories that contribute most significantly to the environmental burden of electric traction machine manufacturing, thereby guiding the selection of key impact categories for detailed discussion in subsequent sections.

Following this, results for selected midpoint indicators are presented. These include climate change, reported as global warming potential over 100 years (GWP100) based on IPCC 2020 [93], and crustal resource use, reported as

Table 4.18: Key technical performances of investigated induction machines.

Machines	**Ref. PMSM**	**IM1**	**IM2**	**IM3**
General data				
Maximum torque [Nm]	239	242	239	242
Maximum power [kW]	100	101	100	101
Base speed [rpm]	4000			
Power density [kW/kg]	2.2	1.7	1.6	1.4
Power density [kW/L]	25.1	20.2	18.1	14.8
Weight				
Stator core [kg]	11.8	17.6	18.3	22.4
Rotor core [kg]	7.2	8.8	10.8	13.2
Stator winding [kg]	4.8	5.8	6.1	2.0
Magnets/Rotor conductors [kg]	1.3	4.1	3.6	2.0
Al housing and cooling parts [kg]	14.6	19.2	21.8	27.0
Total weight [kg]	44.9	59.5	62.9	71.2
Drive cycle loss due to e-machine				
Due to iron loss per km [Wh/km] ($f_{fe} = 1$)	9.4 63.5%[a]	4.1 24.2%[a]	4.3 23.9%[a]	4.8 24.8%[a]
Due to ohmic loss per km [Wh/km] ($f_{fe} = 1$)	3.6 24.6%[a]	9.8 58.7%[a]	10.8 59.8%[a]	11.3 58.3%[a]
Due to other loss per km [Wh/km] ($f_{fe} = 1$)	0.2 1.4%[a]	0.8 4.8%[a]	0.8 4.4%[a]	0.8 4.1%[a]
Due to road load per km [Wh/km] ($f_{fe} = 1$)	1.5 10.5%[a]	2.1 12.3%[a]	2.2 12%[a]	2.5 12.8%[a]
Energy loss per km [Wh/km] ($f_{fe} = 1$)	14.8	16.8	18.1	19.3
Life cycle energy [kWh] ($f_{fe} = 1$)	2951	3354	3615	3870
Energy loss per km [Wh/km] ($f_{fe} = 1.7$)	21.2	19.6	21	22
Life cycle loss [kWh] ($f_{fe} = 1.7$)	4240	3914	4209	4530

[a]percentage of total loss for respective e-machine

crustal scarcity potential (CSP) according to Arvidsson et al. [75]. Additional midpoint indicators identified through the endpoint assessment are also included, as defined in the ReCiPe 2016 v1.03 package [94], excluding its internal versions of climate change and mineral resource indicators.

4.5.1 Endpoint Categories

The endpoint results are normalized per e-machine and derived from midpoint impact categories, which quantify environmental and health-related damages associated with the technical alternatives under study. These contributions are illustrated in Figs. 4.28a and 4.28b.

Figure 4.28a shows that climate change is the dominant contributor to potential ecosystem damage, followed by acidification and ecotoxicity, which exhibit comparable contributions across both electricity scenarios. Other indicators, such as eutrophication, water use, land use, and photochemical oxidant formation, have relatively minor impacts, with some variation depending on the scenario. For example, eutrophication is negligible under the low GHG-intensity electricity scenario, whereas water use becomes more relevant in that context.

Regarding human health impacts (Figure 4.28b), the primary contributors are climate change, particulate matter formation, and non-carcinogenic human toxicity. Other categories, including ozone depletion, photochemical oxidant formation, and ionizing radiation, contribute negligibly.

Based on these findings, the subsequent analysis focuses on the impact categories that consistently exhibit the highest contributions across scenarios: climate change, acidification, particulate matter formation, and non-carcinogenic human toxicity.

4.5.2 Midpoint Categories

4.5.2.1 Climate Change

Figure 4.29a presents the GWP100 results for the base case, assuming globally averaged virgin Al production and one-piece electrical steel sheet punching (with approximately 50% material loss). Consistent with previous findings [23], under a high GHG-intensity electricity scenario, the use phase dominates total emissions. Consequently, the most energy-efficient option, IM1, exhibits the lowest emissions when accounting for the loss penalty (i.e., including a

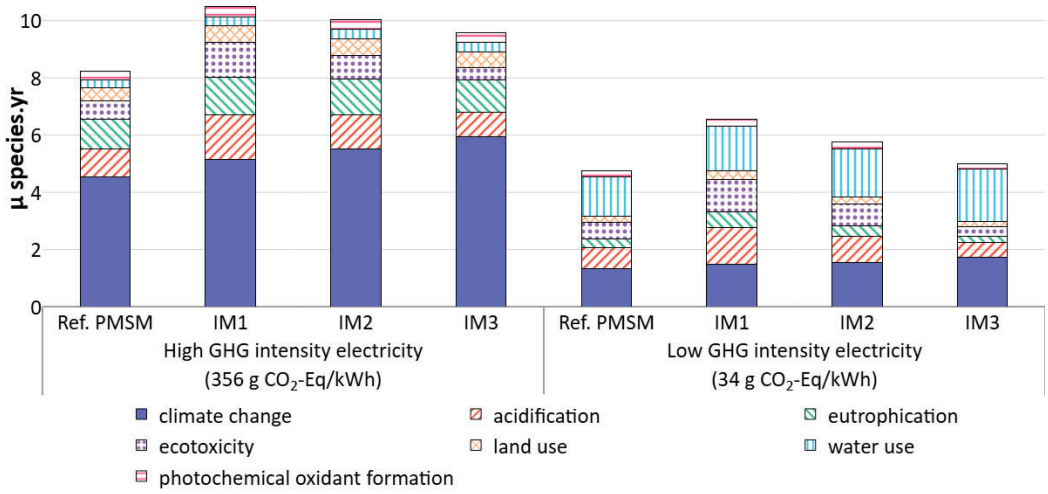

(a) Ecosystem quality.

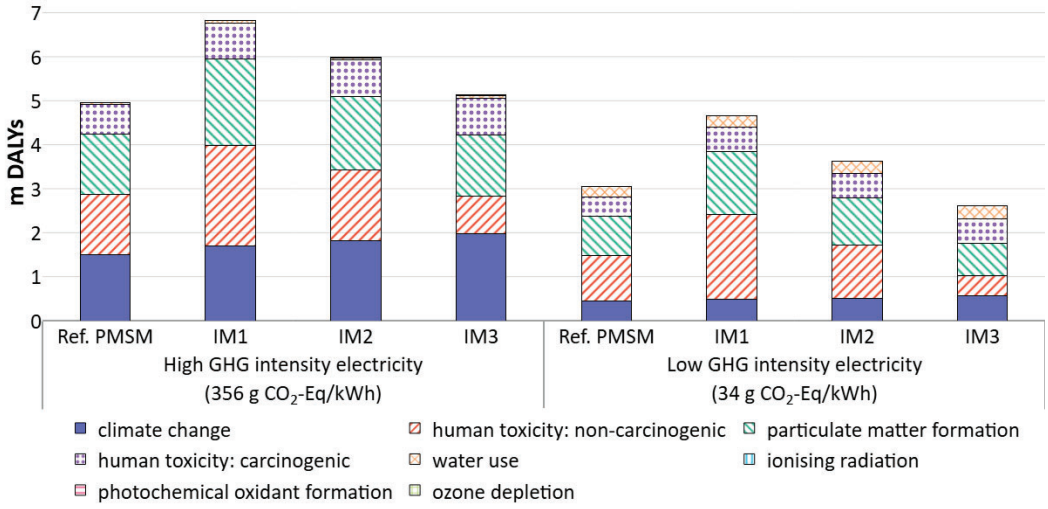

(b) Human health.

Figure 4.28: ReCiPe 1.03 endpoint results for ecosystem quality and human health.

iron loss factor $f_{fe} = 1.7$ to reflect manufacturing effects on electrical steel sheets). Notably, Ref. PMSM and IM2 show similar use-phase emissions; however, Ref. PMSM achieves lower total emissions due to its higher power density. Under a low GHG-intensity electricity scenario, production-related emissions become more significant, making Ref. PMSM the most favorable option. Among production processes, Al housing and electrical steel sheet manufacturing contribute the most, owing to their substantial mass shares.

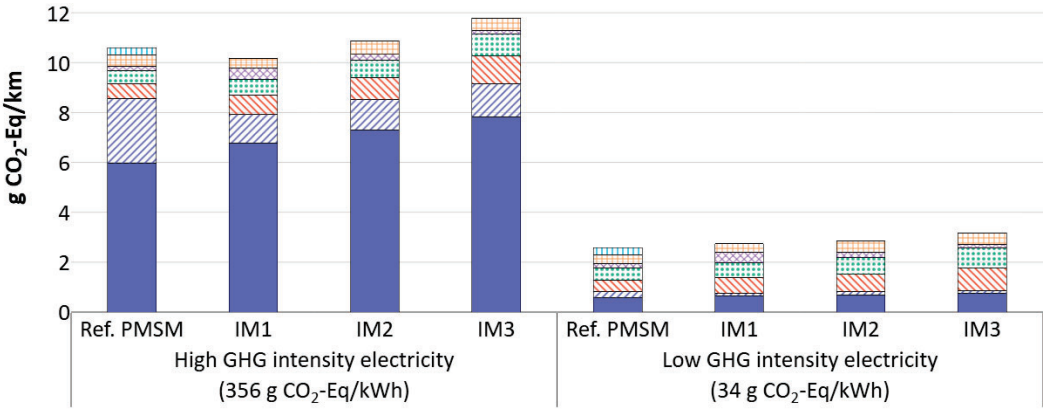

(a) Base case.

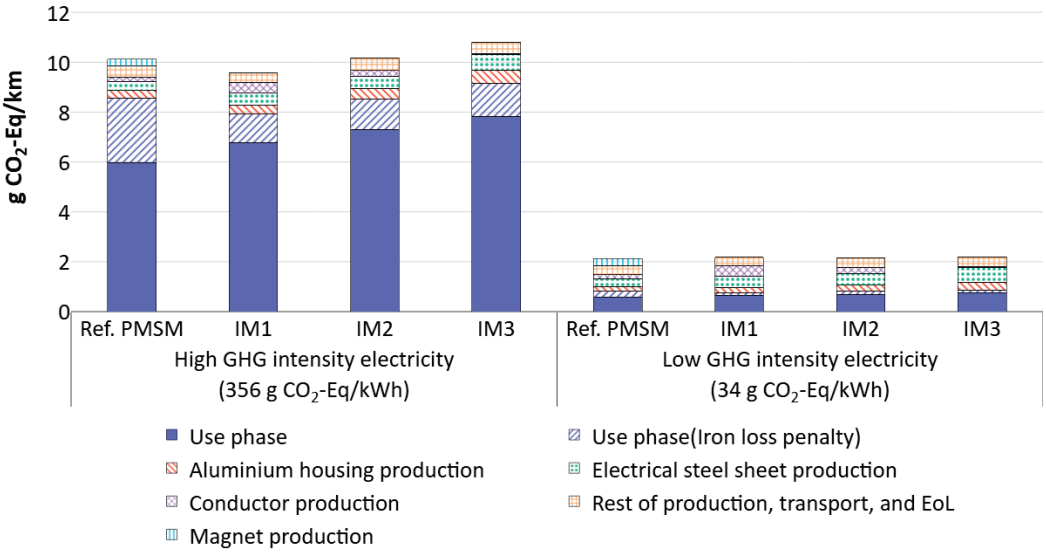

(b) Green manufacturing.

Figure 4.29: IPCC 2021 results for global warming potential (GWP100).

To mitigate emissions, a green manufacturing scenario was assessed, involving segmented laminations and virgin Al sourced from EU countries and produced using 100% hydropower. As shown in Figure 4.29b, all machine options benefit from green manufacturing, with IM3 showing the most significant improvement under low GHG-intensity electricity conditions.

4.5.2.2 Crustal Scarcity Potential (CSP)

Figures 4.30a and 4.30b present CSP results for both base case and green manufacturing scenarios. CSP is a resource-based LCA metric that quantifies the environmental burden associated with the depletion of naturally occurring elements in the Earth's crust. It reflects material scarcity by considering natural abundance and extraction rates, serving as an indicator of long-term resource sustainability. Materials such as Cu, which are less abundant and heavily utilized, exhibit higher CSP values. The results show that Cu conductor production dominates CSP across all scenarios, making IM1 the least favorable option in terms of resource scarcity.

4.5.2.3 Acidification: Terrestrial

Figures 4.31a and 4.31b illustrate terrestrial acidification potential results. Cu production remains the primary contributor due to sulfur dioxide emissions from sulfidic tailings during mining. IM3, which uses only Al conductors, has the lowest impact in this category. Green manufacturing significantly reduces impacts for all options, particularly in Al housing production, due to stricter EU regulations on ore processing.

4.5.2.4 Non-Carcinogenic Human Toxicity Potential

Figures 4.32a and 4.32b show non-carcinogenic human toxicity potential results, which follow a similar trend to acidification. Primary Cu production is the dominant contributor due to heavy metal emissions (e.g., arsenic, zinc, Cu) from sulfidic tailings, significantly affecting ecotoxicity and human health.

4.5.2.5 Particulate Matter Formation

Figures 4.33a and 4.33b present particulate matter formation results. Cu production again accounts for a significant share of emissions, while electri-

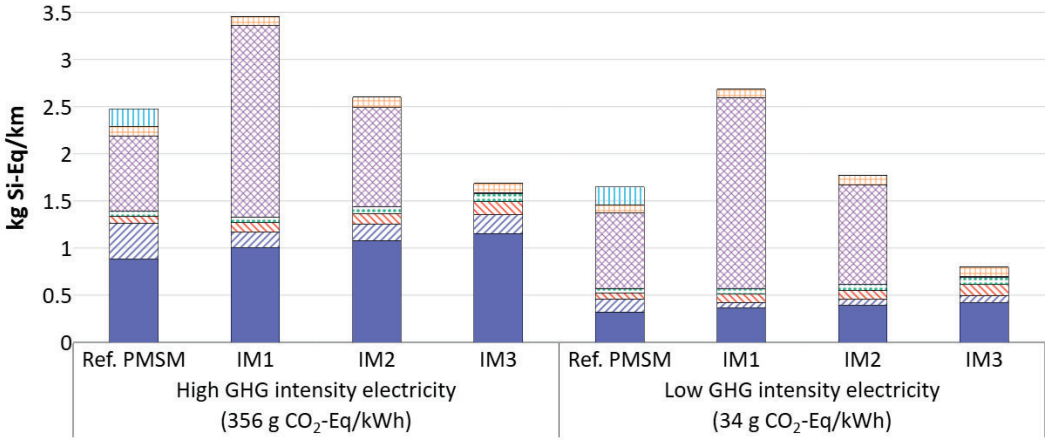

(a) Base case.

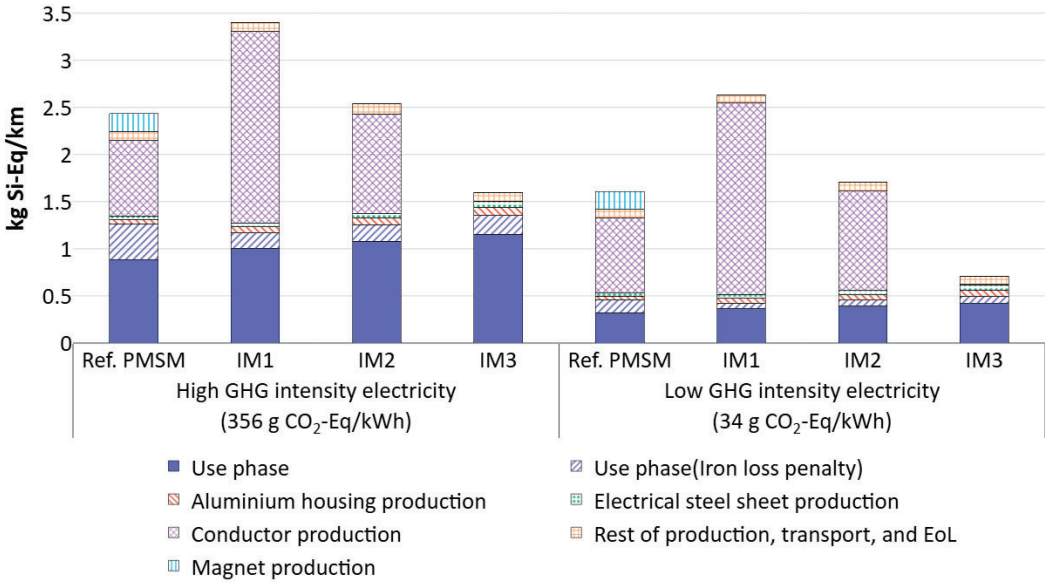

(b) Green manufacturing.

Figure 4.30: Crustal Scarcity Indicator 2020 results for crustal scarcity potential (CSP).

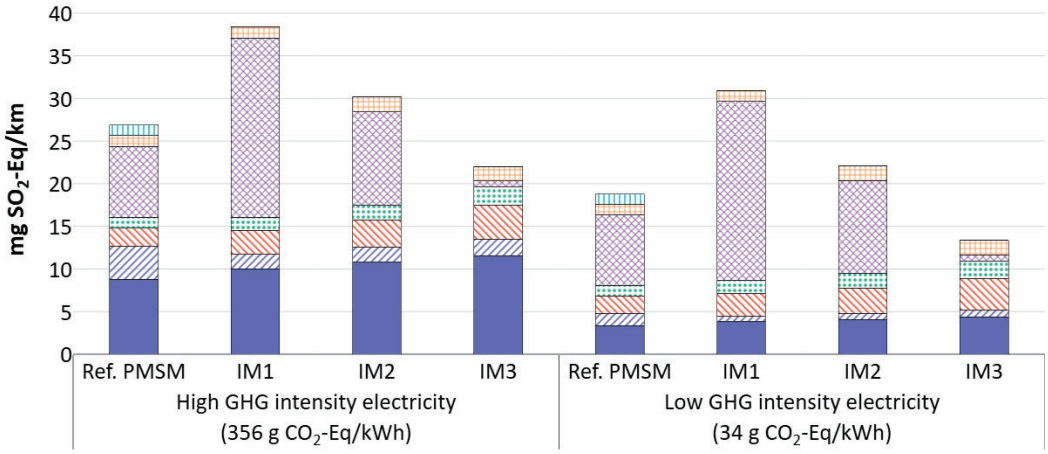

(a) Base case.

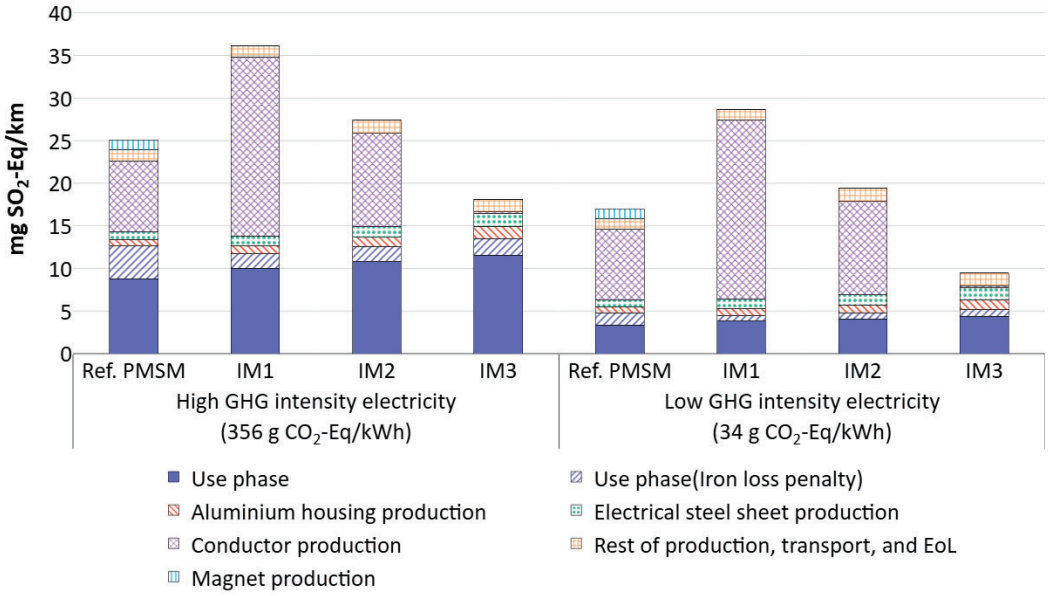

(b) Green manufacturing.

Figure 4.31: ReCiPe 1.03 midpoint results for terrestrial acidification potential.

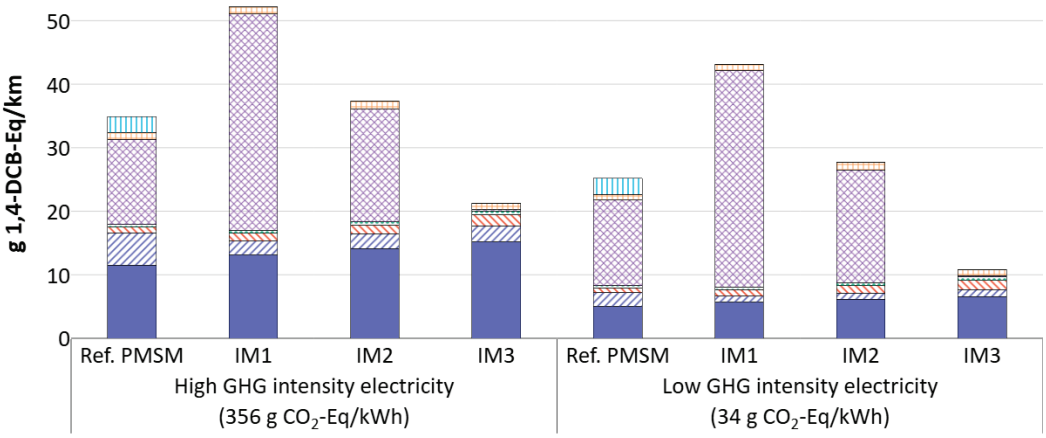

(a) Base case.

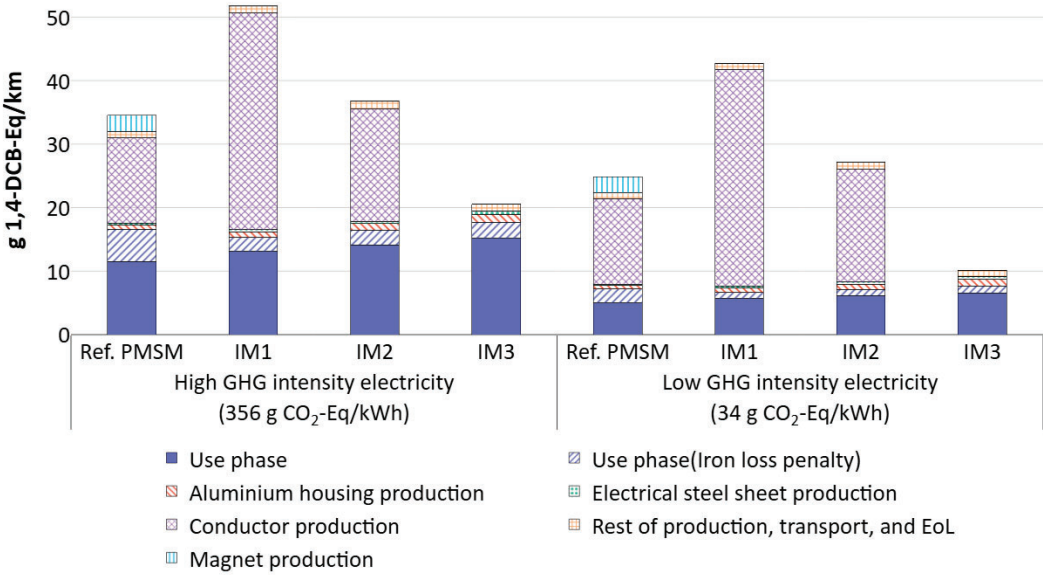

(b) Green manufacturing.

Figure 4.32: ReCiPe 1.03 midpoint results for non-carcinogenic human toxicity potential.

cal steel and Al housing production also contribute. Green manufacturing substantially improves IM3 performance in this category.

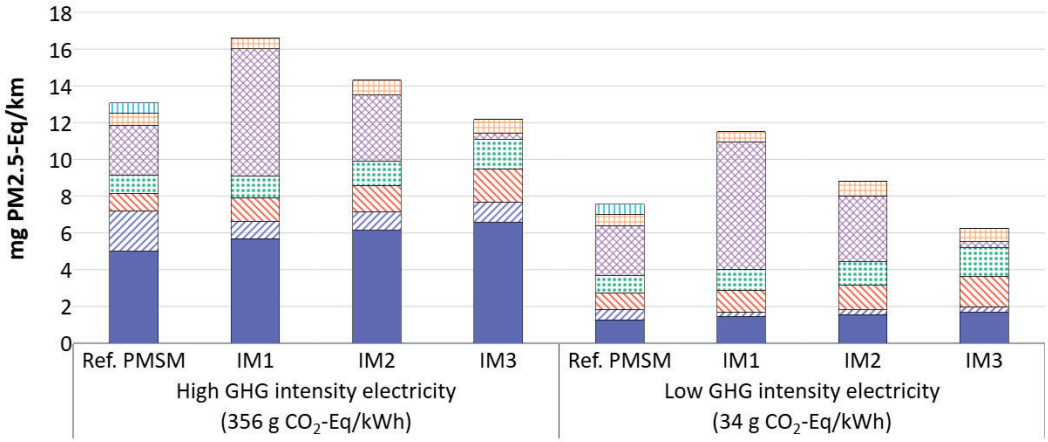

(a) Base case.

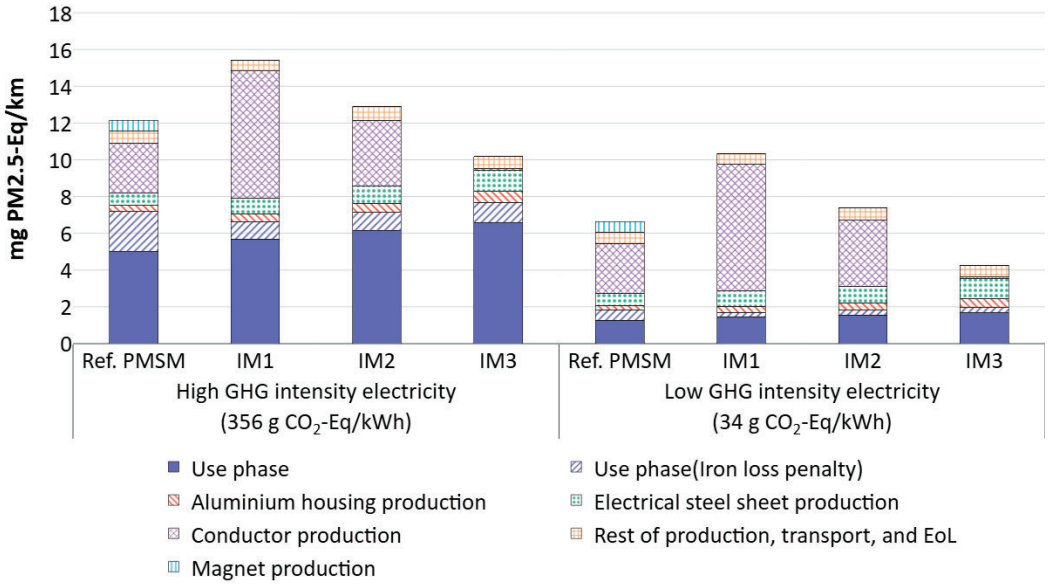

(b) Green manufacturing.

Figure 4.33: ReCiPe 1.03 midpoint results for particulate matter formation potential.

4.5.3 Sensitivity Analysis: Magnet Production Impact

The LCI model for the magnet supply chain utilized in this study builds upon the work of Nordelöf *et al.* [23]. That model originally incorporated Ecoinvent data for rare-earth oxide (REO) concentrate at 70% purity, and included revisions to energy consumption and economic burden allocation for Nd and Dy, based on REE price data from 2014 to 2016. In contrast to the 3.3 version used by Nordelöf *et al.* [23], this study employs Ecoinvent version 3.9, which results in a noticeable change in emissions, from 64 to 58 kg CO_2-eq per e-machine.

Additionally, Nordelöf and Bongards [25] applied economic allocation using REE price data from 2021 to 2024 across two REO supply pathways in a cradle-to-gate LCA of PMSMs for EVs. Depending on the selected supply route, emissions ranged from approximately 90 to 170 kg CO_2-eq per e-machine, representing 22% to 35% of total e-machine production emissions. These results underscore the substantial uncertainty linked to magnet manufacturing.

A review conducted by Schreiber *et al.* [24] highlights that several LCA studies addressing REO extraction and production from raw ore were published between 2016 and 2020. These studies exhibit significant variation in greenhouse gas intensity per kilogram of pure REO, with differences across ore types approaching a factor of five. The datasets forming the basis of Ecoinvent for REEs tend to reflect the lower end of this spectrum [24]. When economic value is used for allocation, these disparities are further magnified [23]. This variability warrants an examination of how sensitive the results are to the choice of magnet supply chain data.

This sensitivity analysis evaluates the effect of variations in the climate impact of magnet production, which is subject to large discrepancies in reported burdens for rare earth element extraction, as highlighted by Schreiber et al. [24]. The baseline scenario uses the original dataset for magnet supply, and two additional cases were modeled by increasing the GHG emissions from magnet production by 100% and 200%, respectively. These variations were combined with four scenarios for the Ref. PMSM option, considering high and low GHG-intensity electricity supply, with and without green manufacturing.

As shown in Fig. 4.34, under high GHG-intensity electricity in the base case, the magnet supply chain accounts for up to 8% of total GHG emissions for the Ref. PMSM at the highest variation level. At this point, IM2 becomes com-

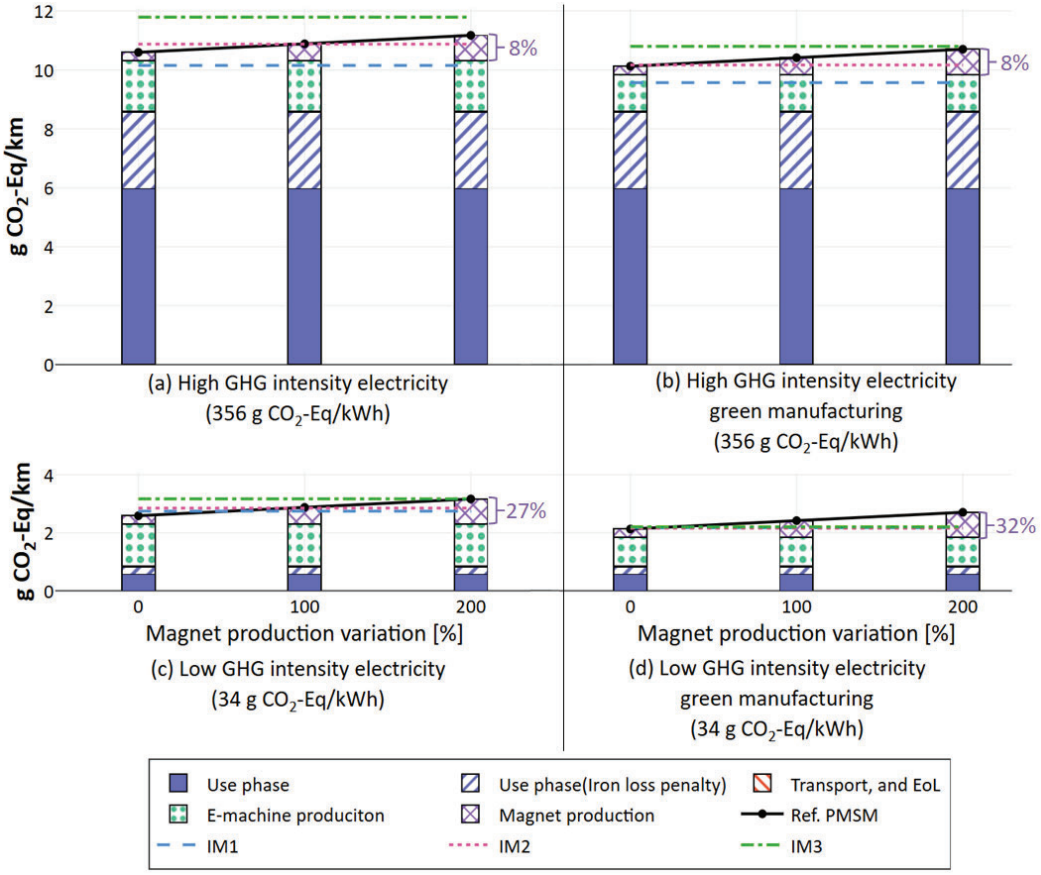

Figure 4.34: Sensitivity analysis of magnet production impacts on GWP100 (IPCC 2021) for four scenarios.

parable to the Ref. PMSM. Furthermore, with green manufacturing, all IM options approach parity with the Ref. PMSM. Under low GHG-intensity electricity, the relative contribution of magnet production increases significantly, reaching nearly one-third of the total emissions for the Ref. PMSM at the 200% increase level. In this scenario, all IM options become competitive with the PMSM. Notably, when green manufacturing is applied, all IM options already outperform the Ref. PMSM at a 100% increase in magnet-related emissions.

CHAPTER 5

Magnet-free synchronous machine modeling and LCA results

In this chapter, four investigated magnet-free synchronous machines were examined:

1. SynRM with dist. Cu stator windings (SynRM1).
2. SynRM with dist. Al stator windings (SynRM2).
3. EESM with dist. Cu stator windings and concentrated Cu rotor windings (EESM1).
4. EESM with dist. Al stator windings and concentrated Al rotor windings (EESM2).

Their design summary is listed in Table 5.1. Their energy loss models (mainly based on electromagnetic FEM model) and LCI models are built and presented, and their LCA results are benchmarked against those of the Ref. PMSM in Chapter 3.

Table 5.1: Design summary of investigated synchronous machines.

Machines	**SynRM1**	**SynRM2**	**EESM1**	**EESM2**
Number of poles N_p	6		8	
Conductor materials in stator/rotor	Cu / -	Al / -	Cu / Cu	Al / Al
Stack length l_a [mm]	272	330	150	180
Number of stator slots	54		48	
Number of winding turns in stator/rotor N_s/N_f	6/-	5/-	13/90	11/78
Number of stator winding parallel branches N_{pb}	3		4	
Stator outer diameter [mm]	200			
Stator inner diameter [mm]	145.8		143	
Air gap length [mm]	0.5		1	
Maximum current density $[A/mm^2]$	20/-	16.7/-	20/13	16.7/11.3
Stator winding temperature $[°C]$	120			
Rotor winding temperature $[°C]$	-		120	
Material loss rate during punching [%]	54		53	

5.1 Synchronous reluctance machine (SynRM)

From (2.13), the torque of the SynRM depends on the difference between L_d and L_q. Thus, many studies have demonstrated that the optimization of the barrier patterns to make the ratio of L_d/L_q as big as possible can be found in [95], [96].

As [95] has studied, the maximum torque envelope of a SynRM is affected by the pattern of the support ribs, whose function is to maintain the mechanical strength of the rotor. To achieve the requirement listed in Chapter 3, both rib-less and magnetic rib rotor designs are modified from the rotor configuration in [95]. Additionally, a rotor design with "added non-magnetic ribs", whose material is stainless steel with relative permeability equal to 1 and bulk conductivity equal to $1.1 \times 10^6 S/m$, is also implemented, inspired by [97]. These added non-magnetic ribs are not formed as part of the punching and stacking process of the iron core laminations; instead, they are separately manufactured and attached to the rotor, whose purpose is to minimize the L_q and simultaneously maintain mechanical strength.

The comparative result of rib-less (solid blue line), magnetic ribs (green dashed line), and added non-magnetic ribs designs (red dotted line) in maximum torque envelopes varying with rotor speed, and their cross-sections are depicted in Figure 5.1. These three rotor designs share the same stator design but with increases in active lengths l_a for magnetic ribs and added non-magnetic ribs designs from the rib-less one. The increment in active lengths is to compensate for the decrease in maximum torque due to the decline in the ratio of L_d/L_q.

As can be seen in Figure 5.1, with increased active lengths, two designs with ribs can reach the same level of maximum torque around $250Nm$. However, the maximum torque envelope of magnetic ribs design drops dramatically after its base speed of $3000rpm$. The added non-magnetic ribs design could maintain a similar level of the maximum torque envelope over the range of rotor speed. Therefore, the added non-magnetic ribs design is chosen to be the technical option in this study to achieve the design boundaries of the e-machine and attain a reasonable mechanical design.

5.1.1 Energy loss model

In Figure 5.2, the cross-section of SynRM1 and SynRM2 is presented. The ef-

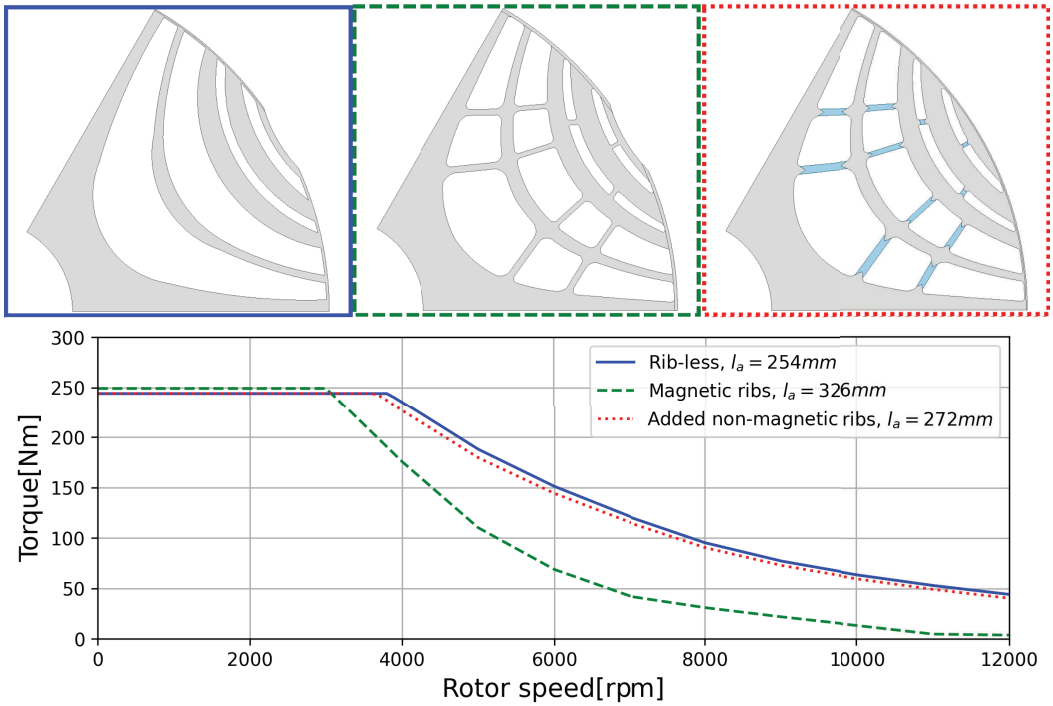

Figure 5.1: Maximum torque envelope varying with rotor speed for three different rotor configurations.

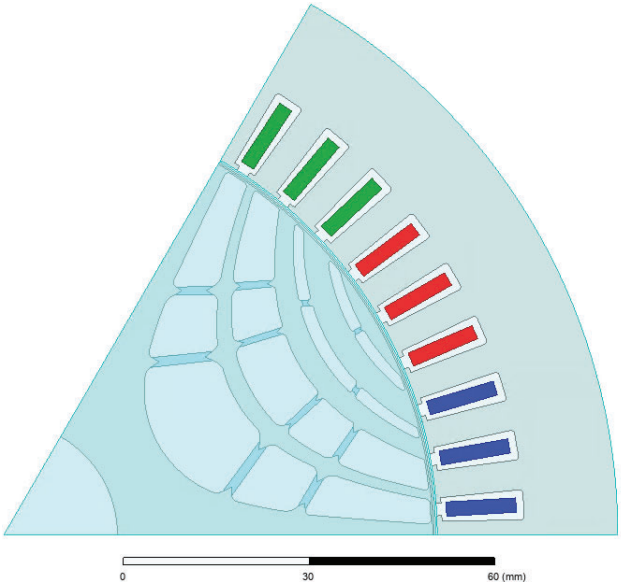

Figure 5.2: Cross-section of SynRM.

ficiency maps and loss maps of SynRM1 and SynRM2 are shown in Figure 5.3a to 5.4b, where in the loss maps the operating points from the WLTC are also presented, which show that the maximum torque envelopes of SynRM1 and SynRM2 fulfill the demand of the WLTC.

5.1.2 LCI model

Figure 5.5 presents an overview of the life cycle up to the production stage for the two SynRM options. As illustrated, most of the data is based on the IPMSM LCI model developed by Nordelöf et al., as documented in a series of publications [51]–[53], with the here updated models highlighted in orange.

The manufacturing processes for the two SynRM technical options are shown in Figure 5.6, which is adapted from the PMSM LCI model by Nordelöf et al. [51]. The updated processes are indicated by red-dotted lines in the figure, where the magnet mounting is replaced by stainless support steel rib mounting. The support ribs are installed with the same step as the rotor electrical steel sheets stacking and are furtherly mounted with the rotor stack and endplates at the two ends on the shaft. The aim of support ribs and rotor endplates is to enhance the mechanical strength and prevent radial and axial displacements of the SynRM rotor.

The masses of the stainless steel parts are listed in Table 5.2, where the added non-magnetic ribs are calculated from their cross sectional shape and active lengths (painted blue between the rotor barriers in Figure 5.2), whereas the end plate model is inherited from [51].

Table 5.2: Estimations made for the masses of stainless steel ribs and rotor endplates.

Parts	**Mass [kg]**	
	SynRM1	SynRM2
Support ribs	1.17	1.42
Rotor endplates	0.58	

Figure 5.7a and 5.7b are the weight share for SynRM1 and SynRM2, respectively.

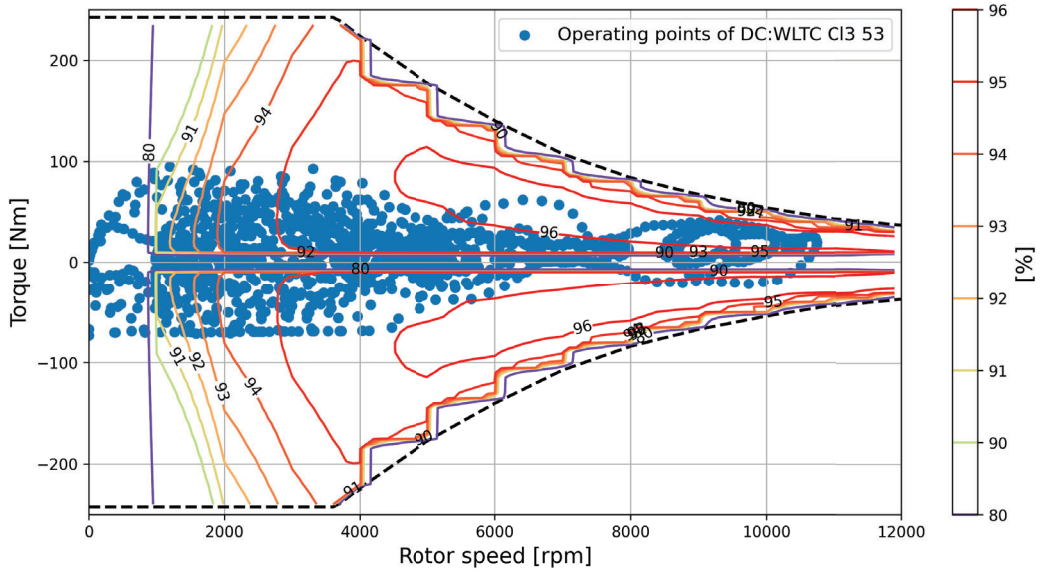

(a) SynRM1.

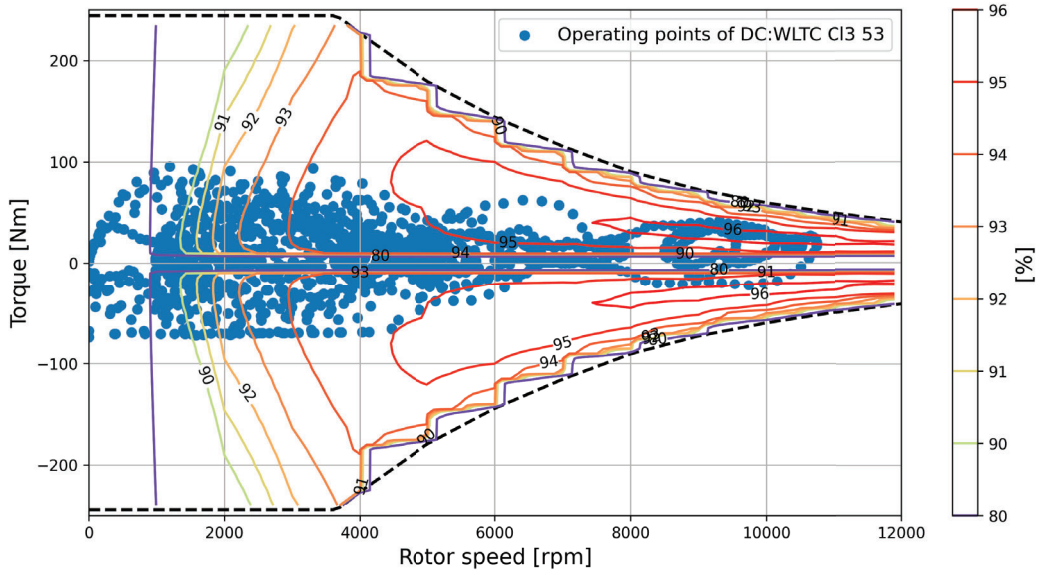

(b) SynRM2.

Figure 5.3: Efficiency maps with operating points from the WLTC.

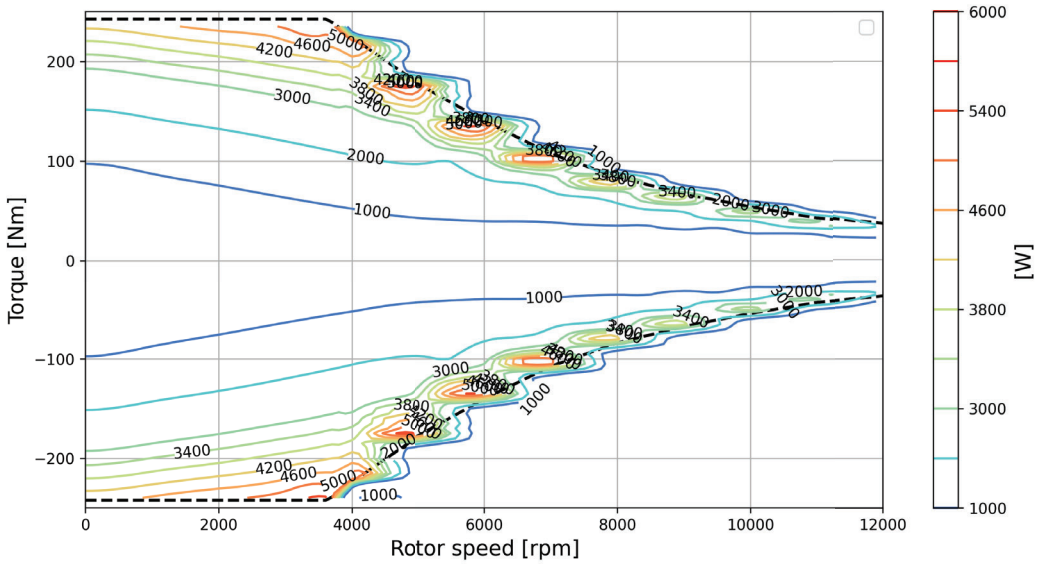

(a) SynRM1.

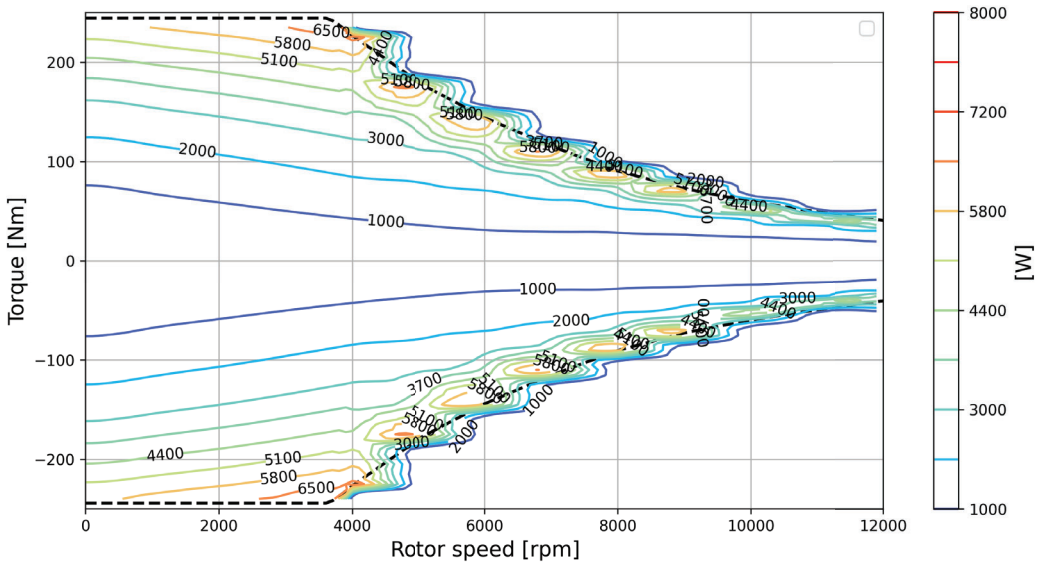

(b) SynRM2.

Figure 5.4: Loss maps.

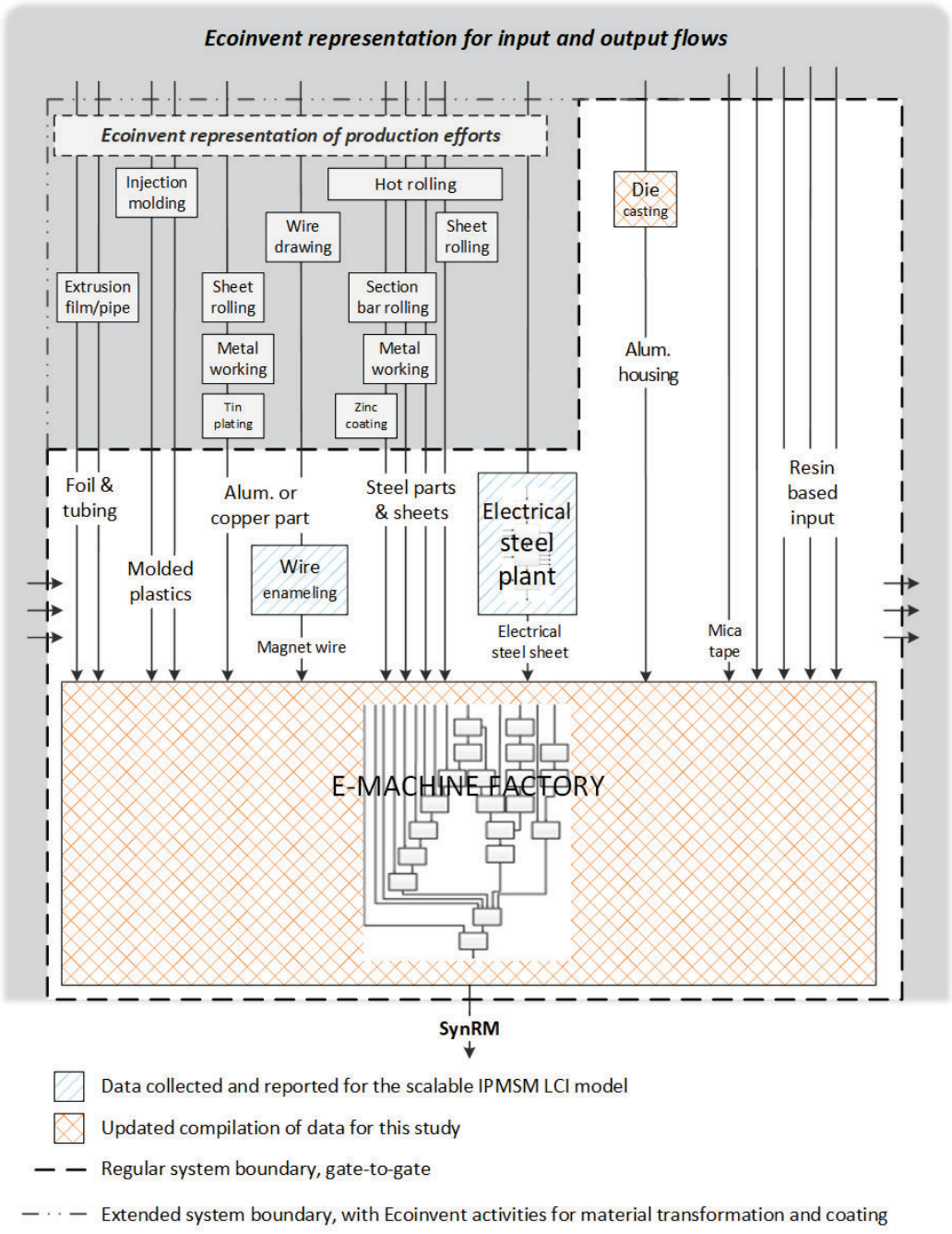

Figure 5.5: Overview of the system model for the production steps of two SynRMs. Reworked from [51]–[53]

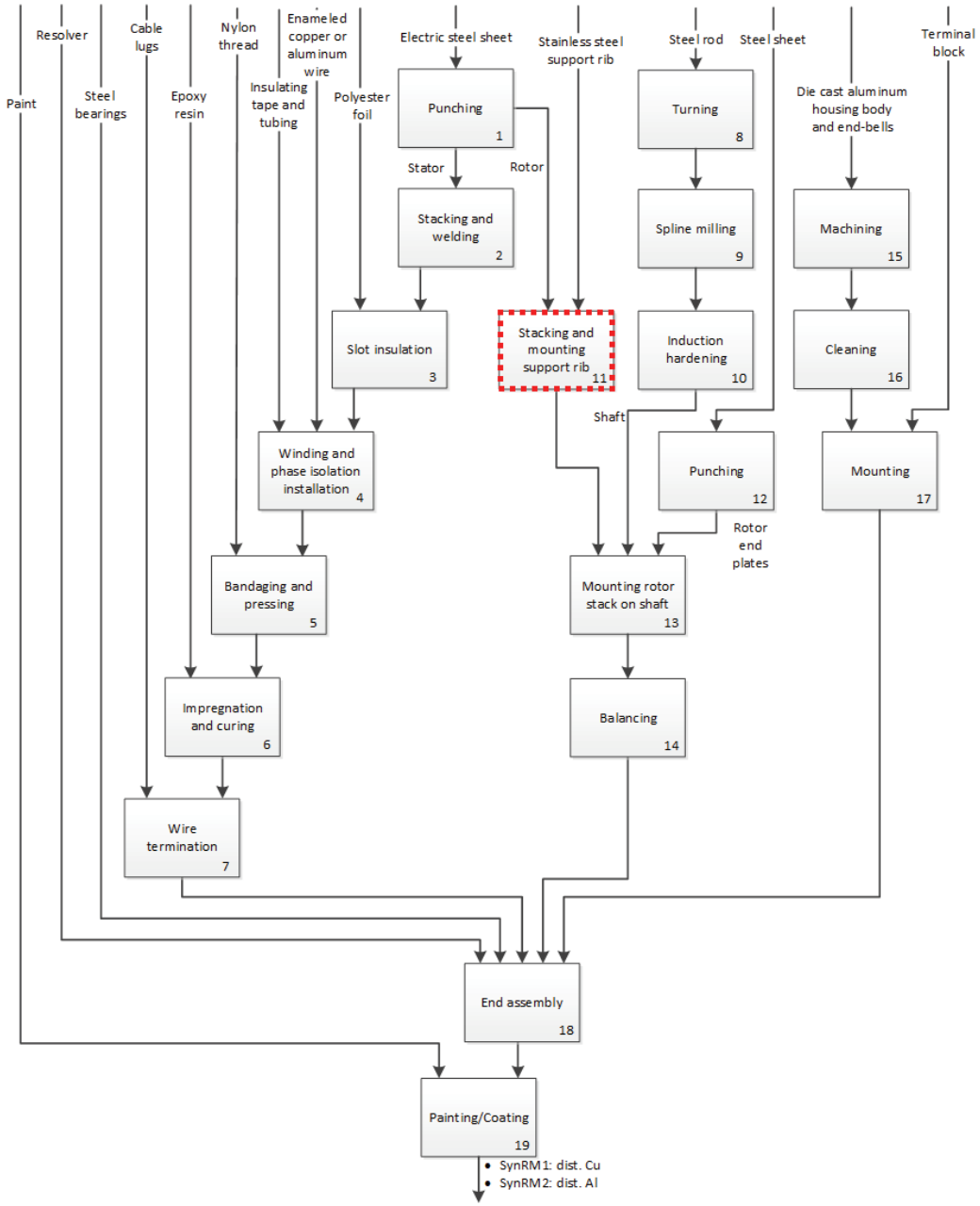

Figure 5.6: SynRM factory process flow chart for the two SynRMs (SynRM1, 2), divided into 19 processes. Reworked from Nordelöf et al. [51].

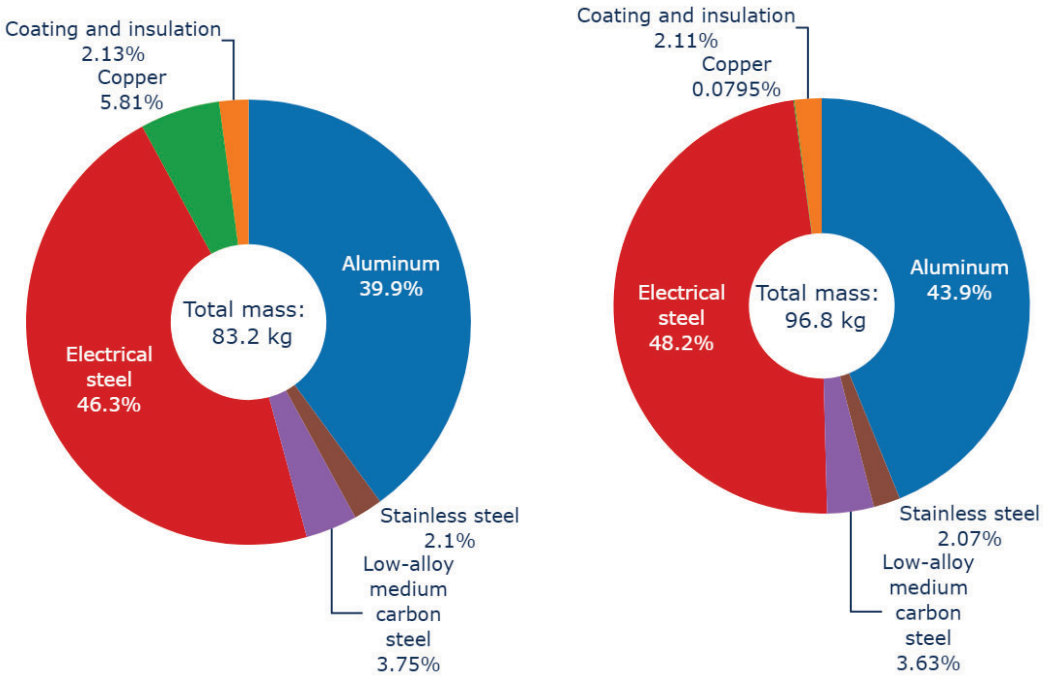

(a) SynRM1. **(b)** SynRM2.

Figure 5.7: Weight share of the two SynRMs.

5.2 Electric excited synchronous machine (EESM)

As mentioned in Section 2.1.4, one of the key advantages of the EESM is its ability to regulate the rotor magnetic field strength through the control of the field current, denoted as i_f. This feature provides a significant operational benefit over PMSMs, which rely on fixed magnetic flux from permanent magnets. In low-load operating conditions, the magnetic flux in PMSMs remains constant, leading to elevated core losses due to unnecessary magnetization. In contrast, EESMs can dynamically adjust their excitation to maintain only the necessary magnetic strength, thereby minimizing iron losses in the stator core.

5.2.1 Energy loss model

The cross section of the investigated EESM1 and EESM2 is shown in figure 5.8.

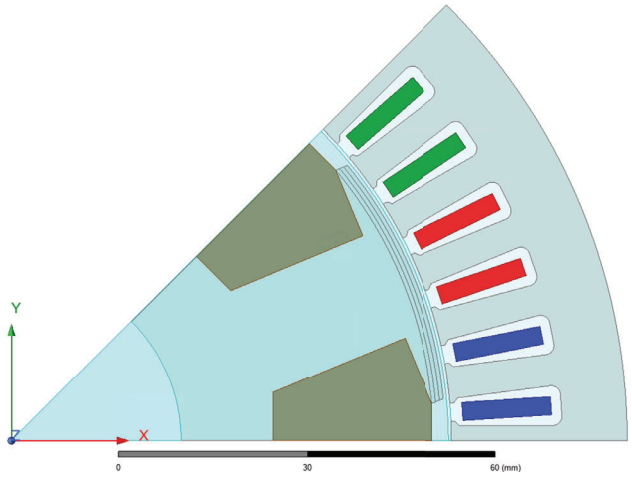

Figure 5.8: Cross-section of EESM for one pole pitch.

The rotor winding is supplied with direct current to generate the magnetic field required for synchronous operation. This excitation is typically delivered through a slip ring and brush assembly, which serves as the mechanical interface between the stationary and rotating components of the machine, as shown in Figure 5.9. While this configuration facilitates continuous excitation, it introduces two primary sources of energy loss that can adversely affect

the machine's overall efficiency.

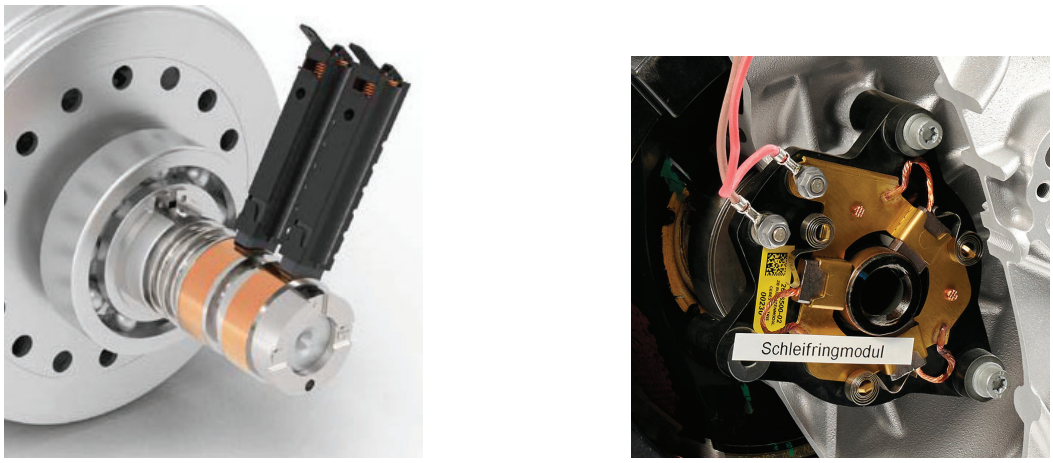

(a) Vitesco Technology[98]. **(b)** BMW[99].

Figure 5.9: Example rotor excitors of vehicular EESMs.

One significant source of loss in the slip ring and brush assembly arises from contact resistance. As current flows through the interface between the brush and the slip ring, a voltage drop occurs due to the finite resistance at the contact surface. The resulting ohmic loss can be expressed as [100], [101],

$$P_{\text{ohmic,brush}} = 2\, i_f^2\, R_{\text{brush}}, \tag{5.1}$$

where R_{brush} is the equivalent resistance of a single brush, calculated by:

$$R_{\text{brush}} = \frac{\rho_{\text{brush}}\, a_{\text{brush}}}{l_{\text{brush}}}, \tag{5.2}$$

with ρ_{brush} denoting the resistivity of the brush material, and a_{brush} and l_{brush} representing the cross-sectional area and length of the conductive path, respectively. The ohmic loss map due to the brushes is illustrated in Figure 5.10.

The mechanical interaction between the brushes and the rotating slip rings also contributes to frictional losses. These losses manifest as heat and wear at the contact interface, leading to energy dissipation and material degradation over time. Frictional losses are influenced by the rotational speed, contact pressure, and lubrication conditions, and can be quantified as [100], [101],

$$P_{\text{friction,brush}} = 10\, \mu_{Br}\, P_{\text{brush}}\, a_{\text{brush}}\, v_{\text{ring}}, \tag{5.3}$$

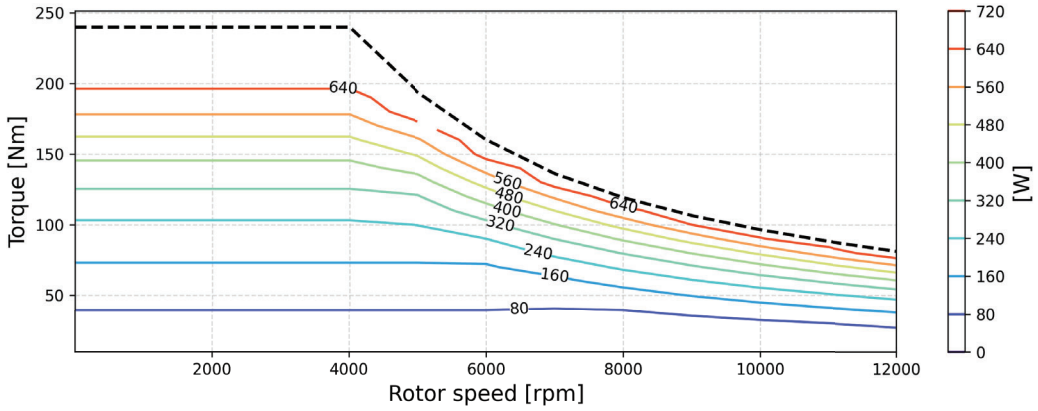

Figure 5.10: Ohmic loss map due to brushes of EESMs.

where μ_{Br} is the coefficient of friction between the brush and the slip ring, P_{brush} is the contact pressure, and v_{ring} is the peripheral speed of the slip ring, given by

$$v_{\text{ring}} = \omega_r \, r_{\text{ring}}, \tag{5.4}$$

with ω_r representing the rotor angular velocity and r_{ring} the outer radius of the slip ring. The distribution of frictional losses is presented in Figure 5.11.

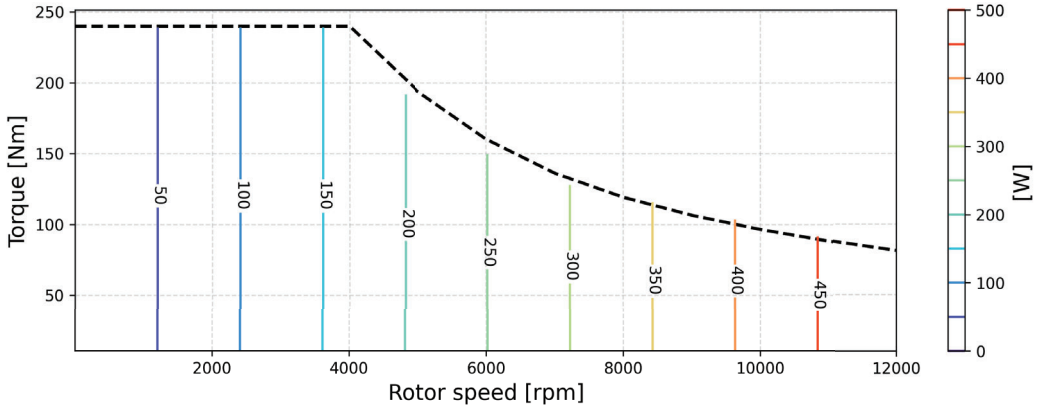

Figure 5.11: Friction loss map due to brushes in EESMs.

Furthermore, the efficiency maps with the operating points from the WLTC and the loss maps of EESM1 and EESM2 are shown in Figure 5.12a to 5.13b.

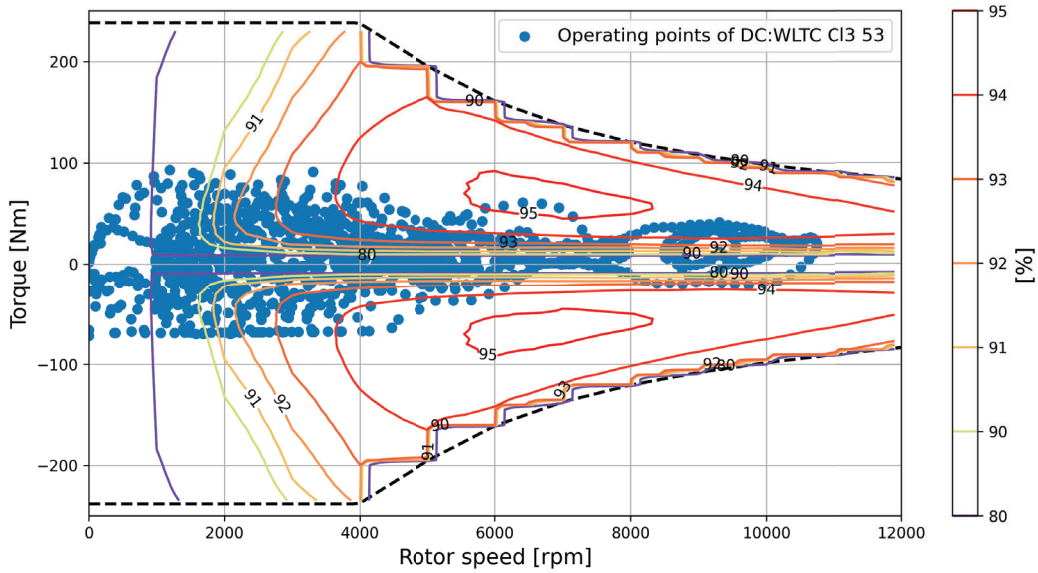

(a) EESM1.

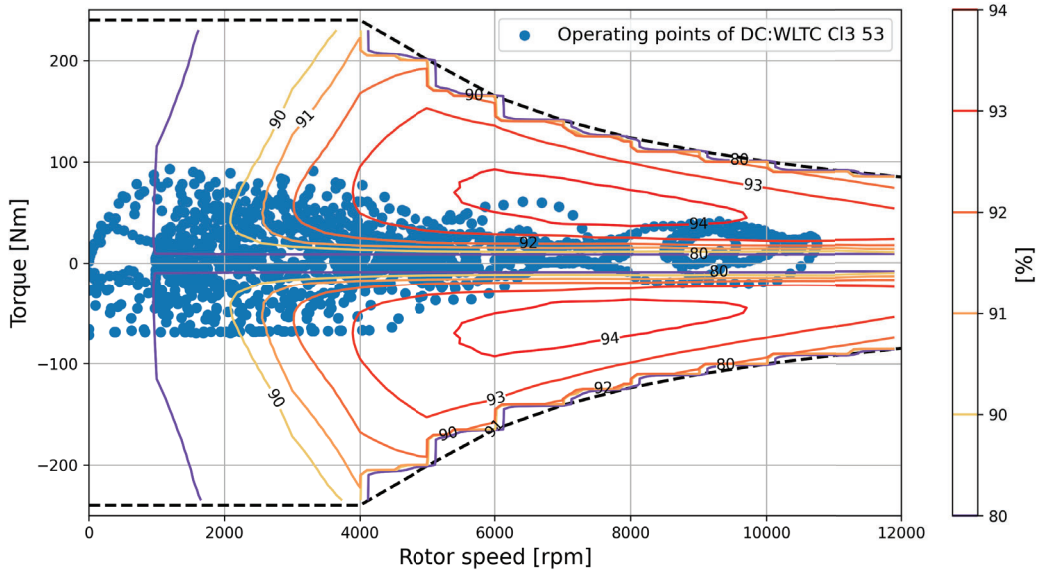

(b) EESM2.

Figure 5.12: Efficiency map with operating points from the WLTC.

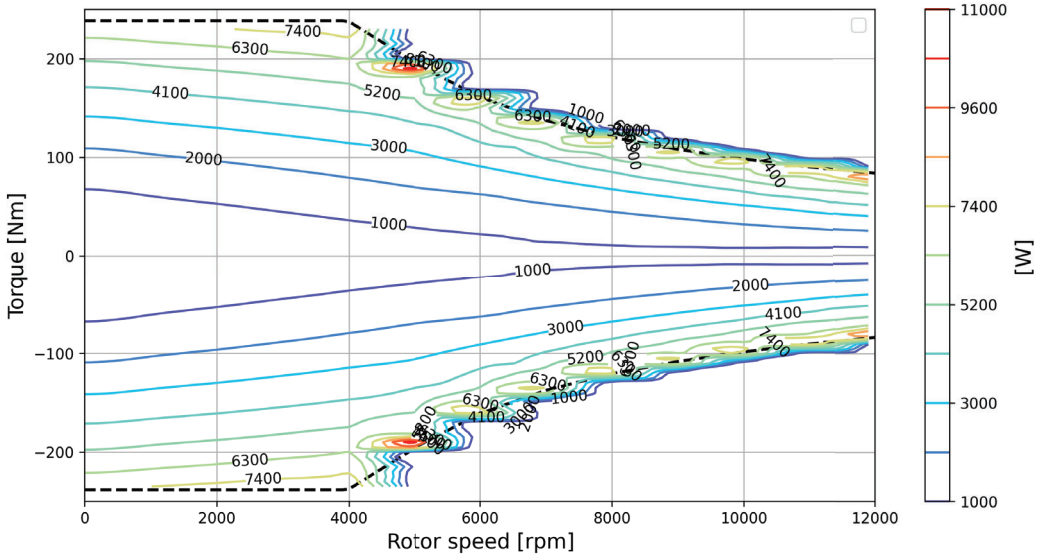

(a) EESM1.

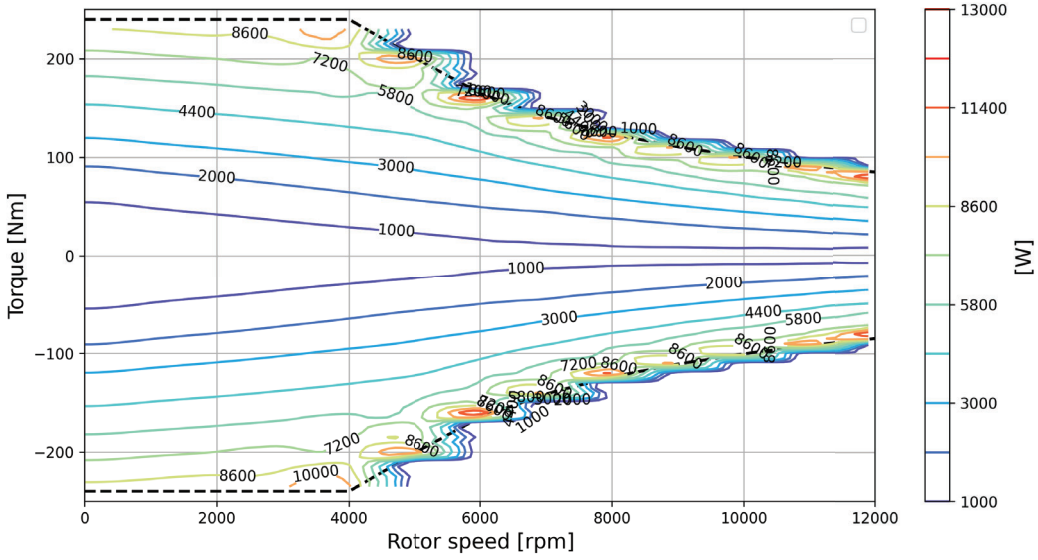

(b) EESM2.

Figure 5.13: Loss maps.

5.2.2 LCI model

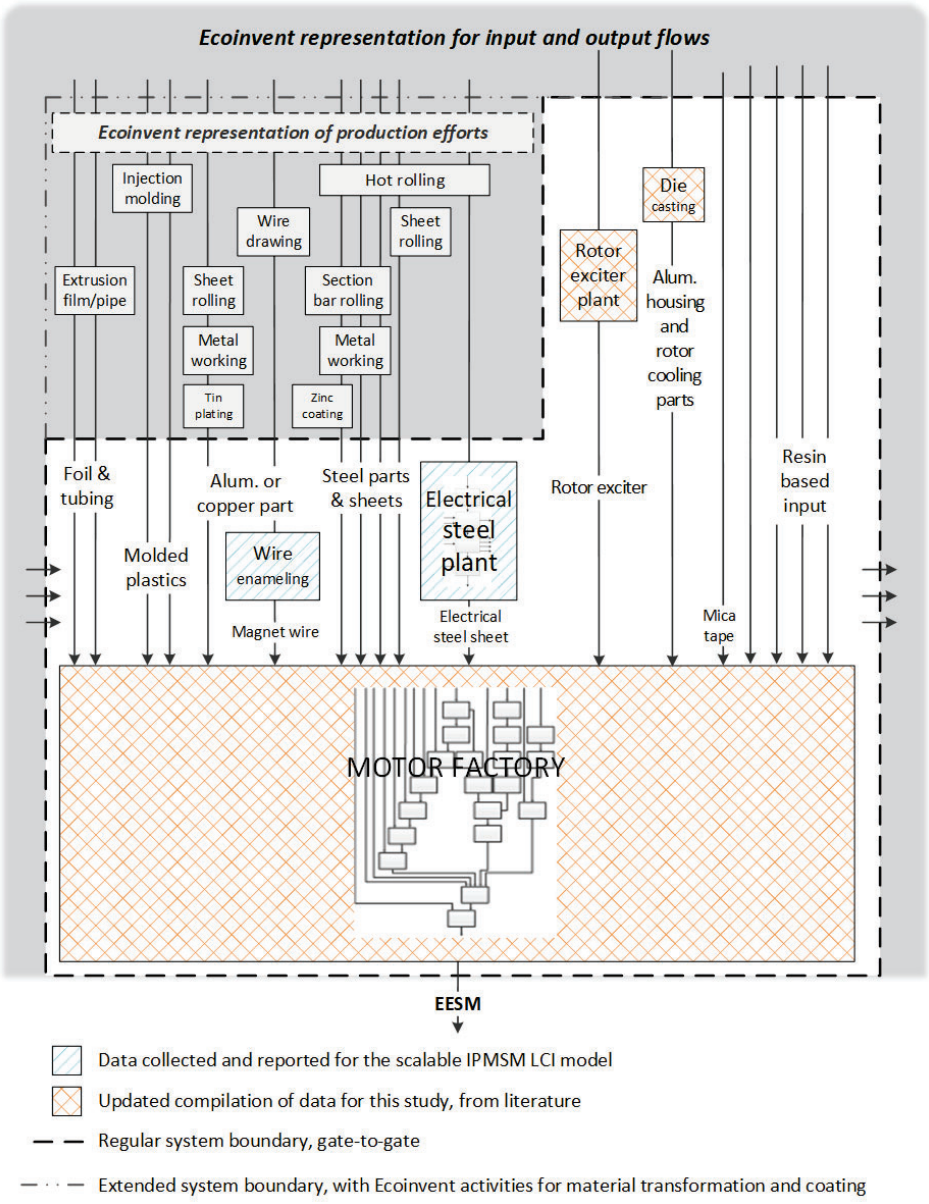

Figure 5.14: Overview of system model for the production steps of two EESMs. Reworked from [51]–[53]

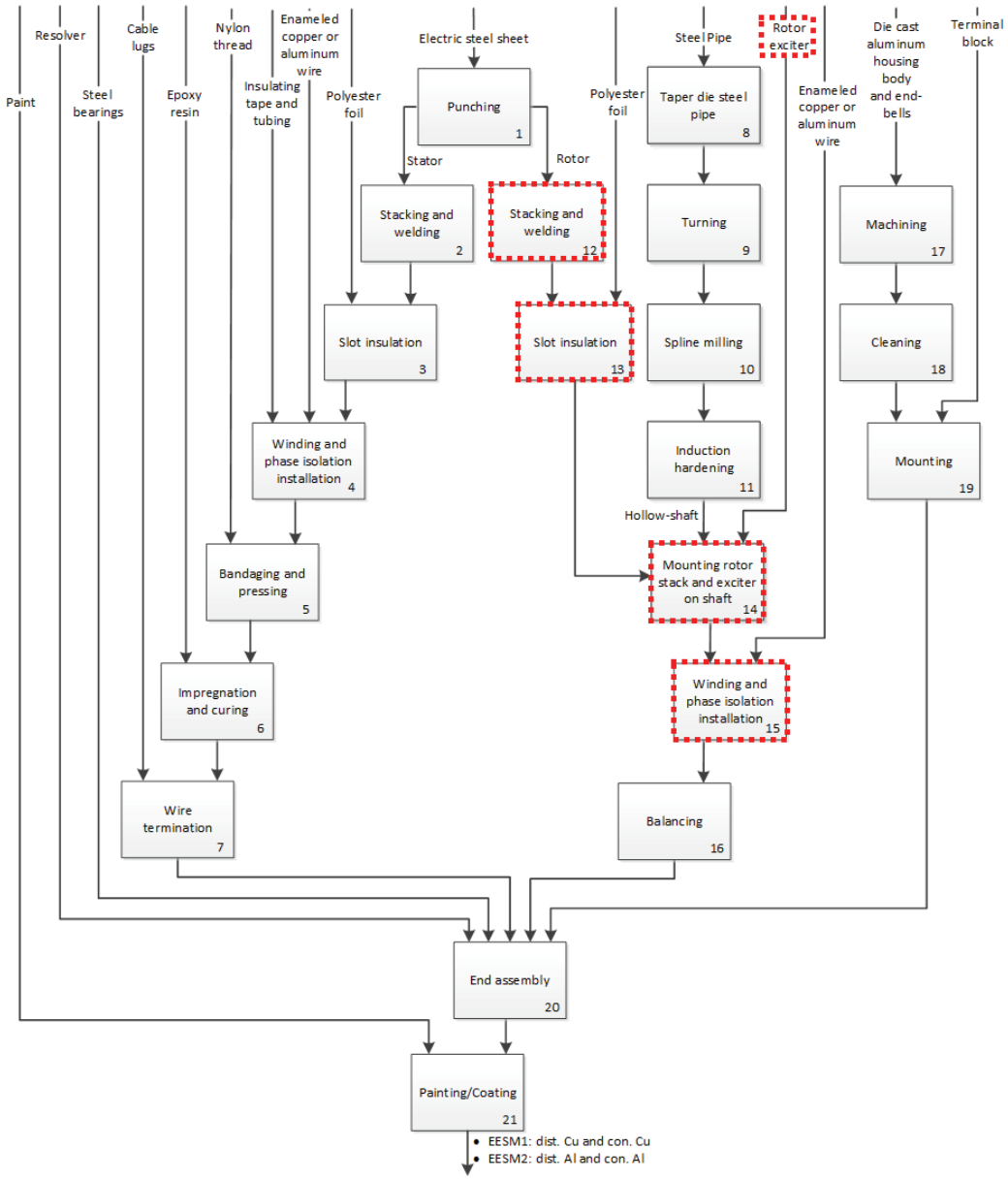

Figure 5.15: SynRM factory process flow chart for the two EESMs (EESM1, 2), divided into 21 processes. Reworked from Nordelöf et al. [51].

Figure 5.14 summarizes the life cycle up to production for both EESM options, based largely on the IPMSM LCI model by Nordelöf et al. [51]–[53], with updates shown in orange. In the updated manufacturing processes for the two

technical options, magnet mounting is replaced by rotor exciter mounting. These processes are illustrated in Figure 5.15, which is adapted from the PMSM LCI model by Nordelöf et al. [51], with the modifications highlighted using red-dotted lines.

Figure 5.16a and 5.16b are the weight share for EESM1 and EESM2, respectively.

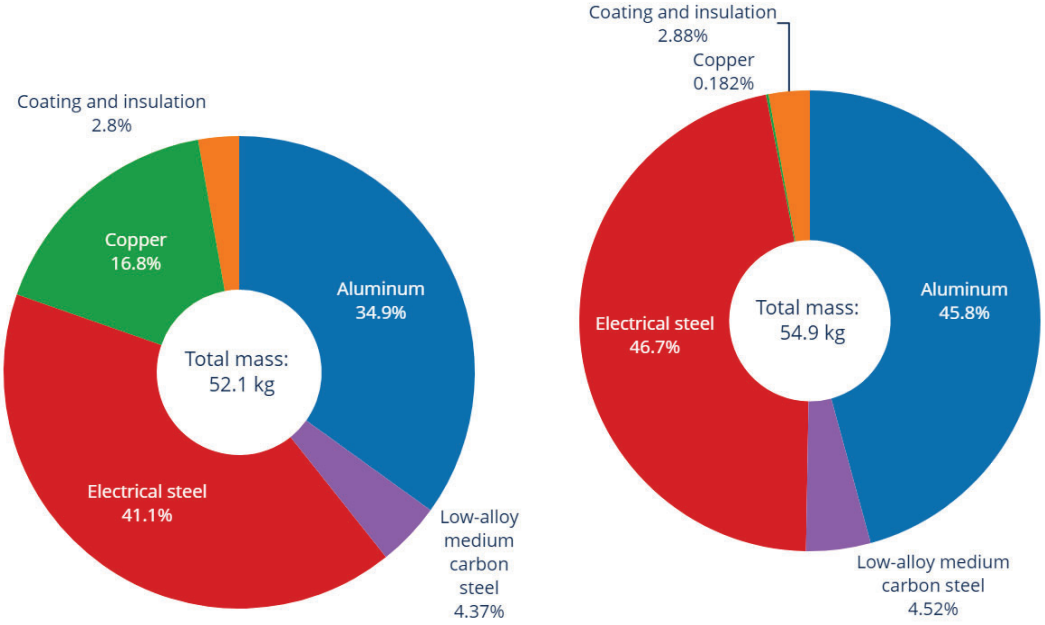

(a) EESM1. **(b)** EESM2.

Figure 5.16: Weight share of the two EESMs.

5.3 Technical performance

Table 5.3 summarizes the key technical performance metrics of four synchronous electric machines benchmarked against the Ref. PMSM for EV applications. The maximum torque values across all configurations are closely aligned, ranging from 239 Nm to 244 Nm, indicating similar mechanical output capabilities. However, differences in base speed influence the maximum power output.

Similarly with the comparison of IM options, when $f_{fe} = 1.7$ is applied

Table 5.3: Key technical performances of investigated synchronous machines.

Machines	**Ref. PMSM**	**SynRM1**	**SynRM2**	**EESM1**	**EESM2**
General data					
Maximum torque [Nm]	239	242	244	239	239
Maximum power [kW]	100	92	93	100	100
Base speed [rpm]	4000	3600	3600	4000	4000
Power density [kW/kg]	2.2	1.1	1.0	1.9	1.8
Power density [kW/L]	25.1	10.8	9.0	21.3	17.7
Weight					
Stator core [kg]	11.8	23.6	28.6	12.2	14.7
Rotor core [kg]	7.2	14.8	18.0	9.1	10.9
Stator winding [kg]	4.8	4.8	1.7	5.2	1.7
Magnets/Rotor conductors [kg]	1.3	-		2.5	1.2
Al housing and cooling parts [kg]	14.6	33.3	40.8	17.4	21.3
Total weight [kg]	44.9	83.2	96.8	52.1	54.9
Drive cycle energy loss due to e-machine					
Due to iron loss per km [Wh/km] ($f_{fe} = 1$)	9.4 63.5%[a]	3.3 29.3%[a]	3.5 24.7%[a]	3.4 20.1%[a]	3.6 18.6%[a]
Due to ohmic loss per km [Wh/km] ($f_{fe} = 1$)	3.6 24.6%[a]	4.8 41.7%[a]	7.0 48.8%[a]	7.2 43.1%[a]	9.8 49.9%[a]
Due to other loss per km [Wh/km] ($f_{fe} = 1$)	0.2 1.4%[a]	0.2 1.6%[a]	0.2 1.3%[a]	4.4 26.1%[a]	4.3 22.2%[a]
Due to road load per km [Wh/km] ($f_{fe} = 1$)	1.5 10.5%[a]	3.1 27.4%[a]	3.6 25.3%[a]	1.8 10.6%[a]	1.8 9.3%[a]
Energy loss per km [Wh/km] ($f_{fe} = 1$)	14.8	11.4	14.3	16.7	19.6
Life cycle energy [kWh] ($f_{fe} = 1$)	2951	2284	2861	3335	3910
Energy loss per km [Wh/km] ($f_{fe} = 1.7$)	21.2	13.7	16.7	19	22
Life cycle loss [kWh] ($f_{fe} = 1.7$)	4240	2745	3347	3797	4410

[a]percentage of total loss for respective e-machine

uniformly across the machine types, the Ref. PMSM exhibits lower efficiency than the Cu-option of EESM. This discrepancy arises because iron losses constitute over 60% of the total losses in the Ref. PMSM, whereas they account for only about 20% in EESM1.

5.4 Environmental Performance by LCIA

This section presents the life cycle impact assessment (LCIA) results for the five synchronous e-machine configurations benchmarked against the Ref. PMSM. The structure and methodology follow the approach described in Chapter 4.5, and similar trends are observed regarding the dominance of certain impact categories. Therefore, only key differences and new insights are highlighted here to avoid repetition.

5.4.1 Endpoint Categories

Endpoint results, normalized per e-machine, are shown in Figs. 5.17a and 5.17b. As in the previous analysis, the subsequent midpoint analysis focuses on the same key indicators identified earlier: climate change, acidification, particulate matter formation, and non-carcinogenic human toxicity. This ensures comparability across both benchmark sets while emphasizing any deviations introduced by the new machine designs.

5.4.2 Midpoint Categories

The midpoint analysis for the five synchronous e-machine configurations follows the same methodology as in Chapter 4.5. To avoid repetition, only key differences and notable observations are highlighted here, while general trends, such as the dominance of the use phase under high GHG-intensity electricity and the significant contribution of Al housing and electrical steel production, remain consistent with earlier findings.

5.4.2.1 Climate Change

Figure 5.18a presents the GWP100 results for the base case, assuming globally averaged virgin Al production and one-piece electrical steel punching (approximately 50% material loss). As in the previous analysis, the use phase

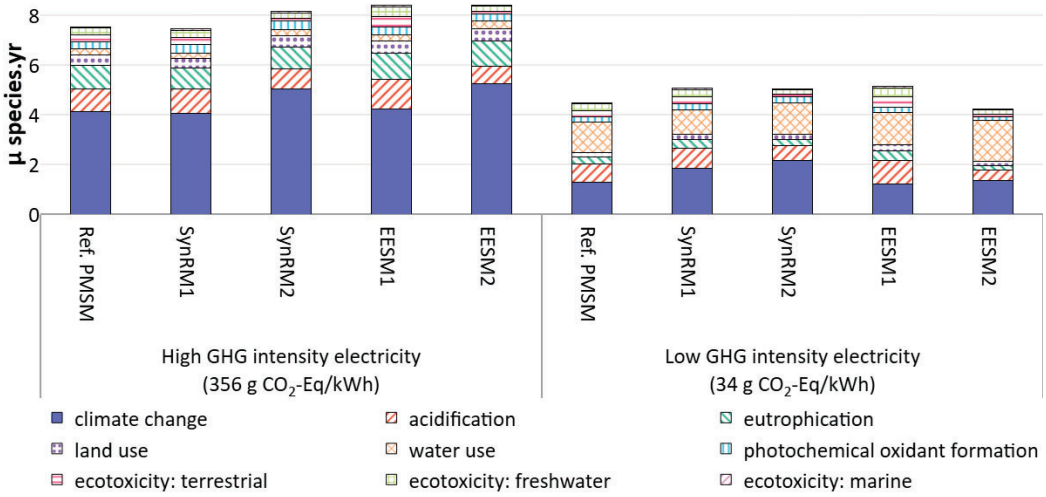

(a) Ecosystem quality.

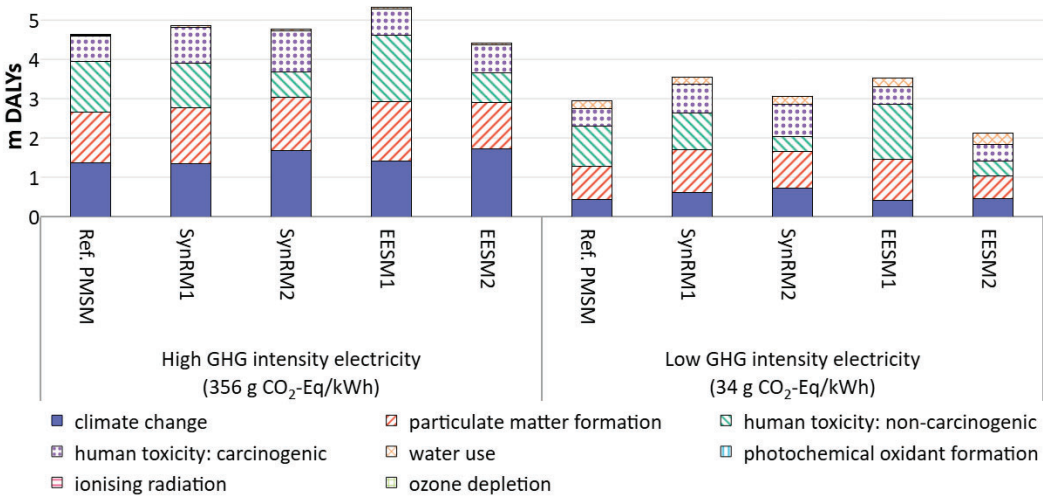

(b) Human health.

Figure 5.17: ReCiPe 1.03 endpoint results for ecosystem quality and human health.

dominates emissions under high GHG-intensity electricity. Consequently, the least energy-efficient option, EESM2, exhibits the highest emissions. However, when applying the iron loss penalty (adding 70% to account for manufacturing effects), EESM2 becomes comparable to the Ref. PMSM, with a difference of less than 0.5 g CO_2-eq/km. Under low GHG-intensity electricity, production impacts dominate, making SynRM1 and SynRM2—the least power-dense designs—the least favorable options. Among production processes, Al housing and electrical steel sheet manufacturing remain the largest contributors.

Green manufacturing, using segmented laminations and EU-sourced Al produced with 100% hydropower, significantly reduces production-related emissions for all options, with SynRM1 and SynRM2 benefiting the most under low GHG-intensity electricity.

5.4.2.2 Crustal Scarcity Potential (CSP)

Figures 5.19a and 5.19b show the CSP results. As before, Cu production dominates scarcity potential, making EESM1 the least favorable option in this category. Machines with Al conductors (e.g., EESM2) perform better in terms of resource sustainability, reinforcing the trade-off between efficiency and material criticality observed in the previous chapter.

5.4.2.3 Acidification and Non-carcinogenic Human Toxicity

The trends for terrestrial acidification (Fig. 5.20a) and non-carcinogenic human toxicity (Fig. 5.21a) mirror those in Section 4.5.2, with primary Cu production as the dominant contributor due to sulfur dioxide emissions and heavy metal release from sulfidic tailings. Consequently, SynRM2 and EESM2 (Al conductors) have the lowest impact in these categories. Green manufacturing further reduces impacts, particularly for Al-intensive components.

5.4.2.4 Particulate Matter Formation

As shown in Figs. 5.22a and 5.22b, particulate matter formation is again strongly linked to Cu production, but electrical steel and Al housing manufacturing also contribute significantly. This explains why SynRM2, despite lacking Cu, still shows a notable burden in this category. Green manufacturing mitigates these impacts, particularly for SynRM2.

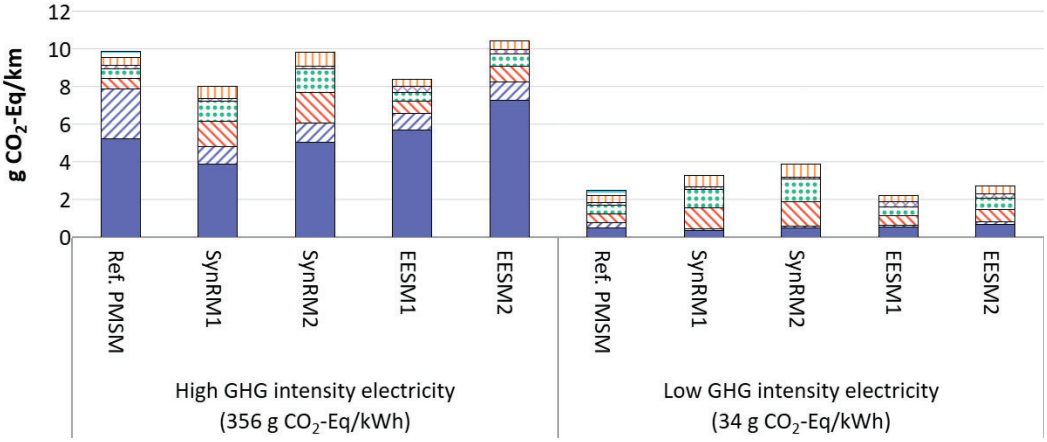

(a) Base case.

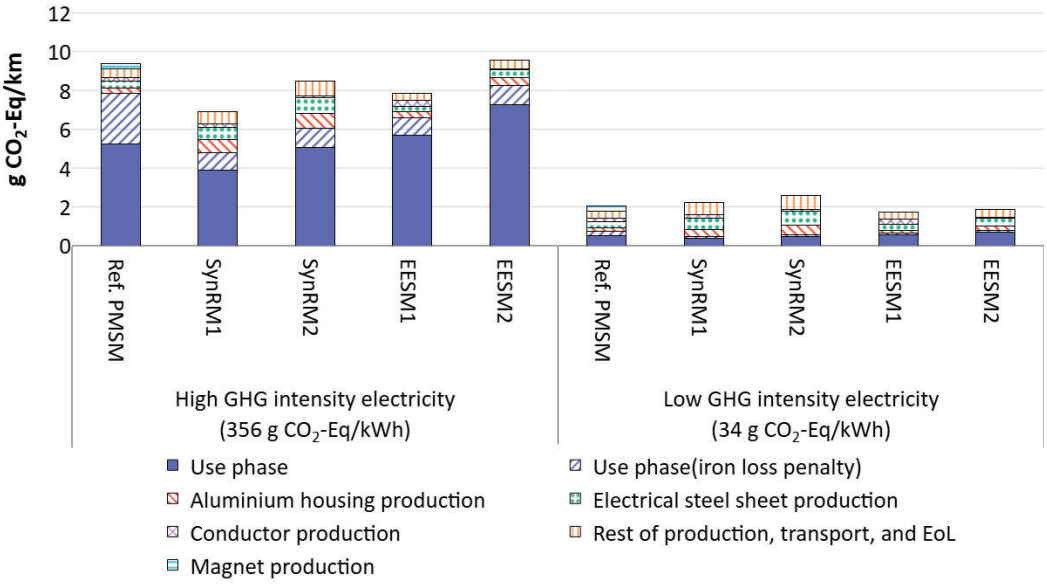

(b) Green manufacturing.

Figure 5.18: IPCC 2021 results for global warming potential (GWP100).

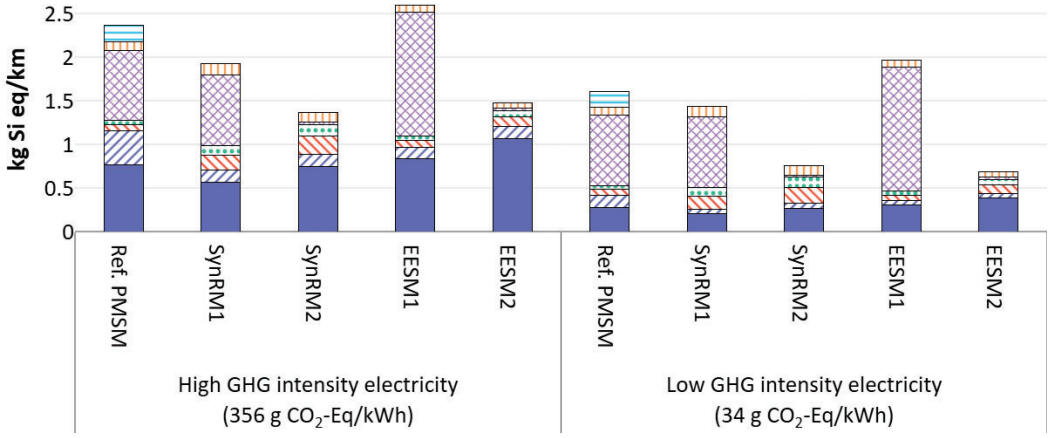

(a) Base case.

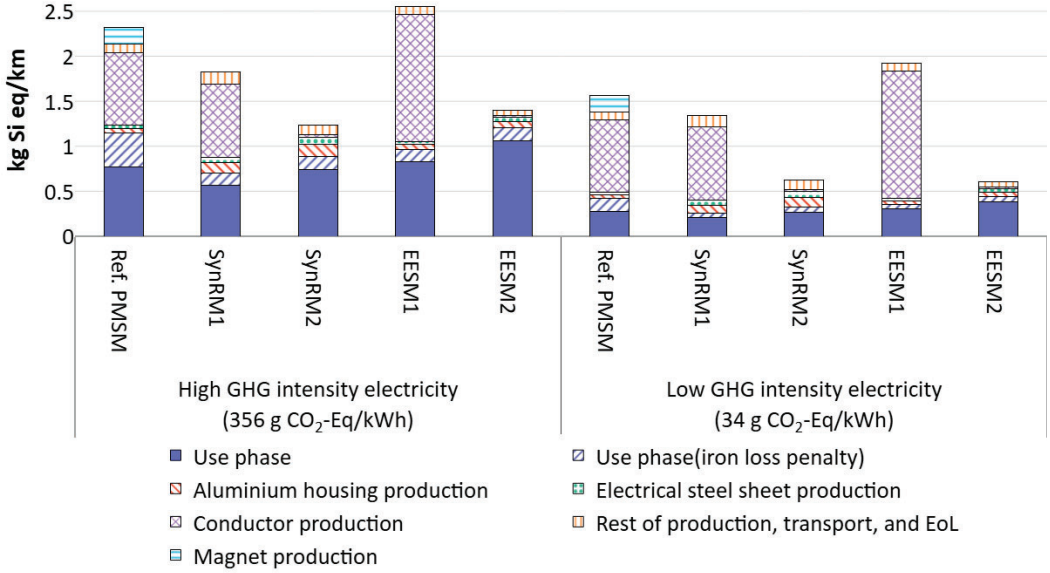

(b) Green manufacturing.

Figure 5.19: Crustal Scarcity Indicator 2020 results for crustal scarcity potential (CSP).

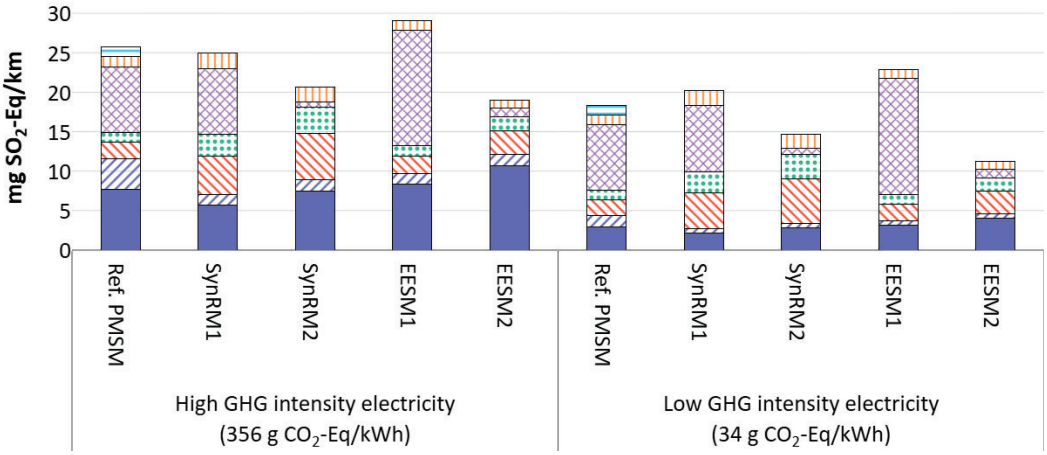

(a) Base case.

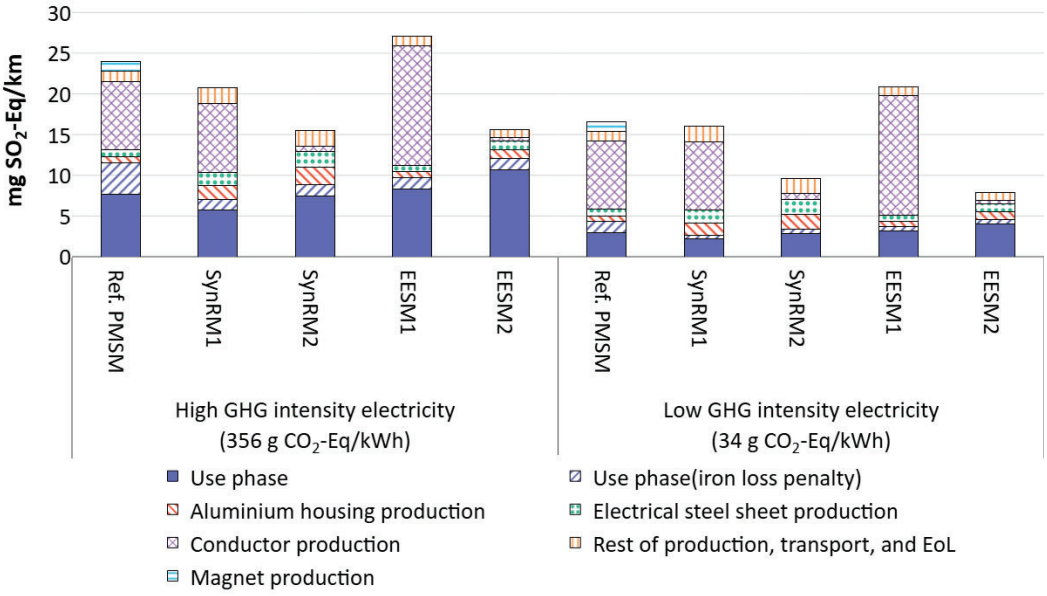

(b) Green manufacturing.

Figure 5.20: ReCiPe 1.03 midpoint results for terrestrial acidification potential.

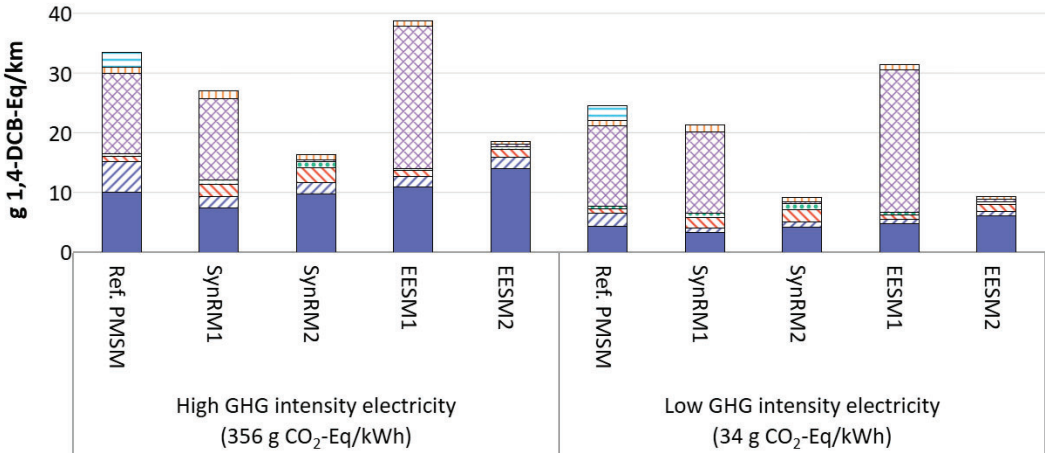

(a) Base case.

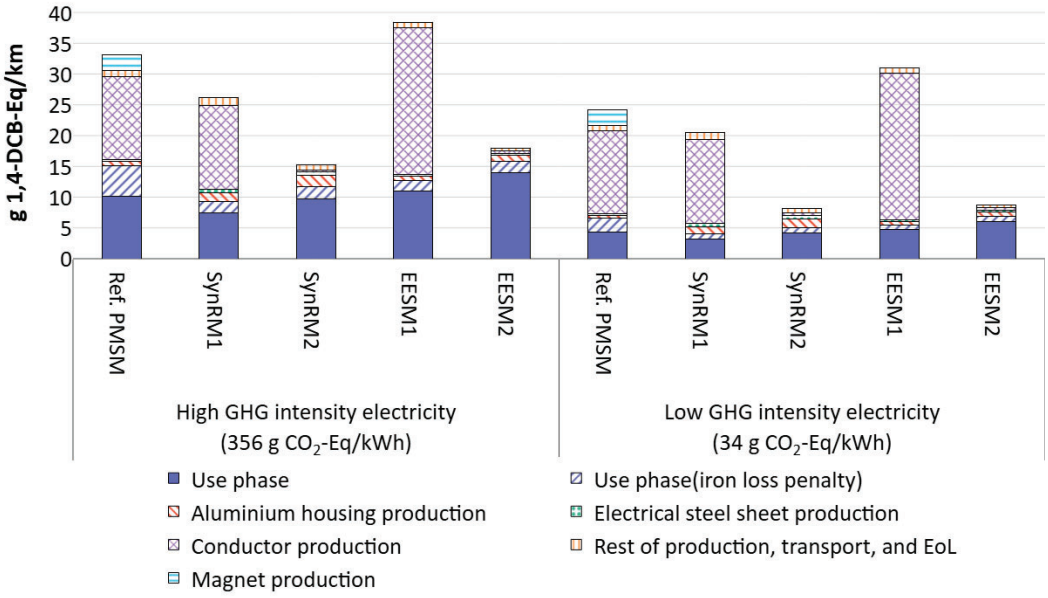

(b) Green manufacturing.

Figure 5.21: ReCiPe 1.03 midpoint results for non-carcinogenic human toxicity.

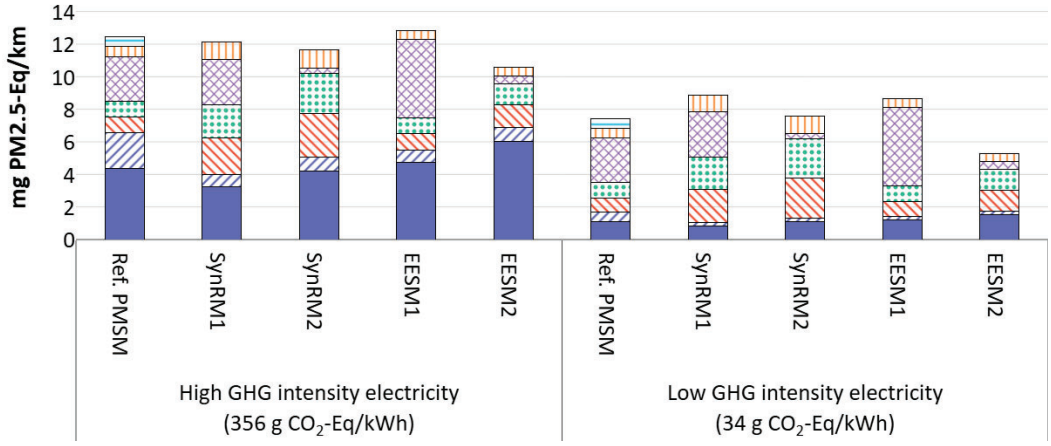

(a) Base case.

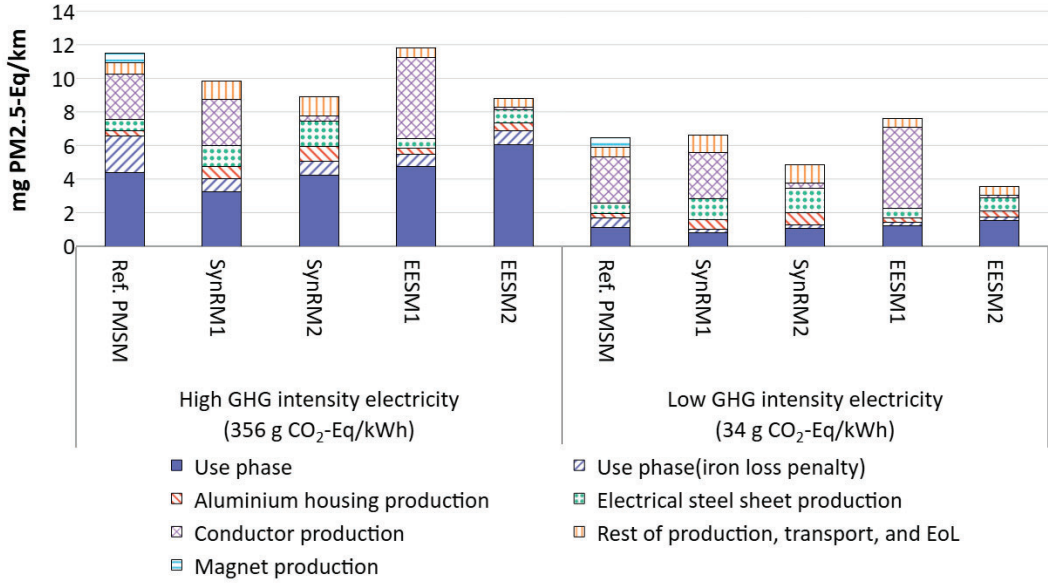

(b) Green manufacturing.

Figure 5.22: ReCiPe 1.03 midpoint results for particulate matter formation potential.

CHAPTER 6

Overall comparison of LCA results

6.1 Technical performance

Table 6.1 presents a comparative overview of the key technical parameters across all technical options in this study, including IMs (IM1–IM3), SynRMs (SynRM1–SynRM2), EESMs (EESM1–EESM2), and Ref. PMSM. The metrics evaluated encompass active length, maximum torque, maximum power, base speed, and power density both in terms of mass (kW/kg) and volume (kW/L).

From the data, it is evident that the PMSM serves as a benchmark with balanced performance across all categories, which exhibits the highest volumetric power density (25.1 kW/L), suggesting its suitability for applications where compactness is critical. Followed by the Cu-based e-machines, EESM1 and IM1 with volumetric power densities over 20 kW/L.

The e-machines with rotor windings, IMs and EESMs show a progressive increase in active length with the increasing use of Al as conductors. However, their power densities remain moderate compared to SynRMs. Two SynRM options, although trailing in power output and power density, maintain competitive torque levels and consume the least energy.

Table 6.1: Key technical performances of all technical options.

Machines	**Ref. PMSM**	**IM1**	**IM2**	**IM3**	**SynRM1**	**SynRM2**	**EESM1**	**EESM2**
Active length $[mm]$	127	158	178	218	272	330	150	180
Conductor or magnet material in stator / rotor	Cu / Nd(Dy)FeB	Cu / Cu	Cu / Al	Al / Al	Cu / -	Al / -	Cu / Cu	Al / Al
Max. torque $[Nm]$	239	242	239	242	242	244	239	239
Max. power at base speed $430V_{dc}[kW]$	100	101	100	101	92	93	100	100
Base speed $[rpm]$	4000	4000	4000	4000	3600	3600	4000	4000
Power density $[kW/kg]$	2.2	1.7	1.6	1.4	1.1	1.0	1.9	1.8
Power density $[kW/L]$	25.1	20.2	18.1	14.8	10.8	9.0	21.3	17.7
Life cycle energy loss due to e-machine $[kWh]$ $(f_{fe} = 1.7)$	4240	3914	4209	4530	2745	3347	3797	4410

Figure 6.1 presents the comparative analysis of material composition across all technical options considered in this study. Electrical steel constitutes the predominant material in all machine types, reflecting its critical role in magnetic flux conduction and core structure. Aluminum follows as the second most significant material, primarily used in housing components. The remaining materials, including copper, stainless steel, and various coatings, collectively account for less than 20% of the total machine weight.

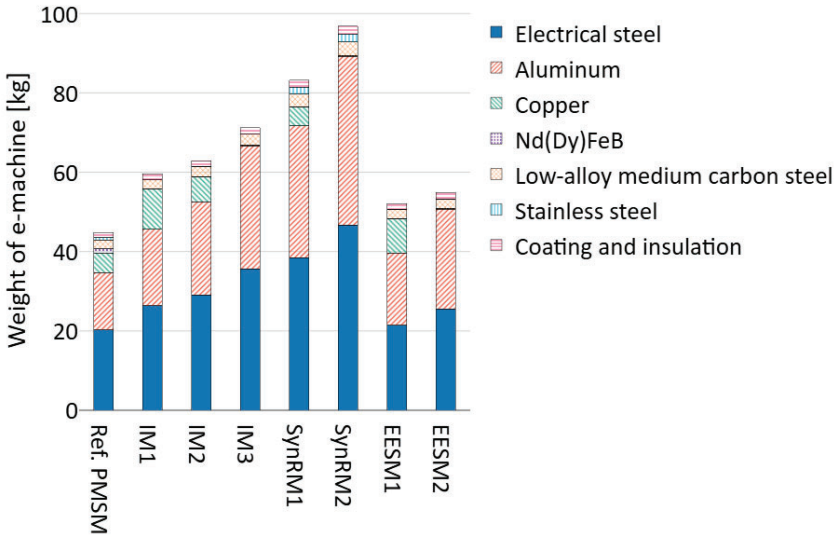

Figure 6.1: Comparison of material composition in all technical options.

Figure 6.2 presents a detailed breakdown of life cycle energy consumption due to the e-machine for all technical options. The losses are categorized into ohmic loss, iron loss (FEM), iron loss (proc+PWM), other losses, and road load. Ohmic loss originates from the internal resistance of conductors and reflects resistive heating in both stator and rotor windings. Iron loss (FEM) is calculated using finite element method simulations, capturing core losses under ideal magnetic conditions. Iron loss (proc+PWM) represents additional core losses induced by manufacturing processes and PWM excitation, and is estimated using the iron loss factor f_{fe}. Other losses include bearing friction and losses associated with the rotor cooling system and brushes. Road load reflects the extra energy required to carry the machine's weight during the EV operation.

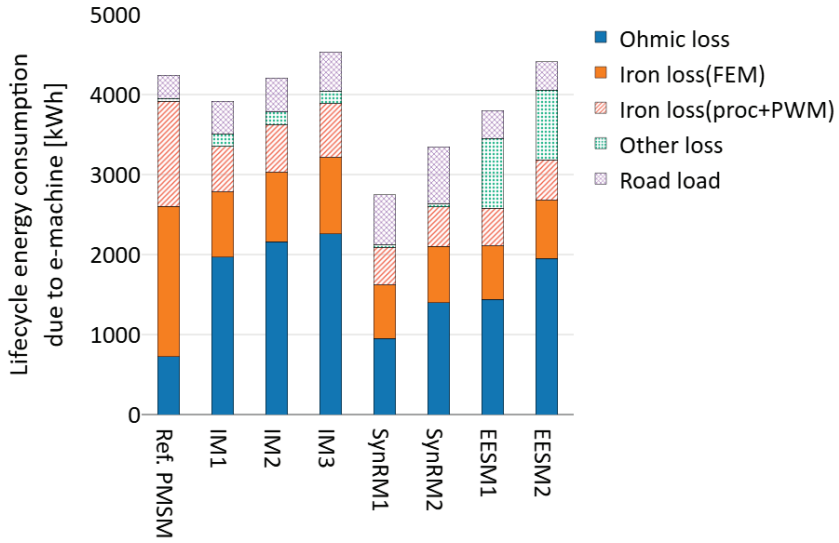

Figure 6.2: Comparison of energy composition due to the e-machine in all technical options for life cycle.

Regarding ohmic loss, the Ref. PMSM demonstrates the lowest one, benefiting from the inherent rotor field provided by permanent magnets, which eliminates the need for rotor excitation and associated resistive losses. The two SynRM configurations follow closely, generating torque through their salient pole structure without the presence of rotor bars or windings, thereby minimizing resistive losses in the rotor. In contrast, the EESM and IM options exhibit significantly higher ohmic losses. This is particularly pronounced in the IM and EESM configurations, where the presence of rotor bars or windings and the use of aluminum conductors contribute to elevated resistive losses over the machine's operational life.

For iron loss, all REE-free options exhibit a comparable level of iron loss; however, the Ref. PMSM shows around twice the iron loss compared to the other configurations. This is primarily due to the generation of back EMF in PMSMs, which contributes to additional iron losses during no-load and low-load conditions, where the operating points of WLTC usually sit. Furthermore, the Ref. PMSM is therefore also more sensitive to adjustments introduced by the iron loss factor f_{fe}, which accounts for losses induced by PWM excitation and manufacturing processes, making the total loss of Ref.

PMSM becoming the third least efficient option.

For other losses, IM and EESM options, which require a rotor hollow-shaft cooling system, exhibit noticeably higher values than the rest. However, this trade-off is justified, as the increase from the cooling system is less than 5%. Moreover, these features effectively eliminate ohmic loss and prevent rotor overheating, thereby enhancing thermal reliability and operational safety. Additionally, EESM machines incur significant brush-related losses from the excitation system, which relies on mechanical contact through brushes and slip rings, accounting for 17-20% of the total e-machine-induced energy consumption.

Regarding road load, SynRMs have the highest road load contribution, exceeding 25% of total e-machine-induced energy consumption due to their substantially higher weight compared to other options.

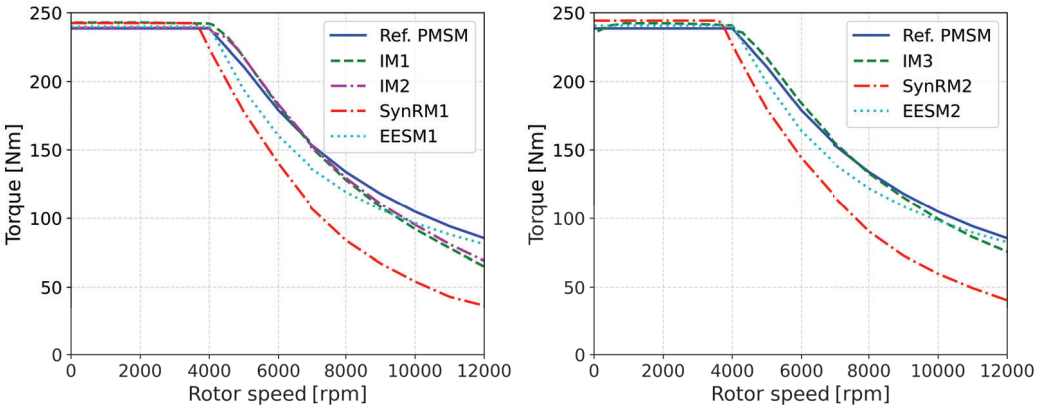

(a) E-machines with Cu windings.

(b) Ref. PMSM and e-machines with Al windings.

Figure 6.3: Comparison of maximum torque envelope.

Figure 6.3 illustrates the maximum torque characteristics as a function of rotor speed for all e-machine options: (a) e-machines with Cu windings and (b) Ref. PMSM and e-machines with Al windings. All e-machines maintain a relatively constant torque output up to approximately 4000 rpm, beyond which a notable decline is observed. Among the configurations, Ref. PMSM demonstrates superior performance, sustaining higher torque levels at elevated speeds. In contrast, SynRMs exhibit more pronounced torque degradation

beyond the base speed. EESMs and IMs exhibit moderate performance, with IMs behaving similarly to those in the Ref. PMSM at medium speed and EESMs getting closer to the Ref. PMSM at high speed. This behavior reflects the inherent differences in excitation mechanisms and magnetic structure, with PMSM benefiting from permanent magnet excitation, EESM1 from active field control, and IMs from induced field, all contributing to improved field-weakening capability, also known as constant power-speed range ability.

6.2 Environmental performance

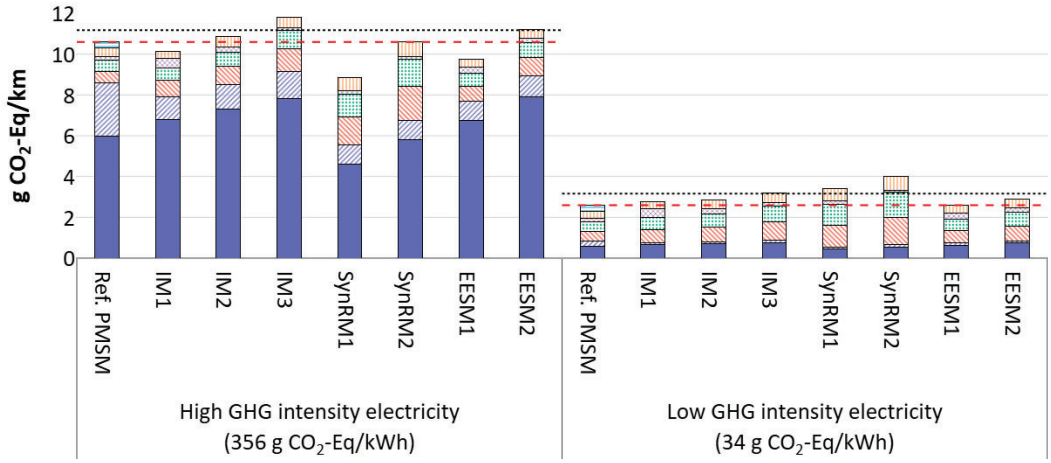

(a) Base case.

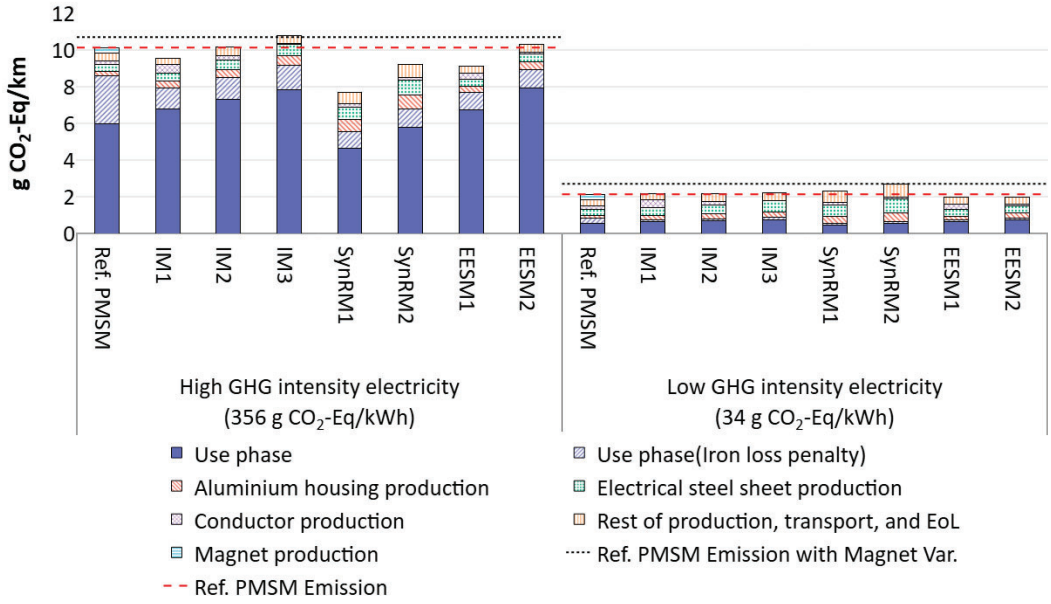

(b) Green manufacturing.

Figure 6.4: Comparison of the global warming potential (GWP100) for all technical options under two scenarios: (a) base case and (b) green manufacturing.

Figure 6.4 shows the global warming potential (GWP100) results based

on the IPCC 2021 methodology for all technical options evaluated in this study under two manufacturing scenarios. Panel (a) represents the base case scenario, while panel (b) illustrates the green manufacturing scenario. The two scenarios correspond to high and low GHG electricity intensities, respectively. In each plot, the total emissions of the reference PMSM are indicated by a red dashed benchmark line, serving as a reference for comparative assessment across configurations. Additionally, the effect of a 200% variation in magnet production is represented by a black dotted benchmark line.

In the base case manufacturing scenario with high-GHG electricity intensity, the REE-free options with Al conductors generally perform worse than the Ref. PMSM, primarily due to their high ohmic losses and low power density. An exception is SynRM2, which benefits from its high efficiency. After applying the green manufacturing scenario, still under high-GHG electricity intensity, the influence of power density is reduced. As a result, IM2 becomes comparable to the Ref. PMSM, while SynRM2 clearly outperforms the Ref. PMSM in terms of global warming potential. When considering a 200% variation in magnet production, IM2 outperforms the reference PMSM in both manufacturing scenarios. Moreover, the Al rotor winding options, IM3 and EESM2, become comparable under green manufacturing.

Under low GHG electricity intensity, carbon emissions from the production phase become the largest contributor to the overall global warming potential. As a result, only one REE-free option with higher power density, EESM1, is comparable to the reference PMSM. After applying the green manufacturing scenario, still under low GHG electricity intensity, the influence of power density is further reduced. Consequently, all REE-free alternatives become comparable to the reference PMSM, except for the SynRM options, which remain less favorable due to their significantly lower power densities, nearly half that of the reference PMSM. When considering a 200% variation in magnet production, all REE-free options become comparable to the reference PMSM under green manufacturing.

Figure 6.4 presents the crustal scarcity potential (CSP), an indicator of long-term resource sustainability, calculated using the Crustal Scarcity Indicator 2020 method for all technical options evaluated in this study under two manufacturing scenarios. Panel (a) shows the base case scenario, while panel (b) illustrates the green manufacturing scenario. These scenarios differ in electricity intensity: the former is characterized by high-GHG electricity,

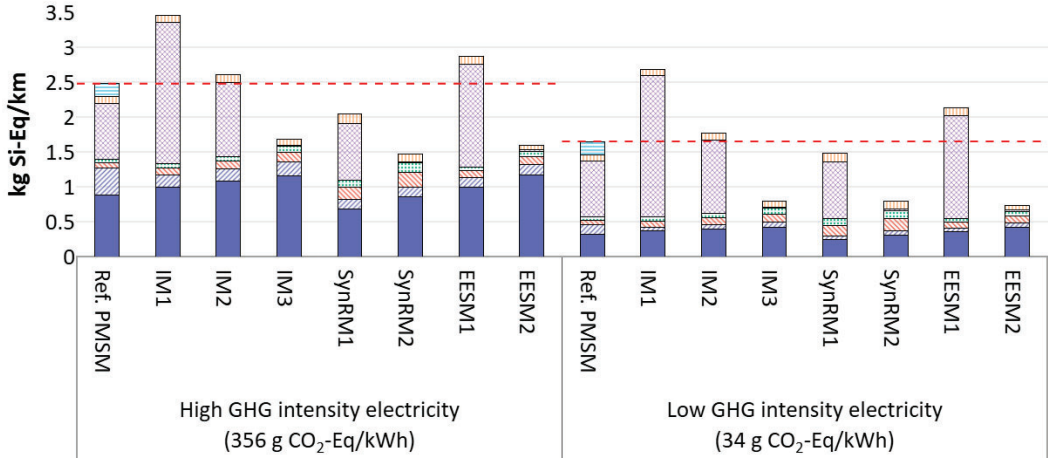

(a) Base case.

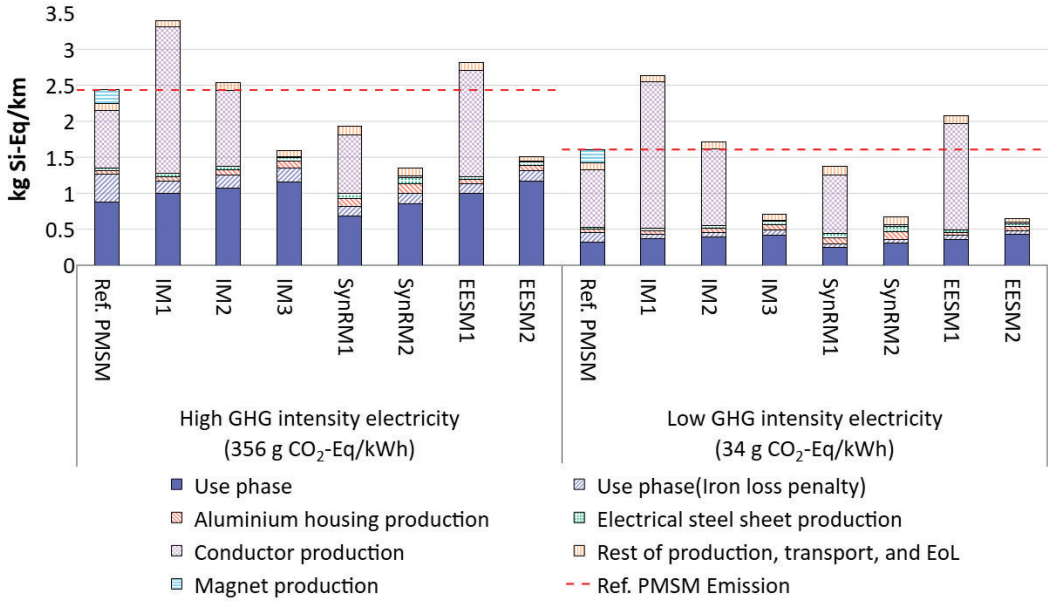

(b) Green manufacturing.

Figure 6.5: Comparison of the crustal scarcity potential (CSP) for all technical options under two scenarios: (a) base case and (b) green manufacturing.

and the latter by low-GHG electricity. In each plot, the total emission of the Ref. PMSM is indicated by a dashed benchmark line, providing a reference for comparative assessment across configurations.

The results clearly show that Cu usage is the dominant contributor to CSP across all technical options in both scenarios with high- and low-GHG electricity. Consequently, the two options with Al windings, IM3, SynRM2, and EESM2, achieve the lowest CSP values and therefore represent the most resource-sustainable choices.

CHAPTER 7

Concluding Remarks and Future Work

7.1 Concluding Remarks

This work has presented a comprehensive evaluation of representative automotive electric traction machines that do not rely on REEs, using FEM simulations and LCA to assess their technical and environmental performance relative to a Ref. PMSM with REE-magnets. The study encompassed multiple configurations of IMs, SynRMs, and EESMs, incorporating variations in conductor materials, namely, Al and Cu.

Initially, to develop IM design tools, a new methodology was proposed to identify the equivalent circuit parameters of IMs, specifically targeting applications involving varying rotor speeds. This approach leverages FEM simulations under different slip conditions and was benchmarked against a conventional method described in [6]. Simulation results and experimental validation demonstrated that the proposed method provides more accurate torque predictions, with discrepancies within 5% and 10%, respectively, across a range of operating speeds. Compared to the conventional method, the observed improvement of 5% to 30% indicates its enhanced suitability for variable-speed applications relative to traditional parameter extraction techniques.

Coming back to the technical comparisons, the two SynRM configurations achieve the highest life-cycle efficiency, generating the least losses over 200,000 km under WLTC conditions. However, they suffer from low power density and poor field-weakening capability, which could be observed in Figure 6.3. The other Cu-based machines (Ref. PMSM, IM1, and EESM1) exhibit decent life-cycle efficiency, characterized by high power density and field-weakening capabilities. IM2, which combines Cu and Al conductors, follows closely, while IM3 and EESM2, both using Al rotor conductors, are the least efficient but maintain acceptable power density and similar field-weakening characteristics with their Cu-based counterparts.

In terms of GHG emissions, when the base case assumes an EV charged with high-GHG electricity, the use phase dominates the life cycle (accounting for 60–80%), favoring more efficient e-machines. Under this scenario, SynRM1, EESM1, and IM1 emit less GHG than the Ref. PMSM, followed by SynRM2 and IM2, which are comparable to the benchmark. In contrast, the fully Al-based options, EESM2 and IM3, result in higher GHG emissions than the Ref. PMSM. When the base case assumes low-GHG electricity, the production stage becomes the primary contributor (70–80%), making power density a more critical factor. In this scenario, only EESM1 outperforms the Ref. PMSM, followed closely by IM1, EESM2, and IM2. The options with power density below 1.5, including IM3, SynRM1, and SynRM2 (see Table 6.1), perform the worst in terms of GHG emissions.

Beyond the base case comparisons, the study also investigated strategies to reduce GHG emissions through green manufacturing practices further. These included the use of green virgin Al and improved material utilization during the punching of electrical steel sheets. All machine types benefited from these strategies, achieving at least a 4% reduction in GHG emissions under high-GHG electricity and up to 18% under low-GHG electricity. The greatest relative improvements were observed in machines with lower power density, such as SynRM1 (13% and 32%), SynRM2 (13% and 34%), and IM3 (8% and 31%) in high- and low-GHG electricity scenarios, respectively. Under the high-GHG electricity scenario, SynRM1, EESM1, SynRM2, and IM1 produced lower GHG emissions than the Ref. PMSM. Additionally, IM2 and EESM2 showed comparable performance to the benchmarking option, while only IM3 resulted in higher emissions. In contrast, under the low-GHG electricity scenario, all options performed similarly to the Ref. PMSM in terms of GHG

emissions, except for SynRM2, which exhibited slightly higher emissions.

Generally, Cu-based configurations outperform their Al-based counterparts in terms of efficiency and power density, leading to lower GHG emissions. However, Cu conductor production is identified as a key concern in terms of acidification, toxicity, and long-term resource scarcity, leading to three full Al-based options being found to perform better in the related categories.

Furthermore, the consideration of iron loss penalties arising from manufacturing processes and PWM feeding highlights the importance of accurate iron loss estimation in the overall performance evaluation of e-machines for EV applications. This aspect is especially critical when comparing different types of e-machines and optimizing designs for both energy efficiency and environmental sustainability.

In the previous findings [23], the magnet production chain contributes around 3% and 12% to the overall GHG emissions of the PMSM with Nd(Dy)FeB magnets at high- and low-GHG electricity for charging EV, respectively. Consistent with this, the baseline results suggest that magnet production is not a major contributor to GHG emissions, primarily due to the relatively low mass share of magnets. However, sensitivity analysis revealed that under certain conditions, particularly in low-carbon electricity scenarios, where the magnet production contributes 28% of all GHG emissions of Ref. PMSM, which alters the conclusion that the Al-based e-machine emits less GHG than the benchmarking target (See Figure 4.34 and Figure 6.4). Due to the variability observed and the impact of the selected REE supply route, it is advisable for the LCA of EV traction e-machines using REE magnets to include sensitivity analyses. This approach helps ensure that the study's conclusions remain reliable across different data sources and assumptions.

Overall, the results underscore the importance of considering both environmental and technical criteria in e-machine selection for EV applications. The integration of sustainable materials and manufacturing practices is shown to be as critical as achieving high efficiency and power density in future e-machine designs.

7.2 Future Work

Building upon the insights gained in this study, several directions for future research are proposed further to advance the development of sustainable and

high-performance automotive e-machines:

- **Iron Loss Characterization:** Given the significance of iron loss penalties due to manufacturing and PWM feeding, future work should focus on refining iron loss estimation techniques, including empirical validation and integration with control strategies.
- **Impact of Segmented Laminations:** Segmented Laminations can improve the punching process by reducing the material loss rate, thereby enhancing the environmental performance of e-machines. However, there is a risk of increasing iron loss due to the cutting-edge effect. Moreover, the mechanical strength could decrease. Future work should investigate these trade-offs through simulation and experimental validation.
- **Conductor Material:** To address the environmental concerns associated with Cu production, further exploration of alternative conductor materials and winding techniques is recommended. For example, optimizing Al hair-pin winding designs could help balance efficiency and sustainability. Additionally, improving Cu mining practices, particularly in waste handling, is essential to reduce long-term environmental burdens [102], [103].
- **Green Manufacturing Integration:** Expanding the scope of green manufacturing strategies, such as improved recycling processes for Al, Cu, and electrical steel, could further reduce the environmental footprint of e-machine production.
- **Lifecycle-Based Design Optimization:** Incorporating full lifecycle data into multi-objective optimization frameworks of e-machines would enable simultaneous consideration of efficiency, cost, and environmental impact during the design phase.
- **System-Level Evaluation:** Future LCA studies could investigate the interaction between e-machines and other EV subsystems, including power electronics and thermal management, to support holistic system-level optimization.

References

[1] IPCC, "Transport," in *Climate Change 2022 - Mitigation of Climate Change: Working Group III Contribution to the Sixth Assessment Report of the Intergovernmental Panel on Climate Change*. Cambridge University Press, 2023, pp. 1049–1160.

[2] IEA, "Tracking clean energy progress 2023," IEA, Tech. Rep., 2023.

[3] C. R. Forsythe, K. T. Gillingham, J. J. Michalek, and K. S. Whitefoot, "Technology advancement is driving electric vehicle adoption," *Proceedings of the National Academy of Sciences*, vol. 120, no. 23, e2219396120, 2023.

[4] Z. Cao, A. Mahmoudi, S. Kahourzade, and W. L. Soong, "An overview of electric motors for electric vehicles," in *2021 31st Australasian Universities Power Engineering Conference (AUPEC)*, 2021, pp. 1–6.

[5] IEA, "Road transport," IEA, Tech. Rep., 2023.

[6] "Ieee standard test procedure for polyphase induction motors and generators," *IEEE Std 112-2017 (Revision of IEEE Std 112-2004)*, 2018.

[7] A. Bonnett and G. Soukup, "Nema motor-generator standards for three-phase induction motors," *IEEE Industry Applications Magazine*, vol. 5, no. 3, pp. 49–63, 1999.

[8] L. Alberti, N. Bianchi, and S. Bolognani, "Variable-speed induction machine performance computed using finite-element," *IEEE Transactions on Industry Applications*, vol. 47, no. 2, pp. 789–797, 2011.

[9] M. Carraro and M. Zigliotto, "Automatic parameter identification of inverter-fed induction motors at standstill," *IEEE Transactions on Industrial Electronics*, vol. 61, no. 9, pp. 4605–4613, 2014.

[10] E. Mölsä, S. E. Saarakkala, M. Hinkkanen, A. Arkkio, and M. Routimo, "A dynamic model for saturated induction machines with closed rotor slots and deep bars," *IEEE Transactions on Energy Conversion*, vol. 35, no. 1, pp. 157–165, 2020.

[11] D. Lin, P. Zhou, and Z. Zhang, "Reduced order modeling and parameter identification of induction motors based on fea solutions," *IEEE Transactions on Energy Conversion*, vol. 38, no. 2, pp. 1108–1117, 2023.

[12] R. Thomas, H. Husson, L. Garbuio, and L. Gerbaud, "Comparative study of the tesla model s and audi e-tron induction motors," in *2021 17th Conference on Electrical Machines, Drives and Power Systems (ELMA)*, 2021, pp. 1–6.

[13] T. Schuhmann, B. Cebulski, and S. Paul, "Comparison of time-harmonic and transient finite element calculation of a squirrel cage induction machine for electric vehicles," in *2014 International Conference on Electrical Machines (ICEM)*, 2014, pp. 1037–1043.

[14] H. Schillingmann, S. Gehler, and M. Henke, "Life cycle assessment of electrical machine production considering resource requirements and sustainability," in *2021 11th International Electric Drives Production Conference (EDPC)*, 2021, pp. 1–7.

[15] B. Cassoret, J.-P. Manata, V. Mallard, and D. Roger, "Comparative life cycle assessment of induction machines made with copper-cage or aluminium-cage rotors," *IET Electric Power Applications*, vol. 13, pp. 712–719, 2019.

[16] A. Rassõlkin, A. Belahcen, A. Kallaste, *et al.*, "Life cycle analysis of electrical motor-drive system based on electrical machine type," *Proceedings of the Estonian Academy of Sciences*, 2020.

[17] D. F. de Souza, J. Fong, C. Hernandez, *et al.*, "Environmental impacts of electric motor technologies: Life cycle approach based on eup ecoreport," *Environmental Impact Assessment Review*, vol. 111, p. 107 741, 2025, ISSN: 0195-9255.

[18] R. Wrobel, M. Ali Rajaeifar, and B. Mecrow, "Life cycle assessment of electrical machines – a case study," in *2024 IEEE Energy Conversion Congress and Exposition (ECCE)*, 2024, pp. 5611–5618.

[19] A. Antonacci, A. Giraldi, E. Innocenti, and M. Delogu, "A scientific approach for environmental analysis: An asynchronous electric motor case study for stand-by applications," *Machines*, vol. 11, no. 8, 2023, ISSN: 2075-1702.

[20] X. Zhang, Z. Xu, F. Zhang, *et al.*, "Carbon emission evaluation and comparison for different electric machines," in *2024 27th International Conference on Electrical Machines and Systems (ICEMS)*, 2024, pp. 3158–3164.

[21] S. Mafrici, A. Accardo, E. Spessa, and A. Tenconi, "A novel scenario analysis framework for the life cycle assessment of permanent magnet synchronous motors for electric vehicles," *IEEE Access*, vol. 12, pp. 156 837–156 848, 2024.

[22] S. Mafrici, V. Madonna, C. Maria Meano, K. Friis Hansen, and A. Tenconi, "Switched reluctance machine for transportation and eco-design: A life cycle assessment," *IEEE Access*, vol. 12, pp. 68 334–68 344, 2024.

[23] A. Nordelöf, E. Grunditz, S. Lundmark, A.-M. Tillman, M. Alatalo, and T. Thiringer, "Life cycle assessment of permanent magnet electric traction motors," *Transportation Research Part D: Transport and Environment*, vol. 67, pp. 263–274, 2019, ISSN: 1361-9209.

[24] A. Schreiber, J. Marx, and P. Zapp, "Life cycle assessment studies of rare earths production - findings from a systematic review," *Science of The Total Environment*, vol. 791, p. 148 257, 2021, ISSN: 0048-9697.

[25] A. Nordelöf and A. Bongards, "Allocating the environmental burdens in co-production of rare earth elements for ev magnets," in *EVS38 International Battery, Hybrid and Fuel Cell Electric Vehicle Symposium, 2025*, 2025.

[26] M. F. Elnaggar, A. Flah, C. Z. El-Bayeh, and M. M. Alrashed, "Optimized foc control strategy for dual stators permanent magnet machine," *Scientific Reports*, vol. 15, 2025, ISSN: 2045-2322.

[27] Matlab. "Tune field-oriented controllers using closed-loop pid autotuner block." (), [Online]. Available: `https://www.mathworks.com/help/slcontrol/ug/tune-field-oriented-controllers-using-closed-loop-pid-autotuner-block.html`.

[28] S.-K. Sul, "Vector control [1 and 2]," in *Control of Electric Machine Drive Systems*. John Wiley & Sons, Ltd, 2010, ch. 5, pp. 230–282, ISBN: 9780470876541.

[29] S.-K. Sul, "Reference frame transformation and transient state analysis," in *Control of Electric Machine Drive Systems*. John Wiley & Sons, Ltd, 2010, ch. 3, pp. 230–282, ISBN: 9780470876541.

[30] L. Harnefors, *Control of variable-speed drives*. Applied Signal Processing and Control, Department of Electronics, Mälardalen University, 2002.

[31] T. R. Hawkins, O. M. Gausen, and A. H. Strømman, "Environmental impacts of hybrid and electric vehicles—a review," *The International Journal of Life Cycle Assessment*, vol. 17, pp. 997–1014, 2012.

[32] F. Uberti, L. Frosini, and L. Szabó, "A new design procedure for rotor laminations of synchronous reluctance machines with fluid shaped barriers," *Electronics*, vol. 11, no. 1, 2022, ISSN: 2079-9292.

[33] J. Tang, "Design and control of electrically excited synchronous machines for vehicle applications," Ph.D. dissertation, Chalmers University of Technology, 2021.

[34] R. Manko, M. Vukotić, D. Makuc, D. Vončina, D. Miljavec, and S. Čorović, "Modelling of the electrically excited synchronous machine with the rotary transformer design influence," *Energies*, vol. 15, no. 8, 2022, ISSN: 1996-1073.

[35] *Environmental management – life cycle assessment – principles and framework*, International Organization for Standardization, 2006.

[36] *Environmental management – life cycle assessment – requirements and guidelines*, International Organization for Standardization, 2006.

[37] M. A. Huijbregts, Z. J. Steinmann, P. M. Elshout, *et al.*, "Recipe2016: A harmonised life cycle impact assessment method at midpoint and endpoint level," *The International Journal of Life Cycle Assessment*, vol. 22, pp. 138–147, 2017.

[38] A. Nordelöf, M. Messagie, A.-M. Tillman, M. Ljunggren Söderman, and J. Van Mierlo, "Environmental impacts of hybrid, plug-in hybrid, and battery electric vehicles—what can we learn from life cycle assessment?.," *Int. J. Life Cycle Assess.*, vol. 19, pp. 1866–1890, 2014.

[39] A. Nordelöf, S. Poulikidou, M. Chordia, F. Bitencourt de Oliveira, J. Tivander, and R. Arvidsson, "Methodological approaches to end-of-life modelling in life cycle assessments of lithium-ion batteries," *Batteries*, vol. 5, no. 3, 2019.

[40] B. Weidema, C. Bauer, R. Hischier, *et al.*, "The ecoinvent database: Overview and methodology, data quality guideline for the ecoinvent database version 3," *Zürich: Ecoinvent Center Retrieved (Der folgende Link führt zur zuvor genannten Veröffentlichung: www ecoinvent org)*, 2013.

[41] G. Wernet, C. Bauer, B. Steubing, J. Reinhard, E. Moreno-Ruiz, and B. Weidema, "The ecoinvent database version 3 (part i): Overview and methodology," *The International Journal of Life Cycle Assessment*, vol. 21, pp. 1218–1230, 2016.

[42] M. Grohol and C. Veeh, *Study on the Critical Raw Materials for the EU 2023*. Publications Office of the European Union, 2023.

[43] IEA, "Executive summary – electricity 2024," IEA, Tech. Rep., 2024.

[44] Y. Dong, M. U. Hossain, H. Li, and P. Liu, "Developing conversion factors of lcia methods for comparison of lca results in the construction sector," *Sustainability*, vol. 13, no. 16, 2021, ISSN: 2071-1050.

[45] P. Arias, N. Bellouin, E. Coppola, *et al.*, "Technical summary," in *Climate Change 2021: The Physical Science Basis. Contribution of Working Group I to the Sixth Assessment Report of the Intergovernmental Panel on Climate Change*, V. Masson-Delmotte, P. Zhai, A. Pirani, *et al.*, Eds. Cambridge, United Kingdom and New York, NY, USA: Cambridge University Press, 2021, pp. 33–144.

[46] R. Arvidsson, M. L. Söderman, B. A. Sandén, A. Nordelöf, H. André, and A.-M. Tillman, "A crustal scarcity indicator for long-term global elemental resource assessment in lca," *The International Journal of Life Cycle Assessment*, vol. 25, pp. 1805–1817, 2020.

[47] M. Chordia, *Taking stock of large-scale lithium-ion battery production using life cycle assessment*. Chalmers Tekniska Hogskola (Sweden), 2022.

[48] E. A. Grunditz and T. Thiringer, "Performance analysis of current bevs based on a comprehensive review of specifications," *IEEE Transactions on Transportation Electrification*, vol. 2, no. 3, pp. 270–289, 2016.

[49] T. D. Gillespie, S. Taheri, C. Sandu, and B. L. Duprey, *Fundamentals of Vehicle Dynamics*. SAE International, 2021.

[50] E. A. Grunditz, T. Thiringer, J. Lindström, S. Tidblad Lundmark, and M. Alatalo, "Thermal capability of electric vehicle pmsm with different slot areas via thermal network analysis," *eTransportation*, vol. 8, p. 100 107, 2021, ISSN: 2590-1168.

[51] M. Andersson, M. Ljunggren Söderman, and B. A. Sandén, "Are scarce metals in cars functionally recycled?" *Waste Management*, vol. 60, pp. 407–416, 2017, Special Thematic Issue: Urban Mining and Circular Economy, ISSN: 0956-053X.

[52] A. Nordelöf, A.-M. Tillman, E. Grunditz, M. Thiringer Torbjörn, and M. Alatalo, "A scalable life cycle inventory of an electrical automotive traction machine—part i: Design and composition," *Int. J. Life Cycle Assess.*, vol. 23, pp. 55–69, 2018.

[53] A. Nordelöf and A.-M. Tillman, "A scalable life cycle inventory of an electrical automotive traction machine—part ii: Manufacturing processes," *Int. J. Life Cycle Assess.*, vol. 23, pp. 295–313, 2018.

[54] IEA, *Electricity generation by source, europe, 1990-2022*, Dec. 2023.

[55] Ecoinvent, *Energy*, Dec. 2023.

[56] IEA, *Electricity generation by source, norway, 1990-2023*, Dec. 2023.

[57] IEA, *Electricity generation by source, china (p.r. of china and hong kong, china), 1990-2022*, Dec. 2023.

[58] Z. Li, A. S. Hamidi, Z. Yan, *et al.*, "A circular economy approach for recycling electric motors in the end-of-life vehicles: A literature review," *Resources, Conservation and Recycling*, vol. 205, p. 107 582, 2024, ISSN: 0921-3449.

[59] T. Thiringer, "Measurements and modelling of low-frequency disturbances in induction machines," Ph.D. dissertation, Chalmers University of Technology, 1996.

[60] M. Nachtsheim, J. Ernst, C. Endisch, and R. Kennel, "Performance of recursive least squares algorithm configurations for online parameter identification of induction machines in an automotive environment," *IEEE Transactions on Transportation Electrification*, vol. 9, no. 3, pp. 4236–4254, 2023.

[61] E. Armando, A. Boglietti, F. Mandrile, E. Carpaneto, and S. Rubino, "A detailed analysis and guidelines for the induction motor flux-decay test," *IEEE Transactions on Industry Applications*, vol. 60, no. 1, pp. 123–131, 2024.

[62] O. Wallmark, *AC Machine Analysis Fundamental Theory*. Department of Eletrical Conversion, KTH Royal Institution of Technology, 2020, pp. 24–25.

[63] M.-J. Hsieh, T. Thiringer, and E. A. Grunditz, "Improved parametric representation of im from fem for more accurate torque predictions," in *2022 International Conference on Electrical Machines (ICEM)*, 2022, pp. 599–605.

[64] G. Kylander, "Temoeraturmätningar på en 15 kw asynkronmotor," Chalmers Tekniska Högskola, Tech. Rep., 1991.

[65] A. Acquaviva, S. Skoog, E. Grunditz, and T. Thiringer, "Electromagnetic and calorimetric validation of a direct oil cooled tooth coil winding pm machine for traction application," *Energies*, vol. 13, no. 13, 2020, ISSN: 1996-1073.

[66] A. Krings, S. Nategh, A. Stening, H. Grop, O. Wallmark, and J. Soulard, "Measurement and modeling of iron losses in electrical machines," in *5th International Conference Magnetism and Metallurgy WMM 2012*, 2012.

[67] W. Tong, *Mechanical Design and Manufacturing of Electric Motors*. CRC PRESS, 2022.

[68] S. Evans. "Electric cars, explained: How porsche, mercedes-benz and audi build evs." (2019-11-10), [Online]. Available: https://robbreport.com/motors/cars/how-do-electric-cars-work-heres-how-porsche-mercedes-benz-and-audi-build-evs-2879081/.

[69] D. T. Peters, J. G. Cowie, and E. F. Brush, "Die casting copper motor rotors: Mold materials and processing for cost-effective manufacturing," in *Energy Efficiency Improvements in Electronic Motors and Drives*, Berlin, Heidelberg: Springer Berlin Heidelberg, 2000, pp. 39–51, ISBN: 978-3-642-59785-5.

[70] V. Voggeser, M. Wolf, T. Schuhmann, and J. Liebold, "Investigation on the mechanical and electromagnetical performance of a squirrel cage induction machine with radially laser welded end ring connections," in *2015 5th International Electric Drives Production Conference (EDPC)*, 2015, pp. 1–8.

[71] M. González, "Refreedrive - lca technologies analyses," Fundación Cidaut, Tech. Rep., 2020.

[72] J. S. Agapiou, "Development on die-cast copper motor rotors – casting considerations," *Manufacturing Letters*, vol. 33, pp. 310–321, 2022, 50th SME North American Manufacturing Research Conference (NAMRC 50,2022), ISSN: 2213-8463.

[73] K. James L., S. Richard F., P. Dale T., and B. Edwin F., "The case for induction motors with die-cast copper rotors for high efficiency traction motors," SAE International, Tech. Rep., 2009.

[74] L. Pryor, R. Schlobohm, and B. Brownell, "A comparison of aluminum vs. copper as used in electrical equipment," *GE Consumer and Industrial*, pp. 1–7, 2008.

[75] R. Arvidsson, M. Chordia, S. Wickerts, and A. Nordelöf, "Implementation of the crustal scarcity indicator into life cycle assessment software," *Chalmers University of Technology, Gothenburg*, 2020.

[76] Wellste. "Understanding the electrical conductivity of aluminum." (2023-12-14), [Online]. Available: https://www.wellste.com/electrical-conductivity-of-aluminum/.

[77] A. O'Neill. "Average prices for copper worldwide from 2014 to 2026." (2025-07), [Online]. Available: https://www.statista.com/statistics/675854/average-prices-copper-worldwide/.

[78] A. O'Neill. "Average prices for aluminum from 2014 to 2026." (2025-07), [Online]. Available: https://www.statista.com/statistics/675845/average-prices-aluminum-worldwide/.

[79] A. Carriero, M. Locatelli, K. Ramakrishnan, G. Mastinu, and M. Gobbi, "A review of the state of the art of electric traction motors cooling techniques," in *WCX World Congress Experience*, SAE International, Apr. 2018.

[80] M. Popescu, D. Staton, A. Boglietti, A. Cavagnino, D. Hawkins, and J. Goss, "Modern heat extraction systems for electrical machines - a review," in *2015 IEEE Workshop on Electrical Machines Design, Control and Diagnosis (WEMDCD)*, 2015, pp. 289–296.

[81] J. Doerr, T. Attensperger, L. Wittmann, and T. Enzinger, "The new electric axle drives from audi," *MTZ worldwide*, vol. 79, pp. 18–25, 2018.

[82] Y. Gai, M. Kimiabeigi, Y. C. Chong, *et al.*, "Pressure loss modelling in a water-cooled hollow-shaft rotor for an automotive traction motor," in *2018 XIII International Conference on Electrical Machines (ICEM)*, 2018, pp. 1297–1302.

[83] Y. Gai, Y. C. Chong, H. Adam, J. Goss, and M. Popescu, "Power losses and thermal analysis of a hollow-shaft rotor cooling system," in *2019 22nd International Conference on Electrical Machines and Systems (ICEMS)*, 2019, pp. 1–6.

[84] SKF. "Bearing friction, power loss and starting torque." (2025), [Online]. Available: https://www.skf.com/uk/products/rolling-bearings/principles-of-rolling-bearing-selection/bearing-selection-process/operating-temperature-and-speed/bearing-friction-power-loss-and-starting-torque (visited on 09/16/2025).

[85] SKF. "Skf catalogue rolling bearings 10000." (2025), [Online]. Available: https://www.skf.com/group/products/rolling-bearings/erratapages/rbc10000 (visited on 09/16/2025).

[86] J. Cowie, D. Peters, E. Brush, and S. Midson, "Materials & modifications to die cast the copper conductors of the induction motor rotor," *Die Casting Engineer*, vol. 45, no. 5, pp. 38–47, 2001.

[87] P. Schiesser, N. Jaouen, J.-B. Martin, D. Dupuis, D. Verlant, and F. Dovergne, "Analyse de cycle de vie comparative entre deux moteurs électriques," Écoeff. and FAVI, Tech. Rep., 2010.

[88] S. Dalquist and T. Gutowski, "Life cycle analysis of conventional manufacturing techniques: Sand casting," in *ASME International mechanical engineering congress and exposition*, vol. 47136, 2004, pp. 631–641.

[89] T. Heinemann, *Energy and resource efficiency in aluminium die casting*. Springer, 2016.

[90] M. Dohi, H. Kamiyama, S.-I. Nishida, Y. Kotani, and H. Watari, "Manufacturing method of increasing hollow steel shaft thickness using uniaxial pressing.," *Applied Mechanics and Materials*, vol. 705, no. 1, pp. 44–50, 2014, ISSN: 16609336.

[91] G. M. GmbH. "Gfu rotorwelle, rotorshaft technology, ev cars, bev cars, umformtechnik, e-drive, umformung, rotor." (2022), [Online]. Available: `https://youtu.be/RCZ_fzqj9vk?si=3vwdIPzuU9zJHSdT`.

[92] F. Mahmouditabar and N. Baker, "A review on the effect of electrical steel manufacturing processes on the performance of electric machines," *Energies*, vol. 16, no. 24, 2023, ISSN: 1996-1073.

[93] P. Jaramillo, S. K. Ribeiro, P. Newman, *et al.*, "Chapter10: Transport, climate change 2022: Mitigation of climate change," Cambridge University Press, Tech. Rep., 2022.

[94] M. A. J. Huijbregts, Z. J. N. Steinmann, P. M. F. Elshout, *et al.*, "Recipe2016: A harmonised life cycle impact assessment method at midpoint and endpoint level - the international journal of life cycle assessment," *SpringerLink*, Jul. 2020.

[95] A. Credo, M. Villani, G. Fabri, and M. Popescu, "Adoption of the synchronous reluctance motor in electric vehicles: A focus on the flux weakening capability," *IEEE Transactions on Transportation Electrification*, vol. 9, no. 1, pp. 805–818, 2023.

[96] B. Ma, Y. Li, J. Zheng, *et al.*, "Multiphysics topology optimization of synrms considering control performance and machinability," *IEEE Transactions on Transportation Electrification*, vol. 11, no. 1, pp. 1287–1297, 2025.

[97] S. Panda, R. K. Keshri, A. Tessarolo, G. Tiwari, and M. Mezzarobba, "Design refinements of synchronous reluctance motor utilising non-magnetic radial ribs for traction applications," *IET Electric Power Applications*, vol. 14, no. 12, pp. 2480–2489, 2020.

[98] G. Mühlberg, "Magnet-free rotor as an emr4 platform option," *MTZ worldwide*, vol. 85, pp. 16–23, 2024.

[99] M. Belcourt. "Bmw's 5th-generation electric drive system wins 2024 ajac best green innovation award." (2024), [Online]. Available: `https://www.press.bmwgroup.com/canada/article/detail/T0440602EN/bmw%E2%80%99s-5th-generation-electric-drive-system-wins-2024-ajac-best-green-innovation-award?language=en` (visited on 11/09/2025).

[100] MERSEN. "Losses in brushes." (2007), [Online]. Available: `https://nuvimek.com/ptt/tds05-losses%20in%20brushes.pdf` (visited on 11/09/2025).

[101] MERSEN. "Carbon brushes for motors and generators." (2024), [Online]. Available: `https://www.mersen.com/sites/default/files/files_imported/2-ptt-carbon-brush-technical-guide-mersen.pdf` (visited on 11/09/2025).

[102] G. Cutuli, D. Barater, S. Nategh, and B. Raghuraman, "Aluminum hairpin solution for electrical machines in e-mobility applications : Part i: Electromagnetic aspects," in *2022 International Conference on Electrical Machines (ICEM)*, 2022, pp. 1770–1776.

[103] B. W. Schipper, H.-C. Lin, M. A. Meloni, K. Wansleeben, R. Heijungs, and E. van der Voet, "Estimating global copper demand until 2100 with regression and stock dynamics," *Resources, Conservation and Recycling*, vol. 132, pp. 28–36, 2018, ISSN: 0921-3449.

Part II

Papers

PAPER A

Improved Parametric Representation of IM from FEM for More Accurate Torque Predictions

Meng-Ju Hsieh, Emma Grunditz, and Torbjörn Thiringer

Published in 2022 International Conference on Electrical Machines (ICEM), pages 599–605, 2022.

The layout has been revised.

Improved Parametric Representation of IM from FEM for More Accurate Torque Predictions

Meng-Ju Hsieh, *Student Member, IEEE* Torbjörn Thiringer, *Senior Member, IEEE* and Emma Arfa Grunditz

2022 International Conference on Electrical Machines (ICEM) | 978-1-6654-1432-6/22/$31.00 ©2022 IEEE | DOI: 10.1109/ICEM51905.2022.9910617

***Abstract*—In this work, an updated methodology to determine the parameters of three-phase induction machines (IMs) is developed and presented. The goal of this determination is for a better representation of machines for the further applications of the parameter-based control system operated with different stator flux linkage levels, such as automotive applications. First, the theory of the T-form model (TFM) and the inverse Γ-form model (IGFM) are reviewed. The former review becomes the brick of the following interpretation of the developing methods for identifying these parameters. Moreover, a 2D electromagnetic finite element method (FEM) model of a 15kW IM is utilized to demonstrate the strength of the methodology on a real machine. Lastly, a comparison of results using the conventional test and the newly proposed method is presented, showing improvement.**

***Index Terms*—induction machine (IM), parameter determination, Finite Element Method (FEM).**

NOMENCLATURE

N_p	Number of pole pairs
N_{pb}	Number of parallel branches of winding connection
N_s	Number of turns per stator coil
c_s	Connection factor; $\sqrt{3}N_{pb}$ for Δ, N_{pb} for Y
Q_s, Q_r	Number of stator and rotor slots
k_1	Winding factor of first-order harmonic
ω_0, ω_1	Synchronous and rotor electrical speed
ω_2	Slip electrical speed, $\omega_2 = \omega_0 - \omega_1$
s	Slip rate, $s = \omega_2/\omega_0$
T_e	Electromagnetic torque
ω_r	Rotor mechanical speed, $\omega_r = \omega_1/N_p$
α-β	Real and imaginary parts of the stator stationary coordinate system, speed: 0
u-v	Real and imaginary parts of the rotor rotational coordinate system, speed: ω_r
d-q	Real and imaginary parts of the stator synchronous rotational coordinate system, speed: ω_0
X	Amplitude of phasor $\underline{x}$ in the α-β coordinate system
X^{uv}	Amplitude of phasor $\underline{x}^{uv}$ in the u-v coordinate system
x^y	y-axis component of phasor $\underline{x}$
$\underline{u}_s, \underline{u}_r$	Stator input and rotor induced voltage phasors
$\underline{u}_{s,ind}, \underline{u}_m$	Stator induced and magnetizing voltage phasor
$\underline{u}^{uv}_{bar,k}$	Induced voltage phasor for rotor bar k at rotor side
$\underline{i}_s, \underline{i}_r, \underline{i}_m$	Stator, rotor, and magnetizing current phasors
$\underline{\psi}_s, \underline{\psi}_r, \underline{\psi}_m$	Stator, rotor, and magnetizing flux linkage phasors
$\underline{\psi}^{uv}_{bar,k}$	Flux linkage phasors for rotor bar k at rotor side
R_s, R_r	Stator and rotor resistance
R^{uv}_{bar}	A single rotor bar resistance at rotor side
L_s, L_r, L_m	Stator, rotor, and magnetizing inductances
$L_{s\lambda}, L_{r\lambda}$	Stator and rotor leakage inductances
$\underline{i}_M, \underline{i}_R$	Transformed magnetizing and rotor current phasor
$\underline{\psi}_R$	Transformed rotor flux linkage phasor
L_M, L_σ	Transformed magnetizing and total leakage inductance
R_R	Transformed rotor resistance
$\theta^{uv}_{\underline{\psi}_r 0}$	Initial electrical angle of phasor $\underline{\psi}_r$ in the u-v coordinate system
$\theta_{u,0}$	Initial electrical angle of the u-axis in the α-β coordinate system
θ_{rf0}	Initial electrical angle between α-β and d-q coordinate systems

Meng-Ju Hsieh, Torbjörn Thiringer, and Emma Arfa Grunditz are with Chalmers University of Technology, Göteborg 41296, Sweden (e-mail: mengju.hsieh@chalmers.se; torbjorn.thiringer@chalmers.se; emma.grunditz@chalmers.se).

Manuscript received ...

I. INTRODUCTION

WITH the increasing usage of electrical machines (EMs) as traction motors in automotive applications, the need to drive effectively, i.e. to utilize the full capability of EMs, gains importance. To find the EMs' optimal operating points and to achieve precise control, the strategies of field-oriented control (FOC) are commonly applied. Then for the optimal operating points, the machine loss and efficiency maps can be constructed and used for performance evaluation.

Today, the two most commonly used machines types in electric vehicles are the permanent magnet synchronous machine (PMSM) and the induction machine (IM). IMs have several advantages such as robustness, cost-effectiveness, and rare-earth-metal-freeness. However, IMs are more complex to control compared to PMSMs, since for one desired output torque and speed combination, there are several possible choices of slip rate. Thus, to find the optimal operating points, a considerable number of finite element method (FEM) simulations may be required. Furthermore, since there are windings in both the stator and the rotor, the FEM simulation computation time for a single point of IMs becomes substantially high compared to the one for PMSMs.

Accordingly, equivalent circuit models, such as the T-form model (TFM) or the inverse Γ-form model (IGFM), are typically used to reduce the number of simulations. Therefore, to make conceptual as well as refined evaluations in automotive industry, accurately predicted IM parameters for precise control are desired already at the design stage, i.e. to reduce the need for repeated prototyping. In [1]–[3], **three** methods and procedures are developed to find the optimal operating points and their constraints based on the FOC. These papers also addressed the iron core saturation phenomenon of IMs(decreasing inductance with the increasing stator flux linkage) that affects the control accuracies, thus, showing the

importance of accurate parameters. These papers focus on the impact of control rather than on parameter determination.

The conventional method to identify the IMs equivalent circuit parameters is to conduct a no-load and a locked-rotor test, as exemplified in [4]. The parameters derived from the conventional method are typically acquired for only a single rated operating point where its stator flux linkage level is usually fixed. There are two main drawbacks of the locked-rotor test. Firstly, to reduce the impact of skin effect in the rotor bars during the locked-rotor test, a reduced stator voltage frequency is preferred. At the same time, the frequency must be high enough to maintain the induction between stator and rotor, and thereby get good results. In [4], 25% of the rated frequency is recommended, which is substantially above the rotor's normal electric frequency. An alternative method to identify the IMs equivalent circuit parameters could be to use load tests. In [5], the rotor resistance was determined experimentally from a load test, and the result was compared to an experimental locked-rotor test, showing a disagreement of above 20%. The results in [5] also shows that the rotor resistance obtained from load test had better representation of the IM compared to the locked-rotor test. However, the results were not coupled to any FEM analysis, which limits the usability. Secondly, another problem with the conventional determination of the equivalent circuit parameters using the locked-rotor test, is that the stator and the rotor leakage inductances cannot be separated. Instead, general ratios are used, for instance according to templates found in [6].

In order to predict the parameters of IMs at the design stage to achieve effective control, there are several related studies employing FEM programs. The studies in [7]–[9], the parameters of the TFM or the IGFM considering saturation characteristics of the magnetizing inductance are identified, and the simulation results show good matches with experimental results. In [7], a suggested procedure to excite both the stator and the rotor windings using the FEM magnetostatic solver is presented. Its main advantage is the significant reduction of expecting simulation time compared to the one by the transient solver. Nevertheless, the procedure would give lower accuracy for cases when IMs have a high skin effect, such as the IMs used in Tesla Model S/X and Audi e-Tron having deep rotor bars [10]. Hence, to avoid degraded accuracy in such applications, the transient solver is utilized in this paper, and [8], [9]. In [8], to identify the parameters of the TFM under three different load tests, the stator's and rotor's current and flux linkage phasors are obtained from the FEM. However, the way how to extract the rotor phasors is not discussed in [8]. In [9], to determine the IGFM parameters, several voltages with small amplitudes and a range of frequencies are fed by the inverter to three different IMs. The nonideal effect from the inverter is included in both the FEM and experiments, which makes this method feasible. Nevertheless, the IMs are tested at a standstill and with a frequency range between 10 to 40 Hz, which is not the typical operating range of the rotor frequency. Furthermore, the performance predictions of torque calculated by equivalent parameters are lacking in both [8], [9].

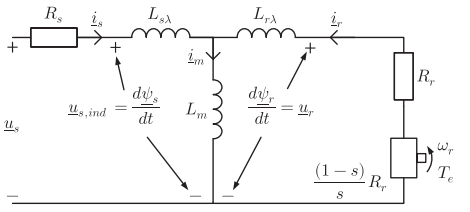

Fig. 1. Steady-state T-form model of IMs.

In this paper a procedure to determine the equivalent circuit parameters of IMs using FEM is proposed, proving higher accuracy compared to using conventional no/load and locked-rotor tests. The proposed method aims to utilise the full capability of FEM analysis to enhance the forecast of equivalent circuit parameters as well as torque prediction. The specific contribution is a step-by-step procedure to determine the parameters of both the TFM and the IGFM from the stator's and rotor's current and flux linkage phasors. The IM is simulated under no-load and load tests using the FEM transient solver. In addition, a verification is presented, of the improvement over the conventional method regarding torque forecast when using the IGFM parameters. The results of the proposed method can be used to find the optimal operating points and to control IMs more precisely with a minimum amount of FEM simulation effort.

II. Theory

Perfect field oriented control (PFOC) based on the IGFM is chosen as a control template in this work, meaning that the control is built on the alignment of a rotating coordinate system with the real axis (d-axis) in the direction of the rotor flux linkage $\underline{\psi}_R$, i.e. to have precise control, an accurate position of $\underline{\psi}_R$ is vital. Thus, in this section, the background theory of the two equivalent circuit models and the transformation of phasors from the rotor to the stator side are formulated.

A. T-form model (TFM)

The classical model used for the IM representation is steady-state TFM in the α-β stationary reference frame using amplitude invariant scaling. This model is depicted in Fig. 1. The relation of current phasors can be found as

$$\underline{i}_m = \underline{i}_s + \underline{i}_r \tag{1}$$

The stator and rotor flux linkage phasors $\underline{\psi}_s$ and $\underline{\psi}_r$ can be expressed as

$$\underline{\psi}_s = L_s \, \underline{i}_s + L_m \, \underline{i}_r \tag{2}$$

$$\underline{\psi}_r = L_r \, \underline{i}_r + L_m \, \underline{i}_s \tag{3}$$

where $L_s = L_m + L_{s\lambda}$ and $L_r = L_m + L_{r\lambda}$. In practice, these inductances vary with the magnitude of the magnetizing current I_m due to the iron core saturation.

In this paper, FEM analysis is used to determine the currents and flux linkages, and then (1-3) is for the estimation of the magnetizing current $\underline{i}_m$, the magnetizing inductance L_m, the stator inductance L_s, and the rotor inductance L_r.

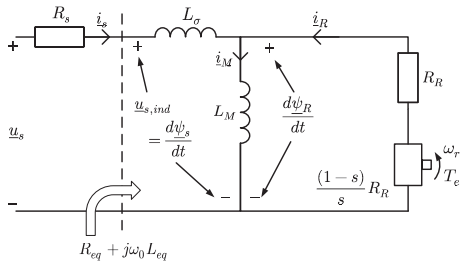

Fig. 2. Steady-state inverse Γ-form model of IMs.

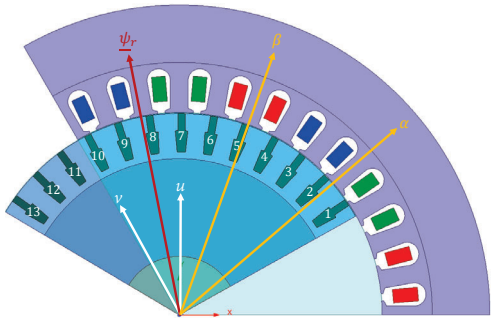

Fig. 3. Schematic of coordination of the 15 kW IM FEM model.

Besides, the rotor resistance R_r can be acquired from the electromagnetic torque T_e and rotor current amplitude I_r as

$$R_r = \frac{2\ T_e\ \omega_r}{3I_r^2} \frac{s}{(1-s)} \tag{4}$$

B. Inverse Γ-form model (IGFM)

Fig. 2 shows the steady-state IGFM, a transformed model from the TFM. It is commonly used as an IM control template. The reason of applying the IGFM instead of the physically relevant TFM is that the TFM is over-parameterized for dynamic analysis controller design [11]. The IGFM parameters can be transformed from the TFM by

$$R_R = \left(\frac{L_m}{L_r}\right)^2 R_r \tag{5}$$

$$L_M = \frac{L_m^2}{L_r} \tag{6}$$

$$L_\sigma = L_s - L_M \tag{7}$$

$$\underline{\psi}_R = \frac{L_m}{L_r}\ \underline{\psi}_r \tag{8}$$

When applying Park's transformation as well as the PFOC, aligning the rotor flux linkage $\underline{\psi}_R$ to the d-axis is assumed. Then there is no q-quantity of the rotor flux linkage ψ_R^q and the d-quantity ψ_R^d equals to Ψ_R. Hence, the electrical slip speed and electromagnetic torque of IMs can be stated as

$$\omega_2 = \frac{R_R\ i_s^q}{\psi_R^d} \tag{9}$$

$$T_e = \frac{3}{2} N_p\ \psi_R^d\ i_s^q \tag{10}$$

From (9) and (10), if the parameters of R_R, L_M and ψ_R^d are predicted well, an accurate torque determination of the IM by i_s^d and i_s^q can be achieved.

C. Rotor rotational u-v coordinate system

With a FEM software like Ansys/Maxwell, the induced voltage, current, and flux linkage in a single rotor bar can be numerically estimated. In order to map the variables from different rotor bars to one pole, a coordinate system, u-v, fixed to the rotor mechanically, with the u- and v-directions defined as the real and imaginary parts respectively, is implemented.

Fig. 3 is a schematic of how different coordinate systems are located at the cross-section of the investigated six-pole 15 kW IM FEM model. On the stator side, the α-axis is at the direction of the flux linkage of phase A (red wires in the slot), and the β-axis is $\pi/2$ lagging to α-axis. On the rotor side, the u-axis and v-axis are at the electrical angle of π ($Bar07$) and $3\pi/2$ of the rotor respectively. Furthermore, the position of $\underline{\psi}_r$ is the orientation of the d-axis.

The fundamental time-varying variables in different rotor bars of a segment have the same amplitude and frequency (ω_2), and a phase shift of $(2\pi N_p)/Q_r$ between each neighbor bars [12]. Hence, in the u-v plane these variables can be formulated as

$$\begin{gathered} x_{bar,k}^{uv}(t) = X_{bar}^{uv} cos\left[\omega_2 t - \tfrac{(k-1)2\pi N_p}{Q_r}\right] \\ k = 1, 2, ..., Q_r/2N_p \end{gathered} \tag{11}$$

where x can be u, i, or ψ, and X can be U, I, or Ψ.

Next, projecting all variables to the rotor fixed axis, the u- and v-components of these variables, such as the total rotor current variable, can be determined as

$$\begin{cases} x_r^u(t) = \sum\limits_{k=1}^{Q_r/2N_p} x_{bar,k}^{uv}(t) cos\left[\pi - k\frac{2\pi}{Q_r}\right] \\ x_r^v(t) = \sum\limits_{k=1}^{Q_r/2N_p} x_{bar,k}^{uv}(t) sin\left[\pi - k\frac{2\pi}{Q_r}\right] \end{cases} \tag{12}$$

With the components of ψ_r^u, and ψ_r^v at $t = 0$, which can be computed from (12), the initial phase angle of $\underline{\psi}_r$ in the stationary α-β coordinate system can be found as

$$\theta_{rf0} = \theta_{u,0} + \theta_{\underline{\psi}_r 0}^{uv} \tag{13}$$

where the initial phase angles of the u-axis in the α-β axes is $\theta_{u,0}$ and $\underline{\psi}_r$ in the d-q plane is $\theta_{\underline{\psi}_r 0}^{uv}$ respectively.

Oriented in the direction of $\underline{\psi}_r$ with the real part represented by the d-direction, θ_{rf0} is also known as the initial electrical angle between the α-β and d-q axes and it can be utilized to recognize the phase angles of all phasors in the d-q plane.

D. Transferring the rotor quantities to the stator side

As the rotor quantities of the IM are all induced by the stator side, similarly to the secondary and primary sides of a transformer, the amplitude of the rotor variables from the

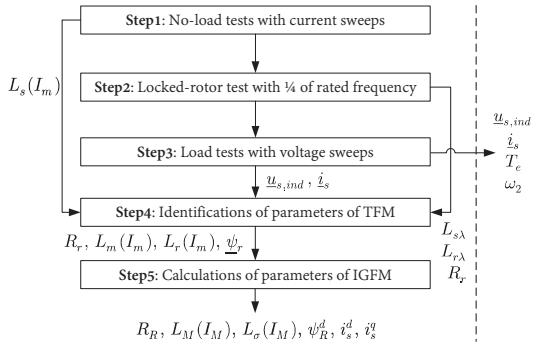

Fig. 4. Flowchart of conventional method.

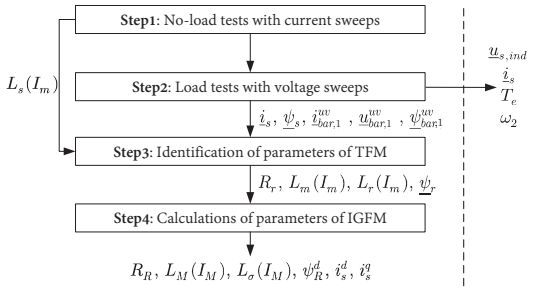

Fig. 5. Flowchart of a new proposed procedure.

rotor side in the u-v coordinate system can be transferred to the stator side by

$$\Psi_r = \frac{2N_s q_s k_1 N_p}{c_s} \Psi_{bar}^{uv} \tag{14}$$

$$I_r = \frac{Q_r c_s}{6N_s q_s k_1 N_p} I_{bar}^{uv} \tag{15}$$

where Ψ_r, I_r, Ψ_{bar}^{uv}, and I_{bar}^{uv} are the amplitudes of the variables.

III. IM PARAMETERS IDENTIFICATION

A. Conventional method

Using the conventional method, the parameters of IMs at their rated point typically a single operating speed, are identified by the no-load and the locked-rotor tests. Since it is the total leakage inductance $L_{s\lambda}+L_{r\lambda}$ that can be determined in the locked-rotor test, a ratio of $L_{s\lambda}/L_{r\lambda}$ needed to be assumed. Here, this ratio is assumed to be 1 according to the recommendation in [4].

The conventional method, summarized in Fig. 4, is applied using Ansys/Maxwell. In the first step, several no-load tests with various stator current magnitudes will be performed to determine the dependence of L_s on I_m. A locked-rotor test with 25% of the rated frequency is applied to find R_r and $L_{s\lambda} + L_{r\lambda}$ in the second step.

To compare with the new method, the phasors of $\underline{u}_{s,ind}$, and $\underline{i}_s$ from the load test are used to find the magnetizing current $\underline{i}_m$ by

$$\underline{u}_m = \underline{u}_{s,ind} - j\omega_0 L_{s\lambda} \tag{16}$$

$$\underline{i}_m = \underline{i}_s + \frac{\underline{u}_m}{R_r + j\omega_0 L_{r\lambda}} \tag{17}$$

The data of $\underline{u}_{s,ind}$, $\underline{i}_s$, T_e, and ω_2 are also saved for later verification.

In the third step, with the amplitude of the magnetizing current I_m by (17), in addition to $L_{s\lambda}$, $L_{r\lambda}$, and $L_s(I_m)$ from the second step, $L_m(I_m)$, $L_r(I_m)$ can be found. Furthermore, the rotor flux linkage phasor $\underline{\psi}_r$ can be obtained by (3).

The final step is to apply (5)-(8) to resolve R_R, $L_M(I_M)$, $L_\sigma(I_M)$, and ψ_R^d. With the amplitude of $\underline{i}_s$ from the third step and ψ_R^d, the d- and q-quantities of stator current i_s^d and i_s^q can also be acquired by

$$i_s^d = \frac{\psi_R^d}{L_M} \tag{18}$$

$$i_s^q = \sqrt{I_s^2 - i_s^{d^2}} \tag{19}$$

B. Proposed method

The flowchart of the proposed method in this paper is shown in Fig. 5. After conventional no-load tests with stator current magnitude sweep to find the relations of L_m and I_m, the stator phasors can be directly obtained from the FEM results in the second step. Moreover, to get the information of the rotor branch, the current and flux linkage phasors from the rotor bar $\underline{i}_{bar,1}^{uv}$, $\underline{\psi}_{bar,1}^{uv}$ are acquired from an end-ring simulation and then transferred to the stator side by (14) and (15), rather than the way to bypass the magnetizing branch in the locked-rotor test.

Then, with the curve of $L_s(I_m)$ from the first step and the other phasors from the second step, R_r, $L_m(I_m)$, $L_r(I_m)$, and $\underline{\psi}_r$ can be obtained in the third step. Finally, the forth step is the same final step as for the conventional method.

C. Verification

In order to verify the usefulness of the proposed improved model, the acquired parameters of the IGFM are utilized to calculate the electromagnetic torque and electrical slip speed as in (10) and (9). The calculated values, $T_{e,cal}$ and $\omega_{2,cal}$, are compared with those derived directly from FEM.

Next, the equivalent impedance in Fig. 2, $R_{eq} + j\omega_0 L_{eq}$, can be formulated via the parameters of the IGFM as

$$R_{eq} = \frac{\omega_0^2 L_M^2 \frac{R_R}{s}}{\left(\frac{R_R}{s}\right)^2 + \omega_0^2 L_M^2} \tag{20}$$

$$L_{eq} = L_\sigma + \frac{L_M \left(\frac{R_R}{s}\right)^2}{\left(\frac{R_R}{s}\right)^2 + \omega_0^2 L_M^2} \tag{21}$$

or by the phasors of the induced voltage $\underline{u}_{s,ind}$ and $\underline{i}_s$, which can be acquired from Ansys/Maxwell directly, as

$$R_{eq} = \mathfrak{Re}\left(\frac{\underline{u}_{s,ind}}{\underline{i}_s}\right) \tag{22}$$

$$L_{eq} = \mathfrak{Im}\left(\frac{\underline{u}_{s,ind}}{\underline{i}_s}\right)\frac{1}{\omega_0} \tag{23}$$

IV. FEM Model

The design details of investigated FEM model are presented in Table I. Its cross-section of one pole-pair is in Fig. 3.

TABLE I
DESIGN DETAILS OF THE 15KW IM.

Parameter	Unit	Value
Rated output power	kW	15
Rated speed	rpm	980
Rated line-to-line input voltage	V_{rms}/Hz	400/50
Number of pole pairs N_p	-	3
Iron core stack length	mm	230
Stator outer diameter	mm	291.2
Stator inner diameter	mm	190.2
Number of stator slots Q_s	-	36
Rotor outer diameter	mm	189.3
Rotor inner diameter	mm	55
Rotor end-ring average diameter	mm	163.3
Number of the rotor slots Q_r	-	39
Number of turns per coil N_s	-	38
Area of a stator turn	mm^2	1.98
Number of parallel strands per turn	-	2
Number of parallel branches N_{pb}	-	3
Terminal connection	-	Y
Stator coil material	-	Copper
Rotor bar material	-	Aluminium
Iron core material	-	M700-50A

V. Results and Comparisons

A. No-load tests

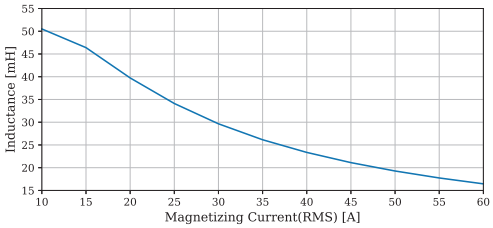

Fig. 6. Stator inductance L_s varying with magnetizing current.

The stator inductance L_s of the 15 kW IM vary with the magnetizing current as sketched in Fig. 6, which is derived from the FEM results.

B. Load test for input line-to-line voltage: 400 V_{rms}/50 Hz

In this paper, it is the rotor phasors that need more post-processing work. Hence, in order to exam if the rotor phasors are reasonable, this section presents the results of a load test with a rotor speed of 980 rpm and a line-to-line voltage of 400 V_{rms}/50 Hz. Besides, a table of IGFM parameters is presented in Table II to show the differences of results between two methods. Figures are presented with time-varying rotor variables in the u-v coordinate system and the phasors in the d-q coordinate system.

Table II lists the parameters of IGFM from both conventional and proposed methods derived under the rated point. Except for L_σ, the differences of other parameters are less than 15%. The usefulness of these parameters will be compared in the next section. In Fig. 7-9 (a), the raw data of the variables in the first rotor bar is derived from the end-ring

TABLE II
IGFM PARAMETERS (INPUT LINE-TO-LINE VOLTAGE: 400 V_{rms}/50 HZ, ROTOR SPEED: 980 RPM).

Parameter	Unit	Conventional	Proposed
L_M	mH	42.6	38.9
L_σ	mH	3.67	1.87
R_R	Ω	0.142	0.146
Ψ_R	Wb	0.897	0.943
i_s^d	A	21.1	24.2
i_s^q	A	42.7	41.0

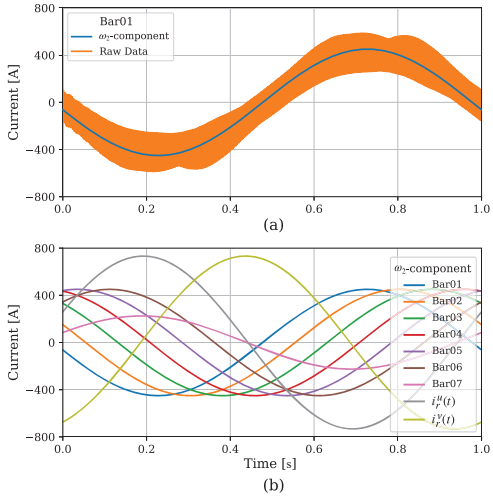

Fig. 7. Current in rotor bars in u-v coordinate system (input line-to-line voltage: 400 V_{rms}/50 Hz, rotor speed: 980 rpm). (a) Raw data from FEM, and its ω_2-component in rotor bar01. (b) ω_2-component in rotor bar01-07, $i_r^u(t)$, and $i_r^v(t)$ for one pole.

calculator of Ansys/Maxwell. Additionally, FFT is applied to get the rotor fundamental frequency (ω_2) component of $Bar01$. With the ω_2-component from $Bar01$, the variables from $Bar02-07$ can be found using (11), and then the u- and v-quantities can be obtained by (12), which are shown in Fig. 7-9 (b). Here, the specific bar number can be referred to Fig. 3. It can be seen that the amplitudes of the variables from $Bar07$ are half of the rest. The reason is that the number of the rotor bars for one pole is $39/6 = 6.5$, meaning that $Bar07$ is only contributing with 50% to the adjacent pole in the u-v plane.

After the identification of the initial phase angle of the rotor flux linkage $\theta_{\overline{\psi}_r 0}^{uv}$ in the α-β coordinate system, the initial electrical angle between the α-β and d-q coordinate system θ_{rf0} can be found. Next, referring the amplitude from the rotor to the stator side by (14) and (15), the phasors in the d-q coordinate system can be obtained, and these are depicted in Fig. 10.

C. Comparisons of the usefulness of the IGFM parameters

Here, two sets of the IGFM parameters from the proposed and the conventional method are used to identify the equivalent impedance determined from (20) and (21), and the electromechanical performance ω_2 and T_e found using (9) and (10) with a range of input voltages from 50-500 V

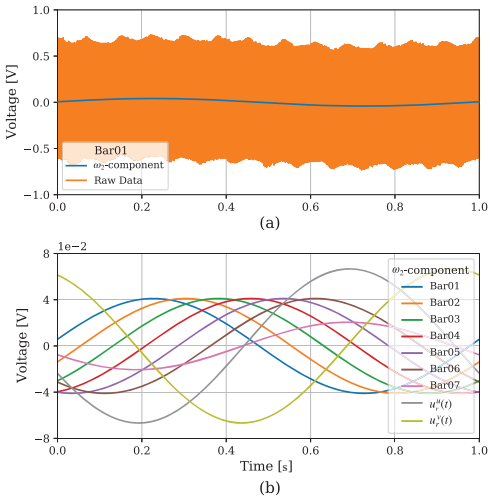

Fig. 8. Induced voltage in rotor bars in u-v coordinate system. (input line-to-line voltage: 400 V_{rms}/50 Hz, rotor speed: 980 rpm). (a) Raw data from FEM, and its ω_2-component in rotor bar01. (b) ω_2-component in rotor bar01-07, $u_r^u(t)$, and $u_r^v(t)$ for one pole.

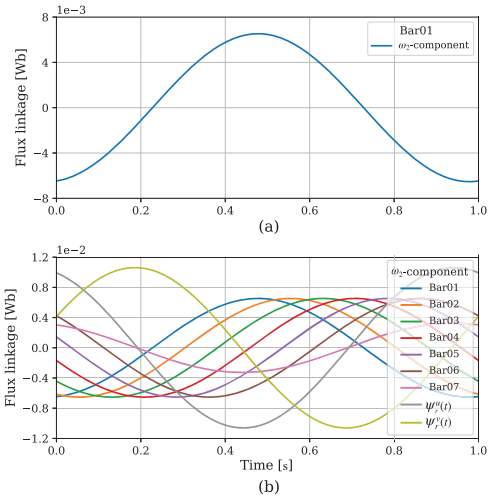

Fig. 9. Flux linkage in rotor bars in u-v coordinate system. (input line-to-line voltage: 400V_{rms}/50 Hz, rotor speed: 980 rpm). (a) ω_2-component in rotor bar01. (b) ω_2-component in rotor bar01-07, $\psi_r^u(t)$, and $\psi_r^v(t)$ for one pole.

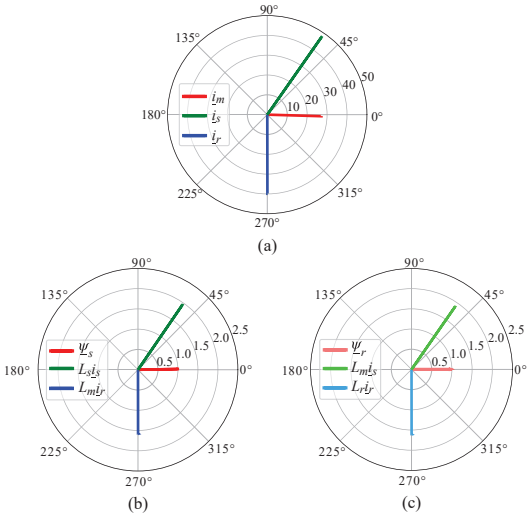

Fig. 10. Current and flux linkage phasors in the d-q coordinate system. (input line-to-line voltage: 400 V_{rms}/50 Hz, rotor speed: 980 rpm). (a) Magnetizing, stator, and rotor current phasors (1). (b) Stator flux linkage, stator and rotor current phasors (2). (c) Rotor flux linkage, stator and rotor current phasors (3).

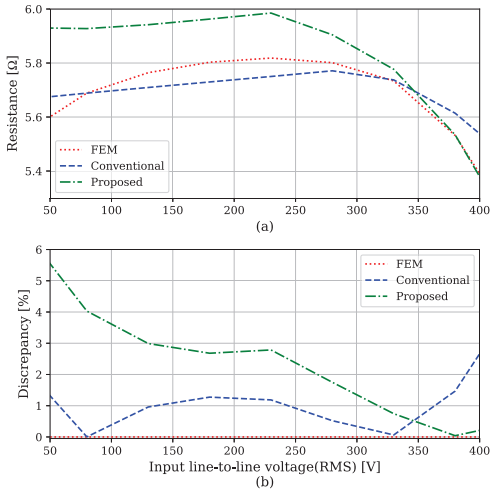

Fig. 11. Equivalent phase resistance R_{eq} (input line-to-line voltage: 50 Hz, rotor speed: 980 rpm). (a) Absolute value. (b) Discrepancy.

and a fixed rotor speed 980 rpm ($s = 2\%$). The results of R_{eq}, L_{eq}, ω_2, and T_e from the two methods are compared to those found directly from FEM and presented in Fig. 11-14, where the curves with the label of "FEM" are those directly from FEM. The absolute values are drawn in Fig. 11-14(a) and the discrepancies to "FEM" are presented in (b).

The proposed method has better matches with torque, slip speed, and equivalent inductance, but the estimation of the equivalent resistance has not been improved compared to the conventional method. Moreover, around the rated voltage (400 V_{rms}), the discrepancies of the investigated parameters from proposed method toward the ones directly from FEM are all under 2%.

VI. Conclusion

A method to determine the equivalent circuit parameters of an IM is proposed. It is aimed to be utilized for machines used in applications with different stator flux linkage levels. Thus, the analysis with different input voltages and currents is performed in Ansys/Maxwell. In addition, a conventional method is applied to benchmark the usefulness of the proposed method. The results have shown that the proposed method has a better forecast of the range of torque, meaning that it has better representation and is more suitable to be applied in various voltage applications than using parameters from the conventional method.

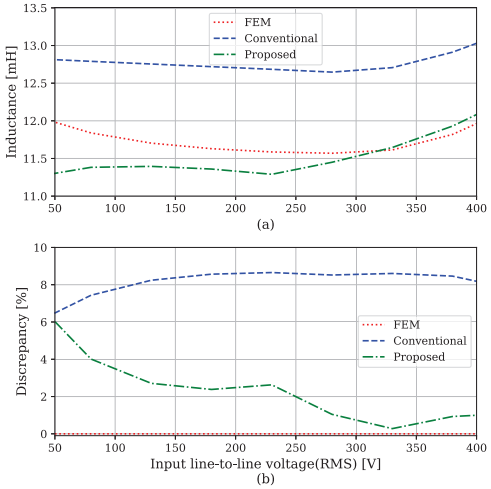

Fig. 12. Equivalent phase inductance L_{eq} (input line-to-line voltage: 50 Hz, rotor speed: 980 rpm). (a) Absolute value. (b) Discrepancy.

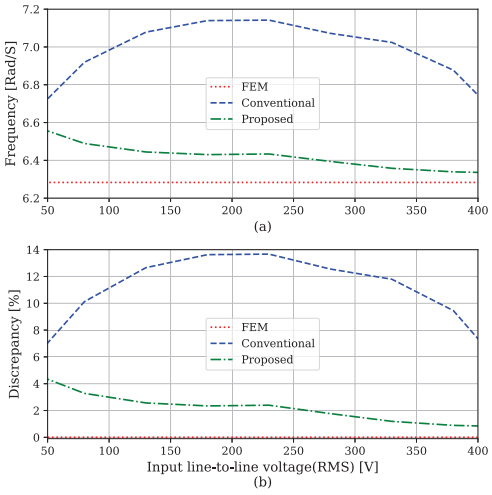

Fig. 13. Slip electrical frequency (input line-to-line voltage: 50 Hz, rotor speed: 980 rpm). (a) Absolute value. (b) Discrepancy.

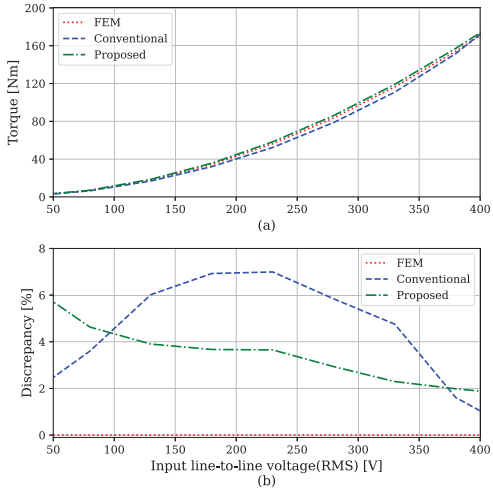

Fig. 14. Electromagnetic torque (input line-to-line voltage: 50 Hz, rotor speed: 980 rpm). (a) Absolute value. (b) Discrepancy.

REFERENCES

[1] S. Bozhko, S. Dymko, S. Kovbasa, and S. M. Peresada, "Maximum torque-per-amp control for traction im drives: Theory and experimental results," *IEEE Transactions on Industry Applications*, vol. 53, no. 1, pp. 181–193, 2017. [Online]. Available: https://doi.org/10.1109/TIA.2016.2608789

[2] H. Cai, L. Gao, and L. Xu, "Calculation of maximum torque operating conditions for inverter-fed induction machine using finite-element analysis." *IEEE Transactions on Industrial Electronics*, vol. 66, no. 4, pp. 2649–2658, 2019. [Online]. Available: https://doi.org/10.1109/TIE.2018.2847700

[3] Z. Peng, "Analysis and implementation of constrained mtpa criterion for induction machine drives." *IEEE Access, Access, IEEE*, vol. 8, pp. 176 445 – 176 453, 2020. [Online]. Available: https://doi.org/10.1109/ACCESS.2020.3024195

[4] "Ieee standard test procedure for polyphase induction motors and generators," *IEEE Std 112-2017 (Revision of IEEE Std 112-2004)*, 2018. [Online]. Available: https://doi.org/10.1109/IEEESTD.2018.8291810

bances in induction machines," Ph.D. dissertation, Chalmers University of Technology, 1996.

[5] T. Thiringer, "Measurements and modelling of low-frequency distur-

[6] A. Bonnett and G. Soukup, "Nema motor-generator standards for three-phase induction motors," *IEEE Industry Applications Magazine*, vol. 5, no. 3, pp. 49–63, 1999. [Online]. Available: https://doi.org/10.1109/2943.758901

[7] L. Alberti, N. Bianchi, and S. Bolognani, "Variable-speed induction machine performance computed using finite-element," *IEEE Transactions on Industry Applications*, vol. 47, no. 2, pp. 789–797, 2011. [Online]. Available: https://doi.org/10.1109/TIA.2010.2103914

[8] M. R. Hachicha, N. Ben Hadj, M. Ghariani, and R. Neji, "Finite element method for induction machine parameters identification," in *2012 First International Conference on Renewable Energies and Vehicular Technology*, 2012, pp. 490–496. [Online]. Available: https://doi.org/10.1109/REVET.2012.6195318

[9] M. Carraro and M. Zigliotto, "Automatic parameter identification of inverter-fed induction motors at standstill," *IEEE Transactions on Industrial Electronics*, vol. 61, no. 9, pp. 4605–4613, 2014. [Online]. Available: https://doi.org/10.1109/TIE.2013.2289903

[10] R. Thomas, H. Husson, L. Garbuio, and L. Gerbaud, "Comparative study of the tesla model s and audi e-tron induction motors," in *2021 17th Conference on Electrical Machines, Drives and Power Systems (ELMA)*, 2021, pp. 1–6. [Online]. Available: https://doi.org/10.1109/ELMA52514.2021.9503055

[11] L. Harnefors, *Control of variable-speed drives*. Applied Signal Processing and Control, Department of Electronics, Mälardalen University, 2002.

[12] O. Wallmark, *AC Machine Analysis Fundamental Theory*. Department of Eletrical Conversion, KTH Royal Institution of Technology, 2020.

BIOGRAPHIES

Meng-Ju Hsieh works at Chalmers university of Technology, in Göteborg Sweden, as a Ph.D. student. She took her M.Sc. (Eng.) at Chang Gung University, Taiwan in 2011. Her areas of interest include the modelling and control of vehicular traction electric machines considering both environmental and electromechanical performances.

Torbjörn Thiringer (Senior Member, IEEE) works as a Professor in electric power engineering at Chalmers University of Technology in Göteborg, Sweden, from which he received his M.Sc. and Ph.D. in 1989 and 1996, respectively. His research interests include the modelling, control, and grid integration of wind energy converters as well as power electronics, battery technologies, and electric machines for various applications.

Emma Arfa Grunditz received her M.Sc. (Eng.) degree 2009 and Ph.D. degree 2016 at Chalmers University of Technology, Göteborg, Sweden, where she is currently working as a post-doc researcher. Her research interest include electric drive systems mainly for vehicular applications, regarding component and system cooling, energy consumption, performance and cost.

PAPER B

An alternative to determine IM parameters trends affected by magnetic saturation using two-stage flux-decay test by FEM

Meng-Ju Hsieh, and Torbjörn Thiringer

Published in 2023 IEEE International Electric Machines & Drives Conference (IEMDC),
pages 1–5, 2023.

The layout has been revised.

An Alternative to Determine IM Parameters Trends Affected by Magnetic Saturation Using Two-Stage Flux-Decay Test by FEM

Meng-Ju Hsieh, *Student Member, IEEE* Torbjörn Thiringer, *Senior Member, IEEE*

2023 IEEE International Electric Machines & Drives Conference (IEMDC) | 979-8-3503-9899-1/23/$31.00 ©2023 IEEE | DOI: 10.1109/IEMDC55163.2023.10239094

***Abstract*—In this work, a two-stage flux-decay test is conducted to determine not only the induction machine parameters for a single current level but also their dependence on the current level. The goal of this work is to find an alternative parameter determination to the conventional method, which has several drawbacks when applied to variable speed applications. First, the theory of the T-form model (TFM) and flux-decay test are reviewed. Second, a new alternative determination method for identifying these parameters is presented. Third, a 2D electromagnetic finite element method (FEM) model of a vehicle traction induction machine (IM) is implemented to show the viability of the proposed method in a real design. Lastly, a comparison of results using the conventional method and analyzed the proposed method is presented, showing a good agreement.**

***Index Terms*—induction machine (IM), flux-decay test, parameters determination.**

I. Introduction

The induction machine (IM) is one of the most commonly used traction electric machines (EMs) for electric vehicles due to its robustness, cost-effectiveness, and rare-earth-metal-freeness. While compared to the other popular EM type, permanent magnet synchronous machines (PMSMs), IMs are more complicated to control, and it is also more difficult to predict their performance at the design stage. This is due to the fact that there is a slip speed between the rotor and stator electrical speeds, which provides a wider degree of freedom for single torque and rotor mechanical speed demand. In addition, the simulation time of the finite element method (FEM) of the IM is, unfortunately, much longer than PMSM per case.

The field-oriented control (FOC) based on the T-form model (TFM) or the inverse Γ-form model (IGFM) is typically applied to find the IM's optimal points. There are two benefits of basing the FOC on these schemes. Firstly, considerable FEM simulations to find optimal points per IM design can be saved from the approach of tracking optimal operating points by sweeping slip and current level combinations using FEM simulations. Secondly, such parameter-based models can be easily applied in a refined evaluation, for example, minimum loss control, benchmark evaluation, etc. Thus, predicting IM parameters precisely is desired already at the design stage.

To identify the IMs' IGFM parameters, the conventional method is to conduct a no-load, and a locked-rotor test [1]. However, parameters determined by the conventional method are usually derived by testing and further operating the IM only at a single rated point with a fixed current level. Moreover, the locked-rotor test has three main disadvantages when applied in variable speed applications. Firstly, it gives the total leakage inductance, whereas the ratio between the stator and rotor leakage inductances must be approximated based on their type in [2]. Next, the skin effect from the fundamental rotor frequency (one-fourth of the rated stator frequency) has a higher degree of skin effect than most of the load points of IMs. Furthermore, the flux leakage path of the rotor in the case of closed rotor slots and the magnetizing path are current-dependant [3]. Where the closed rotor slot designs with iron bridges are often implied in inverter-fed IMs' designs. Such iron bridges have the benefit of reducing the harmonics of flux density in the air gap hence the harmonic losses and torque ripples can be reduced [4], [5]. Thus, a conventional test with only one current level does not give a good enough representation for variable speed applications where the magnetizing and leakage inductances differ due to the iron core saturation.

To find IMs' parameters that suit variable speed applications, various methods are developed. In [6], several no-load and load tests are performed using FEM, and the results show improvement over the conventional method with regards to parameters determination and a good agreement between its FEM model and IGFM when it comes to the prediction of torque. However, the investigated machine is an open rotor slot IM and only one speed is tested. In [7], the focuses are on the use of flux-decay experiments to determine the ratio between rotor resistance and rotor inductance of one wound and two squirrel cage IMs. The authors analyze the time constants of voltage envelopes during IMs' decaying flux periods to investigate the effect of flux linkage levels on the ratio. The results show that the ratio varies with flux linkage levels, especially in closed rotor slot cases. In [8], the authors further analyze the time constants of the beginning and the end of the decay period and find an increment in the time constant at the end of the test. However, it is noted that the results of these papers are not coupled to any FEM analysis, which limits their usability in the initial design phase.

Meng-Ju Hsieh, Torbjörn Thiringer, and Emma Arfa Grunditz are with Chalmers University of Technology, Göteborg 41296, Sweden (e-mail: mengju.hsieh@chalmers.se; torbjorn.thiringer@chalmers.se).

Manuscript received ...

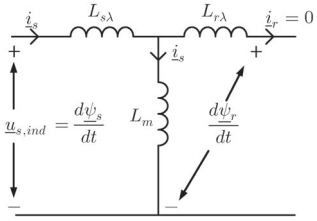

Fig. 1. TFM in the first stage.

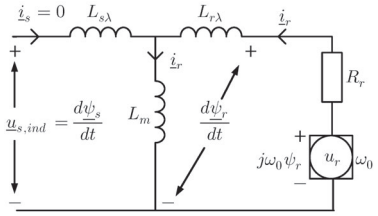

Fig. 2. TFM in the second stage.

In this paper, a method to determine the TFM parameters of IMs using FEM by the flux-decay test is proposed. The specific contribution is to identify rotor resistance, all inductances, as well as their current dependencies with flux-decay tests. The inductances are calculated directly from flux linkages and currents. It is a straightforward procedure to determine the parameters of the TFM in the IM development phase. The studied machine is a closed slot traction IM [9]. In addition, several conventional tests with various stator flux linkage levels are performed in order to verify the usefulness of the proposed method.

II. Theory

The flux-decay test is conducted with two stages in this work. The first stage is to perform a no-load condition to magnetize the iron cores. Then, in the second stage, the input stator current is set to zero, and the magnetic energy stored in the stator and rotor iron cores will decay due to the rotor resistance.

The trend in the second stage can be used to determine the parameters of the T-form model (TFM) depicted in Fig. 1 and Fig. 2, where $u_{s,ind}$ is stator induced voltage, $L_{s\lambda}$ is stator leakage inductance, L_m is magnetizing inductance, $L_{r\lambda}$ is rotor leakage inductance, R_r is rotor resistance, $\underline{i}_s$ is stator current, ψ_s is stator flux linkage, $\underline{i}_r$ is rotor current, ψ_r is stator flux linkage, u_r is rotor induced voltage, $\omega_0 = 2\pi f_0$ is stator electrical speed, and f_0 is stator electrical frequency.

Iron loss and mechanical friction are disregarded in this study. The FEM simulation maintains the rotor mechanical speed at the synchronous speed ω_0/N_{pp}, with N_{pp} representing the number of pole pairs. This setup ensures that the electrical speed always stays at ω_0, which is practical for post-processing the data. However, it is important to note that in reality, both the rotor mechanical and stator electrical speeds decrease gradually over time due to mechanical friction from the shaft and air. Additionally, the iron cores are assumed to have zero loss, resulting in a more identical rotor resistance.

In Fig. 3, the trends of amplitudes of variables are depicted, where the variables with $_{NL}$ mean quantities at the first stage, the ones with $_{FD}$ represent quantities at the second stage, and the ones with $_0$ denote the initial value of the decay. The rotor current $i_{r,NL}$, and rotor induced voltage $u_{r,NL}$ are zero in the first stage since the rotor circuit is open, and the rotor flux linkage $\psi_{r,NL}$ is equal to magnetizing

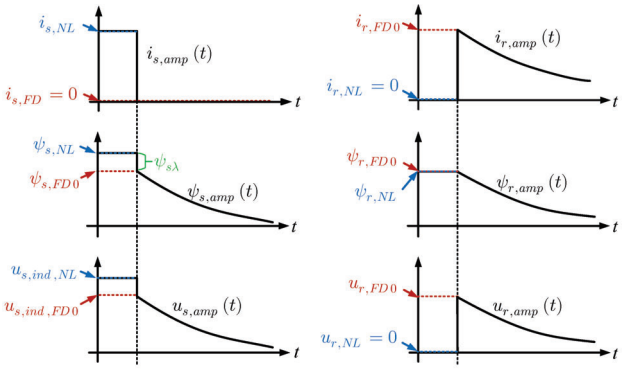

Fig. 3. Trends of variables amplitudes from flux-decay test.

flux linkage in the first stage. Moreover, the stator inductance $L_s = L_m + L_{s\lambda}$ at current level $i_{s,NL}$ can be derived by

$$L_s = \frac{\psi_{s,NL}}{i_{s,NL}} \tag{1}$$

In the second stage, the rotor circuit is shorted, the stator flux linkage ψ_s can be regarded as the main flux linkage, and the rotor current $i_{r,FD}$ can be considered as magnetizing current since the stator current $i_{s,FD}$ is zero. Thus, the magnetizing inductance varying with time can be obtained by

$$L_m(t) = \frac{\psi_{s,amp}(t)}{i_{r,amp}(t)} \tag{2}$$

Moreover, the stator leakage can be determined by $\psi_{s,NL}$ and the initial stator flux linkage in second stage $\psi_{s,FD0}$ as

$$L_{s\lambda} = \frac{\psi_{s,NL} - \psi_{s,FD0}}{i_{s,NL}} \tag{3}$$

Using the decaying rotor quantities, $u_{r,amp}(t)$ and $i_{r,amp}(t)$, the rotor resistance and rotor flux linkage can be derived by

$$R_r(t) = \frac{u_{r,amp}(t)}{i_{r,amp}(t)} \tag{4}$$

$$\psi_{r,amp}(t) = \int u_{r,amp}(t)\, dt \tag{5}$$

Furthermore, the rotor inductance $L_r = L_m + L_{r\lambda}$ and rotor leakage inductance $L_{r\lambda}$ variation with time can be obtained by

$$L_r(t) = \frac{\psi_{r,amp}(t)}{i_{r,amp}(t)} \tag{6}$$

$$L_{r\lambda}(t) = L_r(t) - L_m(t) \tag{7}$$

TABLE I
IM'S DESIGN DATA [9], [10].

Parameter	Value	Unit
Maximum power	165	kW
Maximum torque	355	Nm
Maximum line current	333	A
Number of pole pairs	2	-
Number of turns	6	-
Iron core stack length	210	mm
Stator outer diameter	245	mm
Stator inner diameter	157.2	mm
Air gap length	0.6	mm
Rotor outer diameter	156	mm
Rotor inner diameter	50	mm
Number of stator slots	48	-
Number of rotor slots	58	-
Stator coil material	Copper	-
Rotor bar material	Aluminium	-
Iron core material	M235-35A	-

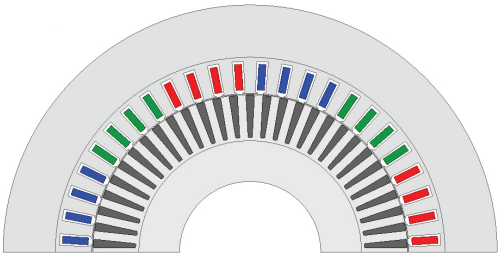

Fig. 4. Cross-section of investigated IM.

III. FEM MODEL

The design details of the investigated 2D FEM model are presented in Table I. Its cross-section of one pole-pair is in Fig. 4. This model is built in Ansys/Maxwell, and a flux-decay test with two stages is performed.

IV. RESULTS

A. Base case

In this section, the results of a two-stage flux-decay test of the base case conducted in FEM are presented. The stator flux linkages of phases A, B and C, as well as their amplitudes, are shown in Fig. 5. The stator current is set to zero at $time = 0s$. It can be seen that there is an obvious jump in stator flux linkage amplitude right at the $time = 0s$, which will be used to calculate the stator leakage inductance. In Fig. 6, the amplitudes of the rotor and stator flux linkages are presented, where the difference between the rotor one and the stator one is considered as the rotor leakage flux in this work. The rotor current in Fig. 7 is calculated from the rotor bar current derived from FEM, the method to refer the rotor bar quantities to the stator side can be found in [6], [11].

All inductances of the TFM, including the dependence on the current derived from the flux-decay test, are shown in Fig.8. It is clear that the rotor inductance, magnetizing inductance, and rotor leakage inductance are decreased by the increase of current due to the saturation of the iron core.

In Fig. 9 and 10, the rotor resistance R_r and the total leakage inductance $L_{t\lambda} = L_{s\lambda} + L_{r\lambda}$ obtained by both flux-decay and locked-rotor tests are displayed, where the locked-rotor test is performed at $f_0 = 10Hz$ in order to eliminate the skin effect. In addition to simulation, a theoretical value of

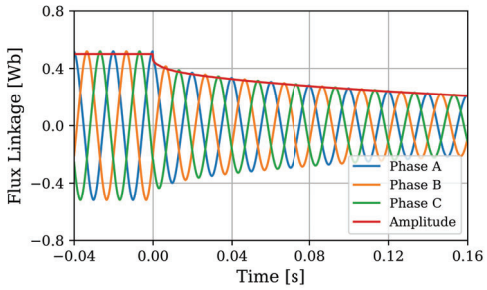

Fig. 5. Stator flux linkage varying with time from the flux-decay test for the base case.

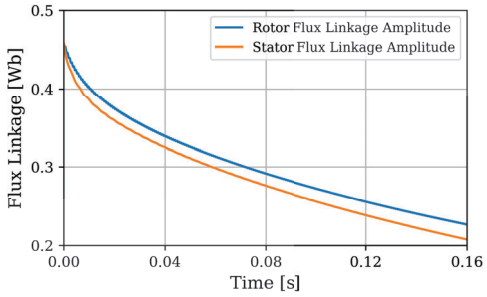

Fig. 6. Stator and rotor flux linkages varying with time in the second stage of the flux-decay test for the base case.

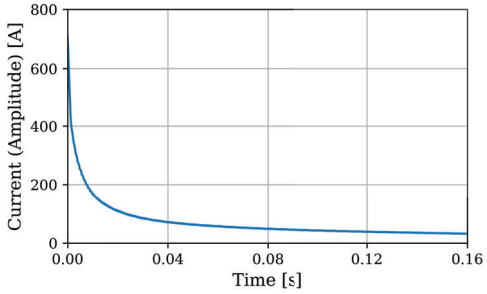

Fig. 7. Rotor current amplitude varying with time in the second stage of the flux-decay test for the base case.

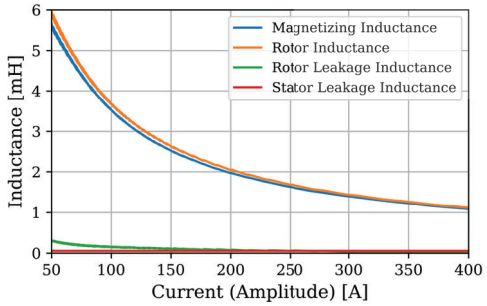

Fig. 8. Inductances varying with the current in the second stage of the flux-decay test for the base case.

R_r is calculated from the design data of IM by the formula in [11]. On the one hand, it can be seen that both curves from two tests in Fig. 9 have no obvious upward or downward trend with the current increment. Furthermore, the one from

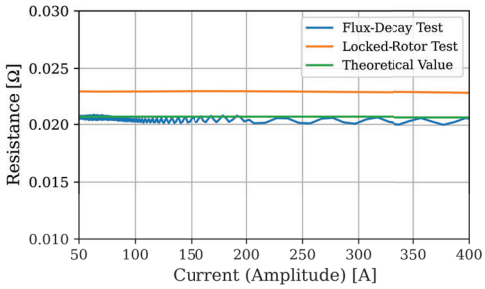

Fig. 9. Inductances varying with the current from the flux-decay and the locked-rotor tests for the base case.

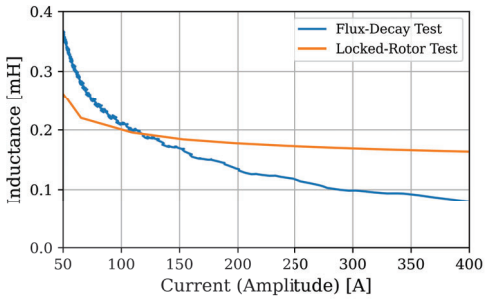

Fig. 10. Total leakage inductance varying with the current from the flux-decay and the locked-rotor tests for the base case.

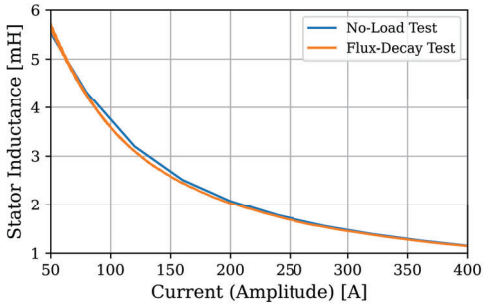

Fig. 11. Stator inductance varying with the stator current from the flux-decay and the no-load tests.

the lock-rotor test is a bit higher than the one from the flux-decay test and the theoretical value, which is expected since there is still a slight skin effect with $f_0 = 10Hz$. On the other hand, $L_{t\lambda}$ from both tests have downward trends with the current increment. However, the discrepancy of $L_{t\lambda}$ between the two tests is comparably high, which should be examined furtherly by implementing them into the control scheme.

The stator inductance L_s varying with current obtained from both no-load and flux-decay tests is presented in Fig. 11. The result shows a great agreement between these two tests.

B. Comparison of three cases for stator leakage inductance

In this section, two additional cases are set up to examine if the difference between the amplitudes of $\psi_{s,NL}$ and $\psi_{s,FD0}$ could represent the major quantity of stator leakage flux. The first base case has been presented in the previous section, and

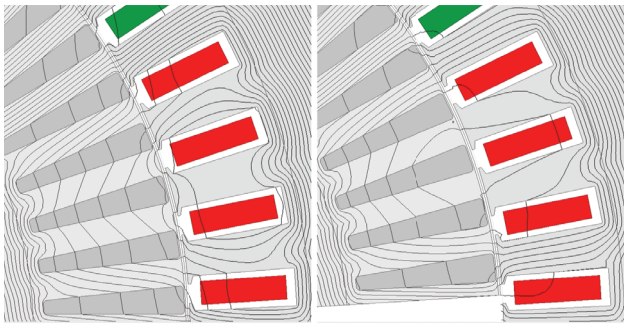

(a) Before cut-off. (b) After cut-off.

Fig. 12. Flux lines for the base case before and after the cut-off from stator current.

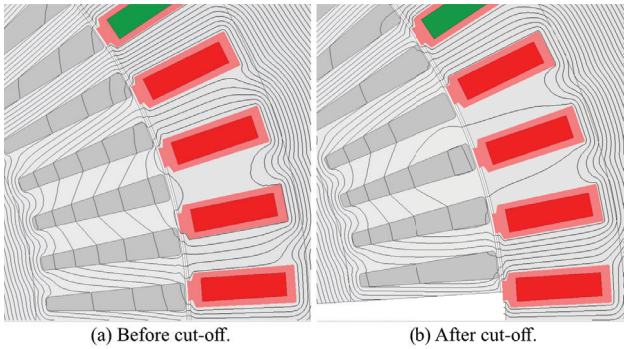

(a) Before cut-off. (b) After cut-off.

Fig. 13. Flux lines for the case with flux stoppers before and after the cut-off from stator current.

its plot of flux lines is shown in Fig. 12. It shows that there did have leakage flux caused by the stator current in the stator, air gap, and head of the rotor slot before the stator current cut-off, and then after the cut-off, it is the rotor current causing the leakage flux. The second one is a case in which the spaces of the stator slots extended to the middle of the air gap are filled by materials with extremely low relative permeability ($\mu_r = 10^{-9}$), called "flux stopper" in this work. They are shown in Fig. 13 (coral red objects), which aim to eliminate stator leakage flux as much as possible. In the last case, the heads of stator slots are changed from 2.9mm to 0.2mm and filled with a magnetic material with relative permeability $\mu_r = 5$, named "magnetic wedge" here, of which purpose is to increase the stator leakage flux. As Fig. 14 has shown, the leakage flux caused by the stator current increased from the base case.

The traces of stator flux linkage amplitudes before and after the moment of the stator current cut-off are depicted in Fig. 15, their values of amplitude, as well as the stator main and leakage inductances are listed in II. The results have shown two adjustments from the base case are aligned with the expectations. In the second case with flux stoppers, the difference between the amplitudes of $\psi_{s,NL}$ and $\psi_{s,FD0}$ dropped to $0.006Wb$ from $0.043Wb$ of the base case, resulting in a much smaller leakage inductance $0.009mH$ The results of another case with magnetic wedges have increments of leakage inductance to $0.078mH$ from $0.061mH$.

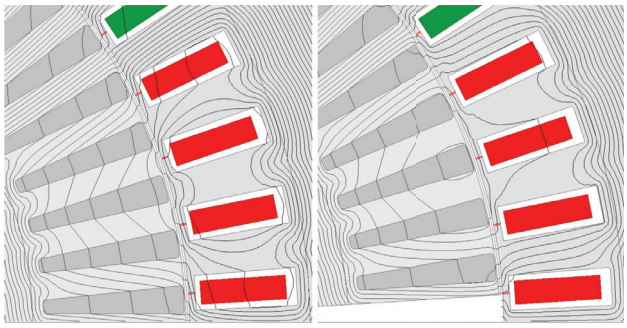

(a) Before cut-off. (b) After cut-off.

Fig. 14. Flux lines for the case with magnetic wedges before and after the cut-off from stator current.

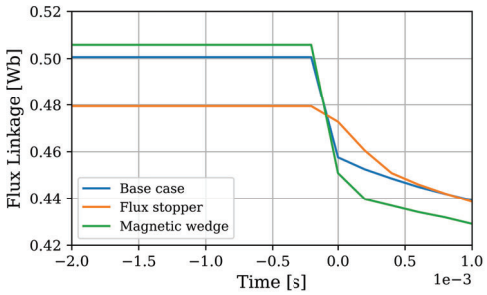

Fig. 15. Stator flux linkage amplitudes for three cases.

TABLE II
STATOR FLUX LINKAGE AMPLITUDE AND STATOR MAIN AND LEAKAGE INDUCTANCES FOR THREE CASES.

Case	$\psi_{s,NL}$ **[Wb]**	$\psi_{s,FD0}$ **[Wb]**	L_s **[mH]**	$L_{s\lambda}$ **[mH]**
Base case	0.501	0.458	0.708	0.061
Flux stopper	0.479	0.473	0.678	0.009
Magnetic wedge	0.506	0.451	0.715	0.078

V. CONCLUSION

A method to determine the T-form model(TFM) parameters of an IM is proposed. The aim is to be utilized to find the optimal points for IMs used in variable-speed applications with a range of operational zone. Thus, the flux-decay with two stages is performed in Ansys/Maxwell. In addition, several conventional methods with various current levels are applied to verify the usefulness of the proposed method. The results have shown that the proposed method has a very good match with the conventional method when it comes to rotor resistance R_r and the stator inductance L_s. The results also reveal that several no-load tests with different current levels can be replaced by a two-stage flux-decay test. Furthermore, two additional cases are implemented in order to show the relationship between the stator leakage flux and the amplitude of stator flux difference before and after the stator current cut-off.

However, the discrepancy between leakage inductance $L_{t\lambda}$ is high. A further study to use these two sets of parameters in control would be great to be conducted in the future.

REFERENCES

[1] "Ieee standard test procedure for polyphase induction motors and generators," *IEEE Std 112-2017 (Revision of IEEE Std 112-2004)*, 2018. [Online]. Available: https://doi.org/10.1109/IEEESTD.2018.8291810

[2] A. Bonnett and G. Soukup, "Nema motor-generator standards for three-phase induction motors," *IEEE Industry Applications Magazine*, vol. 5, no. 3, pp. 49–63, 1999. [Online]. Available: https://doi.org/10.1109/2943.758901

[3] M. Matsushita, S. Mizuno, and F. Ishibashi, "Bridge and rotor inductances of closed slots induction motor," in *2015 IEEE International Magnetics Conference (INTERMAG)*, 2015, pp. 1–1. [Online]. Available: https://doi.org/10.1109/INTMAG.2015.7156887

[4] H.-P. Nee, "Rotor slot design of inverter-fed induction motors," in *1995 Seventh International Conference on Electrical Machines and Drives (Conf. Publ. No. 412)*, 1995, pp. 52–56. [Online]. Available: https://doi.org/10.1049/cp:19950834

[5] K. Delaere, R. Belmans, and K. Hameyer, "Influence of rotor slot wedges on stator currents and stator vibration spectrum of induction machines: a transient finite-element analysis," *IEEE Transactions on Magnetics*, vol. 39, no. 3, pp. 1492–1494, 2003. [Online]. Available: https://10.1109/TMAG.2003.810552

[6] M.-J. Hsieh, T. Thiringer, and E. A. Grunditz, "Improved parametric representation of im from fem for more accurate torque predictions," in *2022 International Conference on Electrical Machines (ICEM)*, 2022, pp. 599–605. [Online]. Available: https://doi.org/10.1109/ICEM51905.2022.9910617

[7] E. Armando, A. Boglietti, S. Musumeci, and S. Rubino, "Flux-decay test: A viable solution to evaluate the induction motor rotor time-constant," *IEEE Transactions on Industry Applications*, vol. 57, no. 4, pp. 3619–3631, 2021. [Online]. Available: https://doi.org/10.1109/TIA.2021.3076425

[8] E. Armando, A. Boglietti, F. Mandrile, E. Carpaneto, and S. Rubino, "A detailed analysis of the electromagnetic phenomena observed during the flux-decay test," in *2022 International Conference on Electrical Machines (ICEM)*, 2022, pp. 767–773.

[9] H. Husson, R. Thomas, and L. Garbuio, "2d finite element model of the audi e-tron induction motor," in *2021 IEEE Vehicle Power and Propulsion Conference (VPPC)*, 2021, pp. 1–6. [Online]. Available: https://doi.org/10.1109/VPPC53923.2021.9699149

[10] J. Doerr, T. Attensperger, L. Wittmann, and T. Enzinger, "The new electric axle drives from audi," *MTZ worldwide*, vol. 79, pp. 18–25, 2018.

[11] O. Wallmark, *AC Machine Analysis Fundamental Theory*. Department of Eletrical Conversion, KTH Royal Institution of Technology, 2020.

BIOGRAPHIES

Meng-Ju Hsieh works at Chalmers university of Technology, in Göteborg Sweden, as a Ph.D. student. She took her M.Sc. (Eng.) at Chang Gung University, Taiwan in 2011. Her areas of interest include the modelling and control of vehicular traction electric machines considering both environmental and electromechanical performances.

Torbjörn Thiringer (Senior Member, IEEE) works as a Professor in electric power engineering at Chalmers University of Technology in Göteborg, Sweden, from which he received his M.Sc. and Ph.D. in 1989 and 1996, respectively. His research interests include the modelling, control, and grid integration of wind energy converters as well as power electronics, battery technologies, and electric machines for various applications.

PAPER C

Maximum Torque Control Operating Points Estimation for Variable-Speed IM Applications by Parameter-Based Model

Meng-Ju Hsieh, and Torbjörn Thiringer

In *IECON 2023- 49th Annual Conference of the IEEE Industrial Electronics Society*,
pages 1–6, 2023.

The layout has been revised.

IECON 2023- 49th Annual Conference of the IEEE Industrial Electronics Society | 979-8-3503-3182-0/23/$31.00 ©2023 IEEE | DOI: 10.1109/IECON51785.2023.10311892

Maximum Torque Control Operating Points Estimation for Variable-Speed IM Applications by Parameter-Based Model

1st Meng-Ju Hsieh
Division of Electric Power Engineering
Department of Electrical Engineering
Chalmers University of Technology
Göteborg 41296, Sweden
mengju.hsieh@chalmers.se

2nd Torbjörn Thiringer
Division of Electric Power Engineering
Department of Electrical Engineering
Chalmers University of Technology
Göteborg 41296, Sweden
torbjorn.thiringer@chalmers.se

***Abstract*—In this work, a follow-up study of estimating optimal operating points by an improved parameter-based model of three-phase induction machines (IMs) is conducted and presented. The main objective is to examine the representation of IMs' parameters within a specified operating boundary. The paper begins by reviewing the theory behind the inverse Γ-form model (IGFM) and maximum torque control. This review serves as a foundation for developing methods for estimating operating points. Finally, the study compares the results obtained using a 2D electromagnetic finite element method (FEM) model of a 15kW IM with those derived using a parameter-based model obtained through the conventional method, demonstrating the practical utility of the improved parameter-based model.**

***Index Terms*—induction machine (IM), maximum torque control, parameter-based model.**

NOMENCLATURE

N_{pp}	Number of pole pairs
ω_0, ω_1	Synchronous and rotor electrical speed
ω_2	Slip electrical speed, $\omega_0 - \omega_1$
T_e	Electromagnetic torque
n_r	Rotor mechanical speed, $n_r = 60\omega_1/(2\pi N_{pp})$
$n_{r,base}$	Base rotor mechanical speed
d-q	Real and imaginary parts of the stator synchronous rotational coordinate system, speed: ω_0
$\underline{u}_s, \underline{i}_s$	Stator voltage and current phasors
$\underline{\psi}_s$	Stator flux linkage phasor
$\underline{\psi}_R$	Inverse Γ-form rotor flux linkage phasor
$\underline{i}_M, \underline{i}_R$	Inverse Γ-form magnetizing and rotor current phasors
$\underline{u}_R$	Inverse Γ-form rotor induced voltage phasor
R_s, R_R	Stator and inverse Γ-form rotor resistances
L_M, L_σ	Inverse Γ-form magnetizing and leakage inductance
U_s, u_s^d, u_s^q	Stator phase voltage amplitude and d-q components
I_s, i_s^d, i_s^q	Stator current amplitude and d-q components
ψ_R^d, ψ_R^q	Rotor flux linkage d-q components
$\theta_{u,dq}, \theta_{i,dq}$	Stator voltage and current angles on d-q plane
max	Subscript indicating the maximum value

Swedish Electromobility Center, Swedish Energy Agency

I. INTRODUCTION

The induction machine (IM) is widely used as a traction electric machine (EM) for electric vehicles due to its durability, cost-effectiveness, and rare-earth-metal-freeness. However, compared to permanent magnet synchronous machines (PMSMs), another popular type of EM, IMs are more complex to control, and their performance is harder to predict during the design phase. This complexity arises from the slip speed between the rotor and stator electrical speeds, which introduces greater flexibility in torque and rotor mechanical speed demands. Additionally, the simulation time for finite element method (FEM) analysis of IMs is, unfortunately longer than that of PMSMs. To design IMs suitable for variable speed applications without repeating prototyping, the authors in [1] recommend employing the FEM model to accurately ascertain the range of optimal operating points throughout the complete torque-speed map. To minimize the computational burden, a distinct simulation workflow with the knowledge of IMs' maximum torque control is also proposed. Experimental evidence validates the results derived through the use of FEM. However, the computing load and time to derive a complete torque-speed map remain considerable, particularly when optimizing IMs' designs due to redundant FEM simulations.

Parameter-based models like the T-form model (TFM) or inverse Γ-form model (IGFM) are used to reduce the number of required simulations. These approaches offer two advantages. Firstly, they reduce the need for extensive FEM simulations to identify optimal operating points during IM design. Instead, optimal points can be determined by sweeping slip and current level combinations using FEM simulations. Secondly, parameter-based models like TFM and IGFM can be easily applied for refined evaluations such as minimum loss control or benchmark assessments. Therefore, it is crucial to build IM parameter-based model during the design stage accurately.

Several studies have utilized FEM programs to predict the parameters of IMs during the design stage for effective control.

In [2], a proposed approach involved exciting both the stator and rotor windings using the FEM magnetostatic solver. This method significantly reduced the expected simulation time compared to the transient solver. However, it may lead to lower accuracy when IMs with high skin effects. Therefore, this paper, along with [3], [4], utilized the transient solver to maintain accuracy in such applications. In [3], the authors employed three different load tests to identify the parameters of the TFM. The stator and rotor current and flux linkage phasors were obtained from FEM analysis. However, the extraction of rotor phasors was not discussed in detail in [3]. In [4], the authors determined the IGFM parameters by applying several voltages with small amplitudes and a range of frequencies to three different IMs through an inverter. However, the IMs were tested at a standstill, and the frequency range of 10 to 40 Hz used did not align with the typical operating range of the rotor frequency. Furthermore, both [3], [4] lacked performance predictions for torque based on equivalent parameters. The study [5] primarily investigates the application of flux-decay experiments to extract the ratio between rotor resistance and rotor inductance, as known as rotor time constant, in one wound and two squirrel cage IMs. The authors conducted an analysis of voltage envelope time constants during the flux decay stages of IMs, exploring the influence of flux linkage magnitudes on the said ratio. It is evident from the results that the ratio is subject to changes based on flux linkage magnitudes, particularly for closed rotor slot scenarios. A follow-up study, [6], delves deeper into analyzing the time constants at the start and finish of the decay phase, observing an increase in the time constant towards the conclusion of the test. Nevertheless, it's worth noting that the outcomes of these research studies are not coupling with FEM analysis, which limits their practicality in the early design stage. In [7], multiple no-load and load tests were performed using FEM. The results showed improved parameter determination compared to the conventional method, and a good agreement between the FEM model and IGFM in torque prediction. While the investigated machine is only operated at one speed. Thus, a further control strategy is needed to examine the usefulness of the parameter-based model using the proposed method.

This study focuses on examining the degree of representative of IGFM parameters using a proposed method from [7] by applying maximum torque control within a specified operating boundary. The results demonstrate that the proposed method offers higher accuracy compared to conventional approaches such as no-load and locked-rotor tests. The main contribution of this paper is the step-by-step procedure for estimating optimal operating points using an improved parameter-based model. Furthermore, the study verifies the enhanced estimation of operating points using maximum torque control compared to the conventional method. The findings indicate that the improved parameter-based model can more precisely determine optimal operating points with acceptable discrepancy from the ones by the FEM model.

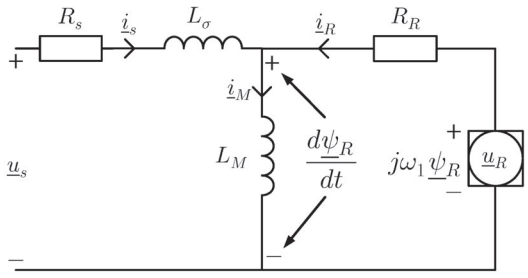

Fig. 1. Dynamic inverse Γ-form model of IMs.

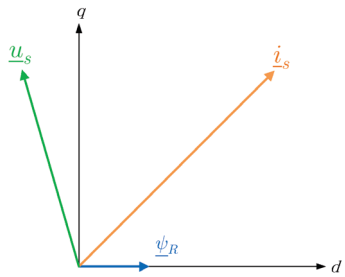

Fig. 2. Stator current phasor, stator voltage phasor and rotor flux phasor on d-q plane.

II. Control Template

In this work, the perfect field-oriented control (PFOC) based on the IGFM is applied as a control template. The IGFM's dynamic form is presented in Fig. 1. The rotor flux linkage $\underline{\psi}_R$ is aligned to the d-axis and the d-quantity ψ_R^d equals to the amplitude of $\underline{\psi}_R$ as shown in Fig. 2. The amplitude of the magnetizing and the rotor current is equal to i_s^d and i_s^q, respectively.

$$\begin{cases} |\underline{\psi}_R| = \psi_R^d \\ |\underline{i}_M| = i_s^d = I_s cos(\theta_{i,dq}) \\ |\underline{i}_R| = i_s^q = I_s sin(\theta_{i,dq}) \end{cases} \tag{1}$$

where $I_s = |\underline{i}_s|$ is the stator current amplitude, $\theta_{i,dq}$ is the stator current angle on d-q plane.

Consequently, the d-axis rotor flux linkage, electromagnetic torque and electrical slip speed can be stated as

$$\psi_R^d = L_M \, i_s^d \tag{2}$$

$$T_e = \frac{3}{2} N_{pp} \, \psi_R^d \, i_s^q \tag{3}$$

$$\omega_2 = \frac{R_R \, i_s^q}{\psi_R^d} \tag{4}$$

Accordingly, the R_R, L_M and ψ_R^d are crucial to predict operating points.

Additionally, the stator phase voltage at d-q plane can be stated as

$$\begin{cases} u_s^d = (R_s + R_R) i_s^d + L_\sigma \dfrac{di_s^d}{dt} - \omega_0 L_\sigma i_s^q - \dfrac{R_R}{L_M} \psi_R^d \\ \\ u_s^q = (R_s + R_R) i_s^q + L_\sigma \dfrac{di_s^q}{dt} + \omega_0 L_\sigma i_s^d + \omega_1 \psi_R^d \end{cases} \tag{5}$$

III. Maximum Torque Control

Maximum torque control aims to extract the maximum electromagnetic torque per stator current. However, due to the limitation of the inverter and the IM capability, different constraints are applied at low-, medium-, and high-speed ranges.

A. Maximum torque per ampere (MTPA) region

In the low-speed region, the only constraint is the stator current limit. The optimal operating points are the maximum torque for the given stator current. Insert (2) into (3) and (4), the electromagnetic torque and electrical slip speed can be expressed as the function of $\theta_{i,dq}$ and I_s.

$$\begin{cases} T_e = \dfrac{3}{4}\, N_{pp}\, L_M\, I_s^2\, sin(2\theta_{i,dq}) \\ \\ \omega_2 = \dfrac{R_R}{L_M}\, tan(\theta_{i,dq}) \end{cases} \tag{6}$$

From (6), it can be seen that the maximum torque would happen at $\theta_{i,dq} = 45^\circ$ if the other parameters (R_R and L_M) are fixed. While, with the increase of the stator current level, IGFM parameters would differ due to the saturation of the iron core and affect the control accuracy. Hence, improved IGFM parameter sets derived by the proposed method in [7] are used in this work.

B. Field-weakening (FW) region

When IMs reach the limitation of dc bus voltage limit, it is when the FW strategy should be applied to extract maximum torque at medium speed. Insert (2) and (4) into (5) and consider only steady-state control of IMs, d-q quantities of the stator phase voltage can be expressed as

$$\begin{cases} u_s^d = R_s i_s^d - \omega_0 L_\sigma i_s^q \\ \\ u_s^q = R_s i_s^q + \omega_0 (L_\sigma + L_M) i_s^d \end{cases} \tag{7}$$

From (7), it can be observed that the rotor flux magnitude ψ_R^d should be reduced with the increase of frequency to maintain the stator phase voltage level below its limitation. To achieve this, the approach is to increase the d-q plane stator current angle $\theta_{i,dq}$ and electrical slip speed, which means the less current (i_s^d) goes to magnetizing branch and the more (i_s^q) enters the rotor branch of IGFM.

The effect from R_s to stator phase voltage can be neglected when the injected frequency is high. Then, the constrain could be set as

$$u_s^{d^2} + u_s^{q^2} = \omega_0^2 \left[(L_\sigma i_s^q)^2 + \left((L_\sigma + L_M) i_s^d \right)^2 \right] \leq U_{s,max}^2 \tag{8}$$

where $U_{s,max}$ is the maximum stator phase voltage limited by dc-link.

C. Maximum torque per voltage (MTPV) region

With the increase of the IM's rotor rotational speed and injected frequency, the slip rate ($slip = \omega_2/\omega_0$) reaches the breakdown torque point where the maximum torque per voltage happens. Insert (7) and (2) into (3) and (4), and neglect the effect from R_s, the torque and slip frequency equation at maximum voltage can be expressed as

$$T_e = \frac{-3 N_{pp} L_M U_s^2}{4\omega_0^2 L_\sigma (L_\sigma + L_M)}\, sin(2\theta_{u,dq}) \tag{9}$$

$$\omega_2 = \frac{-R_R (L_\sigma + L_M)}{L_M L_\sigma}\, cot(\theta_{u,dq}) \tag{10}$$

where $U_s =$, $\theta_{u,dq}$ is the d-q plane voltage angle.

D. Optimal stator current trajectory

Fig. 3 depicts the optimal stator current trajectory for maximum torque control. The blue, orange, and green solid lines represent the current trajectories of the MTPA, the FW, and the MTPV regions respectively [1]. With improved IGFM and (6), the maximum torque points can be derived by sweeping $\theta_{i,dq}$ and I_s. It is practical to start the iteration from the minimum current $I_{s,min}$ and minimum $\theta_{i,dq} = 45^\circ$ to get $\theta_{i,dq,MTPA}$ where the maximum torque happens for given I_s. Furthermore, the $\theta_{i,dq,MTPA}$ for the lower stator current level can be the starting point for the next higher stator current level. Once the I_s reaches $I_{s,max}$, the maximum torque $T_{e,max}$ for a given current limit can be estimated. The base speed $n_{r,base}$ can be estimated by (8) as

$$n_{r,base} = \frac{60}{2\pi N_{pp}} \left[\frac{U_{s,max}}{\sqrt{(L_\sigma i_s^q)^2 + ((L_\sigma + L_M) i_s^d)^2}} - \omega_{2,T_{e,max}} \right] \tag{11}$$

where the boundary between the MTPA and the FW regions.

In the MTPV region, since the stator flux linkage is rather low, hence, low saturation at this point, the inductance values are almost fixed and the maximum torque would happen at $\theta_{u,dq} \approx 135^\circ$. Thus, the slip frequency can be derived by

$$\omega_{2,MTPV} \approx \frac{R_R (L_\sigma + L_M)}{L_M L_\sigma} \tag{12}$$

Then, the needed synchronous electrical speed for a given rotor speed can be yielded to

$$\omega_{0,MTPV} \approx \frac{2\pi n_r N_{pp}}{60} + \omega_{2,MTPV} \tag{13}$$

With the needed synchronous electrical speed and $U_s = U_{s,max}$, the torque T_e and stator current i_s^d and i_s^q can be derived by (9) and (7). In this region, it is feasible to start the estimation from the maximum voltage $u_{s,max}$ and rotor speed $n_{r,max}$, and reduce the rotor speed until I_s reaches $I_{s,max}$ which is the boundary between the MTPV and the FW regions.

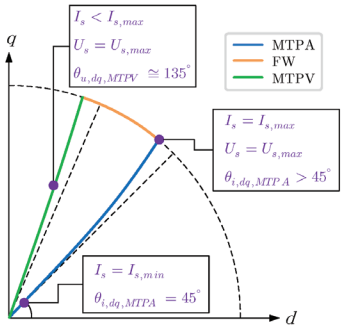

Fig. 3. Stator current trajectory on d-q plane.

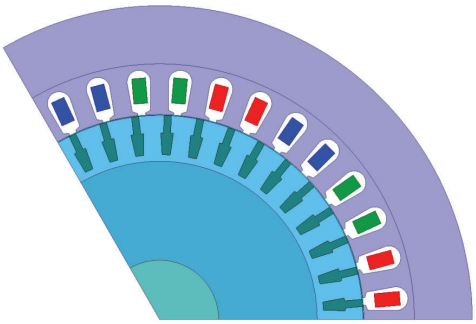

Fig. 4. Cross-section of the 15 kW IM FEM model.

TABLE I
DESIGN DETAILS OF THE 15KW IM.

Parameter	Unit	Value
Max speed	rpm	4000
Max DC-link voltage U_{DC}	V	400
Max current $I_{s,rms}$	A	32
Number of pole pairs N_{pp}	-	3
Iron core stack length	mm	230
Stator outer diameter	mm	291.2
Stator inner diameter	mm	190.2
Number of stator slots Q_s	-	36
Rotor outer diameter	mm	189.3
Rotor inner diameter	mm	55
Rotor end-ring average diameter	mm	163.3
Number of the rotor slots Q_r	-	39
Number of turns per coil N_s	-	38
Area of a stator turn	mm^2	1.98
Number of parallel strands per turn	-	2
Number of parallel branches N_{pb}	-	3
Terminal connection	-	Y
Stator coil material	-	Copper
Rotor bar material	-	Aluminium
Iron core material	-	M700-50A

IV. MODEL

A. FEM Model

The design details of investigated FEM model are presented in Table I. Its cross-section of one pole-pair is in Fig. 4.

B. Parameter-based model using proposed and conventional methods

The IGFM parameters are derived by the proposed method in [7] and are listed in Table II and depicted in Fig. 5. These

TABLE II
IGFM PARAMETERS.

Parameter	Unit	Conventional	Proposed
R_R	Ω	0.148	0.142
L_σ	mH	3.71	3.16

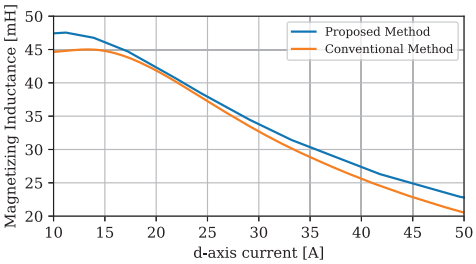

Fig. 5. Magnetizing inductance varying with the IGFM magnetizing current amplitude i_s^d from two different methods.

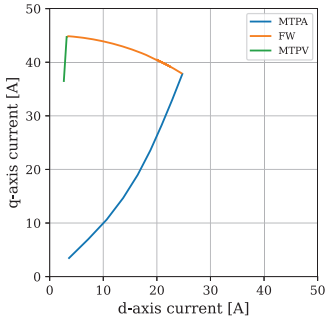

Fig. 6. Estimated stator current trajectory.

parameters are used to estimate the maximum torque operating points in this work. In addition, a conventional method is performed to show the improvement of the proposed method.

V. RESULTS

A. Operating points estimated by a parameter-based model using proposed method

In this section, the results of operating points calculated by the improved parameter-based model are presented. In Fig. 6, the estimated stator current trajectory shows that the trend matches as expected, $\theta_{i,dq}$ starts from 45° and increases with I_s. In the MTPV region, i_s^d almost remains at the same value, and it is mainly i_s^q that varies with I_s. Fig.7-10 present the torque-speed map of estimated stator current magnitude, rotor flux linkage magnitude, slip electrical frequency, and stator phase voltage magnitude respectively.

B. Validation

The comparisons between the three models for IM's performance, including torque, rotor mechanical speed and slip electrical frequency, are shown in Fig. 11 and 12, where the upper plots are in real value and lower plots are the discrepancies between the results estimated by the parameter-based models

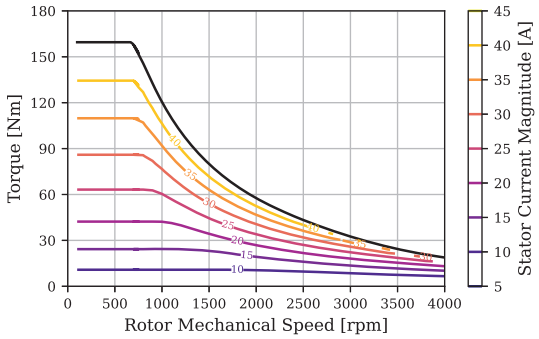

Fig. 7. Estimated stator current magnitude I_s map.

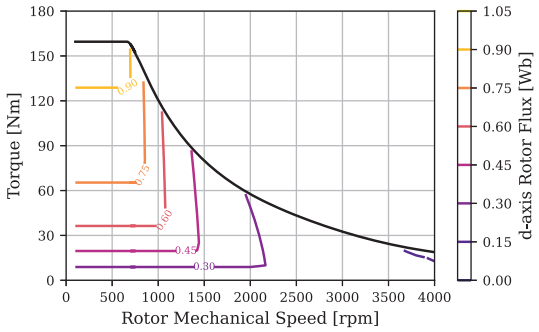

Fig. 8. Estimated rotor flux linkage magnitude ψ_R^d map.

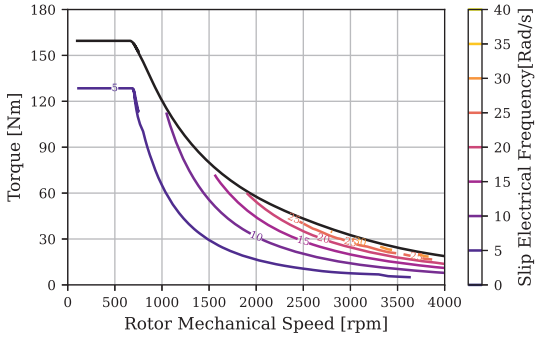

Fig. 9. Estimated slip electrical speed ω_2 map.

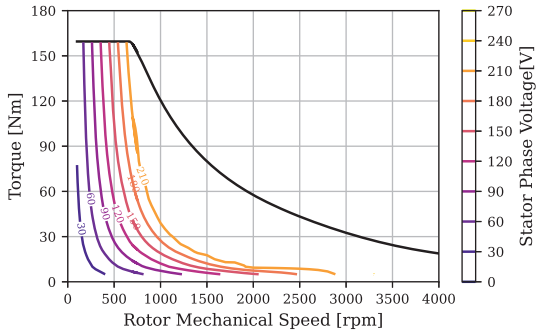

Fig. 10. Estimated stator voltage magnitude U_s map.

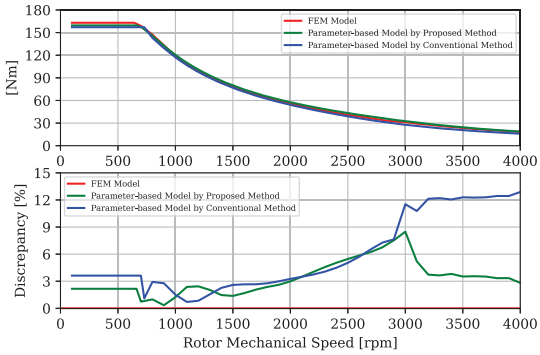

Fig. 11. Comparison of estimated maximum torque varying with rotor speed.

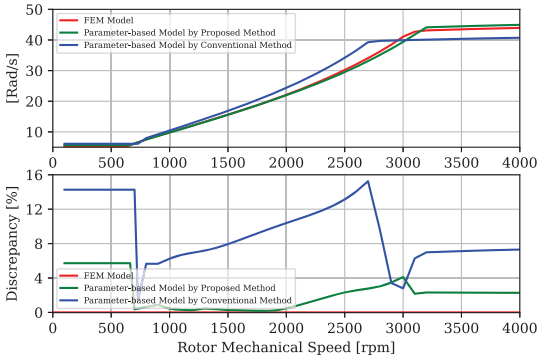

Fig. 12. Comparison of estimated slip electrical frequency varying with rotor speed.

and the FEM model. The results show that estimated operating points by parameters from the proposed method better match the ones from the FEM than the conventional method in the FW and the MTPV regions for both T_e and ω_2 calculations. While in the MTPA region, the differences between the three models are rather nonidentical. A hypothesis is that the leakage inductance is overestimated from the conventional method, which makes the estimation reaches the MTPV region at a lower speed in the model with parameters compared to using the conventional method.

VI. Conclusions

This work reviews the theory of maximum torque control at low-, medium-, and high-speed regions. Then, an improved parameter-based model using the proposed method in [7] is applied with maximum torque control to predict the optimal operating points of a 15kW IM. A FEM model and a parameter-based model derived from the conventional method are also applied to verify the usefulness and improvement of IM performance estimation. The results show the parameters by the proposed method have a better representation of this

IM over a given operating zone.

ACKNOWLEDGMENT

The authors would like to thank the Swedish Energy Agency and Swedish Electromobility Center for their financial support.

REFERENCES

[1] H. Cai, L. Gao, and L. Xu, "Calculation of maximum torque operating conditions for inverter-fed induction machine using finite-element analysis." *IEEE Transactions on Industrial Electronics*, vol. 66, no. 4, pp. 2649–2658, 2019. [Online]. Available: https://doi.org/10.1109/TIE.2018.2847700

[2] L. Alberti, N. Bianchi, and S. Bolognani, "Variable-speed induction machine performance computed using finite-element," *IEEE Transactions on Industry Applications*, vol. 47, no. 2, pp. 789–797, 2011. [Online]. Available: https://doi.org/10.1109/TIA.2010.2103914

[3] M. R. Hachicha, N. Ben Hadj, M. Ghariani, and R. Neji, "Finite element method for induction machine parameters identification," in *2012 First International Conference on Renewable Energies and Vehicular Technology*, 2012, pp. 490–496. [Online]. Available: https://doi.org/10.1109/REVET.2012.6195318

[4] M. Carraro and M. Zigliotto, "Automatic parameter identification of inverter-fed induction motors at standstill," *IEEE Transactions on Industrial Electronics*, vol. 61, no. 9, pp. 4605–4613, 2014. [Online]. Available: https://doi.org/10.1109/TIE.2013.2289903

[5] E. Armando, A. Boglietti, S. Musumeci, and S. Rubino, "Flux-decay test: A viable solution to evaluate the induction motor rotor time-constant," *IEEE Transactions on Industry Applications*, vol. 57, no. 4, pp. 3619–3631, 2021. [Online]. Available: https://doi.org/10.1109/TIA.2021.3076425

[6] E. Armando, A. Boglietti, F. Mandrile, E. Carpaneto, and S. Rubino, "A detailed analysis of the electromagnetic phenomena observed during the flux-decay test," in *2022 International Conference on Electrical Machines (ICEM)*, 2022, pp. 767–773.

[7] M.-J. Hsieh, T. Thiringer, and E. A. Grunditz, "Improved parametric representation of im from fem for more accurate torque predictions," in *2022 International Conference on Electrical Machines (ICEM)*, 2022, pp. 599–605. [Online]. Available: https://doi.org/10.1109/ICEM51905.2022.9910617

PAPER D

Improved parametric representation of IM from FEM for more accurate torque predictions: Simulations and experimental validations

Meng-Ju Hsieh, Emma Grunditz, Torbjörn Thiringer

Published in IEEE Transactions on Industry Applications,
60(5):6660–6671, 2024.

The layout has been revised.

Improved Parametric Representation of IM From FEM for More Accurate Torque Predictions: Simulations and Experimental Validations

Meng-Ju Hsieh, *Graduate Student Member, IEEE*, Emma Arfa Grunditz, *Member, IEEE*, and Torbjörn Thiringer, *Senior Member, IEEE*

***Abstract*—In this work, an updated methodology to determine the parameters of three-phase induction machines (IMs) is developed and presented. The goal of this determination is to achieve a better model representation of induction machines for the usage of a circuit-based control system. First, the theory of the T-form model (TFM) and the inverse Γ-form model (IGFM) are reviewed. The former review becomes the foundation of the following interpretation of the developing methods for identifying the needed parameters. Next, a 2D electromagnetic finite element method (FEM) model of a 15 kW IM is utilized to demonstrate the strength of the methodology on a real machine. Furthermore, a comparison of results using the conventional test and the newly proposed method is presented, demonstrating the strength of the proposed procedure with enhanced accuracy for the torque and slip prediction. Lastly, experimental results using a 15 kW IM are utilized to demonstrate the usefulness of the proposed parameter determination procedure.**

***Index Terms*—Induction machine (IM), parameter determination, finite element method (FEM), equivalent circuits, perfect field-oriented control (PFOC).**

NOMENCLATURE

N_p	Number of pole pairs.
N_{pb}	Number of parallel branches of winding connection.
N_s	Number of turns per stator coil.
c_s	Connection factor; $\sqrt{3}N_{pb}$ for Δ, N_{pb} for Y
Q_s, Q_r	Number of stator and rotor slots.
k_1	Winding factor of first-order harmonic.
ω_0, ω_1	Synchronous and rotor electrical speed.
ω_2	Slip electrical speed, $\omega_2 = \omega_0 - \omega_1$
s	Slip rate, $s = \omega_2/\omega_0$
T_e	Electromagnetic torque.
ω_r	Rotor mechanical speed, $\omega_r = \omega_1/N_p$
α-β	Real and imaginary parts of the stator stationary. coordinate system, speed: 0
u-v	Real and imaginary parts of the rotor rotational. coordinate system, speed: ω_r
d-q	Real and imaginary parts of the stator synchronous rotational coordinate system, speed: ω_0
X	Amplitude of phasor $\underline{x}$ in the α-β coordinate system.
X^{uv}	Amplitude of phasor $\underline{x}^{uv}$ in the u-v coordinate system.
x^y	y-axis component of phasor $\underline{x}$
$\underline{u}_s, \underline{u}_r$	Stator input and rotor induced voltage phasors.
$\underline{u}_{s,ind}, \underline{u}_m$	Stator induced and magnetizing voltage phasor.
$\underline{u}^{uv}_{bar,k}$	Induced voltage phasor for rotor bar k at rotor side.
$\underline{i}_s, \underline{i}_r, \underline{i}_m$	Stator, rotor, and magnetizing current phasors.
$\underline{\psi}_s, \underline{\psi}_r, \underline{\psi}_m$	Stator, rotor, and magnetizing flux linkage phasors.
$\underline{\psi}^{uv}_{bar,k}$	Flux linkage phasors for rotor bar k at rotor side.
R_s, R_r	Stator and rotor resistance.
R^{uv}_{bar}	A single rotor bar resistance at rotor side.
L_s, L_r, L_m	Stator, rotor, and magnetizing inductances.
$L_{s\lambda}, L_{r\lambda}$	Stator and rotor leakage inductances.
$\underline{i}_M, \underline{i}_R$	Transformed magnetizing and rotor current phasor.
$\underline{\psi}_R$	Transformed rotor flux linkage phasor.
L_M, L_σ	Transformed magnetizing and total leakage inductance.
R_R	Transformed rotor resistance.
$\theta^{uv}_{\underline{\psi}_r 0}$	Initial electrical angle of phasor $\underline{\psi}_r$ in the u-v coordinate system.
$\theta_{u,0}$	Initial electrical angle of the u-axis in the α-β coordinate system.
θ_{rf0}	Initial electrical angle between α-β and d-q coordinate systems.
P_{in}, Q_{in}	Input active and reactive powers.
P_{strand}	Stator ohmic loss.
P_{fe}, R_{fe}	Iron loss and its equivalent resistance.
$P_{friction}$	Friction loss.

Manuscript received 8 November 2023; revised 21 February 2024; accepted 21 April 2024. Date of publication 21 May 2024; date of current version 23 September 2024. Paper 2023-EMC-1295.R1, presented at the 2022 International Conference on Electrical Machines, Valencia, Spain, Sep. 05–08, and approved for publication in IEEE TRANSACTIONS ON INDUSTRY APPLICATIONS by the Electric Machines Committee of the IEEE Industry Applications Society [DOI: 10.1109/ICEM51905.2022.9910617]. This work was supported in part by Swedish Energy Agency and in part by Swedish Electromobility Center. *(Corresponding author: Meng-Ju Hsieh.)*

The authors are with the Chalmers University of Technology, 41296 Göteborg, Sweden (e-mail: mengju.hsieh@chalmers.se; emma.grunditz@chalmers.se; torbjorn.thiringer@chalmers.se).

Color versions of one or more figures in this article are available at https://doi.org/10.1109/TIA.2024.3403806.

Digital Object Identifier 10.1109/TIA.2024.3403806

I. Introduction

With the increasing usage of electrical machines (EMs) as traction motors in automotive applications, the need to drive effectively, i.e., to utilize the full capability of EMs, gains importance. To find the EMs' optimal operating points, such as maximum-torque-per-ampere points, and to achieve precise control, the strategies of field-oriented control (FOC) are commonly applied. Then, for the optimal operating points, the machine loss and efficiency maps can be constructed and used for performance evaluation.

Today, the two most commonly used machine types in electric vehicles are the permanent magnet synchronous machine (PMSM) and the induction machine (IM). IMs have several advantages, such as robustness, cost-effectiveness, and rare-earth-metal-freeness. However, IMs are more complex to control compared to PMSMs since there are several possible slip rate choices for one desired output torque and speed combination. Thus, to find the optimal operating points, a considerable number of finite element method (FEM) simulations may be required. Furthermore, since there are windings in both the stator and the rotor, the FEM simulation computation time for a single operating point of IMs becomes substantially high compared to the one for PMSMs.

Accordingly, equivalent circuit models, such as the T-form model (TFM) or the inverse Γ-form model (IGFM), are typically used to reduce the number of simulations. Therefore, to make conceptual and refined evaluations in the automotive industry, accurately predicted IM parameters for precise control are desired already at an early design stage, i.e., to reduce the need for repeated prototyping. In [2], [3], [4], three methods and procedures are developed to find the optimal operating points and their constraints based on the FOC. These papers also addressed the iron core saturation phenomenon of IMs (decreasing inductance with increasing stator flux linkage) that affects the control accuracies, thus showing the importance of accurate parameters. Parameter identification methods are, however, not covered.

The conventional method to identify the IMs equivalent circuit parameters is to conduct a no-load and a locked-rotor test, as exemplified in [5]. The parameters derived from the conventional method are typically acquired for only the rated operating point, where its stator flux linkage level is usually fixed. There are two main drawbacks of the locked-rotor test. Firstly, a reduced stator voltage frequency is preferred during the test to reduce the impact of skin effect on the rotor bars. At the same time, the frequency must be high enough to maintain the induction between the stator and rotor and thereby get good results. In [5], 25% of the rated stator frequency is recommended, which still is substantially above the rotor's normal electric frequency. Secondly, the stator and the rotor leakage inductances cannot be separated. Instead, general ratios are used, for instance, according to templates found in [6].

Several alternative methods to the locked-rotor test for identification of the IMs equivalent circuit parameters in [7], [8], [9] showed improvement in experiments. In [7], the rotor resistance of a 15 kW IM was determined experimentally from a load test, and the result was compared to an experimental locked-rotor test, showing a disagreement of above 20%. In [8], the author introduces a recursive least squares algorithm tailored for online parameter identification in dynamic automotive control of IMs to address parameter changes. Dynamic regression models are also proposed, considering iron losses depending on the operational points. The research in [9] focuses on utilizing flux-decay experiments to ascertain the ratio between rotor resistance and rotor inductance in a 15 kW squirrel cage IM. Through analysis of voltage envelope time constants during the flux decay phases of IM, the authors investigate the impact of flux linkage levels on this ratio. The findings reveal that the ratio exhibits variation with different flux linkage levels. However, the results from these studies were not coupled to any FEM analysis, which limits the usability during the early design stage.

In order to predict the parameters of IMs at the design stage to achieve effective control, there are several related studies employing FEM programs. In the studies in [10], [11], [12], [13], the parameters of the equivalent circuits considering saturation characteristics of the magnetizing inductance are identified, and the predictions from parameter-based models show good matches with experimental or simulation results. In [10], a suggested procedure to excite both the stator and the rotor windings using the FEM magnetostatic solver is presented. Its main advantage is the significant reduction of expected simulation time compared to the one by the transient solver. Nevertheless, the procedure would give lower accuracy for cases with high skin effects, such as those used in Tesla Model S/X and Audi e-Tron with deep rotor bars [14]. Hence, to avoid degraded accuracy in such applications, on the one hand, in [13], the author suggested an updated TFM to represent the components due to the iron saturation effect and deep-bar effect of rotor circuits by time-harmonic solvers. The comparison of the simulated results from the proposed model with those from transient FEA demonstrates the effectiveness of both the model and its parameter identification algorithm. However, the results have not yet been validated by experiments. On the other hand, the transient solver, which is recommended to predict the torque of nonlinear models in [15], is utilized in this paper, and [11], [12]. In [11], to determine the IGFM parameters, several voltages with small amplitudes and a range of frequencies are fed by an inverter to three different IMs. The nonideal effect from the inverter is included in the FEM and experiments, which makes the method feasible. The research in [12], an extended dynamic IM equivalent model, addressed magnetic saturation and the deep-bar effect. It presents a procedure for parameterizing the augmented model using standstill self-commissioning algorithms, verified through experiments. Nevertheless, the IMs are tested at standstill and with a frequency range between 10 and 40 Hz, which is not the typical operating range of the rotor frequency. Furthermore, the performance predictions of torque calculated by equivalent parameters are lacking in both [11], [12].

In this paper, a procedure to determine the dynamic equivalent circuit parameters depending on the magnetizing current of IMs using FEM is proposed, proving higher accuracy compared to using conventional no-load and locked-rotor tests. The proposed

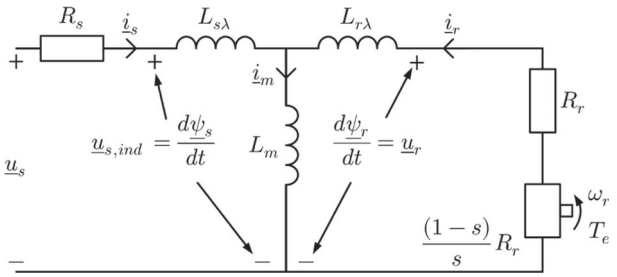

Fig. 1. Steady-state T-form model of IMs.

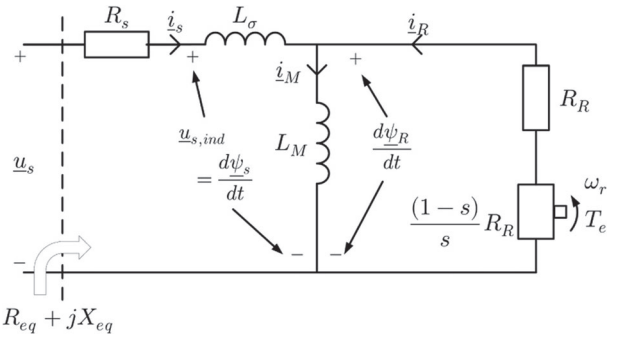

Fig. 2. Steady-state inverse Γ-form model of IMs.

method aims to utilize the full capability of FEM analysis to enhance the forecast of dynamic equivalent circuit parameters as well as torque prediction. The specific contribution is a step-by-step procedure to determine the parameters of both the TFM and the IGFM from the stator's and rotor's current and flux linkage phasors. The IM is simulated under no-load and load tests using the FEM transient solver for catching the effects of iron saturation and deep-bar. In addition, a verification of the improvement over the conventional method regarding torque forecast when using the IGFM parameters is presented. The results of the proposed method can be used to find the optimal operating points and to control IMs more precisely with a minimum amount of FEM simulation effort.

II. Theory

Perfect field-oriented control (PFOC) based on the IGFM is chosen as a control template in this work, meaning that the control is built on the alignment of a rotating coordinate system with the real axis (d-axis) in the direction of the rotor flux linkage $\underline{\psi}_R$, i.e., to have precise control, an accurate position of $\underline{\psi}_R$ is vital. Thus, in this section, the background theory of the two equivalent circuit models and the transformation of phasors from the rotor to the stator side are formulated.

A. T-Form Model (TFM)

The classical model used for the IM representation is the steady-state TFM in the α-β stationary reference frame using amplitude invariant scaling. This model is depicted in Fig. 1. The relation of current phasors can be found as

$$\underline{i}_m = \underline{i}_s + \underline{i}_r. \tag{1}$$

The stator and rotor flux linkage phasors $\underline{\psi}_s$ and $\underline{\psi}_r$ can be expressed as

$$\underline{\psi}_s = L_s\, \underline{i}_s + L_m\, \underline{i}_r \tag{2}$$

$$\underline{\psi}_r = L_r\, \underline{i}_r + L_m\, \underline{i}_s \tag{3}$$

where $L_s = L_m + L_{s\lambda}$ and $L_r = L_m + L_{r\lambda}$. In practice, these inductances vary with the magnitude of the magnetizing current I_m due to the iron core saturation.

In this paper, FEM analysis is used to determine the currents and flux linkages, and then (1)–(3) is used for the estimation of the magnetizing current $\underline{i}_m$, the magnetizing inductance L_m, the stator inductance L_s, and the rotor inductance L_r.

Besides, the rotor resistance R_r can be acquired from the electromagnetic torque T_e and rotor current amplitude I_r as

$$R_r = \frac{2\, T_e\, \omega_r}{3 I_r^2} \frac{s}{(1-s)}. \tag{4}$$

B. Inverse Γ-Form Model (IGFM)

Fig. 2 shows the steady-state IGFM, a transformed model from the TFM. It is commonly used as an IM control template. The reason for applying the IGFM instead of the physically more relevant TFM is that the TFM is over-parameterized for a dynamic analysis controller design [16]. The IGFM parameters can be transformed from the TFM by

$$R_R = \left(\frac{L_m}{L_r}\right)^2 R_r \tag{5}$$

$$L_M = \frac{L_m^2}{L_r} \tag{6}$$

$$L_\sigma = L_s - L_M \tag{7}$$

$$\underline{\psi}_R = \frac{L_m}{L_r}\, \underline{\psi}_r. \tag{8}$$

When applying Park's transformation as well as the PFOC, aligning the rotor flux linkage $\underline{\psi}_R$ to the d-axis is assumed. Then there is no q-quantity of the rotor flux linkage ψ_R^q and the d-quantity ψ_R^d equals Ψ_R. Hence, the electrical slip speed and electromagnetic torque of IMs can be stated as

$$\omega_2 = \frac{R_R\, i_s^q}{\psi_R^d} \tag{9}$$

$$T_e = \frac{3}{2} N_p\, \psi_R^d\, i_s^q. \tag{10}$$

From (9) and (10), if the parameters of R_R, L_M and ψ_R^d are predicted well, an accurate torque determination of the IM by i_s^d and i_s^q can be achieved.

C. Rotor Rotational u-v Coordinate System

With a FEM software like Ansys/Maxwell, the induced voltage, current, and flux linkage in a single rotor bar can be

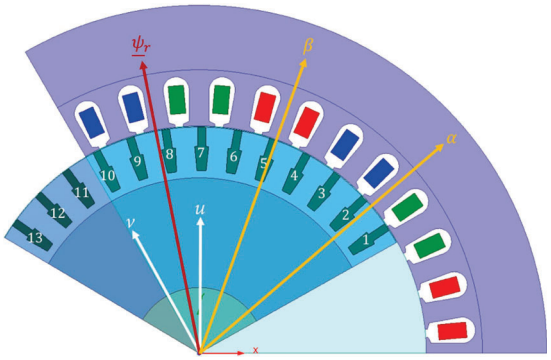

Fig. 3. Schematic of coordination of the 15 kW IM FEM model.

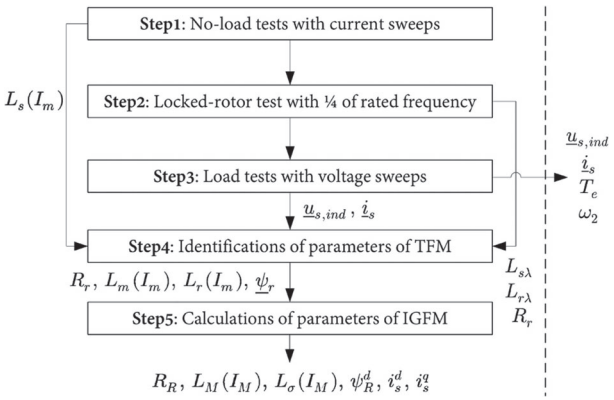

Fig. 4. Flowchart of conventional method.

determined. As mentioned in [15], results with higher quality can be obtained by using a transient solver rather than a time-harmonic solver regarding saturation and deep-bar effects, and accordingly, in this work, the transient solver has been used. In order to map the variables from different rotor bars to one pole, a coordinate system, u-v, fixed to the rotor mechanically, with the u- and v- directions defined as the real and imaginary parts respectively, is implemented.

Fig. 3 is a schematic of how different coordinate systems are located at the cross-section of the investigated six-pole 15 kW IM FEM model. On the stator side, the α-axis is at the direction of the flux linkage of phase A (red wires in the slot), and the β-axis is $\pi/2$ lagging to α-axis. On the rotor side, the u-axis and v-axis are at the electrical angle of π ($Bar07$) and $3\pi/2$ of the rotor, respectively. Furthermore, the position of $\underline{\psi}_r$ is the orientation of the d-axis. The fundamental time-varying variables in different rotor bars of a segment have the same amplitude and frequency (ω_2), and a phase shift of $(2\pi N_p)/Q_r$ between each neighbour bars [17]. Hence, in the u-v plane these variables can be formulated as

$$x^{uv}_{bar,k}(t) = X^{uv}_{bar}\cos\left[\omega_2 t - \frac{(k-1)2\pi N_p}{Q_r}\right] \quad k = 1, 2, \ldots, Q_r/2N_p \tag{11}$$

where x can be u, i, or ψ, and X can be U, I, or Ψ.

Next, projecting all variables to the rotor fixed axis, the u- and v-components of these variables, such as the total rotor current variable, can be determined as

$$\begin{cases} x^u_r(t) = \sum_{k=1}^{Q_r/2N_p} x^{uv}_{bar,k}(t)cos\left[\pi - (k-0.5)\frac{2\pi N_p}{Q_r}\right] \\ x^v_r(t) = \sum_{k=1}^{Q_r/2N_p} x^{uv}_{bar,k}(t)\sin\left[\pi - (k-0.5)\frac{2\pi N_p}{Q_r}\right] \end{cases}. \tag{12}$$

With the components of ψ^u_r, and ψ^v_r at $t = 0$, which can be computed from (12), the initial phase angle of $\underline{\psi}_r$ in the stationary α-β coordinate system can be found as

$$\theta_{rf0} = \theta_{u,0} + \theta^{uv}_{\underline{\psi}_r 0} \tag{13}$$

where the initial phase angles of the u-axis in the α-β axes is $\theta_{u,0}$ and $\underline{\psi}_r$ in the d-q plane is $\theta^{uv}_{\underline{\psi}_r 0}$ respectively.

Oriented in the direction of $\underline{\psi}_r$ with the real part represented by the d-direction, θ_{rf0} is also known as the initial electrical angle between the α-β and d-q axes and it can be utilized to recognize the phase angles of all phasors in the d-q plane.

D. Transferring the Rotor Quantities to the Stator Side

As the rotor quantities of the IM are all induced by the stator side, similarly to the secondary and primary sides of a transformer, the amplitude of the rotor variables from the rotor side in the u-v coordinate system can be transferred to the stator side by

$$\Psi_r = \frac{2N_s q_s k_1 N_p}{c_s}\Psi^{uv}_{bar} \tag{14}$$

$$I_r = \frac{Q_r c_s}{6N_s q_s k_1 N_p} I^{uv}_{bar} \tag{15}$$

where Ψ_r, I_r, Ψ^{uv}_{bar}, and I^{uv}_{bar} are the amplitudes of the variables.

III. IM Parameters Identification

A. Conventional Method

Using the conventional method from [5], the parameters of IMs at their rated point, typically a single operating speed, are identified by the no-load and the locked-rotor tests. Since it is the total leakage inductance $L_{s\lambda} + L_{r\lambda}$ that can be determined in the locked-rotor test, a ratio of $L_{s\lambda}/L_{r\lambda}$ needed to be assumed. Here, this ratio is assumed to be 1 according to the recommendation in [5].

The conventional method, summarized in Fig. 4, is applied using Ansys/Maxwell. In the first step, several no-load tests with various stator current magnitudes will be performed to determine the dependence of L_s on I_m. A locked-rotor test with 25% of the rated frequency is applied to find R_r and $L_{s\lambda} + L_{r\lambda}$ in the second step.

To compare with the new method, the phasors of $\underline{u}_{s,ind}$, and $\underline{i}_s$ from the load test are used to find the magnetizing current $\underline{i}_m$ by

$$\underline{u}_m = \underline{u}_{s,ind} - j\omega_0 L_{s\lambda} \tag{16}$$

$$\underline{i}_m = \underline{i}_s + \frac{\underline{u}_m}{R_r + j\omega_0 L_{r\lambda}}. \tag{17}$$

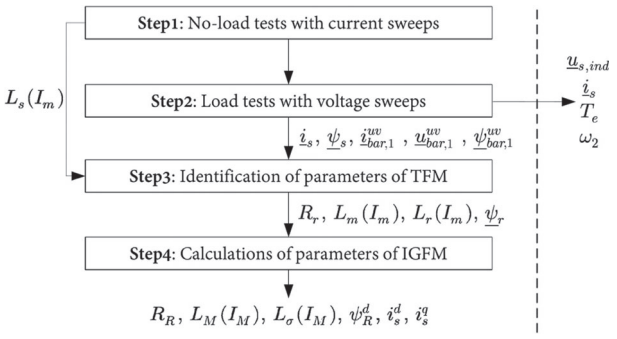

Fig. 5. Flowchart of a new proposed procedure.

The data of $\underline{u}_{s,ind}$, $\underline{i}_s$, T_e, and ω_2 are also saved for later verification.

In the third step, with the amplitude of the magnetizing current I_m by (17), in addition to $L_{s\lambda}$, $L_{r\lambda}$, and $L_s(I_m)$ from the second step, $L_m(I_m)$, $L_r(I_m)$ can be found. Furthermore, the rotor flux linkage phasor $\underline{\psi}_r$ can be obtained by (3).

The final step is to apply (5)–(8) to resolve R_R, $L_M(I_M)$, $L_\sigma(I_M)$, and ψ^d_R. With the amplitude of $\underline{i}_s$ from the third step and ψ^d_R, the d- and q-quantities of stator current i^d_s and i^q_s can also be acquired by

$$i^d_s = \frac{\psi^d_R}{L_M} \tag{18}$$

$$i^q_s = \sqrt{(I_s)^2 - (i^d_s)^2}. \tag{19}$$

B. Proposed Method

The flowchart of the proposed method in this paper is shown in Fig. 5. After a no-load test with the stator current magnitude sweep to find the relations of L_m and I_m, the stator phasors can be directly obtained from the FEM results in the second step. Moreover, to get the information of the rotor branch, the current and induced voltage phasors from the rotor bar $\underline{i}^{uv}_{bar,1}$, $\underline{u}^{uv}_{bar,1}$ are acquired from an end-connection in Ansys/Maxwell which represents the end-rings in 2D FEA simulation. The rotor bar flux linkage phasor $\underline{\psi}^{uv}_{bar,1}$ can be derived by

$$\psi^{uv}_{bar,1}(t) = \int u^{uv}_{bar,1}(t)dt. \tag{20}$$

Then transferred to the stator side by (14) and (15), rather than the way to bypass the magnetizing branch in the locked-rotor test.

Then, with the curve of $L_s(I_m)$ from the first step and the other phasors from the second step, R_r, $L_m(I_m)$, $L_r(I_m)$, and $\underline{\psi}_r$ can be obtained in the third step. Finally, the fourth step is the same final step as the conventional method.

C. Performances of IM Calculated From IGFM

In order to verify the usefulness of the proposed improved model, the acquired parameters of the IGFM are utilized to calculate the performances of IM, and the results are compared with the ones from FEM simulations.

The electromagnetic torque can be derived as in (10). Next, the equivalent impedance in Fig. 2, $R_{eq} + jX_{eq}$, can be formulated via the parameters of the IGFM as

$$R_{eq} = R_s + \frac{\omega_0^2 L_M^2 \frac{R_R}{s}}{\left(\frac{R_R}{s}\right)^2 + \omega_0^2 L_M^2} \tag{21}$$

$$X_{eq} = \omega_0 \left[L_\sigma + \frac{L_M \left(\frac{R_R}{s}\right)^2}{\left(\frac{R_R}{s}\right)^2 + \omega_0^2 L_M^2} \right]. \tag{22}$$

Furthermore, the amplitude of input phase voltage (U_s), input active power (P_{in}), input reactive power (Q_{in}),and power factor ($p.f.$) can be derived by

$$U_s = I_s \sqrt{R_{eq}^2 + X_{eq}^2} \tag{23}$$

$$P_{in} = \frac{3}{2} I_s^2 R_{eq} \tag{24}$$

$$Q_{in} = \frac{3}{2} I_s^2 X_{eq} \tag{25}$$

$$p.f. = \frac{P_{in}}{\frac{3}{2} U_s I_s}. \tag{26}$$

IV. Verification by FEM Simulations

In [1], the results have shown that the proposed method has better representation in the range of input voltage levels with the same rotor speed 980 rpm than the conventional method from [5]. In this work, a range of rotor speeds $995 - 950\tilde{}rpm$ (Slip = 0.5%–5%) with the same input voltage level are applied to examine the robustness of the proposed method further.

A. FEM Model

The design details of investigated FEM model are presented in Table I. Its cross-section of one pole-pair is in Fig. 3.

B. IGFM Parameters From the Proposed and Conventional Methods

Two parameter sets from the proposed and conventional methods by FEM simulations with sweeping input voltages are presented in Fig. 6 and Table II. The approaches are stated in Figs. 4 and 5.

These two sets of IGFM parameters will be used to find stator current's d- and q-quantities (i^d_s and i^q_s). Next, the performance of a 15 kW IM could be predicted by (21)–(26).

C. Results of the Performance of a 15 kW IM From FEM Model and IGFMs

The comparative results of the performance of a 15 kW IM derived directly from the FEM model and two IGFMs from the proposed and conventional methods are shown in Fig. 7–12. The blue solid lines with triangle markers are the results directly from the FEM model described in Section IV-A, using the rated voltage with slip values ranging from 0.5% to 5% is applied. The

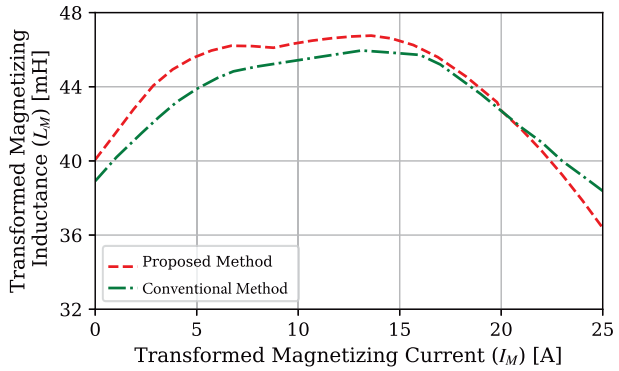

Fig. 6. Transformed magnetizing inductance curve.

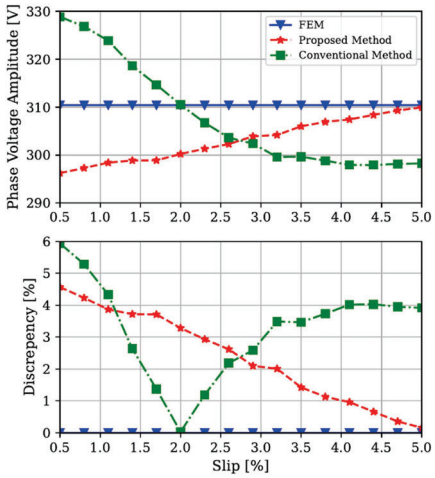

Fig. 7. Comparisons of phase Voltage (Amplitude U_s) from the FEM model and two IGFMs.

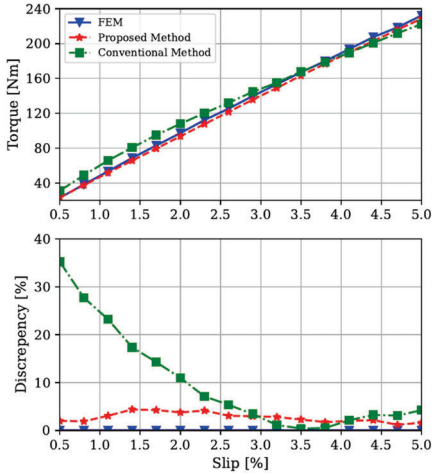

Fig. 8. Comparisons of torque (T_e) from the FEM model and two IGFMs.

TABLE I
DESIGN DETAILS OF THE 15 KW IM

Parameter	Value	Unit
Rated output power	15	kW
Rated speed	980	rpm
Rated line-to-line input voltage (RMS)	380/50	V/Hz
Number of pole pairs N_p	3	-
Iron core stack length	230	mm
Stator outer diameter	291.2	mm
Stator inner diameter	190.2	mm
Number of stator slots Q_s	36	-
Rotor outer diameter	189.3	mm
Rotor inner diameter	55	mm
Rotor end-ring average diameter	163.3	mm
Number of the rotor slots Q_r	39	-
Number of turns per coil N_s	38	-
Area of a stator turn	1.98	mm^2
Number of parallel strands per turn	2	-
Number of parallel branches N_{pb}	3	-
Terminal connection	Y	-
Stator coil temperature	70	°C
Stator coil material	Copper	-
Rotor bar temperature	102	°C
Rotor bar material	Aluminium	-
Iron core material	M700-50A	-

TABLE II
TRANSFORMED ROTOR RESISTANCES AND LEAKAGE INDUCTANCE

Parameter	Unit	Conventional	Proposed
L_σ	mH	4.38	3.89
R_R (102°C)	Ω	0.199	0.215

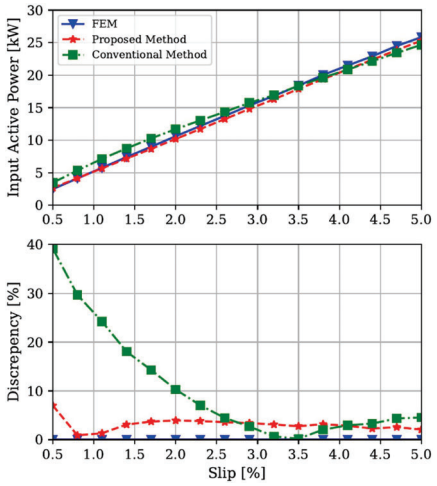

Fig. 9. Comparisons of input active power (P_{in}) from the FEM model and two IGFMs.

amplitude of the stator current derived from the FEM simulations and the same degree of slip with the FEM model are the boundary conditions of the two IGFMs in Section IV-B. The predictions from the proposed methods are presented as red dashed lines with star markers, and the ones from the conventional method are shown as green dash-dotted lines with square markers.

From Fig. 7, both methods have certain skews from ones of the FEM model, however, they can maintain the discrepancies under 6% in terms of phase voltage amplitudes (U_s). In terms

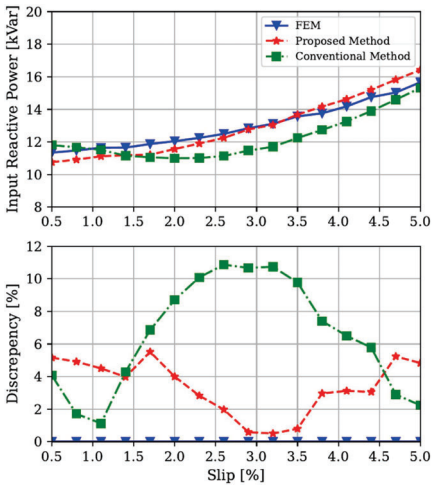

Fig. 10. Comparisons of input reactive power (Q_{in}) from the FEM model and two IGFMs.

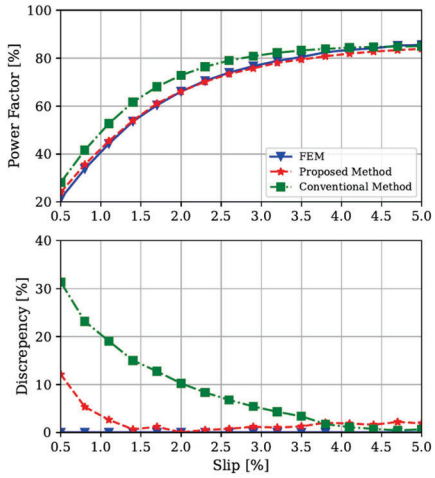

Fig. 11. Comparisons of power factor ($p.f.$) from the FEM model and two IGFMs.

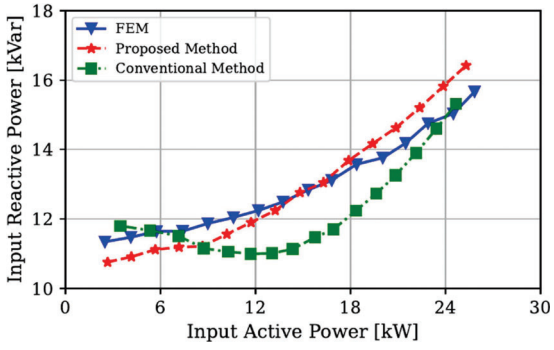

Fig. 12. Comparisons of power curve from the FEM model and two IGFMs.

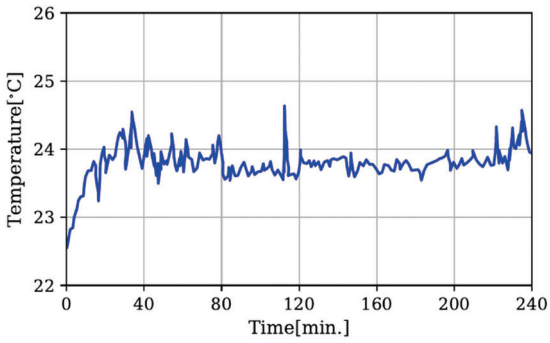

Fig. 13. Example of ambient temperature fluctuations.

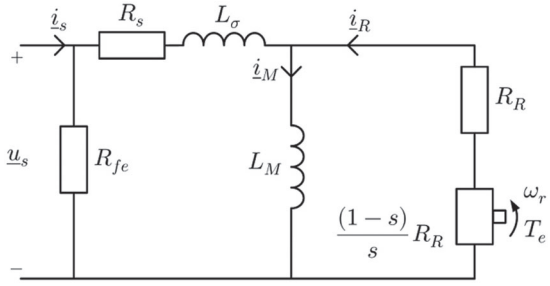

Fig. 14. Inverse-Γ form model with iron loss resistance (R_{fe}).

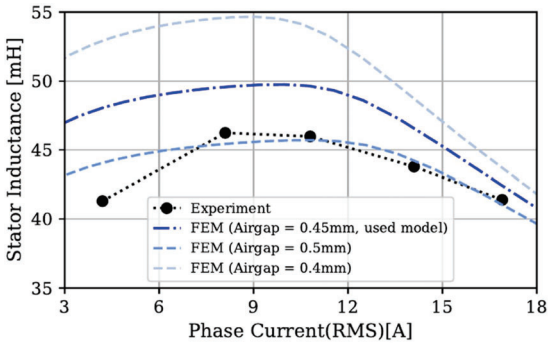

Fig. 15. Curve of the stator inductance at no-load tests.

of electromagnetic torque (T_e), input active power (P_{in}), input reactive power (Q_{in}), and power factor ($p.f.$), most of the estimations by the proposed method outweigh the ones by the conventional method as shown in Figs. 8–12.

V. Verification by Experimental Results

Measurements from a 15 kW 6-pole machine [18] are used in the work. Results from five no-load tests and three load tests with sinusoidal feeding have been run for four hours to make sure the steady-state temperature is achieved, which are shown in Fig 13. The temperatures of stator conductors and rotor conductors are recorded during tests.

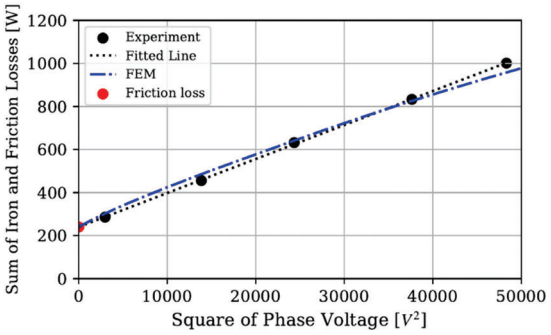

Fig. 16. Curve of the sum of iron and friction losses at no-load tests.

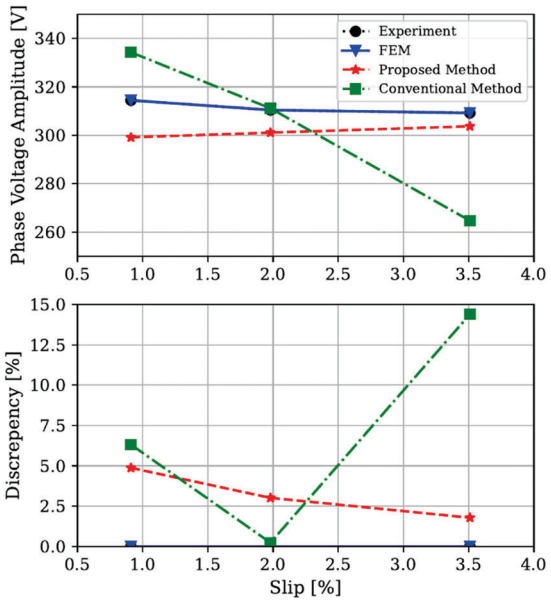

Fig. 17. Comparisons of phase Voltage (Amplitude U_s) from experiments, the FEM model, and two IGFMs.

A. Description of Measurements Set-Up

The machine under investigation was an ABB MBT-180 L, with mark plate 15 kW, 970 rpm, 380 V, 32 A. It was equipped with a PT100 thermal sensor in the end ring of the rotor bar as well as in the stator conductors. The induction machine was connected to a driving DC-machine, a DMP 160-4S 40.1 kW 2470 rpm driven by a TYRAK S 120 A thyristor converter. The power was measured by a Siemens B4301 three-phase power meter. The torque was measured using a 500 Nm HBM torque sensor.

B. IGFM With Iron Loss Resistance

In Fig. 14, an updated model of the IGFM considering iron loss is presented. In the following verification, this updated parameter-based model will be used. The iron loss representation, R_{fe}, is extracted from experimental no-load tests, and the rest of the parameters are from Section IV-B.

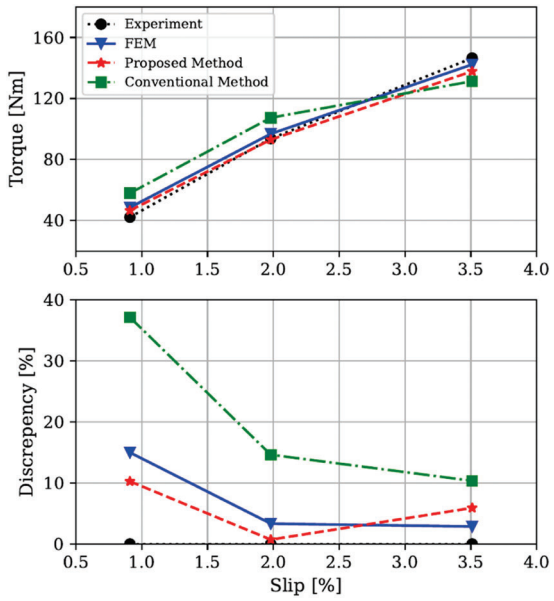

Fig. 18. Comparisons of torque (T_e) from the FEM model and two IGFMs.

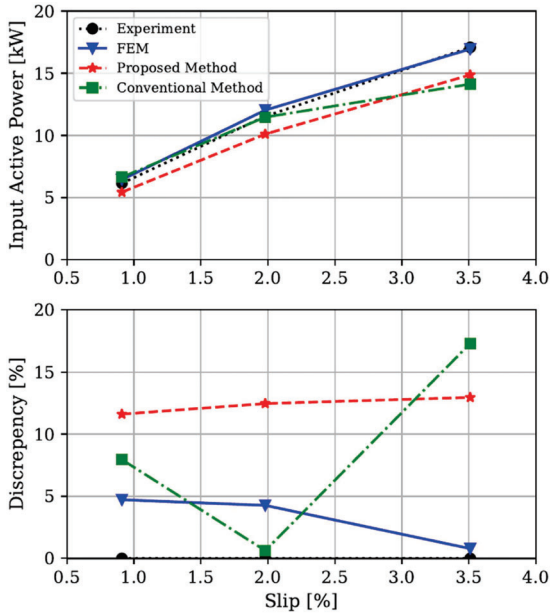

Fig. 19. Comparisons of input active power (P_{in}) from experiments, the FEM model, and two IGFMs.

C. No-Load Tests

The results of the five no-load tests with frequency of 50 Hz are listed in Table III.

Furthermore, to examine the usefulness of the FEM model, a comparison of stator inductance varying with the stator current is shown in Fig. 15. The blue dash-dotted line is the used FEM model with airgap length equals $0.45\tilde{}mm$, and the dotted black

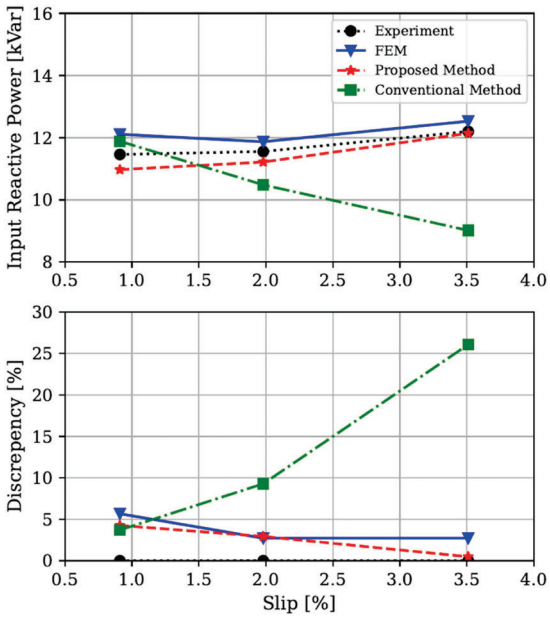

Fig. 20. Comparisons of input reactive power (Q_{in}) from experiments, the FEM model, and two IGFMs.

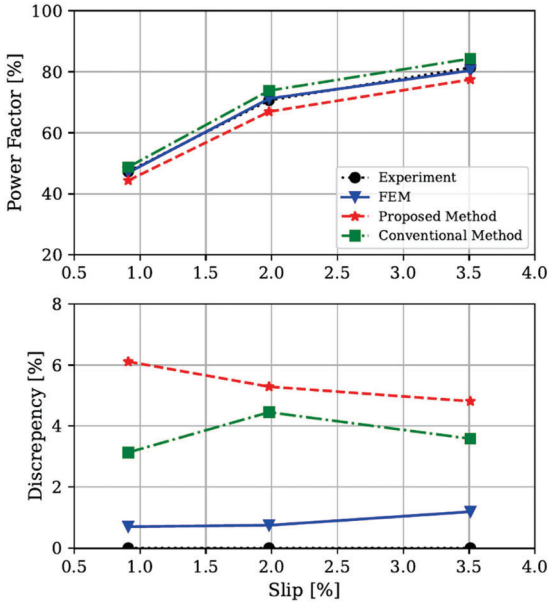

Fig. 21. Comparisons of power factor ($p.f.$) from experiments, the FEM model, and two IGFMs.

TABLE III
EXPERIMENTAL RESULTS OF NO-LOAD TESTS

No-load test	1	2	3	4	5
Line-to-line voltage [V]	94.4	203.8	270.2	336	380.7
Phase Current (RMS) [A]	4.2	8.1	10.8	14.1	16.9
Input power [kW]	0.296	0.494	0.701	0.953	0.1178
Winding temperature [°C]	28.38	34.29	39.46	46.25	52.53

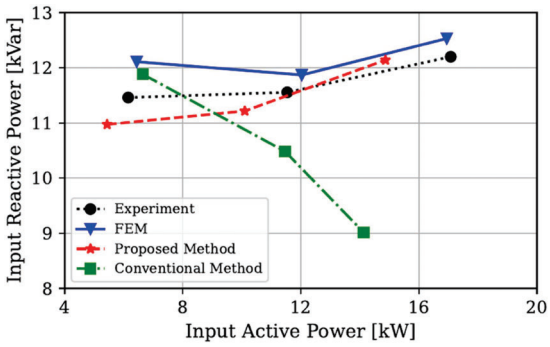

Fig. 22. Comparisons of power curve from experiments, the FEM model, and two IGFMs.

TABLE IV
EXPERIMENTAL RESULTS OF NO-LOAD TESTS

Parameters	Unit	Value
Iron loss resistance (R_{fe})	Ω	191.02
Friction loss ($P_{friction}$)	W	240.29

line is from the experiment. It is clear that the discrepancy from the used FEM model decreases with the stator's current level.

There are two possible reasons for the discrepancy. First, the magnetizing inductance values are very sensitive to the exact airgap length, and only 0.05 mm would make the discrepancy [7]. As shown in Fig. 15, the variations of 0.05 mm make increase and decrease in 5 mH of stator inductances. Second, the effect of end-winding leakage inductance is not included in this 2D FEM model, which would produce more discrepancy between FEM simulations and experiments.

Since the output power is zero in no-load tests, the input power represents the sum of stator ohmic loss (P_{strand}), core loss (P_{fe}), and friction loss ($P_{friction}$). With the design details in Table I and stator winding temperature, the stator resistance R_s and P_{strand} can be calculated and separated from the no-load loss. In Fig. 16, curves of the sum of P_{fe} and $P_{friction}$ versus the square of phase voltage are depicted from experiments and FEM simulations. The black dots are the data points from experimental results, and the dotted line is the fitting curve of data points. Since the rotor speeds of these tests are almost the same, which is almost synchronous speed, the friction loss can be identified at the crossing of the y-axis and the fitted curve listed in Table IV.

In addition, in order to make the FEM model closer to reality, a factor due to the manufacturing process is applied to iron loss calculations in FEM simulations [19]. Such compensation factors for iron losses vary in the given literature, typically between 1.7–2, and here the value given in [20], 2, used. The blue dash-dotted line is the sum of the adjusted iron loss from the FEM simulation and experimental friction loss.

D. Load Tests

The results of three load tests with an injected frequency of 50 Hz are listed in Table V. The output power and torque could be separated by deducting all losses, where P_{strand} is from R_s

TABLE V
EXPERIMENTAL RESULTS OF LOAD TESTS

Load test	1	2	3
Line-to-line voltage	385.1	380.2	378.7
Phase current [A]	19.5	24.8	32
Input power [kW]	6.15	11.54	17.08
Rotor Speed[rpm]	990.9	980.2	964.9
Winding temperature [°C]	57.25	69.79	102.82
Rotor end-ring temperature [°C]	78.75	102.49	158.32

with temperature adjustment and P_{fe} as well as $P_{friction}$ are from no-load tests.

E. Results of the Performance of a 15 kW IM From Experiments, FEM Model, and Two IGFMs

The comparative results of the performance of a 15 kW IM derived from experiments directly from the FEM model and two IGFMs from the proposed and conventional methods are shown in Figs. 17–22.

It can be observed that the predictions directly from the FEM simulations are most close to the experimental results generally. However, the proposed method makes the best estimations in terms of torque, as shown in Fig. 18 for these three load tests. The predictions of P_{in} from the proposed method are lower than the ones from experiments and the FEM model. Furthermore, the discrepancies are higher than the ones in Sections IV-C from within 10% to 15%. The main reason is the calculations of iron losses (P_{fe}) of circuit-based models depend on U_s. Thus, the underestimations of U_s from the proposed method make the discrepancies larger in P_{in}. Nevertheless, the proposed method still shows improvement in predicting U_s, T_e, and Q_{in} compared to the conventional method.

VI. CONCLUSION

A novel methodology to determine the equivalent circuit parameters of an IM is proposed. It is aimed to be utilized for machines with different rotor speeds in applications. Thus, an analysis with different slips is performed in Ansys/Maxwell. In addition, a conventional method from [5] is applied to benchmark the performance of the proposed method. Moreover, experimental results are included to examine the usefulness of all three models. The results have shown that the proposed method has a better forecast of the torque, meaning that it has better representation and is more suitable to be applied in various speed applications than using parameters from the conventional method.

A very valuable effort for future work would be to bring the stator supply disconnection test toward standardization. Furthermore, the incorporation of end winding leakage inductance, in addition to the 2D FEA analysis, would be very valuable as well.

APPENDIX

An experimental flux-decay test was also made on the 15 kW IM. The reason is that with this methodology, the rotor resistance can be determined in particular. There is yet no standard for this test, and accordingly, [5] was used as the main reference in this article.

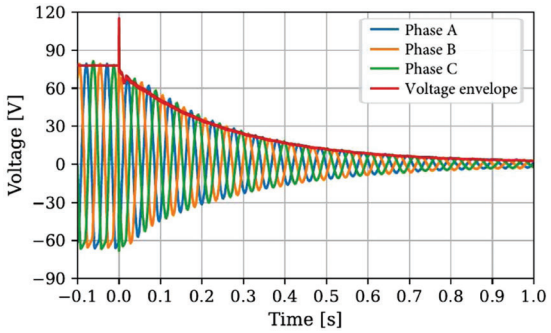

Fig. 23. Three-phase stator phase voltage and their envelope during flux-decay test.

The flux-decay test in this study comprises two stages. Initially, a no-load condition is implemented to magnetize the iron core. In the second stage, the supply power is cut off, and the stator current becomes zero. After a voltage spike, the rotor flux decays to zero, which is reflected in the stator voltage.

Several tests at various flux levels were made. In the case selected for presentation, the input phase voltage is $54V_{rms}$ and 20 Hz to make the input current become around $10A_{rms}$. The reason for selecting this input voltage is to derive a decay period when the saturation level of the iron core is moderate, leading to a relatively stable mutual inductance L_M, at least initially.

The three-phase stator voltages and their envelope is presented in Fig. 23. It is worth noting that there is an obvious step down in the stator voltage envelope at the $time = 0^{\tilde{}}s$, which is contributed by stator leakage inductance [9]. A hypothesis of this work is to calculate stator leakage inductance $L_{s\lambda}$ by

$$L_{s\lambda} = \frac{U_{s,NL} - U_{s,FD0}}{2\pi f_0 i_{s,NL}} \tag{27}$$

where $U_{s,NL}$ and $I_{s,NL}$ is the amplitude of stator voltage and current at the first stage, respectively, $U_{s,FD0}$ is the initial amplitude of stator voltage in the second stage, and f_0 is supplied frequency. In Fig. 23, the fitted curve by

$$U_{s,FD} = U_{s,FD0} e^{-\frac{t}{\tau_r}} \tag{28}$$

is shown, where τ_r is the rotor time constant and can be stated by

$$\tau_r = \frac{L_r}{R_r}. \tag{29}$$

Here, the rotor leakage inductance $L_{r\lambda}$ is assumed to be equal to $L_{s\lambda}$ at the flux-decay test, which means $L_r = L_s$.

The calculated parameters from this flux-decay test, together with the ones obtained through the conventional method from [7], are listed in Table VI.

In Fig. 25, three sets of parameters of R_r are compared. The red dotted line is the value from a 10 Hz locked-rotor test from [7], the blue dots are results from 0.1 s intervals (when assuming a constant magnetising inductance), and the green

TABLE VI
PARAMETERS FROM EXPERIMENTAL RESULTS (RESISTANCES REFERRED TO 20 °C)

Parameter	Flux-decay test	Conventional method	Unit
L_s	46.56	47.55	mH
R_r	0.168	0.19	Ω
$L_{s\lambda}$	2.38	2.55	mH
$L_{r\lambda}$	2.38	2.00	mH

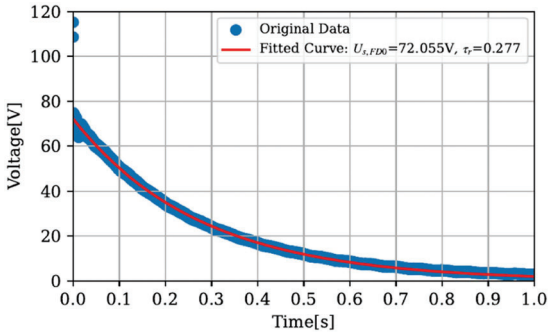

Fig. 24. Original voltage envelope and its fitted curve during flux-decay test.

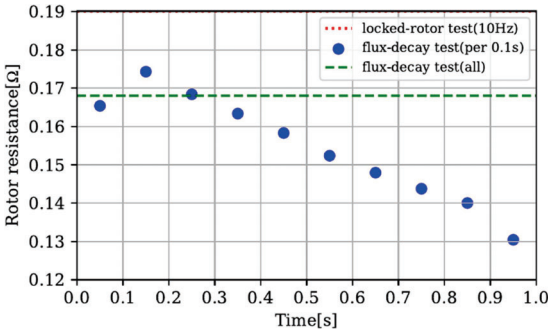

Fig. 25. Comparisons of rotor resistances at 20 °C from three different approaches.

dashed line refers to the curve-fitting of the flux-decay test for the whole period, respectively. The results are similar to the trend found in [9]. However, in [9], it was moreover found that a value of about 20 % of the rotor resistance should be deducted to account for the iron losses in the stator, which seemed to give a rotor resistance that would have been very low compared to what the load test predicted.

REFERENCES

[1] M. J. Hsieh, T. Thiringer, and E. A. Grunditz, "Improved parametric representation of IM from FEM for more accurate torque predictions," in *Proc. Int. Conf. Elect. Mach.*, 2022, pp. 599–605, doi: 10.1109/ICEM51905.2022.9910617.

[2] S. Bozhko, S. Dymko, S. Kovbasa, and S. M. Peresada, "Maximum torque-per-amp control for traction IM drives: Theory and experimental results," *IEEE Trans. Ind. Appl.*, vol. 53, no. 1, pp. 181–193, Jan./Feb. 2017, doi: 10.1109/TIA.2016.2608789.

[3] H. Cai, L. Gao, and L. Xu, "Calculation of maximum torque operating conditions for inverter-fed induction machine using finite-element analysis," *IEEE Trans. Ind. Electron.*, vol. 66, no. 4, pp. 2649–2658, Apr.. 2019, doi: 10.1109/TIE.2018.2847700.

[4] Z. Peng, "Analysis and implementation of constrained MTPA criterion for induction machine drives," *IEEE Access*, vol. 8, pp. 176445–176453, 2020, doi: 10.1109/ACCESS.2020.3024195.

[5] "*IEEE Standard Test Procedure for Polyphase Induction Motors and Generators*," IEEE Standard 112-2017 (Revision of IEEE Standard 112-2004), 2018, doi: 10.1109/IEEESTD.2018.8291810.

[6] A. H. Bonnett and G. C. Soukup, "NEMA motor-generator standards for three-phase induction motors," *IEEE Ind. Appl. Mag.*, vol. 5, no. 3, pp. 49–63, May/Jun.. 1999, doi: 10.1109/2943.758901.

[7] T. Thiringer, "Measurements and modelling of low-frequency disturbances in induction machines," Ph.D. dissertation, Chalmers University of Technology, Gothenburg, Sweden, 1996.

[8] M. Nachtsheim, J. Ernst, C. Endisch, and R. Kennel, "Performance of recursive least squares algorithm configurations for online parameter identification of induction machines in an automotive environment," *IEEE Trans. Transport. Electrific.*, vol. 9, no. 3, pp. 4236–4254, Sep.. 2023.

[9] E. Armando, A. Boglietti, F. Mandrile, E. Carpaneto, and S. Rubino, "A detailed analysis and guidelines for the induction motor flux-decay test," *IEEE Trans. Ind. Appl.*, vol. 60, no. 1, pp. 123–131, Jan./Feb.. 2024.

[10] L. Alberti, N. Bianchi, and S. Bolognani, "Variable-speed induction machine performance computed using finite-element," *IEEE Trans. Ind. Appl.*, vol. 47, no. 2, pp. 789–797, Mar./Apr.. 2011, doi: 10.1109/TIA.2010.2103914.

[11] M. Carraro and M. Zigliotto, "Automatic parameter identification of inverter-fed induction motors at standstill," *IEEE Trans. Ind. Electron.*, vol. 61, no. 9, pp. 4605–4613, Sep.. 2014. [Online]. Available: https://doi.org/10.1109/TIE.2013.2289903

[12] E. Mölsä, S. E. Saarakkala, M. Hinkkanen, A. Arkkio, and M. Routimo, "A dynamic model for saturated induction machines with closed rotor slots and deep bars," *IEEE Trans. Energy Convers.*, vol. 35, no. 1, pp. 157–165, Mar.. 2020.

[13] D. Lin, P. Zhou, and Z. Zhang, "Reduced order modeling and parameter identification of induction motors based on FEA solutions," *IEEE Trans. Energy Convers.*, vol. 38, no. 2, pp. 1108–1117, Jun.. 2023.

[14] R. Thomas, H. Husson, L. Garbuio, and L. Gerbaud, "Comparative study of the tesla model S and audi e-tron induction motors," in *Proc. 17th Conf. Elect. Mach., Drives Power Syst.*, 2021, pp. 1–6. doi: 10.1109/ELMA52514.2021.9503055.

[15] T. Schuhmann, B. Cebulski, and S. Paul, "Comparison of time-harmonic and transient finite element calculation of a squirrel cage induction machine for electric vehicles," in *Proc. Int. Conf. Elect. Mach.*, 2014, pp. 1037–1043.

[16] L. Harnefors, "*Appl. Signal Process. Control*," Västerås, Sweden, Department of Electronics, Mälardalen University, 2002, p. 68.

[17] O. Wallmark, "*AC Mach. Anal. Fundam. Theory*," Stockholm, Sweden: Department of Eletrical Conversion, KTH Royal Institution of Technology, 2020, p. 15.

[18] G. Kylander, "Temoeraturmätningar på en 15 kw asynkronmotor," Chalmers Tekniska Högskola, Gothenburg, Sweden, Tech. Rep. R-91-08, 1991.

[19] A. Krings, S. Nategh, A. Stening, H. Grop, O. Wallmark, and J. Soulard, "Measurement and modeling of iron losses in electrical machines," 2012. [Online]. Available: https://api.semanticscholar.org/CorpusID:34581380

[20] A. Acquaviva, S. Skoog, E. Grunditz, and T. Thiringer, "Electromagnetic and calorimetric validation of a direct oil cooled tooth coil winding PM machine for traction application," *Energies*, vol. 13, no. 13, 2020, Art. no. 3339. [Online]. Available: https://www.mdpi.com/1996-1073/13/13/3339

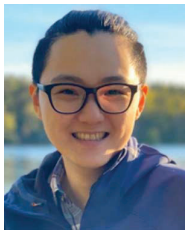

Meng-Ju Hsieh (Graduate Student Member, IEEE) received the M.Sc. degree in electrical engineering from Chang Gung University, Taiwan, in 2011. She is currently working toward the Ph.D. degree with the Chalmers University of Technology, Göteborg, Sweden. Her research interests include designing, modeling, and controlling vehicular traction electric machines, considering both environmental, and electromechanical performances.

Emma Arfa Grunditz (Member, IEEE) received the M.Sc. and Ph.D. degrees from the Chalmers University of Technology, Göteborg, Sweden, in 2009 and 2016, respectively. She is currently a Postdoc Researcher with the Chalmers University of Technology. Her research interests include electric drive systems, mainly for vehicular applications, regarding component and system cooling, energy consumption, performance, and cost.

Torbjörn Thiringer (Senior Member, IEEE) received the M.Sc. and Ph.D. degrees from the Chalmers University of Technology, Göteborg, Sweden, in 1989 and 1996, respectively. He is currently a Professor in electric power engineering with the Chalmers University of Technology. His research interests include the modelling, control, and grid integration of wind energy converters and power electronics, battery technologies, and electric machines for various applications.